THE EVOLUTION OF DISCHARGES WITH TWO AND THREE DIMENSIONAL TRAJECTORIES

A thesis submitted in partial fulfilment of the requirements for the

Degree of Doctor of Philosophy in Civil Engineering

in the University of Canterbury

by E. Scheepbouwer

University of Canterbury

2013

Table of Contents

Acknowledgements

First and foremost I would like to express my sincere gratitude to my supervisor Associate Professor Mark Davidson for his guidance, support, expertise and patience. During the many ups and downs of the work, his opinion and reassuring words on the topic at hand and on academic life in general were a source of stability and energy. I also thank Professor Roger Nokes for his comments on the work and his support.

I would like to thank the technical support that Mr. Ian Sheppard, Mr. Kevin Wines and Mr. Alan Stokes provided. Necessary adjustments and alterations to the experimental equipment were handled quickly and the work was of great quality, enabling the results that are the basis of this thesis. I also thank Mr. Peter McGuigan for his assistance in the environmental lab.

I thank my wife for supporting me in the decision to undertake the work.

I appreciate the financial support that the Canterbury Doctoral Scholarship provided.

Abstract

In the literature there is limited data available on the behaviour of discharges with three dimensional trajectories, although these are the most commonly found in the flows exiting (ocean) outfalls. The necessary three dimensional trajectory data requires cumbersome experimental systems and specialised laboratory setup. Therefore, results from two dimensional trajectory experiments are commonly extrapolated to enable prediction of the flow trajectories and dilutions of discharges that follow three dimensional paths. Importantly, there are also still some aspects of the behaviour of discharges with two dimensional trajectories that are not entirely clear. Non-buoyant flows discharged at an angle to the ambient flow, oblique discharges, behave either like a strongly advected jet or a momentum puff, depending on the discharge angle. Previous research indicated that the transition angle lies between 20° and 40°. Furthermore there is no clear distinction made between the cross sectional flow structure of buoyant and non-buoyant discharges in a cross flow, advected thermals and momentum puffs, and flow prediction models, like Visjet or Corjet, which assume these flows spread at the same rate.

The primary objectives of this research are to create a more comprehensive dataset for discharges with three dimensional trajectories; to ascertain the transitional discharge angle that separates flows that behave as a strongly-advected jet or a line momentum puff, and to establish whether there is a difference in the cross sectional concentration profiles of buoyant and non-buoyant discharges in a cross flow. The application of a double Gaussian distribution will be carried out for line advected thermals complimenting earlier work with line momentum puffs. The work feeds into these models and therefore can have an indirect impact on outfall design. A light attenuation system is employed to study the various discharges and the dynamic range is extended by developing a multiple dye system. This enables the evolution of the discharges to be measured over much greater distances. The light attenuation system is described in detail to substantiate the experimental results.

The new data shows that the mean tracer distributions for buoyant and non-buoyant discharges in a cross flow are distinct, with the former having a greater peak separation than the latter. This leads to differences in the relationships between peak and centreline concentrations. In addition, while the experimental spreading rates for the two flows are similar, the different forms of the puff and thermal profiles require distinctly different spreading rates for

standardised flow profile models, such as the ‘top hat’ models. Differences are also evident in the conversions needed to estimate peak values from the predictions of these standardised profiles and the implications of these differences are discussed in the context of integral models, which are commonly employed to predict the behaviour of such flows. The experimental data from the oblique discharge experiments showed that flows discharged at acute angles up to 32.4° displayed strongly advected jet behaviour, flows discharged at obtuse angles greater than 39.0° displayed momentum puff behaviour, while the intermediate 35.9° discharge appeared as some combination of the aforementioned flows.

A comprehensive experimental investigation into the behaviour of discharges with 3D trajectories has been carried out. The flows were released horizontally at an angle of 90°, 45°, or at 22° to the ambient current and the ambient to initial velocity ratio varied from 0.0042 to 0.057, extending the range of initial conditions previously considered. The experiments show limited variability in trajectory and dilution results around the average values. This provides the basis for conducting future experiments with fewer repetitions. The flows with initial discharges angles of 90° and 45° to the ambient motion, display initially line momentum puff and afterwards advected thermal behaviour. The consistent appearance of the characteristic double peaked distributions alleviates previously published concerns about the ability to transfer the understanding gained from discharges that follow a two dimensional path. However, the different orientations of the two peaks within these flow regimes introduces additional complexity into the transition region. In experiments with an initial discharge angle of 22° the double peak distribution did not develop until the flow evolved into an advected thermal, which was consistent with expectations based on the experiments with oblique discharges.

List of Figures

List of Tables

List of Notations

A	Absorbance, absorption
b	Velocity spread
B_0	Buoyancy
b_c	Concentration spread
b_{c1}, b_{c2}	Tracer spreads of the individual Gaussians
b_T	Velocity spread of top-hat distribution
b_{Tc}	Top hat concentration spread
C,c	Local tracer concentration
C_0	Initial tracer concentration
C_c	Tracer concentration at centre of double-Gaussian approximation
C_1, C_1	Maximum concentrations of the individual Gaussians
C_{i0}	Integrated initial tracer concentration
C_{iy}	Local integrated tracer concentration in the y direction
C_{iz}	Local integrated tracer concentration in the z direction
C_{Ju}	Trajectory constant
C_m	Peak tracer concentration within cross-section
C_T	Local top-hat concentration
C_{Tc}	Top-hat tracer concentration
d	Diameter of the source
D	Dark current
F, f_1, f_2	Distance between peaks of individual Gaussians non-dimensionalised by the spread
Fr	Initial Froude number
g	Gravitational constant
h, h_1, h_2	Ratios of the spreading rates in the z and y directions
i	Pixel location
I	Intensity of light that is transmitted through the sample.
I_c	Integral constant
I_{cdg}, I_{qc}, I_m	Shape constants
I_0	Intensity of light that illuminates the sample
I_q	Non-dimensional flow cross-sectional area
j	Pixel location
k	Gaussian spread constant

k_T	Top-hat spread constant
k_T	Spreading rate of the top-hat profiles
$k_{T,mp}$	Spreading rate of the momentum puff top-hat profile
K, K_{jm}, K_{pt}, K_{mt}	Spread constants
l_{jp}	Distance from the source to the jet-to-plume transition point
l_{jwj}	Length scale for weakly-advected jet to strongly-advected jet
l_{jmp}	Length scale for weakly-advected jet to momentum puff
l_{amp}	Distance of the projection of the *s* coordinate in the *y*-*z* plane from the virtual source
L	Length scale measured along the projection of the initial discharge direction in the *y*-*z* plane
M	Number of binned pixels
M_0	Initial momentum flux
M_a	Entrained ambient momentum flux
M_b	Buoyancy-generated momentum flux
M_{e0}	Initial-excess momentum flux
M_s	Total momentum flux
M_x	Momentum flux in the *x*-direction
M_y	Momentum flux in the *y* direction
M_z	Momentum flux in the *z* direction
N_r	Read noise
P	Incident photon flux
Q_e	CCD quantum efficiency
Q_0	Initial flow rate
$Q_{\square 0}$	Initial density deficit flux
r	Radial coordinate
Re	Initial discharge Reynolds number
s	Distance from source along trajectory
S_{jp}	Length-scale for the transition between jet and plume regions
S_{jmp}	Length-scale for the transition between jet and momentum puff regions
SNR	Signal to noise ratio
t	Time
u	Local velocity

U_0	Initial velocity
U_a	Ambient velocity
U_e	Excess velocity
U_{ar}	Ratio between ambient and initial flow velocity
u_T	Velocity in excess of the ambient velocity
x	Cartesian coordinate in the same direction as the ambient velocity; (in the direction of the horizontal component of the initial velocity for still ambient flows)
x_{amp}	Distance in the direction of the ambient velocity from the virtual source
y	Cartesian coordinate perpendicular to the x-coordinate in the horizontal plane
z	Cartesian coordinate in the same direction as the vertical component of the initial velocity
z_{pt}	Vertical distance from source to plume to advected thermal transition point
z_{vs}	Z location of the visual source
α, β	Angles
Δ	Local density deficit
Δ_0	Initial density deficit
Δ_i	Integrated centreline buoyancy
Δ_{i0}	Integrated initial buoyancy
ϕ	Angle between the initial discharge and the ambient fluid velocity in the x-y plane
θ	Angle between the initial discharge and the ambient fluid velocity in the x-z plane
ρ	Density of jet fluid
ρ_a	Density of ambient fluid
λ	Ratio of the spread of the mean concentration distribution to the spread of the mean velocity distribution
ϵ	Molar extinction coefficient
$*$	Denotes non-dimensionality

Chapter 1 - Introduction

1.1 General Introduction

Oceans continue to be a convenient way to release waste generated on land back into the environment because more than half the world's population lives within 100 km of the ocean. Generally there are three main inputs of pollution into the ocean: direct discharge of waste into the oceans through outfalls, runoff from land into the waters due to rain, and pollutants that are released directly from the atmosphere. In many parts of the world, sewage flows that are treated, under-treated, or untreated, are released into the oceans. This sewage can have direct and indirect negative effects on the marine environment. Harrison (2001) mentions aesthetic effects, temperature changes, deoxygenation, toxicity, disturbances of the pH regime of the ambient water and eutrophication as direct effects. Indirectly these can cause damage to aquatic or human life, changes in biodiversity and the threat of human disease can lead in turn to beach closures and the prohibition of the use of marine life for human consumption. Growing environmental concerns combined with an increased sense of human well-being has led to an increasing awareness of issues surrounding waste management. In 1972, the London Dumping Convention was one of the first global conventions to protect the marine environment from human activities and in 1996 the London Protocol further restricted what could be released into the ocean. This resulted in tightening restrictions for waste disposal set by councils and environmental agencies. Where older sewage systems simply discharged waste into rivers or near the shoreline, modern systems are designed to deliver treated waste off-shore through an outfall pipe and diffuser. To reduce the impact on the environment, the diffusers are designed to increase the dilution of wastewater as it is released into the ambient water. In order to better understand the dilution of waste fluids released into the environment, it is necessary to study the mixing processes near and far from the source. The reduction in concentration of pollutants in the far field is dominated by both mixing and decay processes, while the dilution in the near field is governed by the mixing processes alone. Predicting the initial mixing of wastewater discharges is a critical component in the design of outfall systems.

While the focus here is on marine discharges, the results are also relevant to other types of discharges, such as those released into the atmosphere. However, in the latter case the presence of the atmospheric boundary layer and its associated ambient turbulence limit the applicability

of these results. The strength of the ambient motion in the atmosphere often results in rapid transitions to far-field mixing and these conditions can also have a significant influence on behaviour in the near field. Thus application of the present results to alternative release conditions must be approached with some care. The experiments are conducted with near uniform ambient motion and minimal ambient turbulence, thus the most relevant atmospheric conditions are those where the ambient motions are relatively weak.

The near-field mixing of effluent released into a marine environment has several distinct forms (Jirka 2004). In an idealized context, the nature of this mixing depends on the relative importance of the initial momentum flux imparted to the flow as it is released into the environment, the momentum flux created due to density differences between the released and surrounding fluids (referred to as the buoyancy-generated momentum flux) and the momentum flux entrained with the ambient fluid as mixing takes place. Near the source the initial momentum flux is normally dominant, because it is some distance from the source before the buoyancy generated and entrained ambient momentum fluxes become significant. Where the entrained ambient momentum flux is relatively small or non-existent, the flow is referred to as being weakly advected and if the initial momentum flux dominates the flows behaviour it is referred to as a jet. The continued action of buoyancy forces can result in the buoyancy generated momentum flux dominating the flow behaviour and in this region the flow is referred to as a plume. However, if ambient motion is present the behaviour of the discharged fluid is eventually dominated by the entrained ambient flux and is then described as strongly advected. Several strongly advected regions can form and two of practical interest are the advected line momentum puff and the advected line thermal. In the former case the initial momentum flux plays an important secondary role in driving the mixing process, whereas in the latter case it is the buoyancy generated momentum flux that has this role. Both flows are characterized by mean velocity and tracer distributions that resemble those of a line vortex pair (Chu 1996, Gaskin 1995) as opposed to the weakly-advected regions where these profiles have a Gaussian form.

Numerical models of the evolution of these flow regimes and their associated mixing processes are needed to determine whether or not proposed designs meet the environmental standards set by the local agencies. Integral models such as CorJet (Doneker and Jirka 2007) and VisJet (Cheung et al. 2000) are commonly employed for this purpose. However, the application of these models requires the determination of a number of coefficients to quantify the mixing that is taking place (entrainment or spread coefficients, turbulent flux terms and conversion factors to move between peak and cross-sectional average values of parameters). Thus additional experimental

information has the potential to improve the implementation and interpretation of outputs from these and other similar models. Thus this information can directly feed into relevant applications and therefore have an impact on outfall design.

Over an extended period of time, a large number of experimental studies have been conducted into the nature of the mixing of discharges released into a stagnant ambient and during this time the sophistication of those studies has increased with the application of optical measuring systems (see Law and Wang (2000) for example). There has also been a recent focus on negatively buoyant discharges because of the application to discharges from desalination facilities (recent examples include Lai and Lee (2012), Papakonstantis (2011a, 2011b), and Kikkert et al. (2007)). Similarly the behaviour of discharges released into a moving ambient fluid has also been investigated extensively. However, there the focus has largely been on discharges that move along two dimensional paths, that is, they are discharged such that the initial momentum flux rests in the same plane as the buoyancy generated and entrained ambient momentum fluxes. Relatively few studies have focussed on the behaviour of discharges that follow three dimensional paths, that is, where the direction of the initial momentum flux is not aligned with the plane created by the entrained and ambient momentum fluxes. Indeed recently Kikkert et al. (2009) noted the following:

"It appears that increased flow complexities associated with discharges following 3D paths restrict the use of relatively simple conceptual models to interpret (and predict) their behaviour, particularly if such models are developed based on limited data from less complex discharge configurations. There is a need to obtain additional detailed laboratory data characterizing the behaviour of flows that follow 3D paths, so that predictive capabilities can be improved."

A primary reason for this lack of experimental data is the logistical difficulties in applying planar optical systems to discharges that move through the planar light sheet as opposed to along it, which is the case for discharges that following two-dimensional paths. An important focus of this thesis is the provision of additional data for discharges that follow three-dimensional paths, so that the performance of existing and future numerical models can be evaluated more effectively. The experimental systems developed for this research are also employed to provide additional information about the behaviour of some two-dimensional discharge configurations with the specific aim of aiding the interpretation of data gathered from the more complex three-dimensional discharge configurations. In preparation for this it is useful to firstly review the flow behaviour within the respective flow regimes in more depth,

1.2 Flow Regimes

As noted above turbulent flows created at the point of discharge move along time-dependent paths as they rise towards the ocean surface or fall back to the seabed. Differences in the density between the ambient and discharged fluids and the presence of ambient motion have a significant influence on the mixing processes. The nature of the flow is defined by the relative magnitudes of the initial momentum flux in excess of that required to move with the ambient, M_{e0}, the buoyancy generated momentum flux, M_B, and the entrained ambient momentum flux, M_a. Beyond the initial zone a self-similar flow forms and typically the initial excess momentum flux governs as the entrained ambient and buoyancy generated momentum fluxes develop. Restricting the scope of the study to discharge configurations where counterflowing conditions do not occur, the relative magnitudes of these momentum fluxes define five possible flow regimes and these are shown in Figure 1-1. It is evident in this figure that the flow can evolve from a jet to a line advected thermal through three possible intermediate regimes, the plume, the coflowing jet and the advected line momentum puff and thus there are three possible evolutionary paths. It should be noted that the transitions shown in this figure are not reversible. Once the entrained momentum flux has become larger than the initial excess momentum flux and the flow forms a momentum puff or coflowing jet, the flow can no longer become a plume because the entrained ambient momentum flux increases more rapidly than the buoyancy generated momentum flux with distance from the source. Similarly once the flow enters the plume region it can evolve into an advected thermal but not a momentum puff (or coflowing jet) because the buoyancy generated momentum increases whereas the initial excess momentum flux remains constant. Thus in the absence of boundary interaction and ambient turbulence, the final self-similar form of a buoyant discharge in a moving environment is the line advected thermal.

The cross-sectional form, rates of entrainment/spread and dilution and consequently the path followed can change dramatically as the flow progresses through these regimes and it is therefore important to identify where they occur. The locations of the transitions between these flow regimes can be estimated through a traditional dimensional analysis or through comparisons of relative sizes of the momentum fluxes as discussed above (Kikkert et al, 2009). Given that detailed descriptions of the relevant flow regimes are contained within the likes of Kikkert (2006) and Jirka (2004), there is limited value in repeating this here. However, for completeness brief

descriptions of each of the flow regimes (based on Davidson and Pun 1998) are given below, beginning with the two weakly-advected regimes, that is the Jet and the Plume.

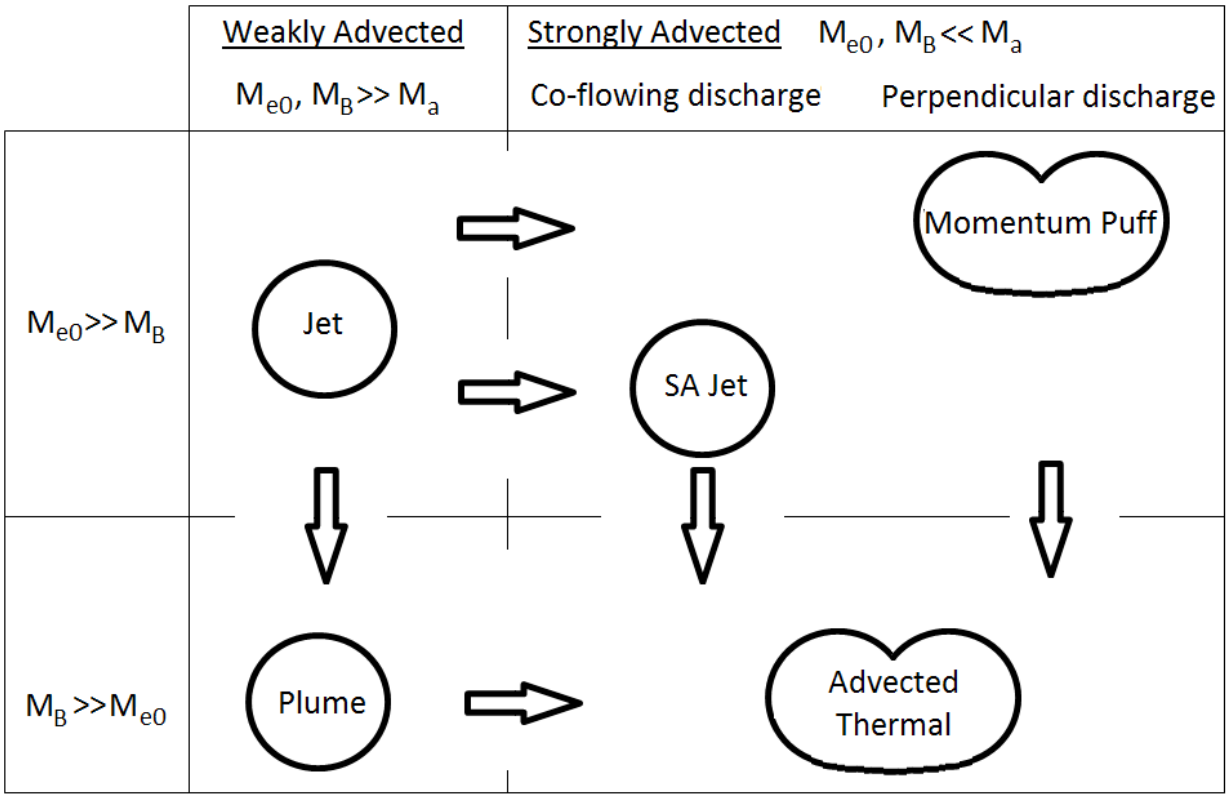

Figure 1-1: The possible flow regions and transitions between them. The regions are shown in their self-similar cross sectional form. The arrows represent the transitions between the flows.

(1) The Jet

This is the simplest of the flow regimes. In the context of the present study, in its purest form a jet is a turbulent flow created by discharging fluid into an ambient that has the same density. After the zone of flow establishment, or initial zone, that extends from the jet nozzle up to approximately six diameters in the flow direction (see for example Chu et al. 1999), the zone of established flow begins in which the crossflow concentration and the velocity profiles have been shown to be approximately Gaussian in form. These profiles have also been shown to be self-similar, so that the form of these profiles does not change with distance from the source. Given their relative simplicity and their ubiquitous nature, the behaviour of these flows has been investigated extensively in the past and additional details with regards to these flows can be obtained from studies such as Papanicolaou (1984), Papanicolaou and List (1988), Chu (1996), Wang and Law (2002) among others. In the context of the present study the key characteristics to note are the dependence on downstream distance of flow bulk parameters, spread, velocity and dilution, which can be written in the following form:

$$b \sim s \tag{1}$$

$$U_e \sim \frac{1}{s} \tag{2}$$

$$\frac{\Delta_0}{\Delta} \sim s \tag{3}$$

Where b represents the spread, s the distance from the source along trajectory, U_e the excess centreline mean velocity in excess of the ambient velocity (if present), Δ is the local density deficit, and Δ_0 is the initial density deficit. In this context the constants have been omitted, see for a more detailed description Davidson and Pun (1998)

(2) The Plume

A pure plume is created through a continuous discharge of buoyant fluid with very little initial momentum flux (Lee and Chu 2003 for example). The buoyancy forces generate the plumes' momentum flux and the flow spreads in a similar way to a pure jet. Like the pure jet the velocity and tracer concentration profiles of the established flow are self-similar and Gaussian in shape (Wang and Law 2002, and Papanicolaou and List 1988). These flows have also been investigated in the past and it is well established that the spread, velocity and dilution have the following dependence on vertical distance from the source:

$$b \sim z \tag{4}$$

$$U_e \sim \frac{1}{z^{1/3}} \tag{5}$$

$$\frac{\Delta_0}{\Delta} \sim z^{5/3} \tag{6}$$

Where z represents the travelled distance in the vertical direction. Despite the similar spreading rates and the Gaussian form of the mean cross sectional profiles, the dependence of key parameters on distance from the flow source differs significantly between jets and plumes. This reflects key differences in the driving mechanisms, which for a jet remains constant, whereas for a plume it continues to grow. These differences are also reflected in significant differences in the turbulent structure of the two flows, with much greater intensity and intermittency of turbulent fluctuations evident in plumes when compared to jets (Wang and Law 2002).

Strongly-Advected Flows

As noted above discharges released into a moving ambient can possess up to three kinds of momentum flux: the initial, buoyancy generated and entrained ambient momentum fluxes. As

the flow mixes with the ambient the total amount of entrained fluid along the trajectory continues to increase, hence eventually the entrained momentum dominates the flow behaviour and the flow becomes "strongly-advected". Once the flow reaches this stage the entrained ambient momentum flux not only plays a role in defining the trajectory of the flow through advection, but in addition it has a direct impact on the mixing processes. Experiments have shown that the presence of even a weak crossflow enhances the dilution considerably (Wright 1977, Lee et al. 1987). In figure 1-1, it is evident that three strongly-advected regimes are possible for the discharge configurations considered here,

(1) The Line Momentum Puff

Line momentum puffs are normally observed when a fluid of the same density as the ambient fluid is discharged perpendicularly to the ambient motion (a crossflow). This configuration creates a more complex interaction between the discharged and ambient fluids. While the flow initially behaves as a jet, once it evolves into a strongly-advected flow the mean cross sectional form of the profiles changes to that of a vortex pair and this cross sectional form has been shown to be self-similar (Keffer and Baines 1963, Smith and Mungal 1998, Chu et al. 1999, Kikkert 2006, Kikkert et al. 2007). There are significant changes to the dependence of the bulk parameters on distance from the source once the flow enters this regime, with the dilution, velocity, spread and trajectory being described by:

$$b \sim l_{amp} \tag{7}$$

$$U_e \sim \frac{sin\phi}{{l_{amp}}^2} \tag{8}$$

$$\frac{\Delta_0}{\Delta} \sim {l_{amp}}^2 \tag{9}$$

$$x_{amp} \sim \frac{{l_{amp}}^3}{sin\phi} \tag{10}$$

Where l_{amp} represents the distance of the projection of the *s*-coordinate in the *y*-*z* plane from the virtual source and ϕ denotes the angle between the initial discharge and the ambient fluid velocity. The virtual source is an assumed point source that has no width and produces instantaneously the velocity and concentration profile of the concerned flow and the *y*-*z* plane is the plane perpendicular to the ambient flow direction.

(2) The Line Advected thermal

This flow, with a similar structure to the advected line momentum puff is created when a pure plume becomes strongly-advected. It is also the final stage of a strongly advected flow with a different density to the ambient (Jirka 2004). The mean cross sectional profiles resemble those of a counter rotating vortex pair and this flow has also been shown to be self-similar (Richards 1963, Chu 1977, Knudsen 1988, Gaskin 1995, Jirka 2004) but the bulk behaviour differs significantly from other regimes. In the case of the line advected thermal the spread, velocity, dilution and trajectory can be approximated through the following relationships:

$$b \sim z \tag{11}$$

$$U_e \sim \frac{1}{z^{1/2}} \tag{12}$$

$$\frac{\Delta_0}{\Delta} \sim z^2 \tag{13}$$

$$x \sim z^{3/2} \tag{14}$$

(3) The Strongly-Advected Jet

The third strongly-advected region occurs in its purest form when a non-buoyant fluid is released in the same direction as the ambient motion (Davidson and Pun 1999). In contrast to the advected line momentum puff, for this discharge configuration the mean cross sectional profiles remain Gaussian when the flow becomes strongly-advected. Previous experimental investigations (examples include Davidson and Wang (2002) and Nickels and Perry (1996)) have shown the behaviour of the bulk parameters in the strongly-advected jet have the following dependence on distance from the source:

$$b \sim x^{1/3} \tag{15}$$

$$U_e \sim \frac{cos\phi^{1/3}}{x^{2/3}} \tag{16}$$

$$\frac{\Delta_0}{\Delta} \sim cos\phi^{2/3}.x^{2/3} \tag{17}$$

In summary it is evident that the behaviour of the bulk flow parameters within the five flow regimes differ significantly and it is therefore important to identify when or indeed if they occur for a given discharge configuration. While it is possible to make use of standardised profiles for all flow regimes, such as top-hat (Visjet – Cheung et al. 2000) or Gaussian (CorJet – Jirka 2004), which simplifies the model formulation, ultimately the details of the flow regime are needed to

map model predictions to peak cross sectional values. These mappings depend on the details of the cross sectional profiles and the peak values are the most significant when assessing potential environmental effects.

1.3 Predictive models

The models introduced in the previous section (Visjet and CorJet) represent a class of predictive tools that are commonly employed in practice to predict the behaviour of buoyant discharges. These numerical models make use of the integral form of the equations of motion, the assumption of self-similar cross sectional profiles and typically an entrainment assumption to model the behaviour of discharges. It is possible to replace the entrainment assumption with an equivalent spread assumption. Analytical solutions of the integral form of the equations are possible within the respective flow regimes and these can provide the basis for identifying the existence of particular flow types (for example Kikkert et al. 2009). It is also possible to make use of dimensional analysis to identify the expected behaviour within the flow regimes where the behaviour is governed by a limited number of flow parameters. However, the use of analytical solutions reduces the number of coefficients that need to be determined when compared to the dimensional analysis approach (Davidson and Pun 1998). While the development of predictive models is not a focus of this thesis, relatively simple numerical and analytical integral models will be developed to aid in the interpretation of the acquired data. Note that it is possible to model these flows with more sophisticated turbulence models employed to close the Navier-Stokes equations, see for examples of large eddy simulations Cui and Street (2001), Yuan et al. (1999) or for an application of a k-ε model, Oliver et al. (2008). However, these sophisticated models are very cumbersome to implement and are therefore not generally employed for predicting these flows, thus are beyond the scope of the present investigation.

1.4 Flow measurement techniques

Difficulties associated with measuring the behaviour of discharges following three-dimensional paths have been noted above. Measurement systems have improved dramatically from the intrusive techniques implemented to measure the mean cross sectional characteristics of buoyant discharges, such as the probe sampling systems implemented by the likes of Knudsen (1988) and Wong and Wright (1988) or the conductivity probe systems employed by Davidson et al. (1991).

Modern systems make use of optical measurement techniques such as Laser-Induced Fluorescence, Light Attenuation, Particle Tracking Velocimetry and Particle Image Velocimetry.

An appropriately calibrated Laser induced Fluorescence (LIF) system provides concentration field information and thus the ability to quantify mixing in aqueous flows. The objective of this experimental spectroscopic technique is to quantify the spatial and temporal distribution of a fluorescent tracer in a given (turbulent) flow. With this method a monochrome light source (laser) is used to excite molecules that will transmit light at a specific wavelength, a process called fluorescence. The laser emits light at a different wavelength to that transmitted from the molecules so it is possible, with the use of filters, to capture only the excited light. The flow of interest is seeded with a small amount of fluorescent dye. The laser beam is transformed into a thin laser 'sheet' usually with a rotating mirror placed in front of the laser. For the fluorescent molecules, rhodamine is often used (Lam and Chan 1995), but it is possible to use other dyes (Lavertu 2006). Rhodamine is practical because the emitted light is in the optical spectrum and can be captured using normal video cameras. If the absorption of the laser through the sample is assumed negligible, a uniformly lit sheet through the specimen can be created. The camera is placed perpendicularly to the laser sheet, and the captured light intensity is a function of the laser intensity and dye concentration, which through appropriate calibration provides the instantaneous concentration field in this sheet. Subsequent images captured by the camera, then provide temporal information. Many authors have made use of this technique to measure the details of mixing that can be associated with outfall discharges, some earlier examples include the works of Papanicolau (1984) , Koochesfahani and Dimotakis (1985, 1986), Lam and Chan (1995, 1997) and Gaskin (1995). Drawbacks of the system include the cost of the equipment, the use of potentially dangerous dyes, the sensitivity of the system to contaminants like dust particles floating in the specimen and the need to set up the light sheet along a specific plane to extract information from the flow.

Where Van Cruyningen et al. (1990) upgraded the Laser-induced Fluorescence technique to the planar systems that are typically used to measure flow behaviour today; Tian and Roberts (2003) have taken the system one step further in developing a 3D LIF system. With this system the planar light sheet is scanned through the flow and its location is correlated with the captured images, so that a series of planar concentration fields are obtained over a short period of time. These images are then processed to create a three-dimensional picture of the flow evolution. This is clearly the most sophisticated form of the Laser-induced Fluorescence systems, but it requires significant resources to implement and to date the primary focus of its application has been

discharges that follow two-dimensional paths, where it has provided considerable insight into the behaviour of these flows.

Particle tracking velocimetry, PTV, is a technique for the determining the in-plane velocity components of particles in a thin volume (see for instance Adamczyk and Rimai 1988 or Khalighi 1991). With this technique the sample flow is seeded with neutrally buoyant particles and a strong light source is used to create a light sheet that illuminates the flow along the direction of interest. The light reflected by the particles is recorded using a camera, set up perpendicularly to the light sheet. From subsequent images, the position of each particle or particle group can be tracked, enabling the creating of a velocity field. The combination of particle dimensions, strength of the light source and camera sensitivity should be such that the particles are small enough as not to interfere with the flow itself, but still able to reflect enough light to be recorded. A drawback of this system is that the particles are tracked within a thin light sheet but generally have a perpendicular velocity component and therefore move in and out of the light sheet. More recently it became possible to use PTV to establish 3D trajectories (Maas et al. 1993, Hoyer et al. 2005) using multiple cameras, and a 3D light 'sheet' (Hoyer et al. 2005).

Particle imaging velocimetry, PIV, is a similar technique to PTV, but where the latter tracks individual particles within the flow, PIV tracks particle patterns between frames using a correlation process (see for example Liu et al. (1991)). The technique has become well established over recent years for the study of flows. Initial attempts to enable the measurement of the third velocity component included using two light sheets of different colour and a colour camera (Cenedese and Paglialunga 1989) and using stroboscopic lights to create multiple light sheets (Halloin and Jotrand 1994). More recently, in PIV, as in PTV, multiple camera systems have been used to capture all three components of the velocity field (Fouras et al. 2009). The attractiveness of PTV and PIV is that they provide an instant overview of the velocities in the flow, allowing individual turbulent eddies to be identified for example. The accuracy of the correlation based PIV technique with twin cameras has been reported to be limited compared to a twin camera PTV system (Bown et al. 2006). The application of these systems to buoyant discharges is also limited, which is partly a reflection of the resources involved, but also the tendency for investigators to focus on concentration field measurements, which cannot be measured with the systems. The concentration field information is however crucial in the application of the research to assess potential environmental effects of such discharges.

It is possible to combine measuring systems to extract additional detail from the flows. Historically this typically involved using digital video to capture flow trajectories and then either

conductivity probes (Ayoub 1971) or suction probes (Knudsen 1988) to capture cross-section details. Application of combined modern techniques has the potential to provide simultaneous velocity and concentration field measurements that provide greater insight to the flow behaviour, particularly in terms of the turbulent transport process, relevant examples include the work of Chu (1996) where both Laser Doppler Anemometry and LIF were utilized to study the behaviour of momentum puffs, and Wang and Law (2002) who employed a combined PIV and LIF system to study the behaviour of jets and plumes. In the context of discharges with three-dimensional trajectories, there is the potential to make use of a dual camera video system to locate the flows and then implement a LIF system to obtain cross sectional profiles of the flow behaviour. However, this becomes particularly cumbersome in situations where the orientation of the light sheet needs to be altered to obtain meaningful cross sectional profiles, that is, profiles that are perpendicular to the flow path. This approach can be simplified by measuring cross sections within the strongly advected region where the flow motion is predominantly with the ambient current and therefore cross sections can be obtained perpendicular to this (Cheung 1991). However, this solution limits the ability to measure the evolution through the flow regimes near the source, where the overall motion is distinct from that of the ambient current.

The Light Attenuation (LA) technique is a relatively simple alternative that has been employed by Kikkert (2006) to study the more complex discharge configurations. This study demonstrates that a twin camera LA system can provide a reasonably complete picture of the flow evolution. The LA system makes use of the light absorption characteristics of discharged fluid to determine its integrated concentration. It is strongly related to chemical spectroscopy, which is used to measure the concentration of certain chemicals dissolved in a liquid. This is achieved by relating the amount of absorbing material to the amount of light it absorbs. The measurement process involves shining a light through the sample and relating the intensity transmitted to the intensity that was transmitted through a clear sample. The loss of intensity is related to the concentration of the chemical and the path length through the sample. If the path length is known and the concentration is uniform, then the chemical concentration can be determined. In the present context the path length through the dyed fluid is not known and the concentration is not uniform, so the system provides integrated concentration information. This integrated information can be converted to local (point) values, if the form of the flow's cross sectional profile is known. Given the relative simplicity of the LA system and the experience gained to date in implementing it to study the behaviour of discharges that follow three-dimensional paths (Kikkert et al. 2009), a similar system has been employed for the present study. Details of this system are presented in Chapter 2.

1.5 Ambient Turbulence

Before proceeding further it should be noted that the potential influences of ambient turbulence on (buoyant) discharge behaviour are not considered here. The assumption being that most of the energy present in turbulence in the ocean are likely to be in the turbulent scales much larger than the scale of the discharge near its point of release. However, where the turbulent scales are of a similar magnitude the buoyant discharge there is the potential for significant impacts. Several authors have argued that the turbulence contained in the ambient has an effect on mixing (Lavertu 2006, Wu and Faeth 1995, Wong 1991) and it is expected to increase mixing. In 2007 Khorsandi et al. concluded that background turbulence with zero-mean velocity affected an axi-symmetric jet such that the spread and dilution increased to the point where the turbulent kinetic energy of the jet was smaller than that of the ambient. However Gaskin et al. studied a plane jet in a shallow coflow (2004) and concluded that if the level of turbulence is great enough, it had an adverse effect on the dilution rates by disrupting the jet flow structure and in 1991 Wong described an extensive study of the advected thermal in which due to turbulence in the ambient fluid in cases with high cross flow and low buoyancy the vortex pair was not entirely clear.

Hunt (1994) discussed the potential impacts of ambient turbulence on entrainment and dilution, where he outlined reasons why ambient turbulence can result in a decrease in dilution. The first experimental confirmation of this was obtained by Gaskin (2004). Khorsandi et al. (2008) and Khorsandi et al. (2011) argued that if the turbulence present in the ambient is able to interfere with the jet structure the jet mean velocity will decay more rapidly. This rapid decay in velocity is consistent with the breakup of the jet structure, reduced jet induced entrainment and lower near-field dilution because the length of the near-field region is reduced. For a more detailed description of the effects of dilution of the ambient and jet dynamics see List and Dugan (1994), Wright (1994), Guo et al (2005) or Cuthbertson (2006).

1.6 Thesis Hypothesis and Overview

In implementing the Light Attenuation system to study discharges with three-dimensional trajectories Kikkert et al. (2009) limited their study to discharge angles that were perpendicular to the ambient cross flow and only considered a single ambient to discharge velocity ratio in each case, 0.031 for all but one case, where this changed to 0.038. The experimental study outlined in

this thesis complements Kikkert et al.'s study by considering buoyant discharges at oblique angles to the ambient motion that have three dimensional trajectories and by extending the range of discharge to ambient velocities considered. Details of this experimental study are provided in Chapter 5 of the thesis.

Before exploring the behaviour of oblique discharges that move along three-dimensional paths, an experimental investigation was conducted into the behaviour of non-buoyant oblique discharges, with the aim of extending the knowledge gained from Kikkert et al. (2009), where it was evident that for oblique discharge angles less than 20° a strongly-advected jet and for discharge angles greater than 40° an advected line momentum puff formed in the strongly-advected region of the flow. At the intermediate angles (between 20° and 40°) Kikkert et al. were not able to clearly identify the form of the strongly-advected flow and the focus of the present study was to gain additional data at these intermediate angles so that the behaviour can be more clearly characterised. Details for this study are presented in chapter 4 of the thesis.

Interpretation of the integrated concentration data obtained from the Light Attenuation system is aided by a more complete understanding of the form of the mean cross sectional profiles. This provided motivation for Kikkert et al. (2007) to explore the application of a double-Gaussian distribution to represent the cross sectional mean concentration profiles of advected line momentum puffs. However, a similar study has not been carried out for the more practically significant line advected thermals, where the double vortex pair is also evident in the mean profiles. In general the line advected puffs and line advected thermals are assumed to have the same mean cross sectional form. The validity of this assumption is investigated in some detail in chapter 3, where new data sets for line momentum puffs and line-advected thermals are presented and the ability of the double-Gaussian approximation to represent the mean concentration profiles is explored.

Details of the Light Attenuation system employed to investigate flow behaviour in chapters 3, 4 and 5 are presented in chapter 2. This includes a description of the multiple dye system that has been developed to extend the dynamic range of the LA system. The implementation of which enables the evolution of the flow behaviour to be measured over much greater distances. Logically a summary of the conclusions from the present study is given in chapter 6, along with thoughts on related future research opportunities. Although the development of improved integral models is not a focus of this study, relevant models are developed within the respective chapters to aid in the interpretation of the data.

Note that because the topics covered in chapters 3, 4 and 5 can be dealt with independently, these chapters have been written in a more complete form, so that they can be read with limited reference to the broader thesis.

Chapter 2 - Experimental Systems

2.1 Introduction

As indicated in the previous chapter, the Light Attenuation technique has a number of advantages when investigating discharges moving along a three-dimensional path and this technique therefore forms the basis of the experimental research outlined in this thesis. In this Chapter details of the Light Attenuation technique are explored in some detail and details are also given of the approach taken to locating the flow, based on the information gained from the twin camera recording system. In order to provide a context for these more detailed discussions, it is important to initially provide an overview of the experimental configuration.

2.2 Experimental Configuration Overview

Experiments described in this thesis were carried out in a tank with dimensions of (length x width x height) 6220mm x 1540mm x 1080mm. The walls of the tank are configured with glass windows of 700mm x 980mm (width x height) set in a metal frame. The ends of the tank have two such windows and the sides eight. In the mid-section the floor of the tank has a glass window of 700mm x 1200mm (length x width). The used glass has not been strengthened by tempering or layering so that it does not affect light measurements (Potter 1995). The thickness of the glass on the bottom is 12 mm and on the sides 10mm. A trolley-system with a variable speed control is mounted on top of the tank and is capable of driving along the length of the tank. The sources for the experiments were attached to a trolley and towed to simulate the presence of a uniform ambient motion. A magnetic flow meter (Krohne RV-100E) was situated on top of the trolley, and measured the instantaneous flow. The trolley-system included a cable-tray that was used to feed through hoses for the source and the necessary electrical cables. Photographs of the setup are shown in Figure 2-1, and Figure 2-2.

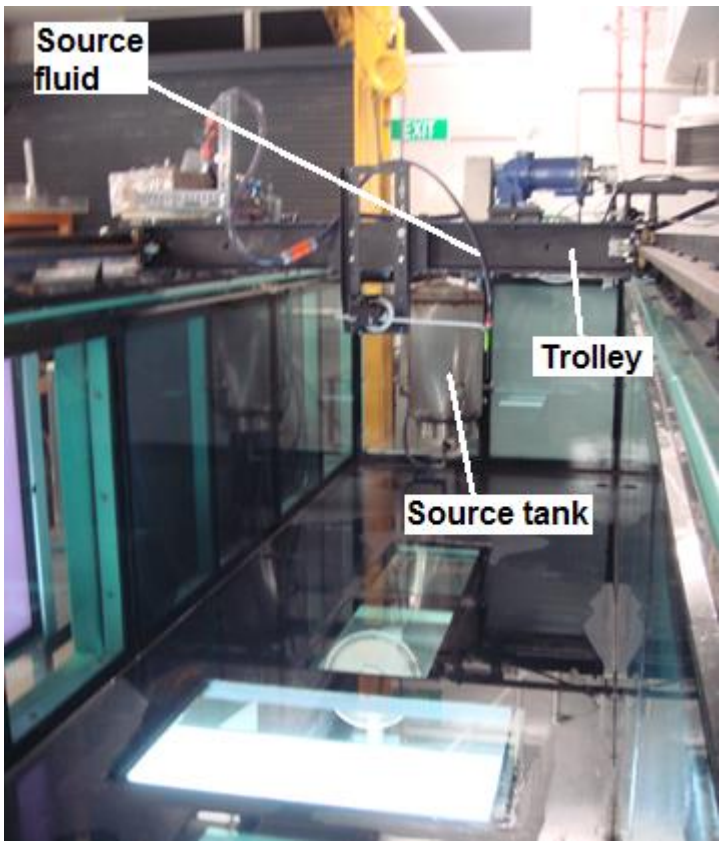

Figure 2-1: Image of laboratory setup, showing the main tank with on top the trolley and cable tray system and in the back the source fluid tank.

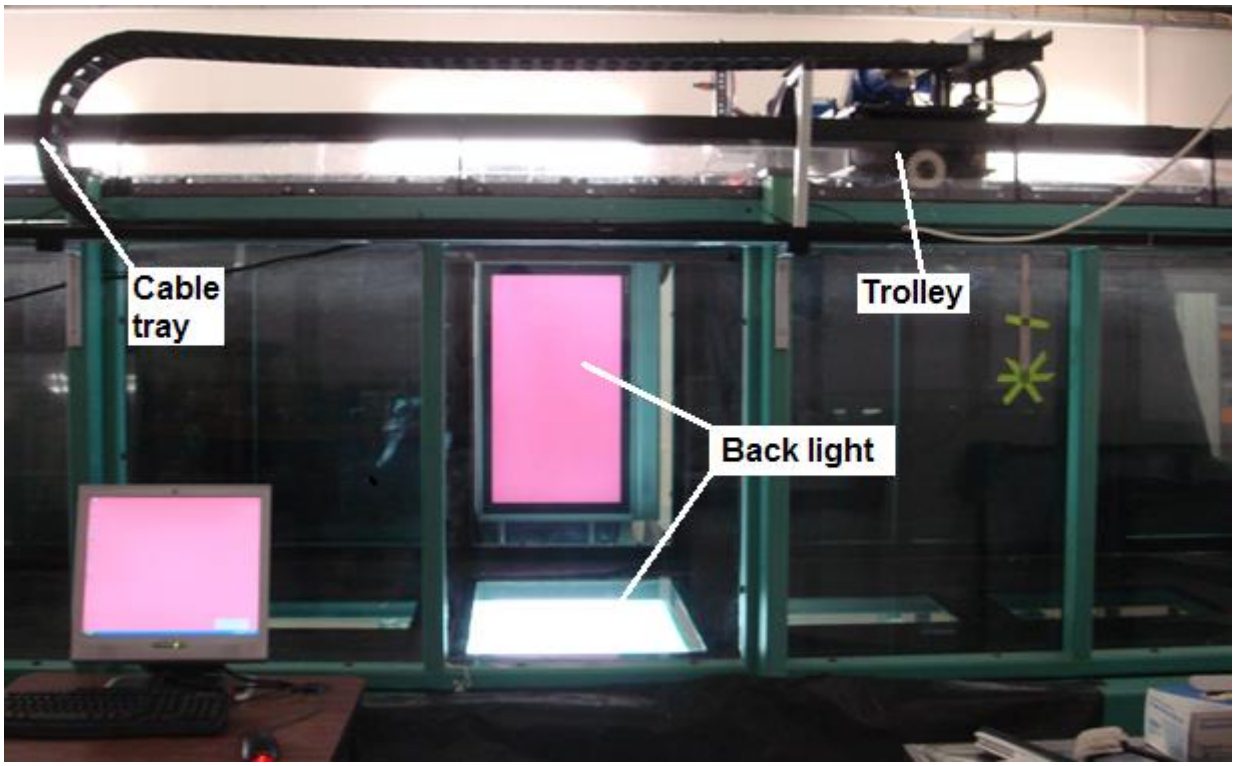

Figure 2-2: Image of laboratory setup, showing the main tank with the trolley, cable tray system and back lights.

A schematic diagram for the experimental configuration viewed from the end of tank is shown in Figure 2-3. In these diagrams the coordinate system employed for the experimental study is defined, with the *z* coordinate directed vertically downwards from the source, the *x* coordinate (not shown in the figure) is in the direction of trolley movement (into the page) and the *y* coordinate is perpendicular to these axes. Also evident in this figure are the basic components of the light attenuation system, that is, the cameras and light sources. Two orthogonal cameras (Jai m7+) were employed to measure the flow behaviour, one was situated approximately 4.8 meters directly above the measurement area, and the other was situated 4.7 meters from the measuring area along the *y* axis, which is perpendicular to the lengthwise axis of the tank (the *x* axis). The camera above the measuring area captured images where light had been absorbed along paths essentially parallel to the *z* axis, where the light source was a bank of fluorescent lights situated below the tank. The fluorescent lights were covered by a diffuser screen to create a reasonably uniform light source. The camera captured images with a frequency of 24 Hz. The camera to the side of the tank captured images where light had been absorbed along paths essentially parallel to the *y* axis and the light source in this case was a 37" LCD screen, which was uniform and therefore no diffuser screen was necessary. It was however necessary to place ventilators below the tank to direct the heat from the fluorescent light source away from the bottom of the tank. Black sheets were also placed around the tank in the vicinity of the recording areas so that the extraneous light could not enter the field of view of the cameras.

The analysis (Kikkert 2007) that was used to calculate the intensity per pixel was:

- Setting a minimum concentration frame ('white' reference frame) by taking an average picture (averaged over 4 seconds) of the experimental setup without dye present.
- Setting a maximum concentration frame ('red' reference frame) by taking an average picture of the maximum amount of dye expected, by placing in the setup (mid line experiment) a cell containing dye solution covering the whole frame of the picture.
- Capturing the experimental images, while running the experiment.

At this stage the result was a set of images with light intensities of the experiment and 2 reference images. The actual absorbed dye comes from scaling the experimental images, or rather each pixel separately on the scale where 0 is the pixel intensity of the white reference frame and 100 is the pixel intensity of the red reference frame. Before this can be done the logarithm of the intensities need to be taken (equation 2-1).

- Calculating the logarithmic values and scaling the resulting intensities, resulting in the total integrated absorbance per pixel for each experimental image.

- All resulting experimental images must now be added together to form a complete picture of the whole experiment. This is done by adding them with each picture translated in accordance with the ambient velocity. These 2 steps can be done with the software Image stream (Nokes 2007).
- The resulted picture is now read into Matlab software which enables taking cross sections and fitting Gaussian distributions on it.

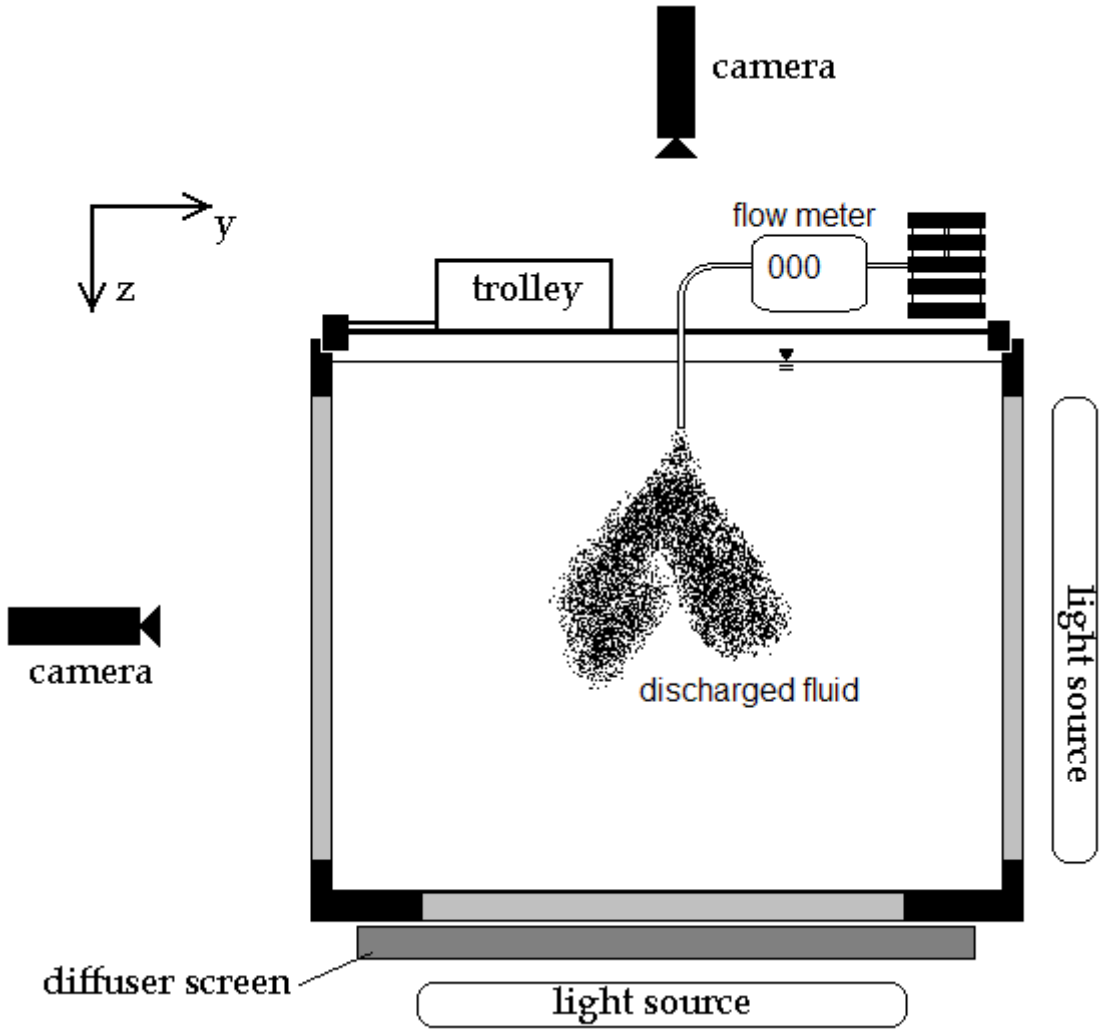

Figure 2-3: Schematic diagram of the experimental configuration as seen from the end of the towing tank. Note the *x* axis is perpendicular to the page.

The source mounted on the trolley was connected to a 100 litre source fluid tank located underwater in a corner of the main tank. Through this placement of the source tank the temperature of the source fluid was equal to the water in the main tank. The source tank was connected to a constant supply of low-pressure air (2.5 bar), which enabled a constant flow from

the source for a wide range of flows. A slight change in source fluid temperature was noted as the fluid was transported from the tank to the point of discharge, particularly when there were significant differences between the air temperature in the laboratory and the ambient tank water. The tube transporting the source fluid was exposed to the air and was of sufficient length to enable the trolley to move the full length of the tank (approximately 9 meters). Numerous experiments showed that after flushing the water from the source tank through the supply tube for 2 minutes, the temperature difference between the source and ambient tank fluids never exceeded 0.2° Celsius (section 2.4.3).

The uncertainty of the LA system has been described by Kikkert (2006). He calibrated the whole system and concluded that the accumulated uncertainty remains below 5%. This value provides general guidance as to the quality of the data presented in this thesis. The uncertainty in the data has not been represented in the form of error bars in the various figures in this thesis, because these errors are generally small in the context of the data ranges presented. This approach is consistent with that taken in a wide range of publications that are relevant to the topics discussed in the thesis.

The source itself, measured 1.3 mm to 6 mm in diameter (depending on the experiment), gives rise to disturbances in the water. The *Re* of the flow around the source varied between 30 and 300 for all experiments except one. These low *Re* numbers do not give rise to turbulence in the water that would interfere with the experiments. For one experiment the *Re* was in the order of 1000, these experiments were horizontally discharged thermals (Chapter 3 set T-2) and to minimize any effects of the flow around the source the release point was extended to more than 40 diameters downstream of the vertical pipe.

2.3 The Light Attenuation Technique

Light attenuation (LA) in its basic form is a technique that measures the amount of light that has been absorbed by a sample and correlates this to the concentration of contaminant in that sample. With the experimental setup described above, the LA system makes use of light that passes from one side of the setup through the sample to the camera. To make the discharged fluid visible or discernible from the ambient fluid, a dye (contaminant) is dissolved in it. The dye is chosen for its known absorbance spectrum. For a given experiment the light intensity that reaches the camera is measured before and during the discharge of dyed fluid, so that the attenuated amount of light

can be deduced, and therefore the dye concentration determined at each camera pixel. When multiple camera angles are used and/or the flow exhibits a known cross-sectional concentration profile, additional details of the concentration field can be deduced.

The Light Attenuation technique is well established in other disciplines of engineering and science. In chemical engineering, absorption spectroscopy is used to measure amounts of chemicals present in a sample, because many chemicals absorb light of a specific wavelength in a known fashion. For an introduction of the use of this technique, see Pavia et al. (2009) or Green (1990). In astronomy, spectroscopy is used to measure chemical composition and physical properties of astronomical objects or alternatively to measure their velocities from the Doppler shift of their spectral lines (Kitchin 1995, Robinson 2007). Closer to home, a similar technique is used in a very basic form with a Secchi disk. With this circular black and white disk the water clarity is measured. To use it, the disk is lowered in a stream or lake and the depth at which the black and white parts are no longer separately discernible with the naked eye, gives a measurement of the clarity of the water. The result is the distance at which the reflected light from the disk falls below the visible intensity threshold of the observer. With a Secchi disk the attenuation of light comes from absorption and refraction, while in the present technique only light absorption is used. Preisendorfer (1986) gives a clear description of the theory, underlying assumptions, consequent strengths and limitations on how to predict luminance levels as a function of depth. More directly relevant to the study described in this thesis is the laser induced fluorescence or LIF flow measurement technique, which makes use of fluorescent spectroscopy where a specific wavelength of light is used to excite atoms or molecules to emit light at a different wavelength. The amount of emitted light is here a measure of the dye concentration (Papanicolaou and List 1988, Papantoniou and List 1989). It is evident that there is a considerable body of relevant research that can guide the further development of the Light Attenuation technique.

Kikkert (2006) described the use of an LA system in some detail. To improve the system further, an in-depth investigation into the laboratory setup including the selection of appropriate dyes has been carried out. Through the examination of important individual components of the experimental system, sources of error can be isolated and the impact on the overall quality of the data assessed. The LA system is in essence a ‘broadband’ spectroscopic device and therefore comparisons with chemical spectroscopy provide a basis for an improved understanding of the system and the errors associated with it.

2.3.1 Chemical Spectroscopy

Light is quantized into photons, the energy of which can be transferred to an electron upon collision. Transfer occurs only when the energy level of the photon equals the energy required for the electron to get promoted onto the next energy state, for example from the ground state to the first excitation state (Boyer 1993). This process is the basis for absorption spectroscopy, the technique used to estimate the quantity of molecules in solution. Generally, light of a certain wavelength and energy illuminates the sample, which absorbs a certain amount of energy from the incident light (Figure 2-4). The energy of the light transmitted through the sample is measured using a photo detector. By knowing the amount of light illuminating the sample and the amount of light that is transmitted through the sample, the absorbance of the sample can be calculated. The absorbance is defined as:

$$\mathrm{A} = \log \frac{I_0}{I} \tag{2-1}$$

Where I_0 is the intensity of light that illuminates the sample and I is the intensity of light that is transmitted through the sample.

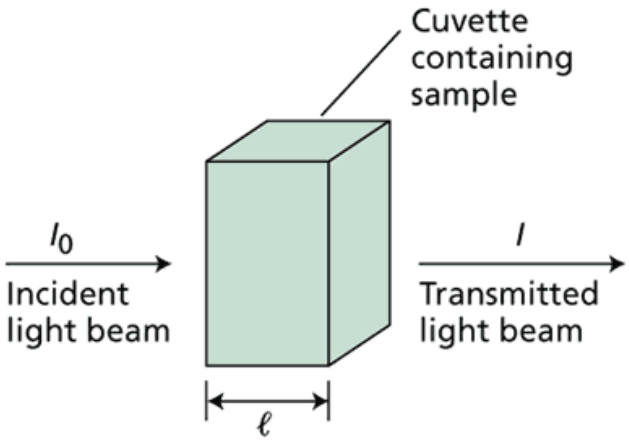

Figure 2-4: Absorbance of light through a sample (reproduced from Taiz and Zeiger, 2010).

A spectrometer is employed to implement the technique shown in Figure 2-4 and in Figure 2-5 a schematic diagram of a spectrometer is presented (Taiz and Zeiger 2010). The light source within a spectrometer generates visible light. Following the light source is a monochromator, which filters light and lets through light at a specific wavelength by using a prism. After the monochromator a series of lenses, slits, mirrors, and filters act as an optical system to concentrate,

increase spectral purity of, and direct monochromatic light towards, the sample chamber where the cuvettes containing the samples are to be tested. However, since the instrument has only a single beam, every time the wavelength has to be changed a blank reading must precede any sample reading (Boyer 1993). The used cuvettes are made from glass and can be utilized for reading absorbance at wavelengths greater than 340 nm, because below this wavelength the glass also absorbs light (Potter 1995). The light-sensitive detector follows the sample chamber and measures the intensity of light transmitted from the cuvettes and passes the information to a meter that records and displays the value.

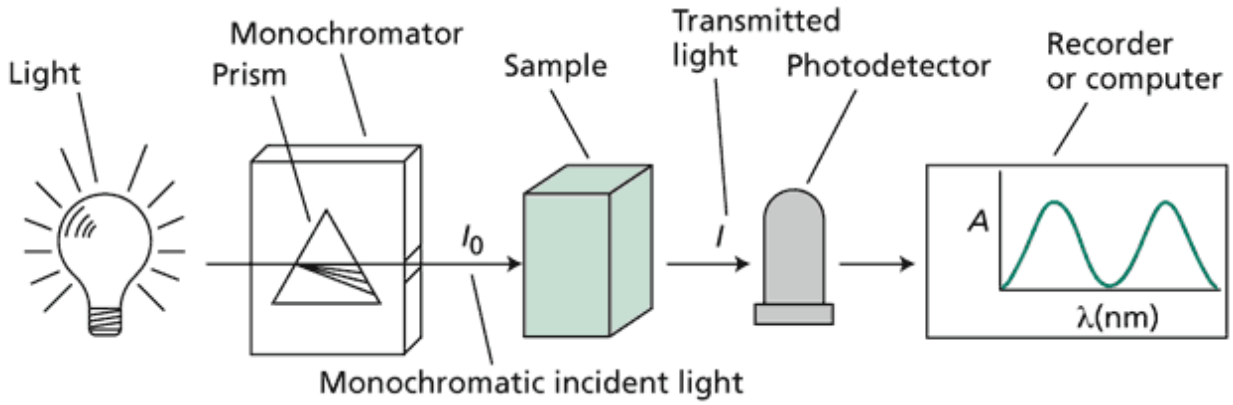

Figure 2-5: Schematic diagram of a spectrometer (reproduced from Taiz and Zeiger 2010).

If a monochromatic incident light beam of intensity I_0 travels through a sample of length l then some of the light is absorbed by particular molecules in the sample, and the intensity of light that emerges is I (Figure 2-4). The absorbance of a sample can be related to the concentration of the absorbing species through Beer's law:

$$A = \epsilon . c . l \qquad (2\text{-}2)$$

Where c is concentration, in moles per litre; l is the length of the light path in centimetres, and ϵ is the molar extinction coefficient, with the units of litres per mole per centimetre. The value of ϵ is a function of both the particular compound being measured and the wavelength of the incident light. A consequence of Beer's law is that there is no effect due to unknown path length and unknown concentration, only the total amount of encountered dye given by the product of the dye per litre and the path length are of consequence.

In spectrometry the light source is monochromatic and nearly all ambient factors like light intensity, sample temperature, sample path length are controllable. The spectrometer has been

designed such that no light can get to the detector other than the light transmitted through the sample. It is also fairly easy to verify that a sample does not have impurities or turbidity. These features result in highly accurate measurements.

2.3.2 Light attenuation

The LA setup is a generalization of chemical spectroscopy. However normal white light is used as a light source, consisting of different wavelengths (Figure 2-6). The recorder is typically a camera with a charge coupled device (CCD). The output is a light intensity level per pixel. Note that each separate pixel (shown as i,j) essentially generates one spectroscopic measurement.

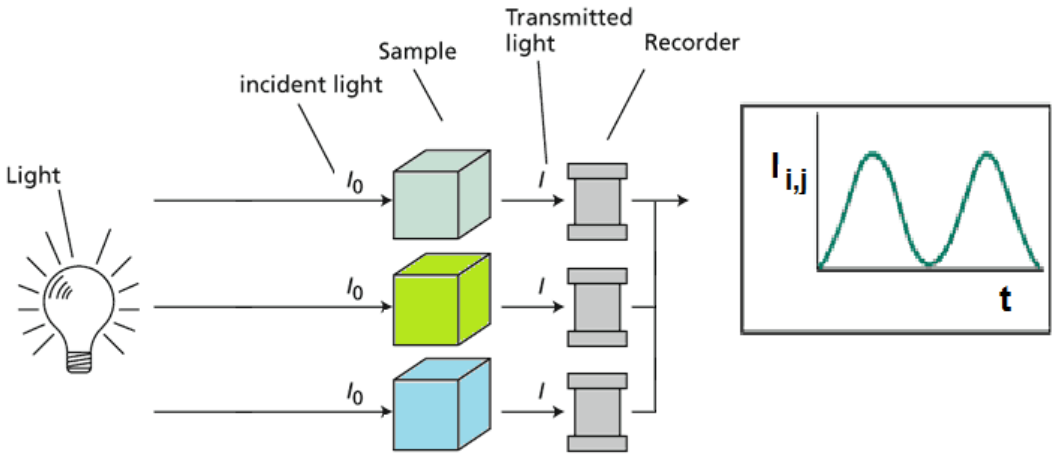

Figure 2-6: Schematic diagram of a Light Attenuation setup.

As the components of the LA system are not automatically calibrated nor designed for spectroscopy they require further detailed investigation. In particular there are significant differences between the two systems in terms of the type of light source and device employed to record the extent of the attenuation, with the LA system employing a broadband light source and standard scientific CCD camera to record the extent of the attenuation. The implications of these changes are now discussed in some detail.

2.3.3 The Cameras

As noted above Jai M7+ cameras were utilised in the LA system developed for the experimental programmes detailed in this thesis. As with most video cameras, they employ a charge coupled device (CCD) to capture light. CCD's are electronic devices consisting of millions of separate light sensitive parts that create an electric current when light hits it. CCD's are not sensitive to colour, although blue light will give a slightly higher current than red light on account of the higher energy transfer. Therefore to perceive colour a camera must have either three CCD's and a different colour light filter in for each of these, or a single CCD with a light filter designed so that the CCD captures blue, red and green light in a particular pattern. In the latter case application of a Bayer filter enables the real colours to be obtained by combining the alternate colour intensities from neighbouring pixels. The cameras that were used were colour cameras and the channel that covered the indicator frequency of the dye, so either red, green or blue was used for the measurements.

A CCD has certain known error sources and generally the CCD signal-to-noise ratio (SNR) represents the ultimate performance of the camera. With a CCD, the SNR value specifically stands for the ratio of the measured light signal to the noise per pixel. Noise is in this case the combined internal and external noise. External noise consists of the natural variation of the incoming light, the incident photon flux. Internal noise consists of the signal components arising in the electronic system. The three primary sources of noise in a CCD imaging system are photon noise, dark noise, and read noise. Noise is an apparent random signal superimposed on the actual signal. As the noise level increases the uncertainty or standard deviation of the measured signal becomes greater and the SNR decreases. A large signal-to-noise ratio is important in the acquisition of high-quality digital images, which is critical if the devise is to be utilised for spectroscopy

The noise consists of the following components which are (theoretically) not correlated (Janesick 2007, Fellers and Davidson 2012):

- Photon noise refers to random spatial arrival of photons as the light energy is carried by a finite number of particles. It is an inherent statistical variation in the arrival rate of photons incident on each pixel on the CCD. The signal within the CCD is generated through photoelectrons and the magnitude at every pixel fluctuates following the Poisson distribution. It cannot be reduced by camera design as it represents a noise floor, the minimum achievable

noise level. The relative effect can be minimized by increasing the number of received photons. The photon noise is equivalent to the square-root of the signal intensity (Poisson distribution). For experiments of the type described here the photon noise is minimised by using the largest photon flux possible by increasing the aperture size (F number) and shutter speed of the camera.

- Dark noise originates from the statistical variation in the number of electrons that are generated thermally within the CCD, which is independent of the incident light, but dependent on the device temperature. The rate of generation of thermal electrons at a given CCD temperature is called dark current. Similar to photon noise, dark noise follows a Poisson relationship to dark current, and is equivalent to the square-root of the number of thermal electrons generated within the image exposure time. Cooling the CCD reduces the dark current, and in practice, high-performance cameras are usually cooled to a temperature at which dark current is negligible over a typical exposure interval. A method of determining the dark current is to capture a dark image (image with camera cap on) and to then assess how much it differs from a black image. This was done for the Jai cameras and the dark noise represents a negligible factor when these cameras are at room temperature.

- Read noise is a combination of system noise components inherent to the process of converting CCD charge carriers into a voltage signal for quantification, and the subsequent processing and analog-to-digital conversion. The major contribution to read noise usually originates from the on-chip preamplifier, and this noise is added uniformly to every image pixel. High-performance camera systems utilize design enhancements that greatly reduce the significance of read noise. This issue is assessed for the two Jai cameras in section 2.3.7, where the significance of this error is assessed, along with methods to minimise it.

Although cameras are made to a high level of accuracy, not all pixels will react the same, differences of 1-2% between pixels are not uncommon and this will grow with the age of the camera. This error is referred to as pixel non-uniformity and the issue is dealt with through the experimental procedure where every pixel is calibrated separately. Thus individual pixel responses are incorporated into the calibration process.

The CCD signal-to-noise ratio calculation uses the following equation, which is simply signal divided by noise (Fellers et al. 2012):

$$\mathrm{SNR} = \frac{\mathrm{P}Q_e\mathrm{t}}{\sqrt{\mathrm{PQ}_e\mathrm{t} + \mathrm{Dt} + \mathrm{N}_r^2}} \tag{2-3}$$

Where P is the incident photon flux (photons per pixel per second), Q_e represents the CCD quantum efficiency (see section 2.4), t is the integration time (seconds), D is the dark current value, and N_r represents read noise. The term $(PQ_et)^{1/2}$ represents the photon noise.

In the current setup there is the potential for unwanted background light and refracted light, which can be added to the photon noise component. Another factor that should be considered is that the values of incoming light and quantum efficiency are functions of wavelength; so when making use of a white light source, the calculation of signal-to-noise ratio requires these variables to be integrated over all the wavelengths utilized for imaging. Refraction is an important phenomenon when there are significant density gradients, here refractive indices should be matched (or not matched depending on the visualisation technique). The density differences in the LA setup were relatively small, particularly given the extent of the mixing that takes place in the studied flows. However, near the source the density gradients were more significant, but data was not extracted from this region. It was evident during the calibration process that no distortion of grid lines nor shadows were observed in the flow area of interest. The effect therefore is taken as part of the error in the whole LA system, which has been calibrated (Kikkert 2007) and found to have a total error smaller than 5%.

In addition to the details of the CCD the Jai cameras also allow adjustments to the binning, gain and black level and these adjustments have implications for image quality and hence their use in spectroscopy. The implications are discussed in some detail below. Gain is the electronic amplification of the signal and the black level is the brightness of the image that is displayed when there is no incident light on the CCD.

2.3.4 Binning

The Jai M7+ CCD cameras allow binning as another mechanism for increasing signal-to-noise ratio. With binning the signal of several pixels is read out as one. However this method involves a sacrifice of some spatial resolution. By improving the signal-to-noise ratio in this way, the

imaging system is able to reach a better SNR at a lower light level and/or shorter exposure time. The used equation for calculating SNR (Equation 2-3) can be modified to account for binning (Fellers et al. 2012):

$$\mathrm{SNR} = \frac{\mathrm{MP}Q_e\mathrm{t}}{\sqrt{\mathrm{MPQ}_e\mathrm{t} + \mathrm{Dt} + \mathrm{N}_r^2}} \qquad (2\text{-}4)$$

In this modified equation, *M* represents the number of binned pixels. In the present experiments the choice was made not to sacrifice spatial resolution, hence binning was not used.

2.3.5 Black levels

The black level setting is sometimes referred to as the 'Brightness' setting. The total signal strength is increased but the error or noise is not magnified. With the Jai cameras a maximum black level setting (255) gave an intensity of 45 without any incident light. For values above a certain minimum light intensity, the black level setting acts as a simple addition to the reported intensity. The effect of the black level (BL) setting is shown in Figure 2-7. In this figure the standard deviation of the measured light intensity is plotted against the light intensity for various black level settings. The data has been extracted from a background image of the experimental setup, where there is an intensity range of approximately 80. However for a BL setting 0, the intensity range only extends from 15 to 70. Increasing the BL setting to 100 improves the intensity range, with the lowest intensity virtually unchanged, but the top intensity increased to approximately 100. At this point the difference between highest and lowest intensity reaches approximately 80. After the BL setting is increased even further, the intensities change in a consistent way and the range remains constant at approximately 80.

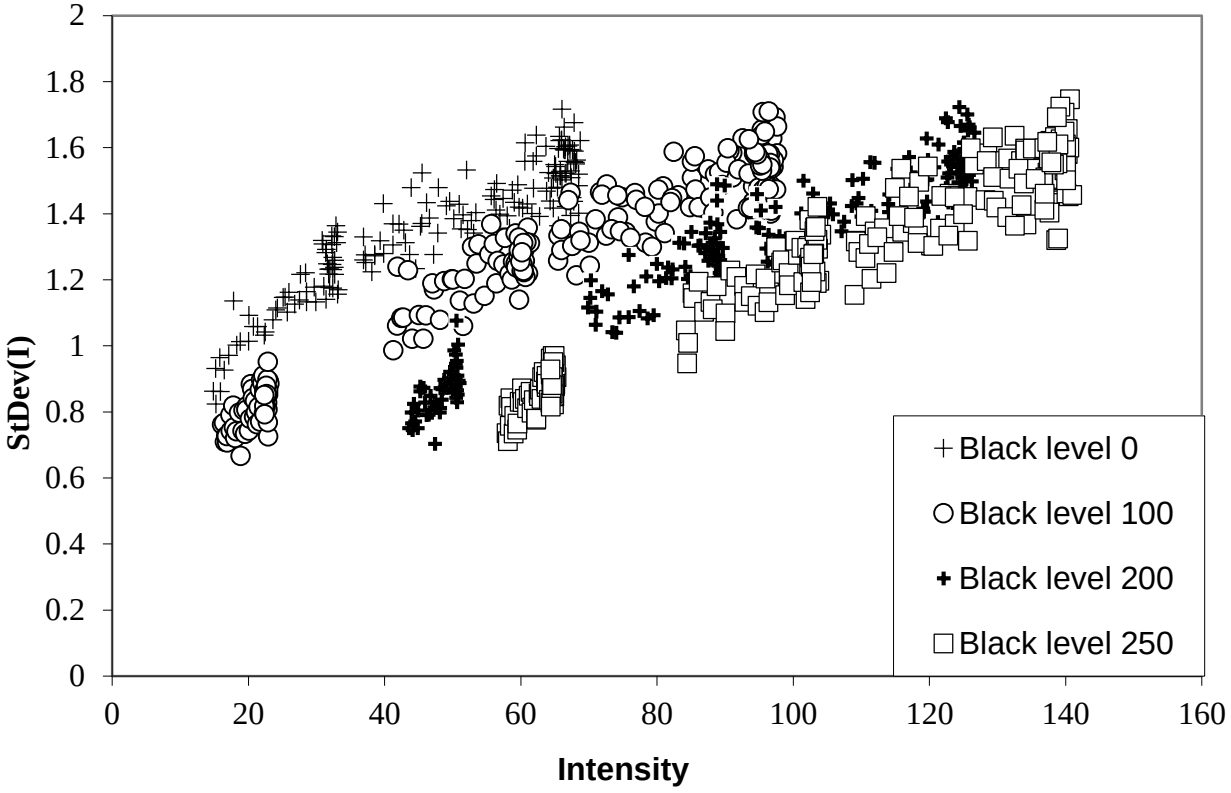

Figure 2-7: Standard deviation of the captured pixel intensity of fluorescent light at various black level settings and a shutter speed 1/100.

Setting the BL at 0 results in a reduced brightness, equivalent to white being reported as grey, while setting the BL to a high value results in increased brightness where black becomes grey. In the former case the range of available intensities is reduced.

It is clearly important to set the black level parameter correctly. This becomes evident when combining Equation 2-1 and Equation 2-2 into the Beer-Lambert formula:

$$\log \frac{I_0}{I} = \epsilon . c . l \tag{2-5}$$

Note that reported intensities, I_0 and I, are not necessarily equal to the pure light intensity. The intensities equal the light intensity plus camera noise, multiplied with the gain setting (see section 2.3.6) to which also a black level is added. Based on Equation 2-6, the black level should cancel out the noise to result in a linear relationship otherwise the concentration can no longer be calculated. The black level value that produces a linear relationship in this setup was approximately 93. This level has been set throughout the experiments.

2.3.6 Gain

On a camera, smaller apertures give greater focal range (the range of distances in focus), while larger apertures capture more light. Turning up the gain can help increase the signal intensity so that faster shutter speeds or smaller (=higher number) apertures can be used. It can be an effective method to improve the visibility of faint images. However it does have a drawback and this is evident in Figure 2-8 and Figure 2-9 where the effect of gain is shown. All images were averaged over a period of 4 seconds, following each other in a series of changes in the camera gain settings. On the vertical scale is the multiplication of the signal intensity, $I_{new}/I_{original}$, where I_{new} is the signal with gain applied and $I_{original}$ is the signal without application of gain. The horizontal axis represents the original signal intensity, $I_{original}$. Values above a certain limit will be multiplied to the maximum value of 255. A gain setting of 100 results in most intensities being multiplied with a factor of 1.5, a gain setting of 300 results in a multiplication of 4.9 and so on. In Figure 2-9 the effect of gain on noise is shown. The noise is calculated as the variance of the signal intensity of a constant image. It is obvious that the multiplication factor becomes more erratic as the gain setting increases.

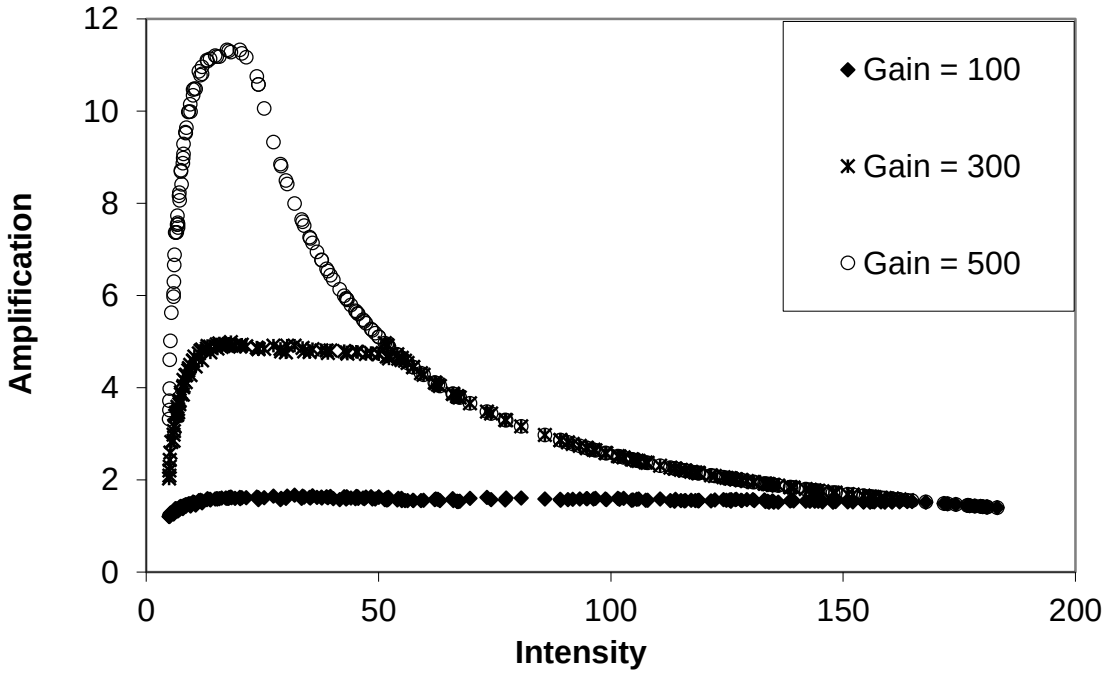

Figure 2-8: Multiplication of the signal at various gain settings

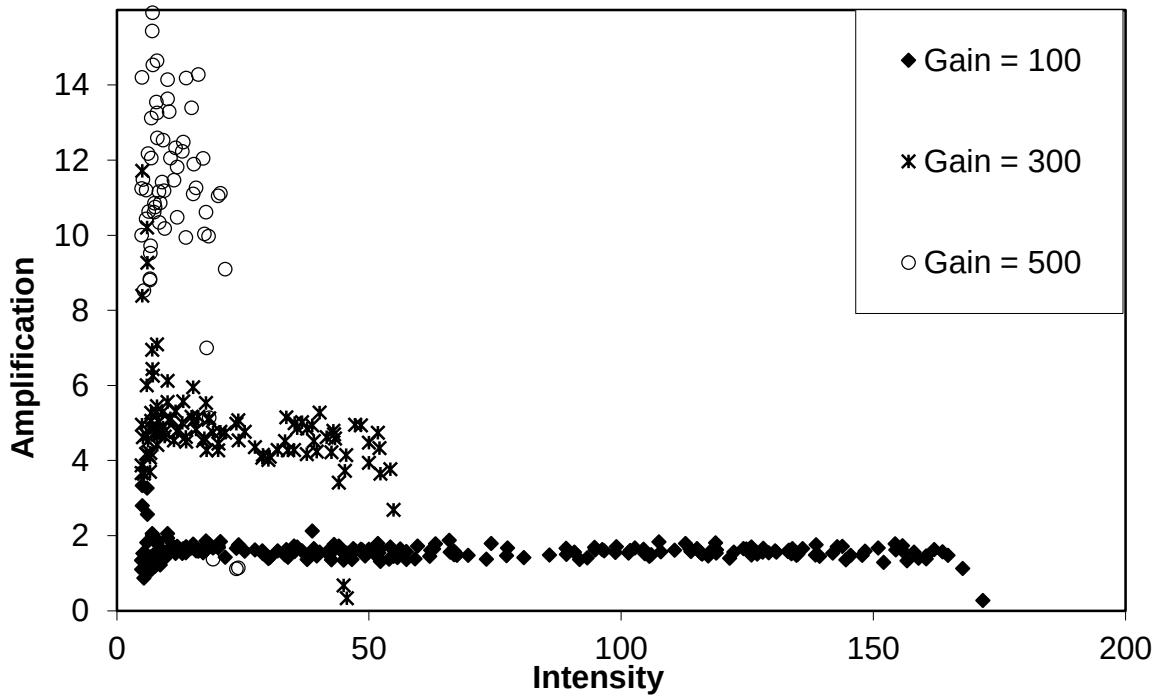

Figure 2-9: Multiplication of noise at various gain settings

When comparing the values of the variances at the different intensities with the values of the signal amplification, it is evident that the noise is multiplied by as much as the signal. Figure 2-10 shows the ratio of noise amplification and signal amplification. The benefits of increasing gain are therefore negligible, because although the range increases, the standard deviation of the signal (noise) increases by the same factor. Gain should therefore only be employed when the largest practical aperture and slowest possible shutter speed for a given experimental setup the signal is still too faint. The gain setting for the present experiments was 0.

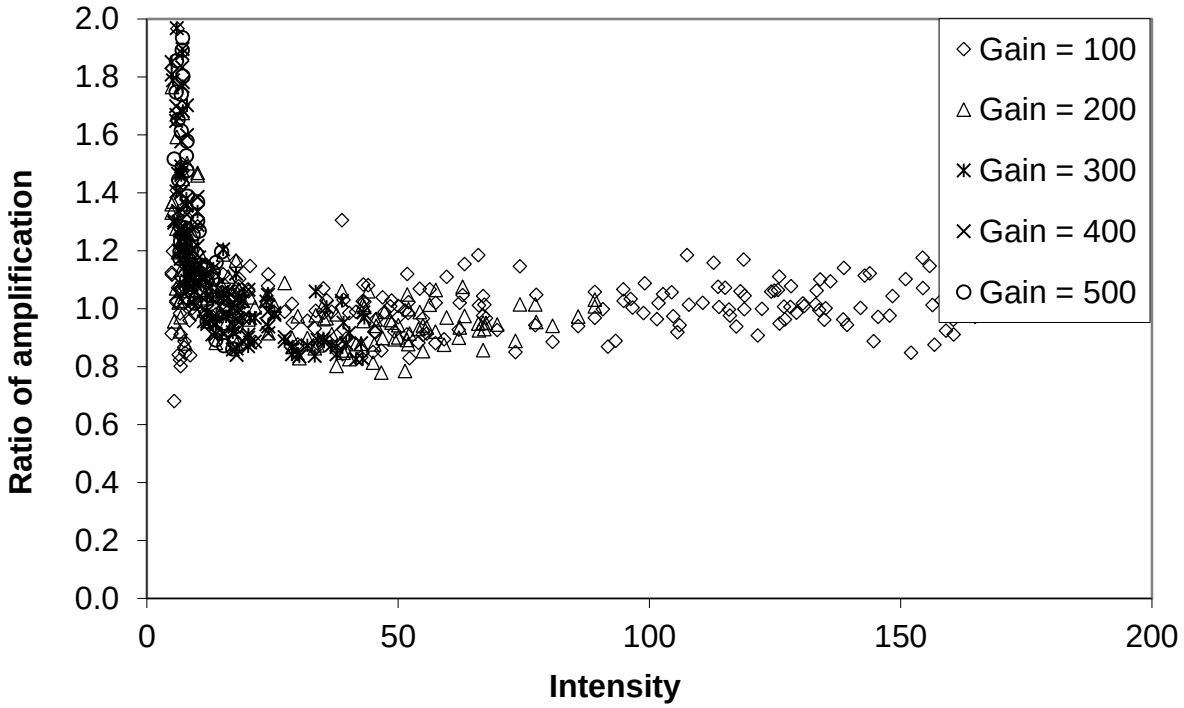

Figure 2-10: Ratio of noise versus signal amplification at different light intensities.

2.3.7 Alternative Cameras

It is possible to make use of higher specification cameras in the LA system, for example the Pulnix 2010. The relative signal noise from this Pulnix camera and the selected Jai cameras is shown in Figure 2-11. The Pulnix is a 10 bit scientific camera and nominally has a higher SNR ratio than the Jai cameras. This is evident in Figure 2-11, where the noise level of the Pulnix lies below the Jai+ for similar settings. For an intensity range of 255 down to 30 the Pulnix noise stays under 2%, however the Jai noise also stays under 2% in the range 70-255. In the present experiments the Jai cameras were utilised, because of their availability, but the analysed data was kept within the intensity range of 70 to 240, so that data quality was similar to that obtained with the higher specification Pulnix camera.

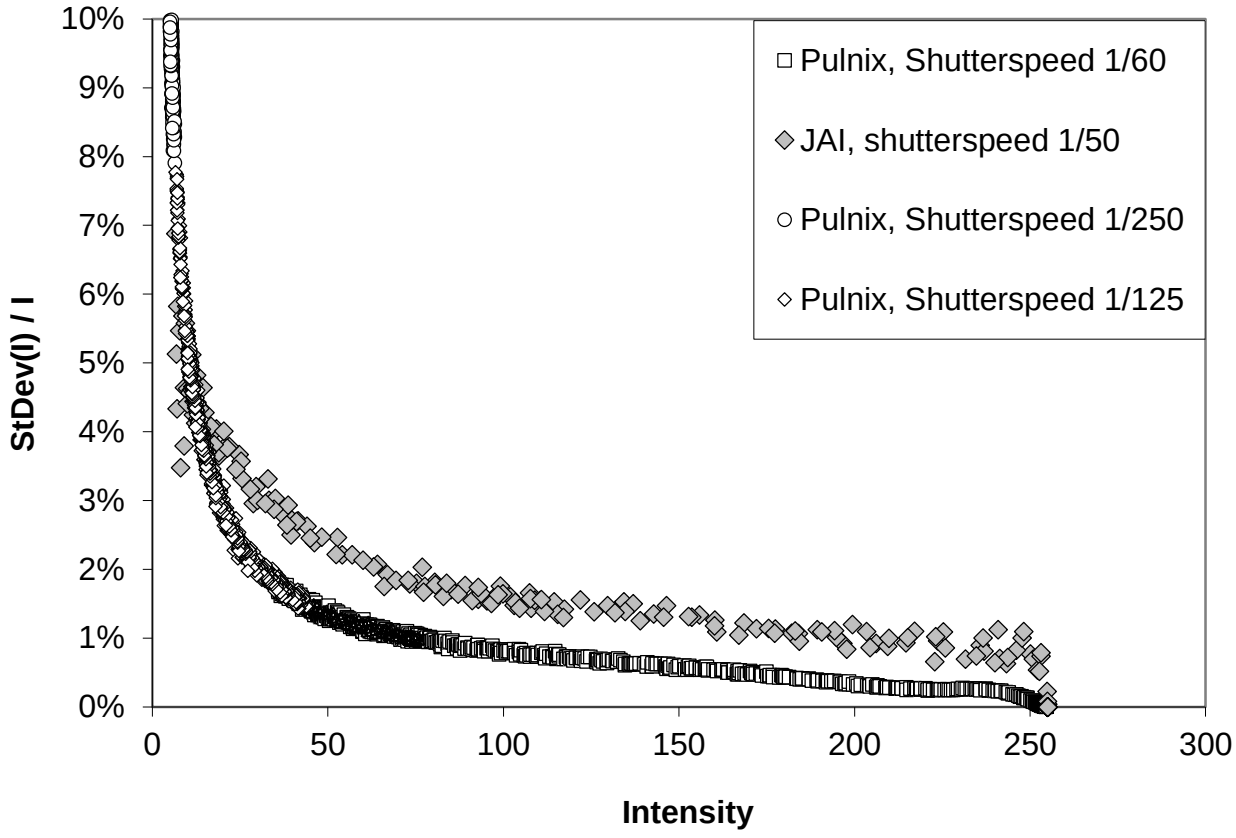

Figure 2-11: Relative standard deviation versus Intensity for the JAI M7+ and Pulnix 2010 cameras

2.3.8 The Light source

As noted above the light source is a critical component of the LA system and in this section the effect of different light sources on the noise levels is discussed. In chemical spectroscopy the lights are DC monochromatic, but in the present experimental setup the light sources are an LCD screen and a bank of fluorescent lights. The impact of light sources on the SNR of the camera images was tested. Figure 2-12 shows the noise level or standard deviation of the light intensities in an image lit with a DC light, a LCD screen and a fluorescent light. The DC light was a light attached to a 12v (direct current) battery. The settings for each image of the different light sources are the same: shutter speed 1/100, gain at 0, black level at 93 and aperture at 2.8. It is evident that standard deviations of the signals do not differ notably from each other, suggesting that the quality of light signals from each of the light sources is similar. The relative noise or SNR drops as the signal intensity increases.

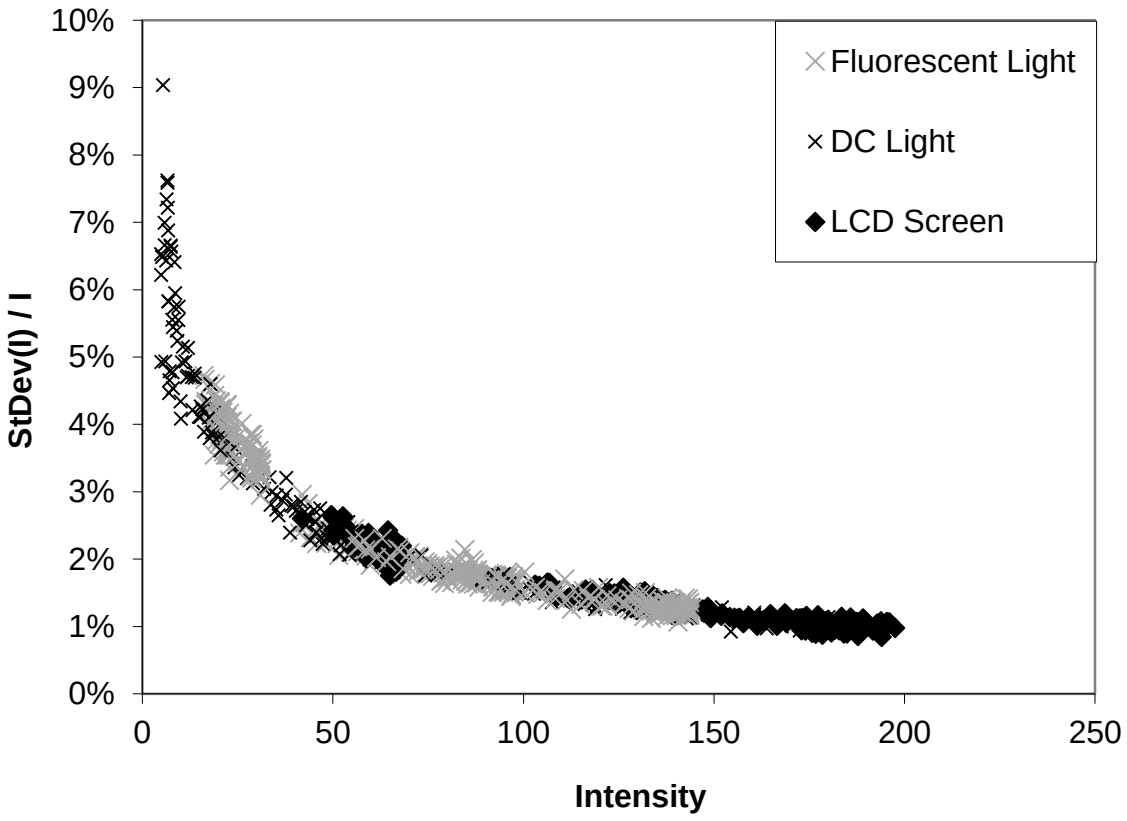

Figure 2-12: Relative Standard deviation of the light intensity as a function of the reported intensity.

However the various light sources have a different refresh rate, DC is constant, fluorescent light 'flickers' with 100Hz, and an LCD screen is refreshed between 50 and 85Hz. In Figure 2-13 the effect of different shutter speeds are depicted and as expected with the use of a DC light, there is no effect. The camera error apparently does not change with prolonged exposures. Figures 2.13 and 2.14 show data obtained by measuring the light intensity over a region of a white translucent screen back lit by a DC light. The shutter speeds of the camera were set to 1/50, 1/100 and 1/200 and the standard deviation was calculated from the measured light intensities. The relative standard deviation (StdDev(I)/I) has been plotted in Figures 2-13 and 2-14.

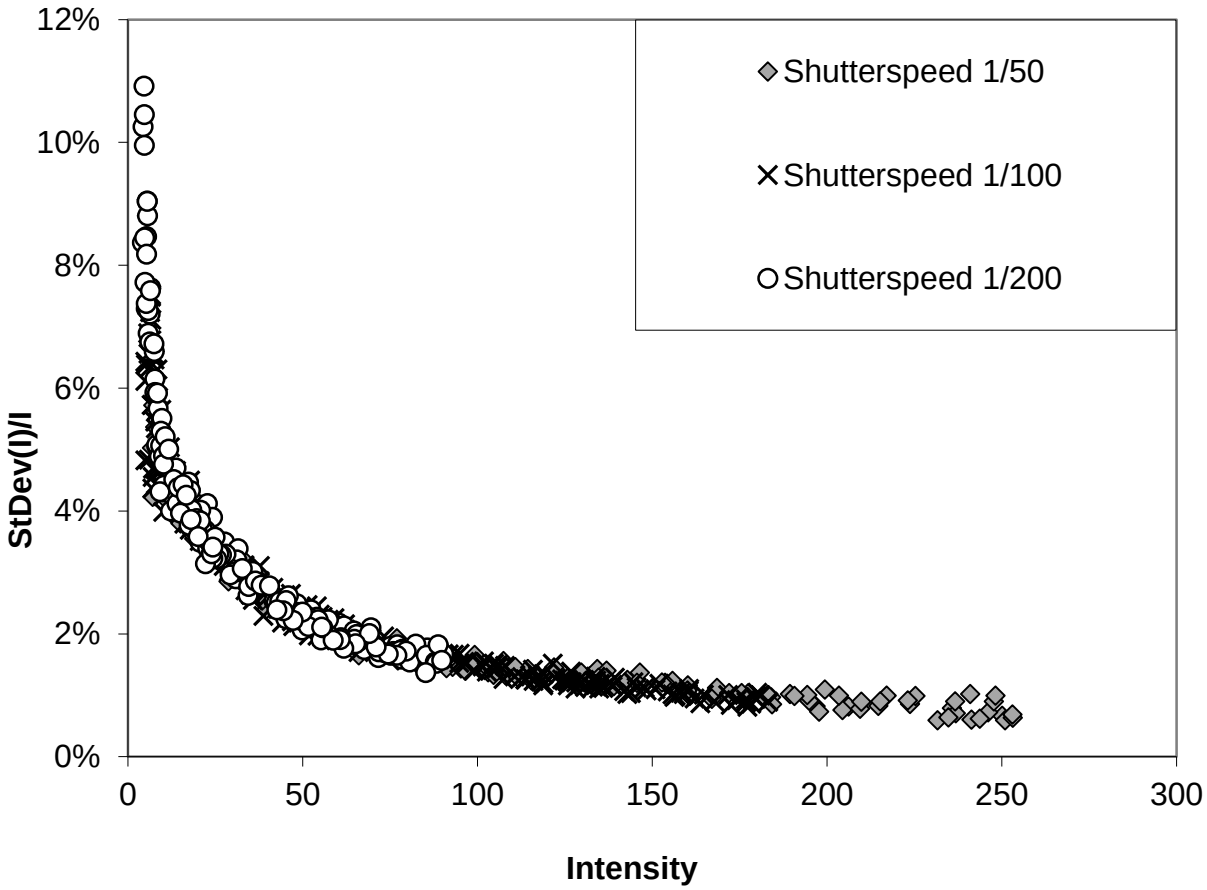

Figure 2-13: Relative standard deviation of the reported intensities of DC light as function of the intensity.

In Figure 2-14 the errors associated with different shutter speeds are depicted for both an LCD screen and a fluorescent light. Here the error increases for shutter speeds of 1/200 or greater. But for shutter speeds below 1/200 the error is comparable to the DC light. It is interesting to note that a shutter speed of 1/100 is sufficient for an LCD screen with a refresh rate of 1/85. For the present experiments shutter speeds of 1/50 or 1/100 will be utilised, depending on the required focal range.

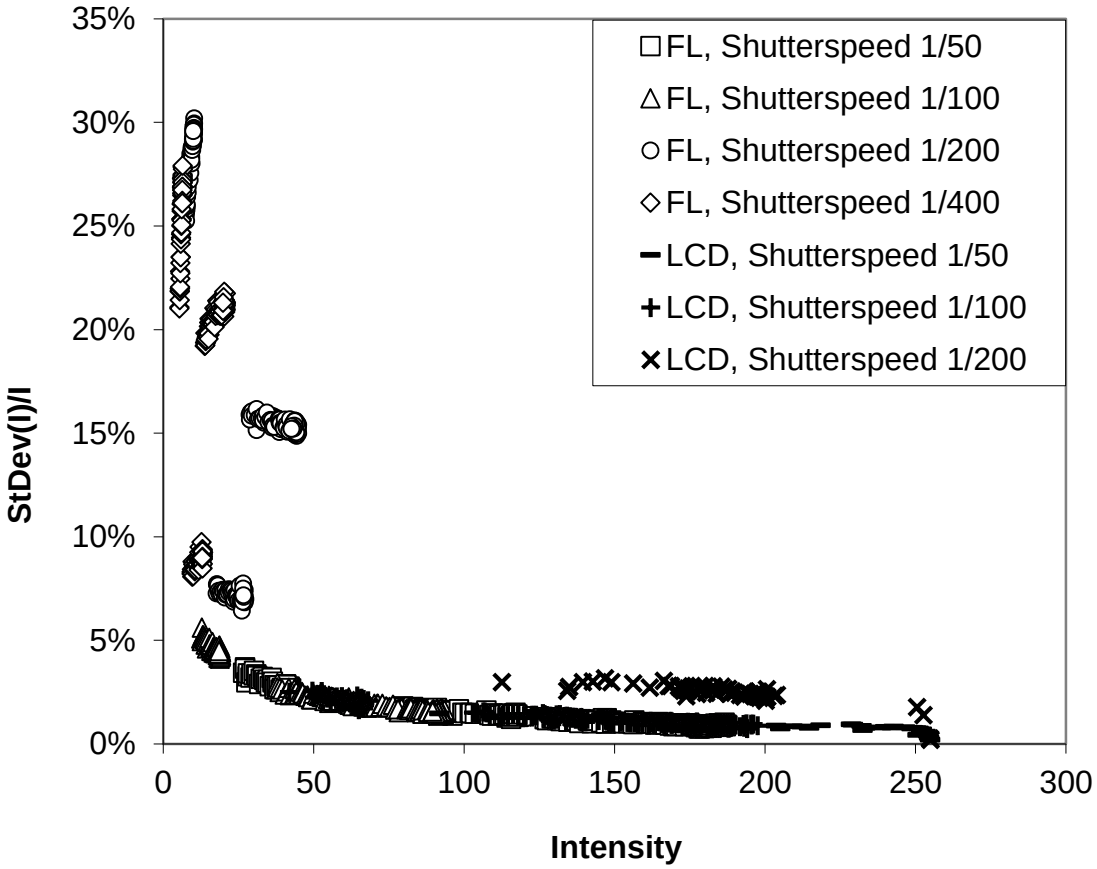

Figure 2-14: Relative standard deviation of the reported intensities of LCD and Fluorescent light as function of the intensity.

The reported noise values can be examined in more detail by considering, in addition to the average and standard deviation, the kurtosis and skewness. This data has been extracted from the LCD and fluorescent light test images and are shown in Figure 2-15. It is evident that for higher reported intensities, both skewness and kurtosis move towards the values of the normal distribution, respectively 0 and 3. This indicates that the assumption of normally distributed noise from the light source is appropriate.

It is evident from the data above that the LCD panels and fluorescent tubes provide sources of light that behave in a consistent manner when compared to a DC light source and that the signals are of reasonably high quality, with relative standard deviations of less than 2% in the practicable range. There is also evidence that this noise is normally distributed. However, a critical difference between these alternative light sources and those employed in a spectrometer is the broad range of wavelengths created, as opposed to the monochromatic source in the spectrometer. The effective use of such a broad range of wavelengths requires a sound understanding of the

responses of the dyes, utilised in the experiments, to these wavelengths and this is investigated in more detail in the following section.

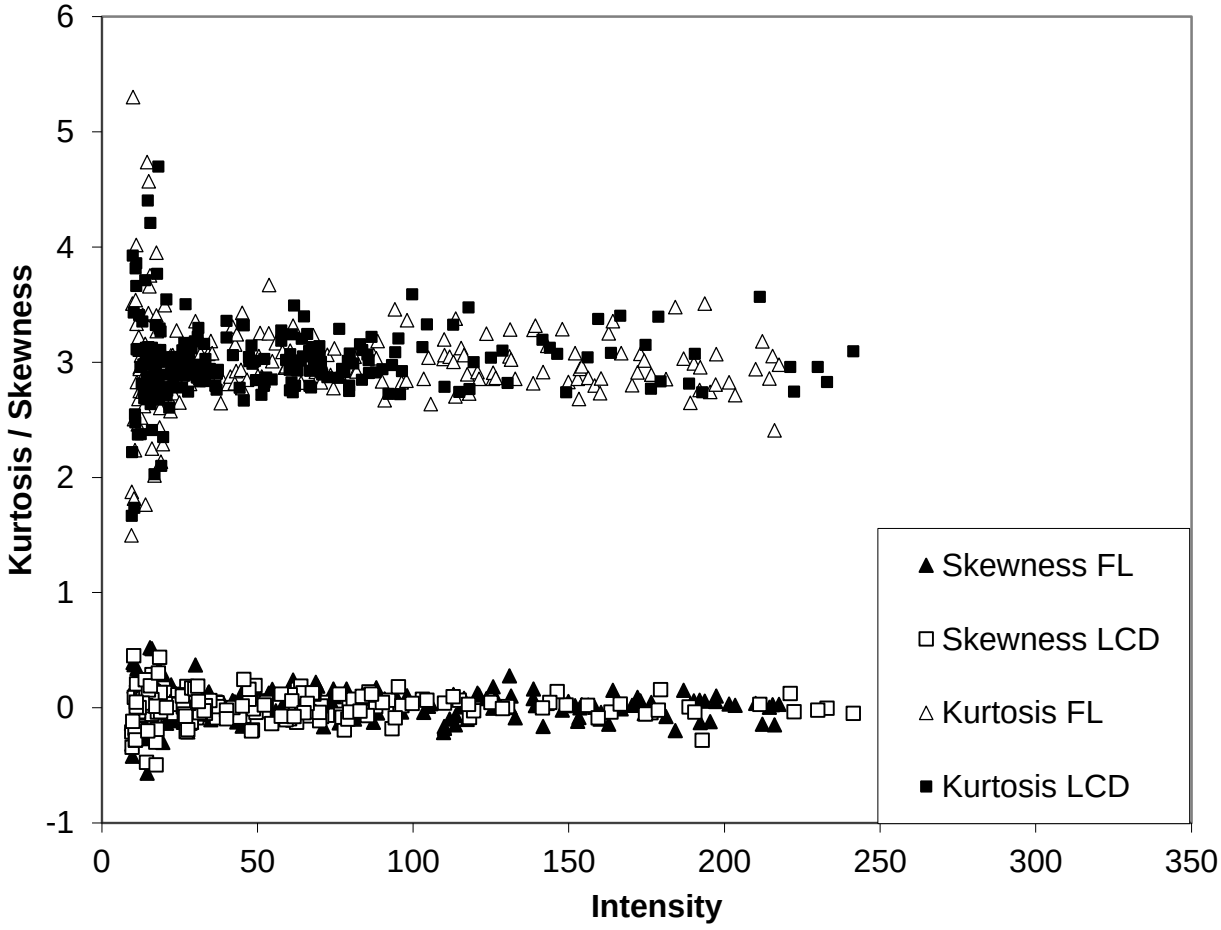

Figure 2-15: Skewness and kurtosis of the reported intensity standard deviations from LCD and Fluorescent light sources.

2.4 Dye Selections

In selecting dyes for the light attenuation technique it is important to recognise that dyes absorb light of different wavelengths in different quantities and that the response of the camera CCD (quantum efficiency) is also different for different wavelengths of light. Figure 2-16 shows the absorption spectra of two dyes, amaranth and hexacol red (Table 2-1). It also shows the spectral sensitivity of the JAI+ camera (Jai 2012). The spectral sensitivity is the relative efficiency of detection as a function of the wavelength. This shows that the camera captures light from a range of wavelengths. For best results the absorbance spectrum of the dye should match the efficiency spectrum of the CCD.

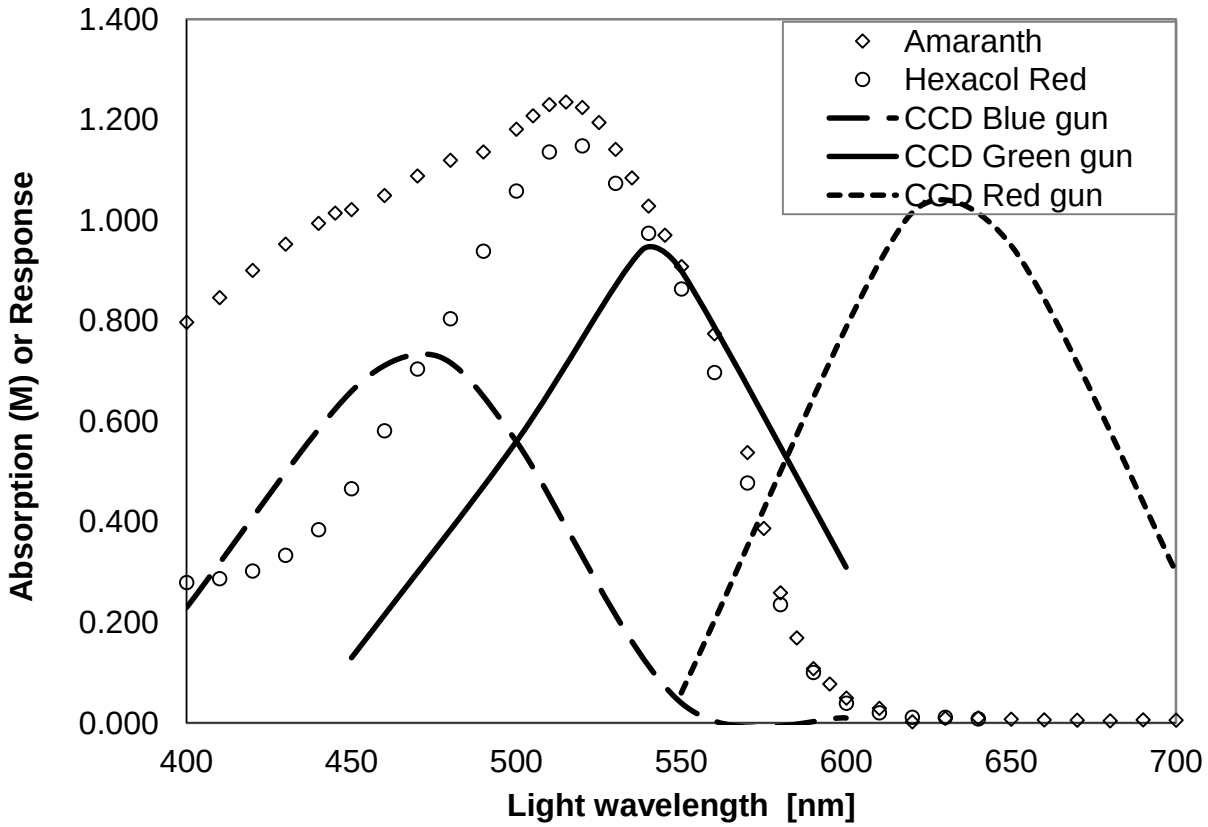

Figure 2-16: The solid lines the spectral sensitivity of the CCD chip over the different wavelengths of visible light. The absorption spectra of the dyes hexacol red (circles) and Amaranth (diamonds) are added for comparison. The source of the point data is the spectrometer measurements and the solid lines were obtained from the CCD specifications.

Table 2-1 lists the dyes that were utilised for the experiments described in this thesis. The dyes are all food additives, and readily available in the food supporting industry in New Zealand.

Green (1990) lists information on a great variety of dyes and stains, and an abbreviated list of this information is given here.

Table 2-1: List of dyes used in the experiments

E-number	Name	Indicator wavelength [nm]	colour	US FD & C[1] nomination
E102	Tartrazine	430	Yellow	Yellow No.5
E127	Erythrosine	525	Red	Red No.3
E132	Indigo carmine	610	Blue	Blue No.2
E133	Brilliant blue FCF	628	Blue	Blue No.1
E129	Hexacol Red	515	Red	Red No.40
E123	Amaranth	520	Red	Red No. 2

[1] US Federal Food Drug and Cosmetic Act.

Although these dyes are readily available and generally used in the food industry, it is important to recognise that they pose certain safety risks and therefore care should be taken when handling them in a laboratory environment. Some of the safety risks are stated below (Green 1990).

Tartrazine is known to provoke asthma attacks although the US food and drug administration (FDA) do not recognise this. Furthermore the US FDA estimates it causes urticaria (nettle rash) in 1:10,000 children. It is also linked to thyroid tumours, chromosomal damage, and hyperactivity. Tartrazine is used to colour drinks, sweets, jams, cereals, snack foods, canned fish, and packaged soups. Erythrosine is the red colour used in cherries, canned fruit, custard mix, sweets, bakery, and snack foods. It can cause sensitivity to light. It was shown to cause thyroid cancer in rats in a study in 1990, and can also increase thyroid hormone levels and lead to hyperthyroidism in humans. Indigo carmine is commonly added to tablets and capsules but it is also used to colour ice cream, sweets, baked goods, confectionary, biscuits, and synthetic coal tar derivatives. It may cause nausea, vomiting, high blood pressure, skin rashes, breathing problems and other allergic reactions. Brilliant blue FCF is used in dairy products, sweets and drinks. Its synthetic usually occurs as ammonium salt. The use of hexacol red has been studied and found increased levels of hyperactivity and ADHD in children. Amaranth has been linked to cancer in female rats at high doses; it has been banned by the FDA and replaced by FD&C Red No. 40.

2.4.1 Dye Absorption

The basis of the LA technique is that the light absorption is linearly reciprocal to dye concentration. However, as noted by Kikkert (2006) and others, the differing responses of dyes to different light wavelengths has the potential to complicate this relatively simple view of light absorption.

In order to investigate this issue further, the absorbance of the dyes listed in Table 2-1 was measured using a Hach Dr2000 spectrometer. The spectrometer measures the absolute value of light absorbed by a sample and an example of these values has been set against the incident light wavelength for the hexacol red dye in Figure 2-17. The absorptions have been measured using the spectrometer at 10 nm intervals and this has been repeated for three different concentrations of the dye, 0.01206 g/l, 0.02411 g/l and 0.04822 g/l.

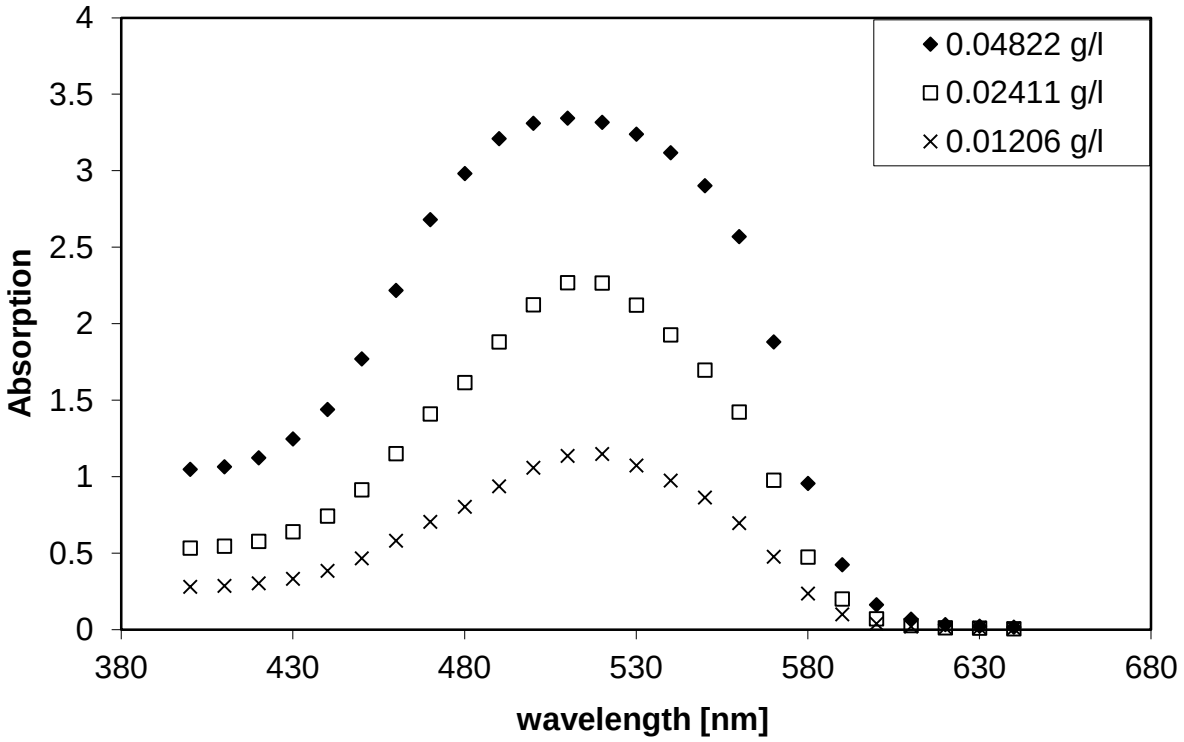

Figure 2-17: Absorption vs wavelength for various concentrations of hexacol dye.

It can be seen from the figure that the dye absorbs most of the light in the lower energy spectrum. The highest absorption occurs at approximately 515 nm, which is the wavelength of maximum light absorption for this dye and this is referred to as the indicator wavelength for the dye. In Figure 2-18 the absorption data has been scaled by the respective dye concentrations. It is clear

the response is linear, when the dye concentration is doubled from 0.01206 g/l to 0.02411 g/l. If however the dye concentration is doubled again, from 0.02411 g/l to 0.04822 g/l, the absorption increases in a non-linear manner. Thus non-linearity becomes significant at a critical dye concentration and this value must be determined accurately to be able to implement that LA system with any confidence. It is also evident that this non-linearity affects wavelengths with the highest absorption first.

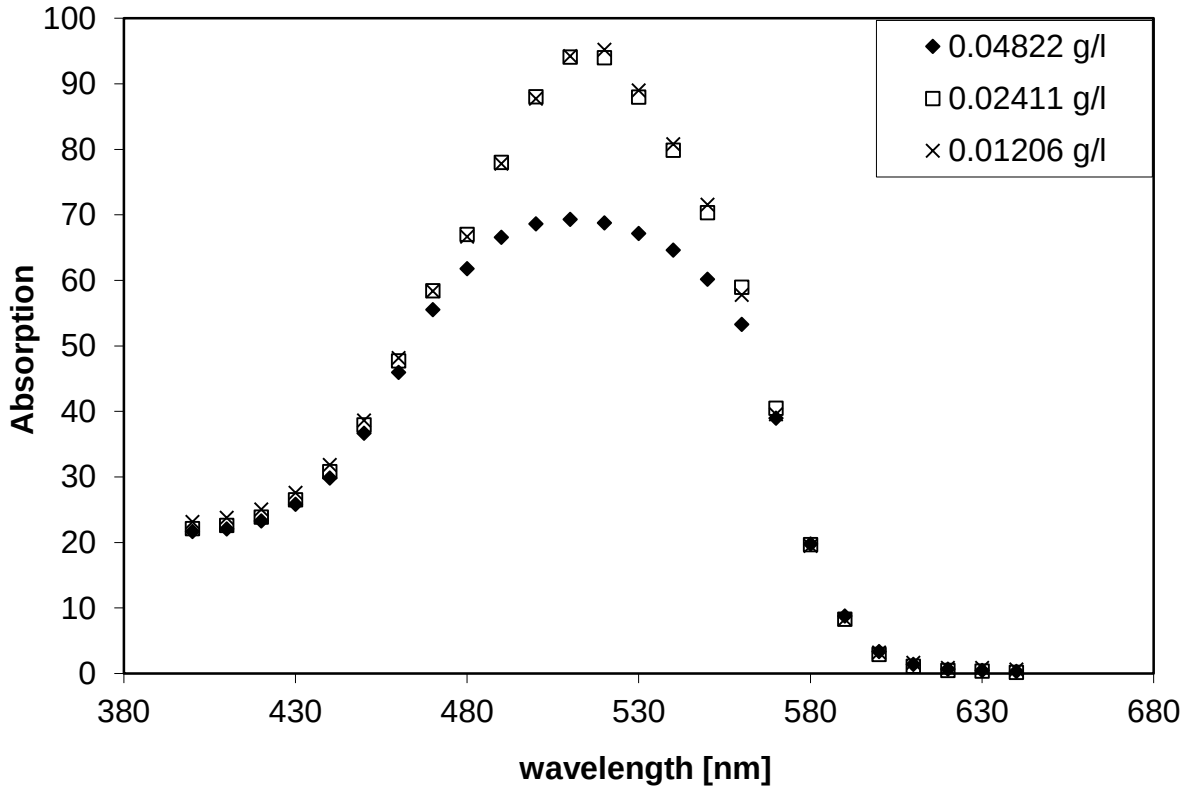

Figure 2-18: Relative Absorption per concentration versus wavelength for concentrations of hexacol dye

In Figure 2-19 the absorption values for different concentrations of the hexacol red dye are shown at the indicator wavelength, averaged over the wavelengths of non-zero response (400-640 nm) both with and without the spectral sensitivity of the CCD. An enlarged version of this figure is presented in Figure 2-20. Linear fits through the data up to a concentration of 0.036 g/l are also shown, along with their associated R^2-values. The R^2-value of the fit of the dye concentrations at the indicator wavelength is the smallest because this is the wavelength with the highest absorption and therefore the first to show evidence of non-linearity as the dye concentration increases (Figure 2-18). The linearity of the absorption data improves (higher R^2-values) when averaged over a range of wavelengths because the non-linearity of the wavelengths with higher absorption characteristics is masked to some extent by the linear responses of the other wavelengths. Including the efficiency of the CCD further improves the linearity of the absorption

data as the point of maximum sensitivity does not coincide with the indicator wavelength of the dyes. Note for a given maximum (critical) dye concentration, the minimum linearity (R^2) is defined by the response at the indicator wavelength. That is, where the response of the CCD is only non-zero at the indicator wavelength, or if the incident light only consists of the indicator wavelength. With the combination of Jai cameras and dyes used, incorporating the effects of the CCD response and a broader range of wavelengths increases the range of the linear response further. Thus the use of a broad spectrum light recorder for the purpose of light attenuation is valid, at least for the dye concentrations where the response is linear at the indicator wavelength.

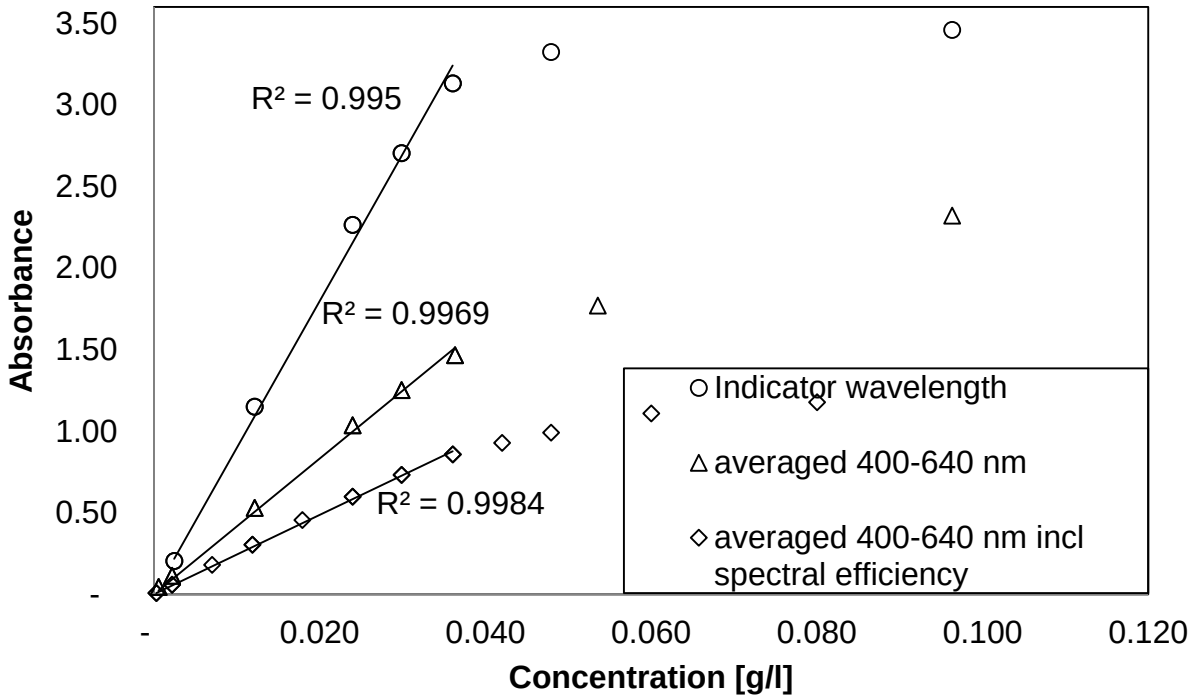

Figure 2-19: Absorbance of hexacol dye at various concentrations in grams per litre, at the indicator wavelength, averaged over 400-640 nm, and averaged over 400-640 nm including spectral efficiency.

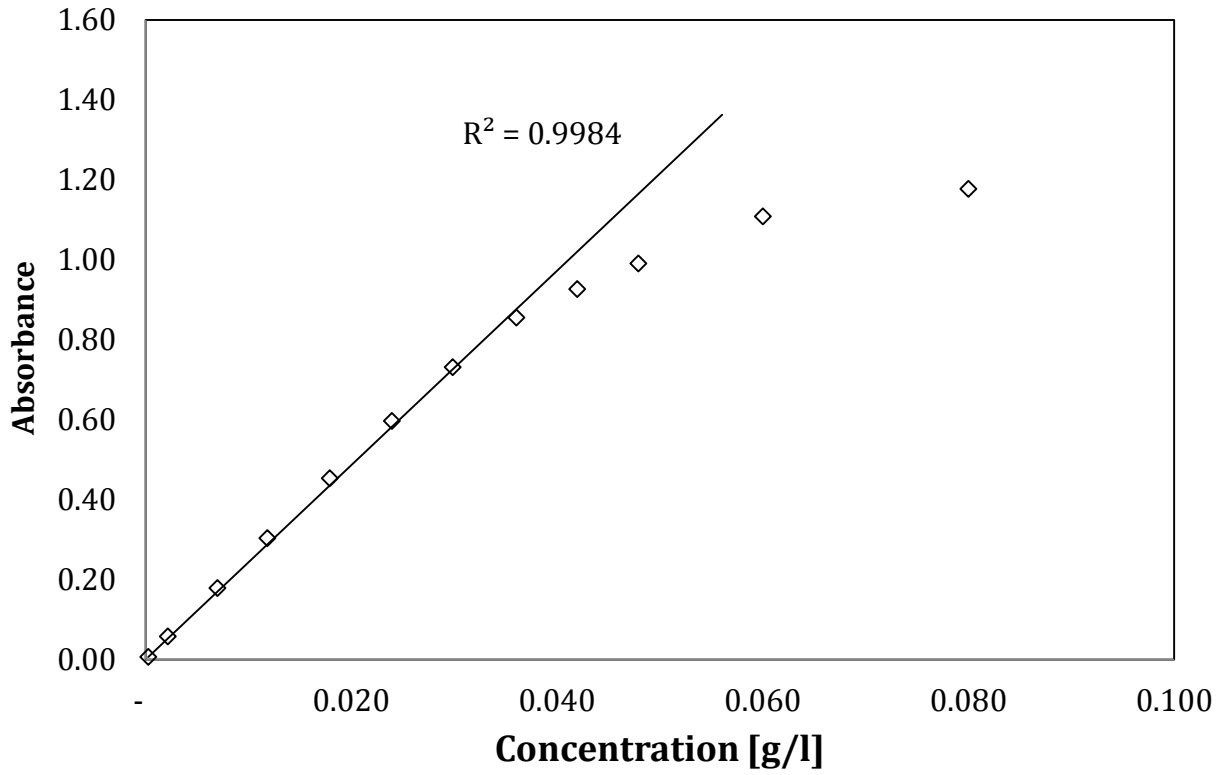

Figure 2-20: Absorbance of hexacol dye at various concentrations averaged over 400-640 nm wavelength including spectral sensitivity.

From Figure 2-20 the error of using a linear approximation can be calculated. The relative errors are depicted in Figure 2-21. The relative error has been taken as the difference between the actual value and the predicted value divided by the actual value. At larger concentrations the relative errors become increasingly problematic. At higher concentrations the spectrometer is measuring a lower light absorbance and this will lead to an underestimation of the concentration. At low concentrations the camera reports somewhat high absorbances, which results in an overestimation of the concentration. This relatively minor effect is inherent to the process of chemical spectroscopy. It is clear that the linear assumption results in an error that is not zero, but which can be kept to a minimum over a reasonable range of dye concentrations. Relatively high concentrations of dye, which are outside the linear range, introduce significant errors.

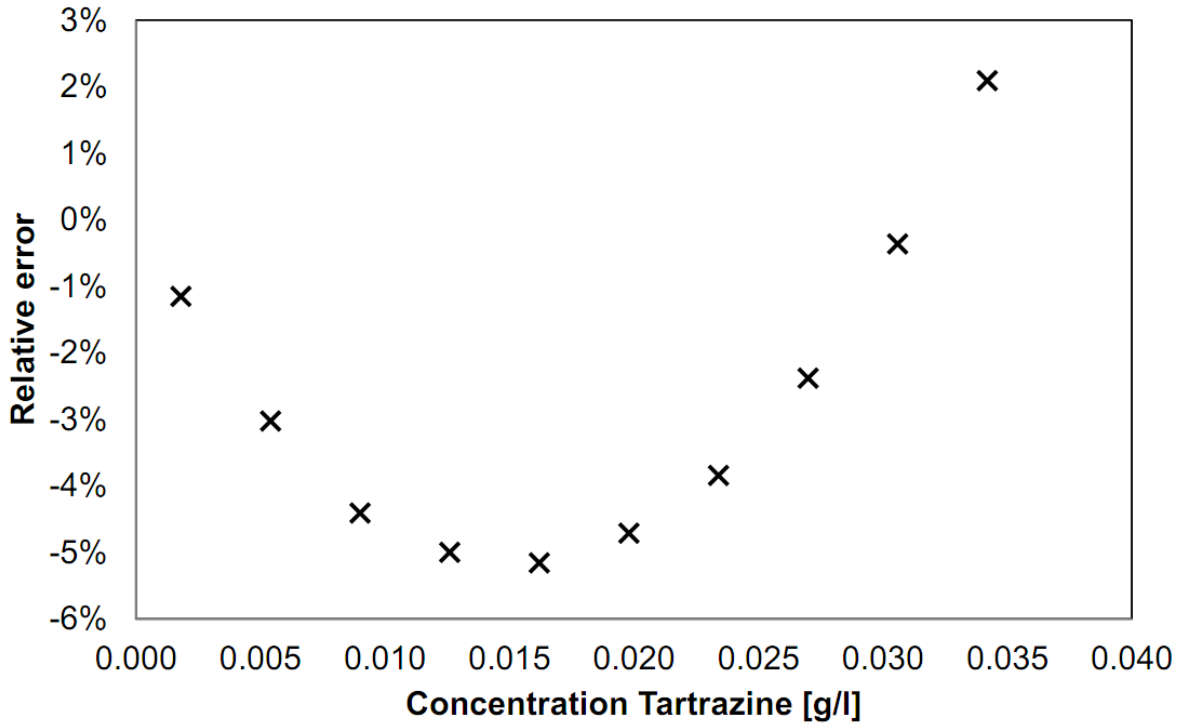

Figure 2-21: Relative error of using a linear best fit to estimate the dye concentration.

Up until this point the used dye samples had a uniform concentration, that is, the dye has been dissolved in a cuvette of water and the absorbance measured with a spectrometer. The flows in the experiments are expected to have some form of Gaussian concentration profile, where the average concentrations vary between maximum at the midline and almost zero at the outer edge of the flow. In order to estimate the errors associated with the linear assumption for a typical range of concentrations, a standard Gaussian profile (referenced to the maximum dye concentration of 0.036 g/l) has been divided in 10 concentration bins (Table 2-2) and based on the expected errors of the linear assumption the cumulative errors have been estimated. Table 2-2 shows the 10 concentration brackets in the first column. The second column is the percentage of the profile that is present in the particular concentration bin, i.e. 25.4% of the profile is expected to have a concentration of between 90 and 100% of the maximum (midline) concentration. The third column is the error associated with the use of a linear assumption instead of the measured values (Figure 2-21). The final column is the product of the error of using a linear assumption and the percentage of the distribution in the bin range.

Table 2-2: Errors associated with using a linear assumption in a Gaussian flow.

Percentage of midline concentration (0.036 g/l)	Part of profile	Error of linear assumption	Cumulative Error
90% - 100%	25.4%	2%	0.53%
80% - 90%	11.0%	0%	-0.04%
70% - 80%	8.4%	-2%	-0.20%
60% - 70%	7.8%	-4%	-0.30%
50% - 60%	7.0%	-5%	-0.33%
40% - 50%	6.4%	-5%	-0.33%
30% - 40%	6.6%	-5%	-0.33%
20% - 30%	6.8%	-4%	-0.30%
10% - 20%	7.6%	-3%	-0.23%
0% - 10%	13.0%	-1%	-0.15%
	100.0%		-1.68%

Note, all measurements have been made with a spectrometer.

The total accumulated error is then the expected error that arises if a light beam travels through the hexacol red dye solution, which is distributed in a Gaussian form along the light path, has a maximum concentration of 0.036 g/l concentration and is captured by the Jai M7+ camera in otherwise perfect conditions. This error is approximately 2.0 %, but the total error is dependent on the maximum concentration, 0.036 g/l. As a flow develops and mixes with the ambient this maximum or centreline concentration lowers and finally all concentrations in the profile will tend towards 0% of the initial concentration and hence the error will increase (Table 2-2). In Figure 2-22, the dependence of the cumulative error on the average midline concentration is shown. In this figure the cumulative error evolves as the flow mixes with the ambient and while at the initial concentration of 0.036 g/l the error is 1.68%, this value increases to a maximum of 3.8% and then reduces towards 1.2%. The cumulative errors associated with assuming a linear response with dye concentration are therefore expected to stay below 4%. Note a non-linear response cannot be used in a cumulative or integrated measurement technique. The total amount of light absorption is measured and has to be related to the amount of dye. This can only be done if the absorption response of the dye is the same for all dye in the ‘slice’ of the experiment. This is the case if the response is linear. Non-linearity would mean that there is no unique solution to the amount of dye.

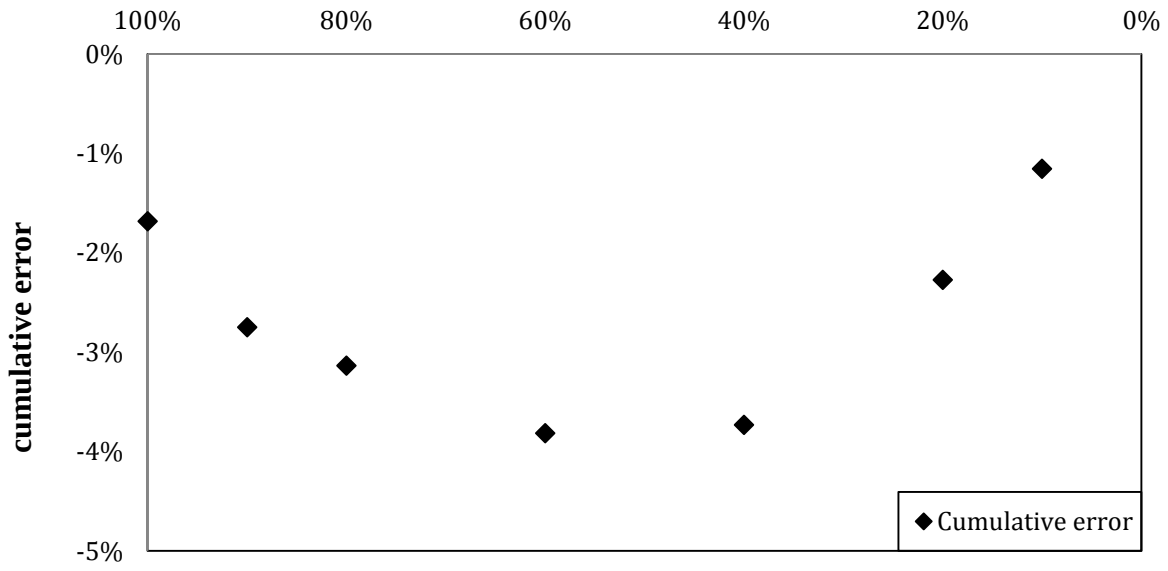

Figure 2-22: Cumulative error due to mixing of the flow.

2.4.2 Dye mixtures.

In the previous section it has been shown that dyes have a maximum concentration above which the relationship between concentration and absorbance is no longer linear. The dynamic range of the LA system is limited by these relatively low maximum concentrations and the minimum concentration required for the cameras to detect dyed fluid. Increasing the dye concentration beyond the maximum limit results in a nonlinear response, thus complicating the analysis. A linear response will not be recovered until the dye has mixed by an appropriate amount with the ambient fluid. Increasing the concentration of the dye not does therefore extend the dynamic range, but instead it relocates the area in which the linear response occurs.

Here the use of two different dyes simultaneously in different concentrations in an LA setup will be investigated. The dyes must be different in that they effectively absorb light of different wavelengths, which is consistent with the two dyes having a different colour. The dyes are also dissolved in different concentrations relative to their respective maximum concentrations in which a linear response is expected (section 2.4.1). One dye is mixed in a relatively high concentration so that it is non-linear in the initial solution, while the concentration of the other dye is such that it remains linear in the initial solution. For this approach to be effective, it needs to be shown that the initially non-linear dye has no detrimental effect or influence on the light

absorbance of the initially linear dye and vice versa. In practice this enables the measurement of light absorbance at two different wavelengths (two different colours), with one colour (lower concentration initially) used in the less diluted zone (near orifice) and the second colour (higher concentration initially) used in the more diluted zone, where the absorbance of this dye will become linear and the concentration of the first dye becomes too low to measure.

An appropriate dye mixture therefore provides the potential to extend the dynamic range of an LA system, but it is essential the dyes in the mixture do not affect each other's absorbance characteristics. As an example the light absorbance of mixtures of two dyes, tartrazine and indigo carmine were measured in a spectrometer. The absorbance was measured at different concentrations and different light wavelengths. Tartrazine absorbs light across the spectrum but has a maximum absorbance at a light wavelength of 430 nm, while Indigo Carmine absorbs most light at a wavelength of 610 nm. The absorbance of tartrazine at 610 nm and Indigo Carmine at 430 nm is very low. Indigo Carmine is linear at concentrations lower than 0.02 g/l and tartrazine is linear for concentrations below 0.014 g/l. Table 2-3 shows the components of the three mixtures of these two dyes. The concentration of indigo carmine was set at the maximum for which the absorbance is linear, while the concentration of tartrazine varied from 0.0140 grams per litre to 0.1270 grams per litre. At the lowest concentration the absorbance of tartrazine is linear, while at higher concentrations a non-linear response is expected.

Table 2-3: Components of the three dye mixtures.

	Tartrazine [g/l]	Indigo Carmine [g/l]
Mixture 1	0.0572	0.0202
Mixture 2	0.1270	0.0196
Mixture 3	0.0140	0.0198

In the Figure 2-23 the results from the spectrometer are shown. The light absorbance of the mixtures has been measured at wavelengths of 430 nm (grey symbols) and 610 nm (open symbols) for various dilutions. Absorbance values from the spectrometer are plotted on the vertical axis, while the horizontal axis shows the concentration of the respective mixtures, C_s/C_0, where C_s represents the concentration of the sample and C_0 for the original concentration (Table 2-3). Best fit linear trend lines have been added to this figure. The absorbance of the 610 nm wavelength of light is linear in both experiments (the 430 nm and 610 nm absorbance tests) across all concentrations. This was to be expected as indigo carmine concentrations are such that a linear

response is expected and tartrazine does not absorb light of this wavelength. Thus the presence of tartrazine did not affect the absorbance characteristics of indigo carmine. The absorbance of the 430 nm light wavelength becomes linear at lower concentrations, which coincides with tartrazine being diluted below its maximum linear concentration.

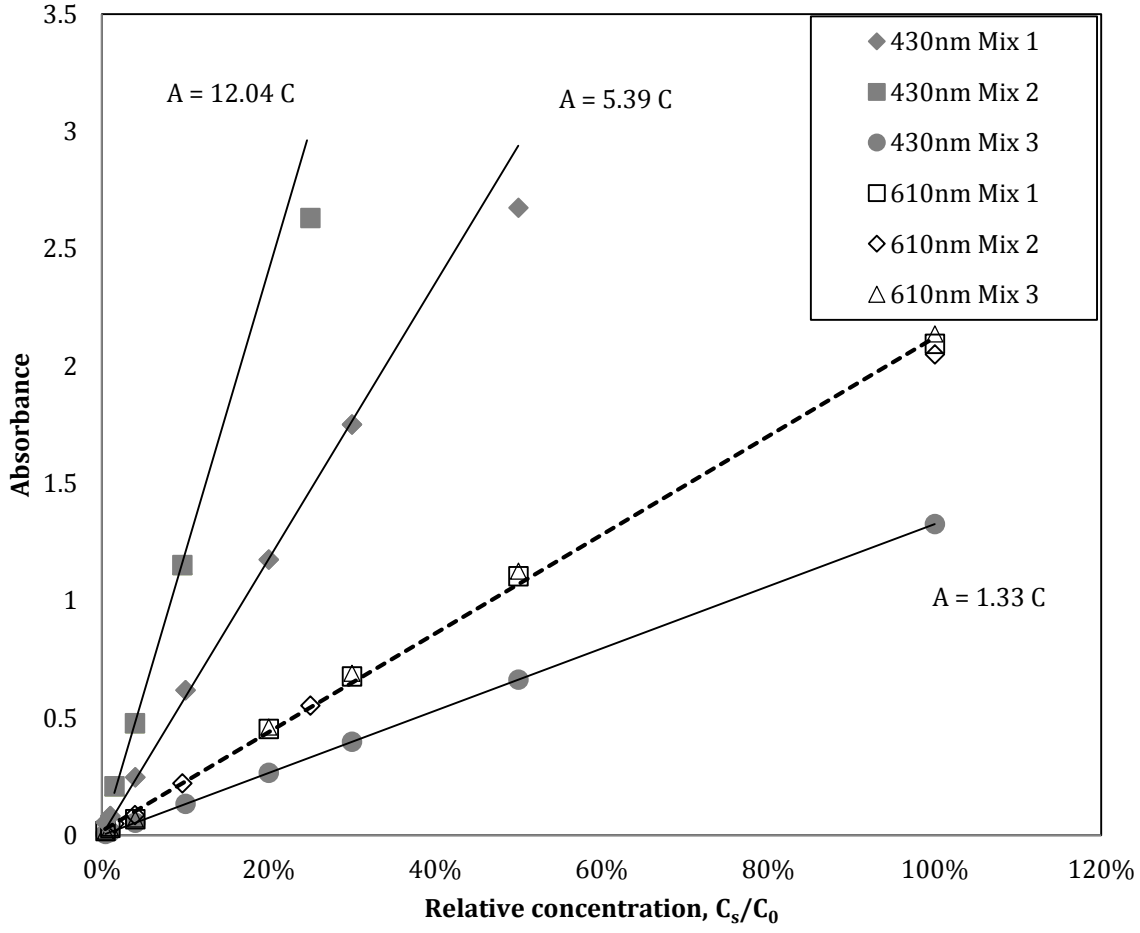

Figure 2-23: Absorbance of the three mixtures at 430nm and 610nm at various concentrations.

In Figure 2-24 the area below 10% concentration (from Figure 2-23) is expanded, so that the dye response at lower concentrations can be more clearly seen. Because of the relatively low concentrations, both dyes are responding in a linear manner and in this situation either dye can be used to determine concentrations. Importantly for a given dilution the signal at 430 nm wavelength (grey symbols) is relatively strong for the mixtures 1 and 2 and is therefore relatively easy to measure, whereas the absorbances at 610 nm (open symbols) are generally weak and therefore more difficult to measure accurately. Thus mixtures of this nature have the more general benefit of being able to extract higher quality low concentration data throughout the flow field.

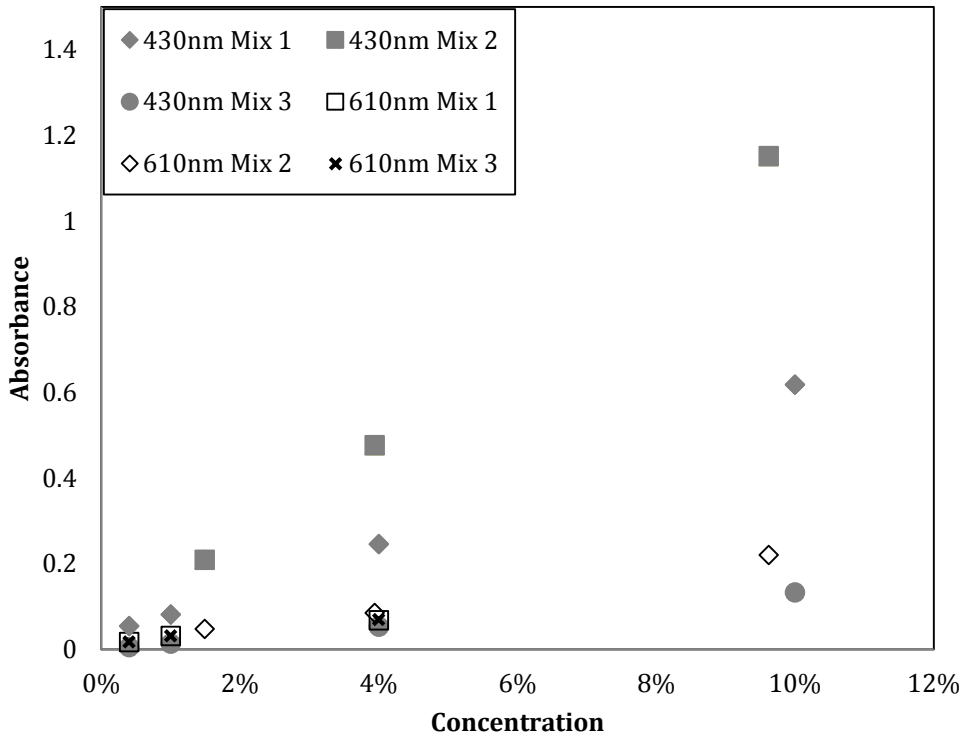

Figure 2-24: Absorbance of the three mixtures at 430nm and 610nm at various concentrations below 12%.

The spectrometer data clearly shows that it is possible to make use of dye mixtures to expand the dynamic range of the LA system and to generally improve the quality of the data measured at higher dilutions. The mixture is designed so that one of the dyes is targeted at measuring relatively high dilutions, this dye initially exhibits a non-linear response because of its higher concentrations at the source, but as the flow is diluted this non-linearity becomes negligible. In contrast the second dye is targeted at lower dilutions and exhibits an initially linear response because of its relatively low initial concentration. This second dye becomes increasingly difficult to detect as the flow becomes more dilute. For the mixture to work effectively, it is critical that the absorbance characteristics of the individual dyes are not compromised within the mixture and the above data indicates that these characteristics are maintained for appropriate mixtures of Indigo Carmine and Tartrazine.

2.4.3 A Note on Temperature Effects

It is possible that the temperature variations could affect the absorbance characteristics of the dyes and hence the performance of the LA system. In Figure 2-25 changes in the measured absorbance of tartrazine, in a 0.014 gram per litre solution, with temperature variations are shown. The best fit trend line is included and it is evident that the absorbance is weakly dependent on temperature. Over the measured temperature range of 10 to 36 degrees Celsius, the trend line indicates a relative change in light absorbance of 0.166% per degree.

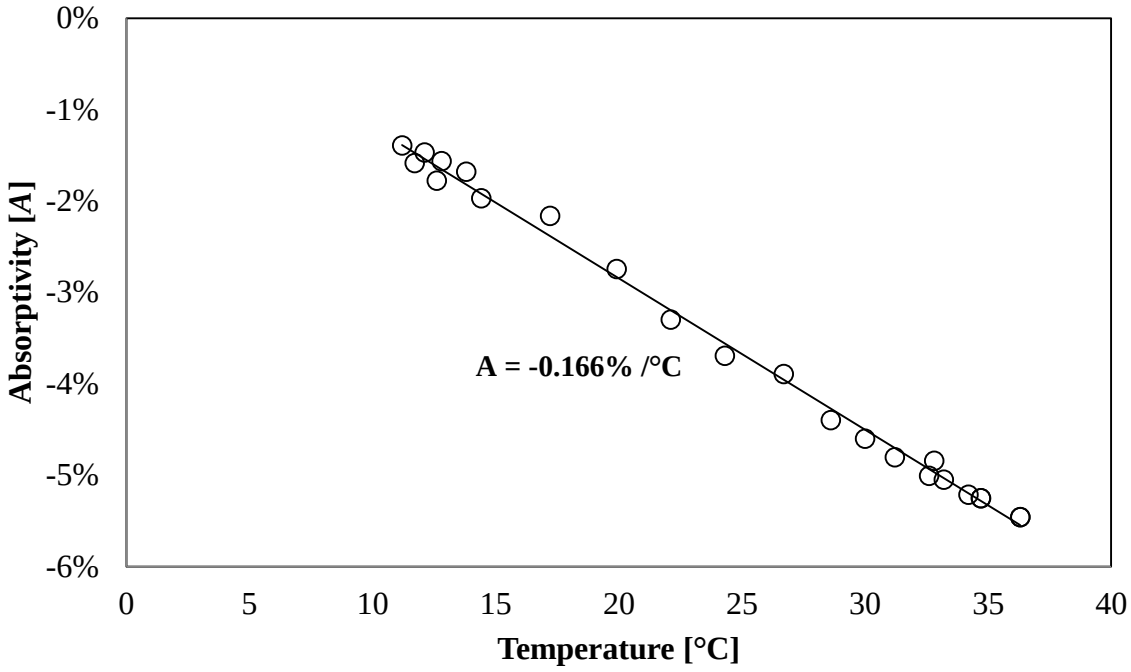

Figure 2-25: Relative change in absorbance of tartrazine at different temperatures, in a 0.014 gram per litre solution and a light beam travel path through the mixture of 13.25 mm measured at 430 nm wavelength.

While the dependence on temperature is weak, associated errors were minimised by keeping the temperatures as constant as possible during a set of experiments, which included the recording of reference images for the LA system. The source tank was submerged in the main tank to ensure that the source fluid and ambient fluid were at the same temperature (Figure 2-26). This shows that the timing is important, the time between the experiment and the calibration must be short so that the ambient water has not time to cool or heat up. It also shows that the temperature of the source and ambient fluid must be approximately equal. If the source fluid changes temperature through mixing, the absorbance will change. The temperatures were tested before and after each experiment. In all cases they were found to be within 0.2 degrees Celsius from

each other. Thus the absorbance could differ by 0.08% because of this temperature difference, which is negligible.

Water has also been tested and has been found to have negligible temperature dependent absorbance. In comparison Langford et al. (2001) reported a maximum water absorptivity temperature dependence of 0.0091% (at wavelength 738 nm) and furthermore after comparing their results to literature values they suggest that organic impurities in the water have a negligible effect on the temperature coefficient of absorptivity in the visible and near-IR regions.

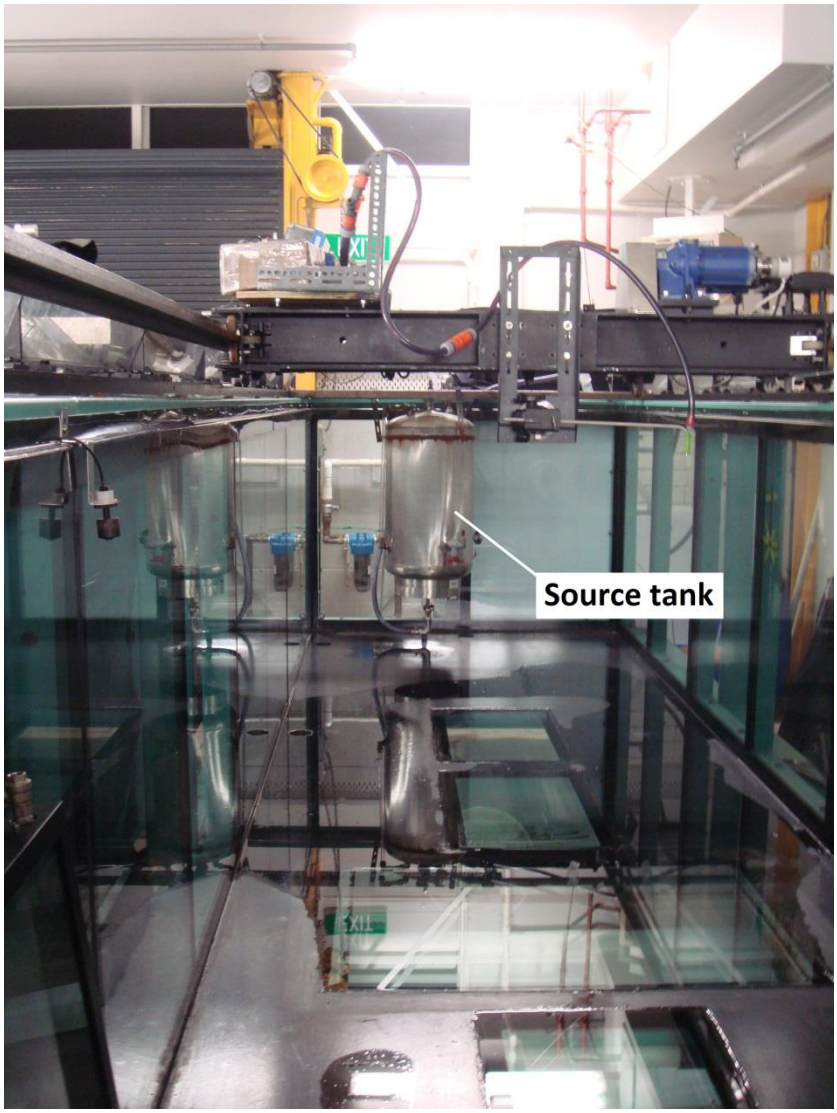

Figure 2-26: Water tank visible at end of the tank.

2.5 Geometry

This section describes the issues relating to the capture of the light through two cameras of an object that is located at a certain distance from the cameras.

Figure 2-27 shows the fields of view of the cameras. The field of view of the side camera is a square in the *x*-*z* plane displaying integrated information along the direction of the camera (*y* direction). The top camera captures integrated information in an *x*-*y* grid.

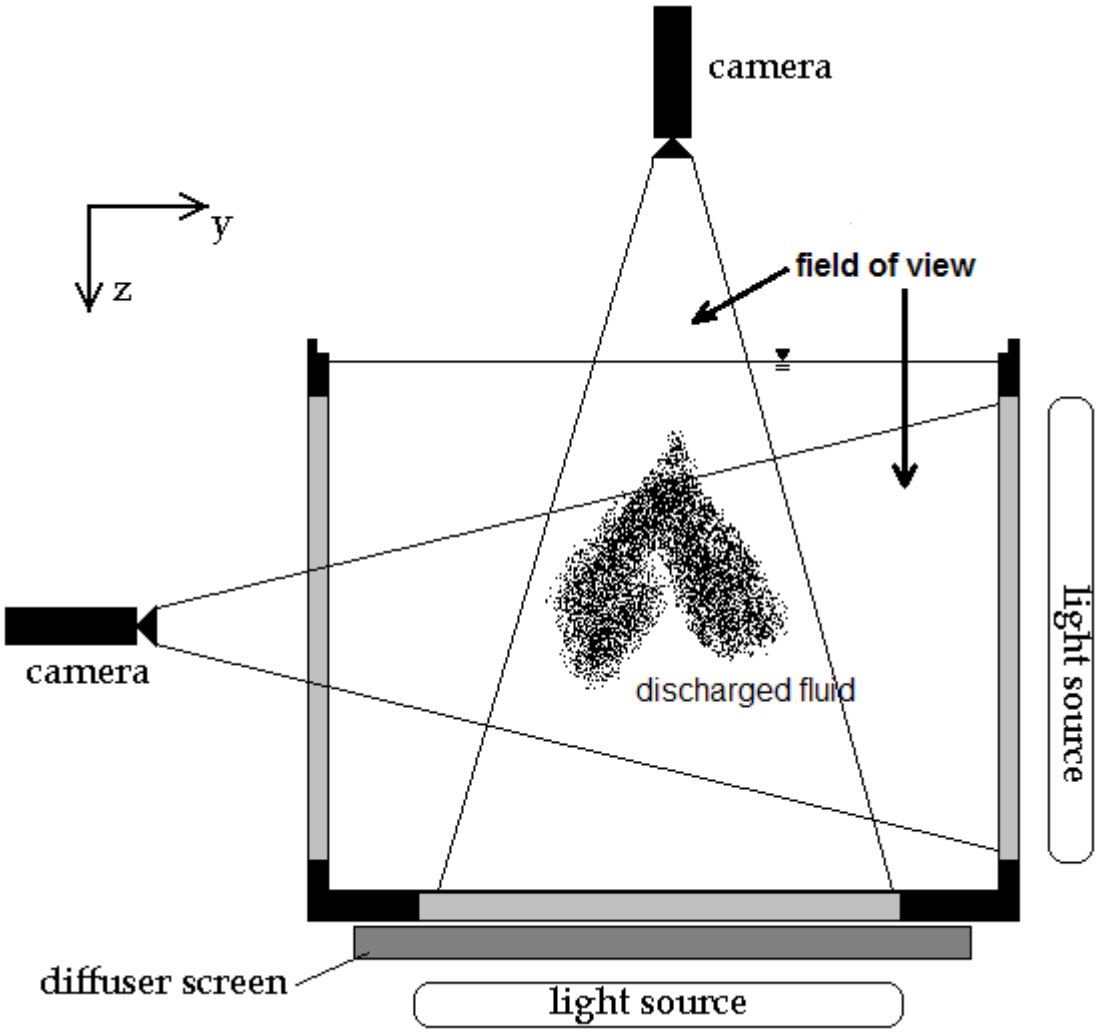

Figure 2-27: Cross cut of setup showing the field of view of the cameras.

The combined information of the two cameras (disregarding the *x* direction here) is 2*n, where n is the number of pixels in *z*-direction for the side camera and also the number of pixels in *y*-direction for the top camera. The whole frame can be divided is n^2 points, so not every point can be measured using this setup, however integrated information can be used with the additional

assumption of flow profile. Also the 2*n pixels are enough information to provide the location of the maximum concentration.

Both cameras give an image that obviously consists of pixels in the *x*-*y* plane (top camera) or *x*-*z* plane (side camera). If the number of pixels of the cameras in the *x* direction is *p* then the above can be restated that the cameras give simultaneously *p* images that in case of a moving source have to be added together. For more information on the addition of the subsequent frames, see Kikkert (2006).

Figure 2-28 shows a schematic of the setup. Two cameras simultaneously capture an object at distance L_1 and L_2 from the respective cameras. The information the cameras give is an intensity of light at a pixel location. P is the point where the midlines of the cameras cross and α_2, β_1 are the angles that the object is away from the respective midlines of the cameras.

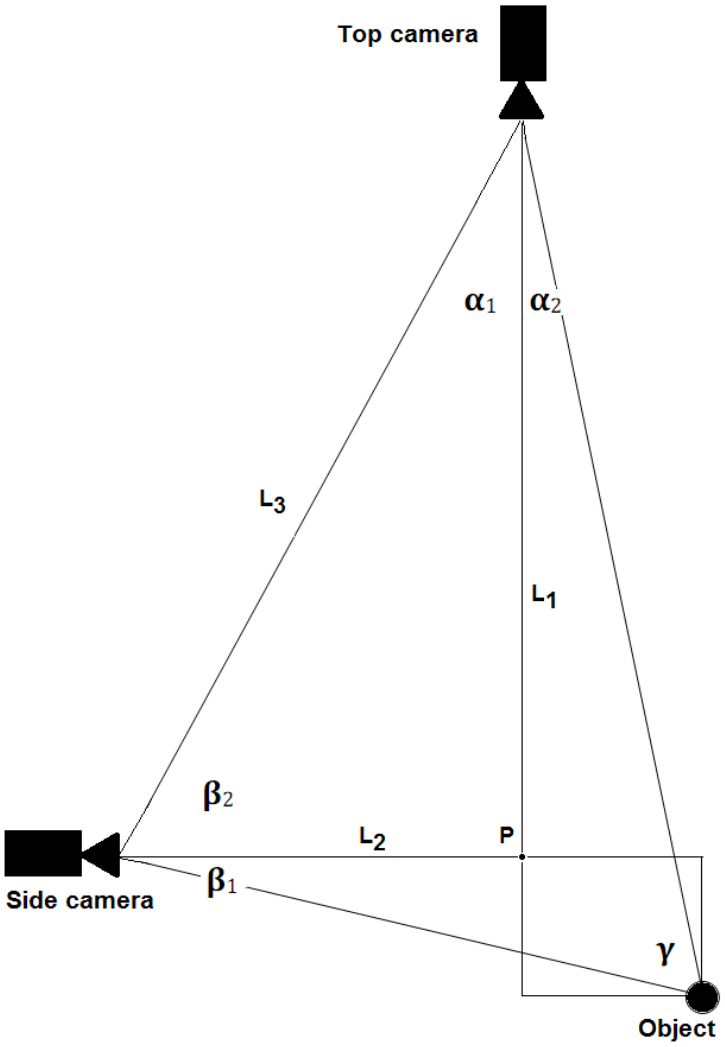

Figure 2-28: Schematic basic camera setup.

In the basic setup the position of the cameras is known and also their field of view. This means that L_3, and the distances from the cameras to P can be calculated with the cosine law. Assuming that L_1 and L_2 are at a right angle then angles $\boldsymbol{\alpha}_1$ and $\boldsymbol{\beta}_2$ can be easily calculated.
The angles $\boldsymbol{\alpha}_2$ and $\boldsymbol{\beta}_1$ follow from recalculation of the pixels from respective cameras. Finally angle $\boldsymbol{\gamma}$ can be calculated, and with length L_3 and the sine formula the other distances from the cameras to the object.

The distances from the camera to the object are used for the calculation of the exact position and for accurate scaling of the object at that position. In the setup the approximate physical distance from the side camera to P is 4500 mm, and the area of experiments 450 mm at either side of the midpoint P. Trigonometry shows that an object at 4050 mm will appear 10% too big and vice versa and an object at 4950 mm 10% too small. In Figure 2-29 an object is portrayed that moves to a distance twice as far from the camera, the camera will perceive the object as twice as small. As the actual object does not shrink it has to be resized, using the distance.

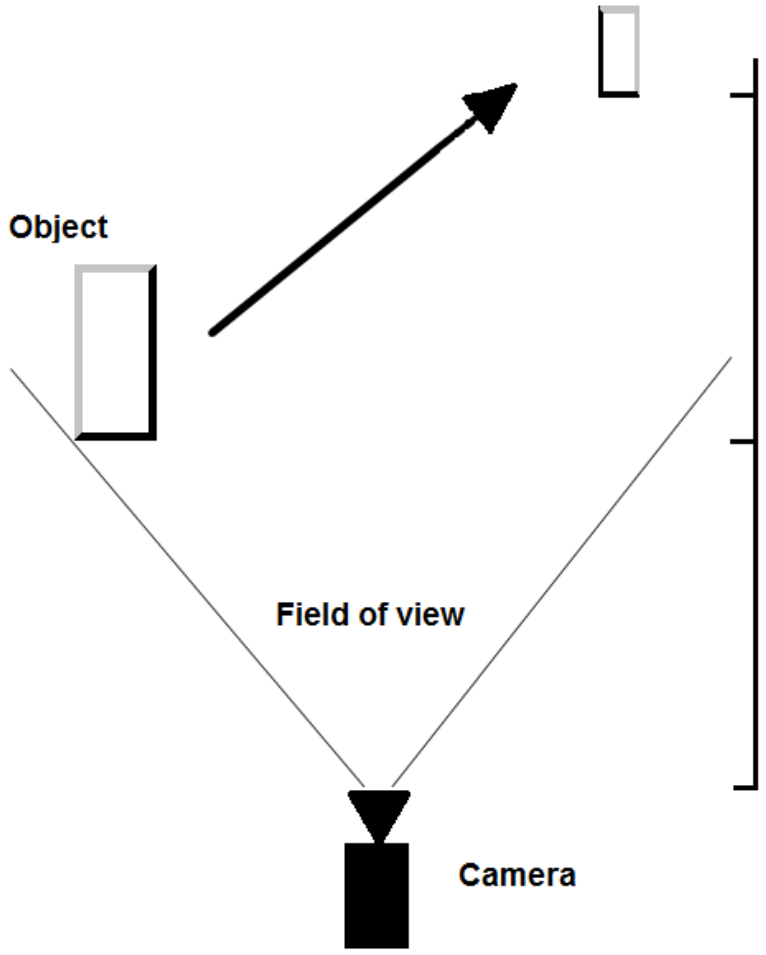

Figure 2-29: Objects may appear smaller than they are.

In the previous calculations the distances from the cameras to the object have been taken as the physical distance. However as the light from the object to the camera passes through three media, water, glass and air (side camera, Figure 2-30) or through two media, water and air (top camera) this distance is not correct. Experimentally it has been verified that if an object moves 10% further away from the camera, from 4500 mm to 4950 mm in the setup, the size only decreases by approximately 8%. The correct 'distance' or pseudo distance has been calculated by measuring the apparent 'shrinking' of an object of known dimensions moving in the main tank away from the cameras. From this calibration the pseudo distances has been calculated to be 5770 mm for the side camera and 6250 mm for the top camera.

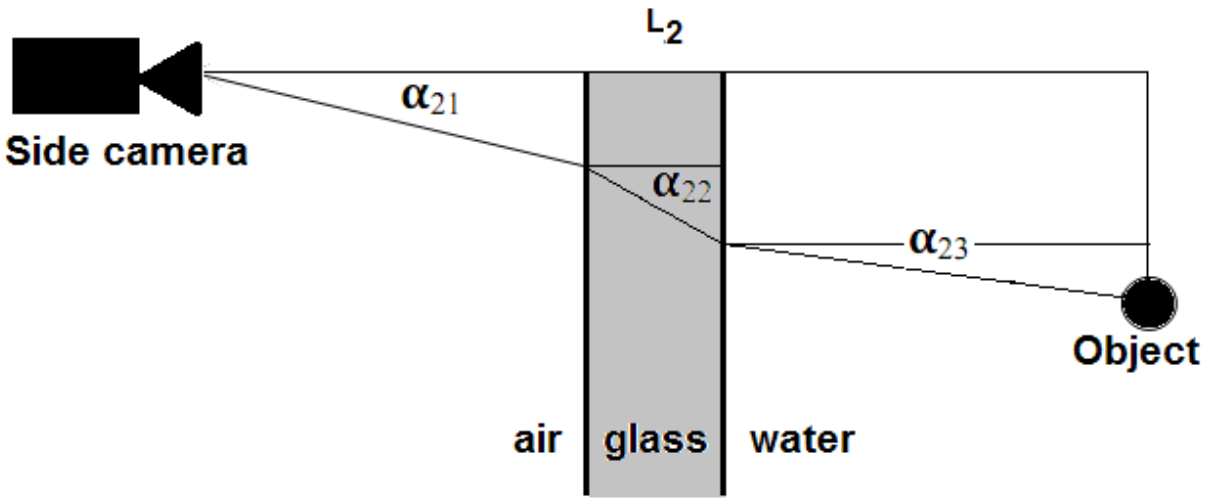

Figure 2-30: Schematic light path from object to camera, through 3 mediums.

In Figure 2-31 a raster of pixels and the corresponding roster of actual positions calculated using the mentioned routine is shown. The horizontal and vertical axes represent both pixels and millimetres. The difference in 'size' depends on the scaling.

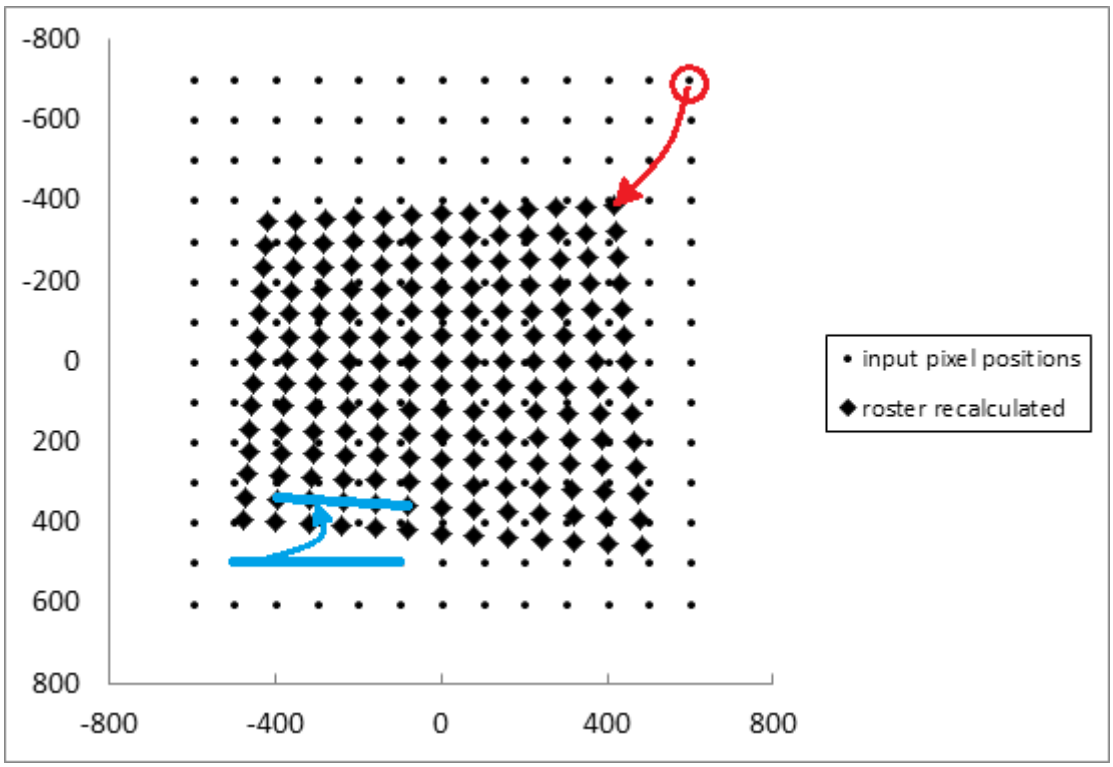

Figure 2-31: Pixel roster recalculated to position roster.

Figure 2-31 represents the *y-z* plane, the side pixels come from the side camera, the horizontal pixels from the vertical camera. The side camera is positioned to the left of the picture and the top camera is positioned above the figure. The recalculated roster (diamonds) are pixel points depicted at their real positions. So the actual position of the top right pixel and the actual location of a bar on the lower left corner are as shown in Figure 2-31. After capture and initial filtering, all pixel positions must be recalculated into real positions. For ease of calculations the top camera has been set up exactly vertical and the side camera exactly horizontal. The only pixel that therefore does not need repositioning is point P(0,0) which is the midpoint of the 2 fields of view of the cameras. The red arrow indicates where the reported position of the pixel is (input pixel position) and where the actual position (recalculated) position is. The same is true for the blue line except the reference is now a line as opposed to a single data point.

2.6 Summary

Light attenuation (LA) is a technique that measures the amount of light that has been absorbed by a sample and correlates this to the amount of contaminant. It can be used to measure the dilution of a flow. The light attenuation system resembles a broadband spectroscopic device as is used in various other scientific disciplines. Research applicable to spectroscopy has been applied to the LA system. In the LA setup two cameras are used to get an appreciation of the flow from the side and from the top. The absorbance of light by the glass and water have been found to be negligible in the experiments and the absorbance of a flow can be related to the concentration of the absorbing contaminant through Beer's law.

There are more differences between LA and spectroscopy which have been reviewed. LA uses a different camera than a spectroscopic device; however for the use of LA the JAI cameras are good enough and in particular for use with multiple dyes the monochrome spectrometer would not suffice. Spectroscopy uses a light source of a single wavelength, to indicate the presence of a certain substance in the wavelength of maximum absorbance. LA uses a non-single wavelength light source although this has been shown to have a negligible effect and even extends the range of linearity, depending on the camera/dye combination.

The most important camera parameter concerning the accuracy is the signal to noise ratio. It is desirable to operate an imaging system under conditions that are limited by the inherent photon noise, with other noise components being reduced to relative insignificance. Photon noise is relatively small if a large amount of light enters the camera, therefore the aperture was set at large and shutter speeds as low as possible. The shutter speed is also limited by the refreshing rates of the back lights and therefore set to 1/50 or 1/100. The dark noise has been found to be negligible and tests have shown that the used Jai+ camera is not as good as a Pulnix, however if the range of values of the measured light intensities lies between 70 and 240 on the 0-255 scale, the error remains below 2%. In the experiments the choice was made not to sacrifice spatial resolution, hence binning was not used. Using gain should only be done when at the smallest number aperture and fastest shutter speeds the signal is still too faint. The gain setting used for the experiments was 0. The black level setting must be determined so that the dyes absorb the light linearly. The black level for the Jai+ cameras was set to 93.

For light attenuation food dyes are used to distinguish a flow. These dyes have been checked and they absorb light in such a fashion that up to a maximum concentration, the initial concentration can be deduced from the amount of absorbed light. The used dyes are readily available but do pose some risks if used in high concentrations. Using a flow with a Gaussian distribution profile introduces an error that is smaller than 4%. It is possible to use two dyes simultaneously to measure the absorbance at two different colours or wavelengths. This extends the range of the experiments. There have been found some temperature related effects, so the temperature should be within 0.2 degrees for the experiments so the effects are negligible.

As the setup uses two cameras that are some distance away from the flow there will be parallax effects and the pixel positions have to be set to actual coordinates. The flows move towards or away from the cameras, this means that the scaling is not constant. A scaling dependent on the distance from the camera has been set up and used for the experiments.

Chapter 3 - Line advected thermals

3.1 Introduction

As discussed in Chapter 1, predicting the initial mixing of wastewater discharges is a critical component of the design of outfall systems. In the case of positively buoyant discharges, the wastewater is typically released near the ocean floor and rises towards the free surface where the initial mixing can be strongly influenced by the ambient currents and stratification. If, after initial discharge, the ambient density is homogeneous, the influence of the ambient currents is of primary interest and it is then possible to observe several distinct forms of the flow behaviour, often referred to as the limiting cases (Jirka 2004, Wood 1993). The form that is present depends on the relative importance of the initial, buoyancy-generated and entrained ambient momentum fluxes. However, given sufficient depth, the entrained ambient momentum flux will eventually dominate the flow behaviour, with the buoyancy flux having a secondary role, and the mean behaviour will resemble that of a line vortex pair. This final self-similar flow regime or limiting case is commonly referred to as a line-advected thermal (Davidson and Pun 1998). Note that a similar line vortex pair can form when the flow evolves from the interaction of the ambient motion and the initial momentum flux; this flow is often referred to as an advected-line momentum puff (Chu 1996, Chu and Lee 1996, Kikkert et al. 2007). Although the mechanisms generating these two distinct flows are different, the mean cross sectional flow structures are similar and have a double vortex form. In contrast key parameters of the flow, such as trajectory and dilution have been shown to differ (Lee and Chu 2003).

It is worth noting that there are a variety of effects that can influence the dilution such as ambient stratification, boundary effects (surface and seabed), variations in flow and/or ambient velocities, changes to the fluid or ambient densities, the presence of solid particles or bubbles in the flow or ambient, salinity variations in the ambient, and temperature effects. While the uncertainties created by this variability are important, they have been neglected in this study where the focus is to provide a more complete picture of the undisturbed near field flow. The measured variability of this near field flow could, in real applications, be overshadowed by sufficiently large variations in any of the above mentioned effects. However assessing the potential influences of these additional parameters, requires that we initially develop a sound understanding of the near field flow in their absence.

Integral models such as Corjet (Doneker and Jirka 2007), Visjet (Cheung et al. 2000) and Visual Plumes (EPA 2001) are commonly employed to predict the initial mixing of wastewater discharges and are capable of incorporating the influences of ambient motion (including ambient stratification) on this mixing. However, in each case the details of the mean cross sectional profiles are not incorporated into the model formulation, instead for simplicity a "standard" cross sectional form is assumed. Top-hat profiles are assumed in the case of Visual Plumes and Visjet, and a single Gaussian in the case of Corjet. These models then rely on conversion factors to transform the predicted data into the peak values associated with specific profiles within particular flow regimes, where these profiles are assumed to be self-similar. The peak mean concentrations, for example, are of particular interest when dealing with the compliance issues that often drive the design of wastewater disposal systems.

The effectiveness of the model predictions is dependent on an accurate determination of the conversion factors within the specific flow regimes and this requires that the mean profiles within these regimes are characterized in a systematic way. While extensive data exists in the case of the weakly advected jet and plume regions (Pun 1998, Law and Wang 2000), where the mean profiles resemble a single Gaussian distribution, less information is available in the strongly-advected thermal and puff regions. Therefore the conversion factors within the latter are defined with less confidence. Indeed in general the advected thermal and line-momentum puff conversion factors are assumed to be equal, as are the flow growth rates. Kikkert et al. (2007) carried out a relatively detailed study into the behaviour of line-momentum puffs. Measurements were made with a light attenuation system, which is similar to that employed in the present study, and their data were shown to be consistent with that from earlier studies carried out by Knudsen (1988), Chu (1996) and Gaskin (1995). Kikkert et al. (2007) employed a double Gaussian approximation to characterize their measured mean-concentration profiles and this provided a basis for more accurately determining the conversion factors. They noted a certain degree of arbitrariness in the definition of top-hat profiles (amongst other things) for these flows and that care must be taken when determining conversion factors for specific model formulations.

In this chapter the work of Kikkert (2006) and Kikkert et al. (2007) is extended to include the behaviour of the more practically relevant line advected thermal regime. Preliminary results from the present investigation were reported in Scheepbouwer et al. (2007, 2008), where the thermals formed as a result of buoyant discharges released perpendicular to the ambient current. In this paper these results are interpreted in more detail and in the context of an additional series of experiments where the thermals were formed as the result of discharges parallel to the ambient current. In addition a

small number of momentum puff experiments have been carried out to provide direct comparison with the results of Kikkert and to highlight any differences between momentum puffs and line advected thermals.

3.2 Theoretical Framework

Following Kikkert et al. (2007), data presentation and interpretation is aided by a relatively simple framework based on relevant analytical solutions and a double-Gaussian approximation. For more information regarding momentum puffs refer to Kikkert (2006) and Kikkert et al. (2007). Here two specific discharge scenarios are considered, one where the buoyant fluid is released in the same direction as the ambient motion (as shown in Figure 3-1) and the other where it is released perpendicular to it, along the z direction (Figure 3-1). The density of the fluid is ρ_0 and it is released with an initial velocity U_0, through a port of diameter d, into an ambient current of strength U_a. The initial momentum flux, M_0, of the discharge per unit density is then $U_0^2\pi d^2/4$, the initial buoyancy flux per unit density, B_0, can be written as $Q_0\Delta_0$, where the initial density deficit, Δ_0, is defined by $g(\rho_a-\rho_0)/\rho_a$. and g represents the gravitational constant. A convenient coordinate system is defined such that z represents the distance moved in the direction of the gravitational vector and x the distance moved in the direction of the ambient current. The y coordinate is then perpendicular to the x-z plane and the origin of the system is located at the point of discharge (Figure 3-1).

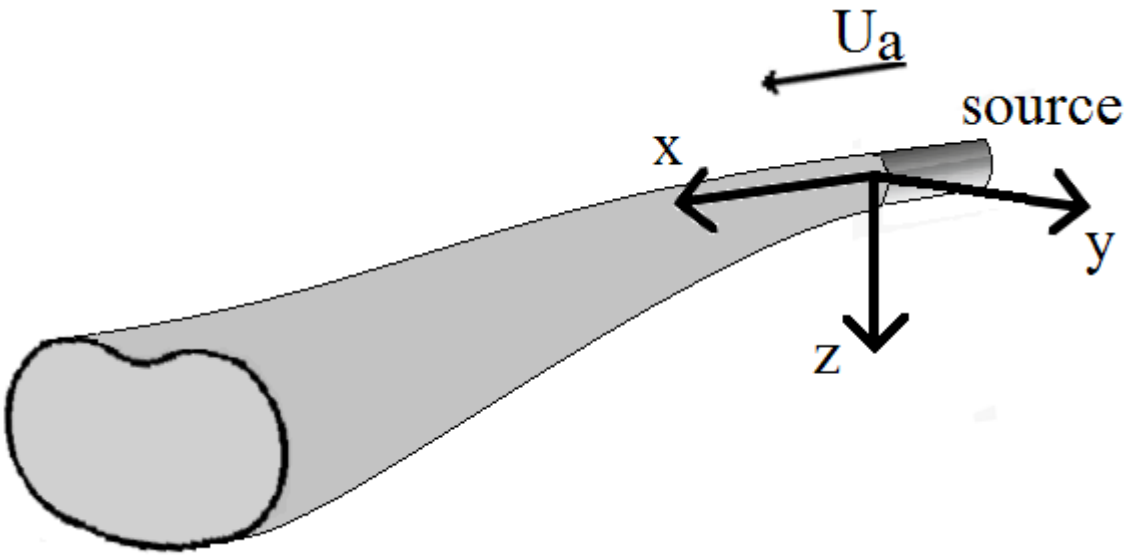

Figure 3-1: Schematic diagram of the discharge configuration.

As noted above, in the strongly-advected region, where the influence of the ambient motion and buoyancy generated momentum fluxes dominate, the tracer and velocity distributions resemble those of a vortex pair in the mean and the flow is referred to as a line advected thermal.

Of principle interest, from an environmental perspective, are the dilution and path of the discharged fluid, which through the assumption of a "top-hat" distribution and application of relevant momentum and mass flux relationships can be written as:

$$\frac{C_0}{C_T}\frac{U_0}{U_a}\left[\frac{d}{B_0/U_a^3}\right]^2 = 4k_T^2\left(\frac{z}{B_0/U_a^3}\right)^2 \tag{3-1}$$

And

$$\frac{z}{B_0/U_a^3} = \left[\frac{3}{2\pi}\frac{1}{k_T^2}\right]^{1/3}\left(\frac{x}{B_0/U_a^3}\right)^{2/3} \tag{3-2}$$

The coefficient k_T is the spreading rate of the top-hat profiles, where the radius of these profiles is written as $b_T = k_T z$. Kikkert (2006) suggests that k_T has a value of 0.73, based on his experimental results from a small number of advected thermal experiments. It is worth noting that the value of this spread coefficient can be determined directly from advected-thermal trajectory or dilution data using equations (3-1) and (3-2). In equation 3-1 C_0 and C_T are the initial tracer concentration and the local "top-hat" concentration respectively. In contrast the trajectory of a line momentum puff is given in Kikkert et al. (2007) as:

$$\frac{z}{M_0^{1/2}/U_a} = \left[\frac{3}{\pi}\frac{1}{k_{T,mp}^2}\right]^{1/3}\left(\frac{x}{M_0^{1/2}/U_a}\right)^{1/3} \tag{3-3}$$

Where the coefficient $k_{T,mp}$ represents the spreading rate of the momentum puff top-hat profile. While the simplicity of the above relationships is attractive, it is the peak mean concentration and actual scale of the flow that are of particular interest when assessing potential environmental impacts or compliance issues associated with a proposed design. It is therefore necessary to convert the top-hat values to those associated with the real profiles and following Kikkert et al. (2007) this can be achieved by matching the volume and tracer fluxes at a given cross section such that:

$$I_q U_a b^2 = \pi U_a b_T^2 \tag{3-4}$$

$$I_c U_a C b^2 = \pi U_a C_{Tc} b_{Tc}^2 \tag{3-5}$$

Where C_{Tc} and b_{Tc} are the top-hat tracer concentration and tracer spread scales, such that $b_{Tc} = \lambda b_T$, where λ represents the velocity to concentration spread ratio.

In equations (3-4) and (3-5), the integral constants I_q and I_c are defined by:

$$I_q = \int_0^\infty 2\pi \frac{r}{b} d\frac{r}{b} U_a \tag{3-6}$$

And

$$I_c = \int_0^\infty \frac{c}{C_m} 2\pi \frac{r}{b} d\frac{r}{b} U_a \tag{3-7}$$

Where I_q equals the non-dimensional flow cross sectional area and b, c and C_m are the spread, local and peak concentration from the measured mean profile. The volume and tracer flux equations can be reduced to:

$$b_{Tc} = \sqrt{\frac{I_q}{\pi}} b \tag{3-8}$$

$$C_{Tc} = \frac{I_c}{I_q} C \tag{3-9}$$

It is therefore necessary to define the local tracer distribution in order to determine the conversion coefficients in equations (3-8) and (3-9). Kikkert et al. (2007) employed a double-Gaussian approximation to characterize the tracer distributions in line-momentum puffs and used this to determine the conversions coefficients for these flows. They noted that there is symmetry to the double-Gaussian distribution that does not reflect the true kidney shape of the vortex pair, but that the distribution is able to approximate the peaks of the distribution reasonably accurately. Scheepbouwer et al. (2008) employed a more general double Gaussian distribution to characterize the tracer distributions of line advected thermals, which enabled the asymmetries evident in the experimental data to be taken into account. This relationship can be written in the following form:

$$\frac{c}{C_m} = \frac{C_1}{C_m} e^{-\left(\frac{z}{h_1 b_{c1}}\right)^2} e^{-\left(\frac{y}{b_{c1}} - f_1\right)^2} + \frac{C_2}{C_m} e^{-\left(\frac{z}{h_2 b_{c2}}\right)^2} e^{-\left(\frac{y}{b_{c2}} + f_2\right)^2} \tag{3-10}$$

where C_1 and C_2 are the maximum concentrations of the individual Gaussians; b_{c1} and b_{c2} are the tracer spreads of the individual Gaussians; $f_1 b_{c1}$ and $f_2 b_{c2}$ are the distances from the centre of the cross

section to the maxima of the two Gaussians, and h_1 and h_2 are the ratios of the spreading rates in the z and y directions (Figure 3-1).

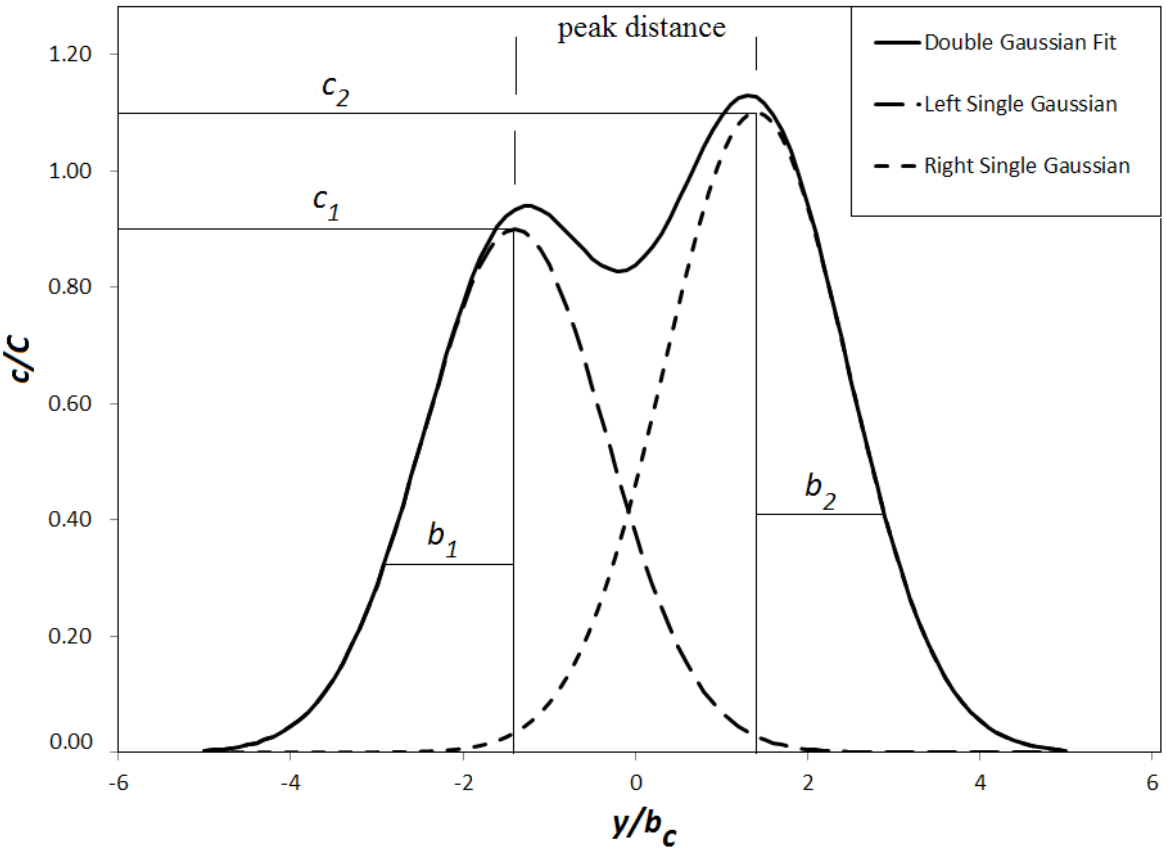

Figure 3-2: Summation of two single Gaussian profiles into a double Gaussian profile.

In Figure 3-2 three profiles are shown, two single Gaussian profiles with a maximum values at respectively y/b_c = -1.5 and y/b_c = 1.5, b_1 and b_2 are the spreads and c_1, c_2 are the maxima of the respective single Gaussian profiles. The double Gaussian fit is the summation of the two single Gaussian profiles. As the two single Gaussian profiles are not equal in b and c, the resultant double Gaussian profile is asymmetric. Note that the maximum concentration in the double Gaussian profile is larger than the maxima of the contributing single Gaussian profiles.

Where the mean profiles are symmetrical (as in the case of Kikkert et al. 2007) equation 3-10 reduces to:

$$\frac{c}{C_m} = \frac{C}{C_m} e^{-\left(\frac{z}{hb_c}\right)^2} \left(e^{-\left(\frac{y}{b_c} - f\right)^2} + e^{-\left(\frac{y}{b_c} + f\right)^2} \right) \tag{3-11}$$

An estimate of the ratio of the centerline mean concentration of the two individual Gaussians to the peak profile concentration can be obtained by setting $y/b_c = f$ (or $-f$) and $z = 0$, which gives:

$$\frac{C_m}{C} = 1 + e^{-4f^2} \tag{3-12}$$

Kikkert et al. (2007) noted that this estimate is conceptually convenient given that the profile's true maximum is less than 1% higher, based on typical f values. The maximum centerline concentration, C_c, occurs at (y,z) = (0,0):

$$\frac{C_c}{C} = 2e^{-f^2} \tag{3-13}$$

Substituting equation 3-11 into equation 3-7 and integrating enables the integral constant I_c to be defined as:

$$I_c = 2\lambda^2 h\pi \tag{3-14}$$

As noted above the integral constant I_q is a dimensionless form of the cross sectional area of the flow and its determination therefore requires a systematic definition of the flow edge. This can be achieved by representing the flow scale as ηb_c, where η defines the flow edge, so that the integral constant can be written as:

$$I_q = 4h\lambda^2 \left\{ \frac{\eta^2 \pi}{4} + \frac{f\sqrt{\eta^2 - f^2}}{2} + \frac{\eta^2}{2} sin^{-1}\left(\frac{f}{\eta}\right) \right\} \tag{3-15}$$

There are two relatively common definitions of flow edge, one is based on a visual boundary and essentially corresponds to the 25% concentration contour (Lai et al. 2011). However, this approach neglects a significant portion of the flow area, whereas setting η = 2 is consistent with a 2% concentration contour and hence it provides a more complete representation of the flow area (Kikkert et al. 2007). On this basis equation 3-15 can be written as:

$$I_q = 4h\lambda^2 \left\{ \pi + \frac{f\sqrt{4 - f^2}}{2} + 2sin^{-1}\left(\frac{f}{2}\right) \right\} \tag{3-16}$$

The above relationships provide the basis for interpreting the line-advected thermal data presented here. However, it is worth noting at this point that the experimental systems employed in the present study are based on the light attenuation technique, which provides an integrated view of the flow

behavior. Thus the data presented is either integrated along the *y* or *z* axis and the measured concentration profiles are expected to have the following forms:

Concentrations integrated in the *y* direction (horizontally, c_{iy}):

$$\frac{c_{iy}}{C_m} = \sqrt{\pi}\left(\frac{C_1}{C_m} b_{c1} e^{-\left(\frac{z}{h_1 b_{c1}}\right)^2} + \frac{C_2}{C_m} b_{c2} e^{-\left(\frac{z}{h_2 b_{c2}}\right)^2}\right) \tag{3-17}$$

Concentration integrated in the *z* direction (vertically, c_{iz}):

$$\frac{c_{iz}}{C_m} = \sqrt{\pi}\left(\frac{C_1}{C_m} h_1 b_{c1} e^{-\left(\frac{z}{b_{c1}} - f_1\right)^2} + \frac{C_2}{C_m} h_2 b_{c2} e^{-\left(\frac{z}{b_{c2}} - f_2\right)^2}\right) \tag{3-18}$$

Where the profiles are symmetrical these integrated profiles can be simplified to:

$$\frac{c_{iy}}{C_m} = 2 b_c \sqrt{\pi} \frac{C}{C_m} e^{-\left(\frac{z}{h b_c}\right)^2} \tag{3-19}$$

And

$$\frac{c_{iz}}{C_m} = h b_c \sqrt{\pi} \frac{C}{C_m}\left(e^{-\left(\frac{z}{b_c} - f\right)^2} + e^{-\left(\frac{z}{b_c} + f\right)^2}\right) \tag{3-20}$$

3.2.1 Ratio of Spreading rates (λ)

As noted previously the coefficient λ represents the ratio of spreading rates of the concentration and the velocity profiles or the ratio of the dispersion of mass to that of momentum. A value of λ, greater than 1 indicates that the concentration spreading rate is larger than the velocity spreading rate (Kikkert 2006, Wang and Law 2002). Wang and Law used digital particle image velocimetry to investigate the mean and turbulent characteristics of a round vertical buoyant jet. In their experiments the flow started as a strong jet and transformed into a plume at some distance from the source. They reported that the velocity spread rate was independent of the flow regime and the concentration to velocity spread ratio, λ, varied from 1.23 to 1.04 during the transition from jet to plume. Wang and Law (2002) proposed that this ratio is dependent on the flow regime and on the local Richardson number (*Ri*). The local Richardson number is given by $Ri = \frac{QB^{1/2}}{M^{5/4}}$. Papanicolaou and List (1988) reported values of λ to be 1.21 for jets and 1.06 for plumes. Chu (1996) reported a value of 1.20 for a turbulent round jet. Kikkert (2006) assumed a value of 1.22 for non-buoyant discharges, based on existing literature values. The adoption of this value for momentum puffs was based on the argument that, as with the jet, the initial momentum continues to play an important role in defining the puff behaviour and hence

the spread ratio is expected to be similar. For the advected thermals the buoyancy generated momentum flux plays an important role in defining the flow behaviour, making the plume parameters more relevant, and therefore in the present study (see equations (3-4) and (3-5)) λ is assumed to have a value of 1.07 for advected thermals. This is consistent with the values suggested by Kikkert (2006) and Papanicolaou and List (1988), and is close to the minimum value proposed by Wang and Law (2002).

3.3 Experimental setup

The experimental systems utilized for this study were essentially the same as those employed in Scheepbouwer et al. (2007, 2008) and a brief description is included here for completeness. Experiments of line advected thermals experiments have been conducted for a range of initial conditions. The present study follows on from the work of Kikkert et al. (2009), where a dual camera light attenuation system was employed to measure the evolution of these complex flows (Figure 3-3). The experiments were carried out in the towing tank facility in the Hydraulics Laboratory at the University of Canterbury, which has a length of 6.0 m, width of 1.5 m and a depth of 1.0m. Discharges were towed along the length of the tank to simulate the influence of ambient motion. The relative density of the source fluid was increased to approximately 1.7% through the addition of salt and released near the free surface, so that the released fluid fell towards the floor of the tank. Thus the line advected thermals created in the laboratory were negatively rather than positively buoyant, but given the relatively small density differences it is expected that these flows are equivalent. The density of the source fluid was measured using an Anton Paar density meter.

The light attenuation system described in Chapter 2 was used to measure the flow behaviour. The system made use of dye mixed in with the source fluid, where the light absorption is a linear function of the dye concentration. The absorption characteristics of a particular dye can therefore limit the dynamic range of the system. However, this limitation has been overcome by creating a mixture of food dyes with different absorption characteristics, so that they system's dynamic range is extended. For these particular experiments mixtures of Tartrazine and Indigo Blue were used (Green 1990). The maximum concentration for Tartrazine was 1.4 g/50 l and for Indigo Blue 0.8 g/ 50 l. The same concentrations were used for all experiments. Through dilution the range of the dyes concentrations was between 0% and 100% of the used concentration.

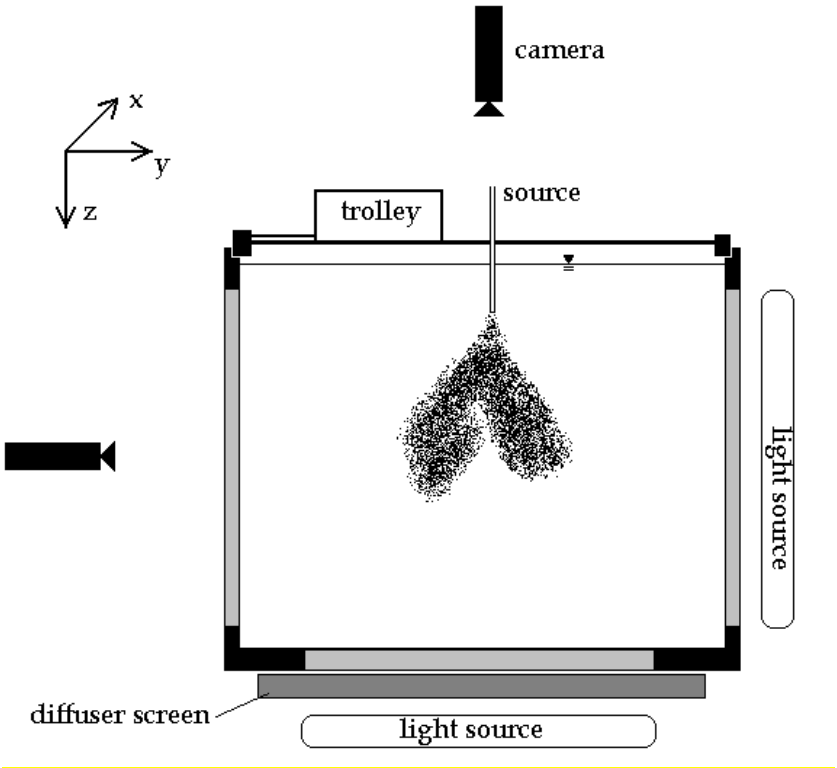

Figure 3-3: The two camera light attenuation capture system employed to conduct the experiments.

Light attenuation systems make use of the reduction in light intensity from a (reasonably) uniform source of light to determine integrated concentrations. Two light sources were employed for these experiments (Figure 3-3). A 37 inch LCD panel provided a programmable light source, which, along with an optimum dye mixture, ensured maximum contrast over the entire image. The second source was less flexible, but had been employed successfully in the past for similar experiments. This source made use of a bank of fluorescent tubes and a diffuser sheet to create a reasonably uniform light source. Images were gathered simultaneously on two colour Jai MV7+ cameras, so that integrated concentration data could be extracted from both the horizontal and vertical perspectives at particular downstream locations of interest. Data was captured directly to disk at a rate of 24Hz for extended periods (typically over 5,000 images per camera). The resolution was approximately 1.4 mm/pixel, which can be calculated by dividing the width of centreline frame (700 mm) by the width of a captured frame in pixels (1000 pixels) multiplied by 2 (RGB effect).

The cameras were fixed at stationary locations in excess of 4 m from the flow centreline (to reduce parallax issues), so that the full evolution of the flow could be observed. Time averaged images were created by transposing the image sequences into a single image, where the source was in a fixed position. This process typically created images of 35,000 x 1,000 pixels, where the averaging time at a given downstream location was dictated by the ratio of the horizontal image scale to the simulated

ambient velocity. Experiments were repeated so that ensemble images could be created, where the averaging times at any given location varied from 35 to 75 seconds, depending on the trolley speed (U_a) and number of ensembles. The captured frames were calibrated and processed using the Imagestream software (Nokes 2007), and finally the results were analysed with Matlab. The light attenuation system was employed to study line-advected thermals evolving from sources that are either parallel or perpendicular (vertically discharged) to the ambient motion.

Table 3-1 shows the initial conditions for the line advected thermal experiments. In this table two sets of seven experiments are described, the first set (T-1) was discharged vertically, perpendicular to the ambient motion; while the second set (T-2) was discharged horizontally and in the same direction as the ambient motion (coflow). In order to maintain sufficiently high Reynolds numbers for the parallel discharged flows, while keeping the initial velocity low enough so that the transition to strongly advected behaviour occurred relatively close to the source, the diameter of the source was increased to 6 mm. The density of the source fluid was respectively 1.71% and 1.60% higher than the ambient fluid. While it is typical to carry out such experiments with a 3% density difference, the smaller density differences employed here reduced the vertical acceleration of the fluid thereby increasing the observation time before the flow interacted with the lower boundary of tank. The ambient velocity or trolley speed was set to encourage the formation of strongly-advected flows near the source, because these were the primary focus of the study. Note that the values for the Reynolds and Froude numbers were determined using the initial velocity, source diameter and initial buoyancy.

Table 3-1: Initial conditions of the Line advected thermal experiments

Set	# of experiments	Exposure time per data point	Source diameter [mm]	U_{ar} $[U_a/U_0]$	Q_0 [ml/s]	Re [initial]	Fr [initial]	g'
T-1	7	~100 sec	1.30	0.0172-0.0260	2.64-4.11	2528-4026	135-210	0.169
T-2	7	~35 sec	6.0	0.109-0.694	6.83-26.9	1450-5706	8-31	0.157

The camera captured images at 24Hz, thus the total amount of data points used per pixel can be calculated by multiplying the exposure time by 24 (Hz). The amount of seconds of exposure time was evenly distributed for each data set. The Froude number, Fr, has been taken as $Fr = \frac{u}{\sqrt{\Delta d}}$, where the

initial values are used. Therefore Fr can be described with Fr_0. The Reynolds number, Re, is given by $Re = \frac{ud}{\nu}$ and again the initial values were used.

For the momentum puff experiments two sets of five experiments were carried out (Table 3-2), where the initial Reynolds number (*Re*) was between 2,930 and 8,733. Although there were no salinity differences between the ambient and source fluids for these experiments, the Froude number (*Fr*) has been calculated based on small temperature differences between the two fluids. These temperature differences were smaller than 0.2°C resulting in Froude numbers of approximately 1,000 and larger. The diameter of the discharge in set P-1 was 2.45 mm and a different discharge, with a diameter of 1.3 mm, was used in set P-2. This reduction in source diameter increased the non-dimensional distance to the region where the flow transitions to a line advected thermal and also increased the Reynolds number for a given flow rate. The increase in the transitional length scale (momentum puff to line advected thermal) ensured no transitional effects were observed during the experiments, prior to the flow interacting with the tank floor. The variation in Reynolds number enabled further exploration of a possible Reynolds number dependence for these flows noted in Scheepbouwer et al. (2008). It is worth noting that some experiments previously reported in Scheepbouwer et al. (2008) have been incorporated in this table. These experiments have been re-analysed and additional information extracted.

Table 3-2: Initial conditions of the Momentum puff experiments

Set	# of experiments	Exposure time per data point	Source diameter [mm]	U_{ar} $[U_a/U_0]$	Q_0 [ml/s]	*Re*	*Fr*
P-1	4	~85 sec	2.45	0.0241-0.0271	5.639-9.139	2930-4749	977-1583
P-2	5	~75 sec	1.30	0.0073-0.0079	8.278-8.917	8107-8733	16399-17665

An indication of the nature of the expected behaviour can be obtained from the transition length scales, which are listed in Table 3-3 and have been calculated following Davidson et al. (1998). Initially in all experiments the flow will start, after the establishment zone, as a jet. Finally all flows evolve to the advected thermal region; however the density differences in the momentum puff experiments are so small that the size of the tank was not sufficient to allow advected thermals to form.

Table 3-3: Transitional lengths of experiments

Set	Jet – Plume S_{jp}/d	Jet - Momentum Puff S_{jmp}/d	Plume – Thermal Z_{pt}/d	Momentum Puff – Thermal L_{mpt}/d
P-1	1,444 – 5,518	33.3 – 37.4	0.00412 – 0.0626	327 – 796
P-2	35,637 – 38,387	114.0 – 122.9	0.00290 – 0.00314	4,018 – 4,329
T-1	292 – 456	34.7 – 52.5	1.01 – 2.429	110 – 166
T-2	17 – 67	N/A	0.0190 – 0.316	N/A

In estimating the transitional lengths, the following constants have been used (Kikkert 2006): K_t = 0.144, K_{jm} = 0.26, K_{jp} = 0.68, K_{pt} = 0.35, K_{mt} = 2.22. Note that a momentum puff cannot form from a coflowing discharge (T-2).

From above results (Table 3-3) the following flow transitions are expected to happen within the observable range:

- Set P-1, jet – momentum puff
- Set P-2, jet – momentum Puff
- Set T-1, jet – momentum puff – line advected thermal
- Set T-2, jet – plume – line advected thermal

The experiments P-1, P-2 and T-1 were designed so that the jet to plume transition did not take place, which is evident in that fact that the transitional lengths from jet to plume are in all cases much larger than the transitional lengths from jet to momentum puff/strongly advected jet. This was inherent in the near neutrally buoyant flows created in the puff experiments and enabled a relatively rapid transition to thermal behaviour for the buoyant discharges. In
Table 3-4 the details are listed per experiment. The identifiers in the second column are the identifiers that are used in the figures in the following sections.

Table 3-4: Details per experiment including used identifiers.

Flow type	Identifier	Initial discharge direction	Q_0 [ml/s]	Source diameter [m]	g'	U_a [m/s]	U_{ar}	Re	Fr
M. Puff	Run I-a	Vertical	5.64	0.00245	0.001	0.032	0.027	2930	977
M. Puff	Run I-b	Vertical	9.14	0.00245	0.001	0.048	0.025	4749	1583
M. Puff	Run I-c	Vertical	8.92	0.00130	0.000	0.049	0.007	8733	17665

M. Puff	Run I-d	Vertical	8.83	0.00130	0.000	0.049	0.007	8651	17500
M. Puff	Run I-e	Vertical	8.50	0.00130	0.000	0.049	0.008	8325	16840
M. Puff	Run I-f	Vertical	8.58	0.00130	0.000	0.049	0.008	8407	17005
M. Puff	Run I-g	Vertical	8.28	0.00130	0.000	0.049	0.008	8107	16399
M. Puff	Run I-h	Vertical	6.25	0.00245	0.000	0.032	0.024	3248	2539
M. Puff	Run I-i	Vertical	6.33	0.00245	0.002	0.032	0.024	3291	664
Adv. Thermal	Run II-a	Vertical	2.72	0.00130	0.168	0.041	0.020	2666	139
Adv. Thermal	Run II-b	Vertical	3.72	0.00130	0.168	0.052	0.018	3646	190
Adv. Thermal	Run II-c	Vertical	3.19	0.00130	0.168	0.052	0.022	3129	163
Adv. Thermal	Run II-d	Vertical	2.64	0.00130	0.168	0.052	0.026	2585	135
Adv. Thermal	Run II-e	Vertical	4.00	0.00130	0.168	0.052	0.017	3918	204
Adv. Thermal	Run II-f	Vertical	3.22	0.00130	0.168	0.052	0.021	3156	164
Adv. Thermal	Run II-g	Vertical	4.11	0.00130	0.168	0.064	0.021	4026	210
Adv. Thermal	Run III-a	Horizontal	26.89	0.00600	0.157	0.103	0.109	5706	31
Adv. Thermal	Run III-b	Horizontal	12.89	0.00600	0.157	0.103	0.226	2735	15
Adv. Thermal	Run III-c	Horizontal	6.83	0.00600	0.157	0.168	0.693	1450	8
Adv. Thermal	Run III-d	Horizontal	8.47	0.00600	0.157	0.168	0.560	1798	10
Adv. Thermal	Run III-e	Horizontal	14.19	0.00600	0.157	0.168	0.334	3012	16
Adv. Thermal	Run III-f	Horizontal	21.33	0.00600	0.157	0.168	0.222	4527	25
Adv. Thermal	Run III-g	Horizontal	18.31	0.00600	0.157	0.168	0.259	3885	21

3.4 Results

In the following section the vertically and horizontally integrated cross sections of the momentum puff and line advected thermals are shown, firstly to establish that they have a self-similar form and highlight any notable differences between the cross sectional forms of the two flow types. Subsequently the variations of the two parameters that describe the form of these profiles (*f* and *h*) with non-dimensional distance from the source are presented, along with the spread, dilution and trajectory data. It is worth noting that the results in the figures are averaged values from the LA system, which does not provide instantaneous local concentration measurements. The instantaneous images from the LA system represent integrated concentration information and hence a significant averaging process is inherent in this system (Appendix II). Thus the focus here is on averaged characteristics of the flows, which is consistent with modelling efforts. The LA system has limited ability to study the detailed fluid dynamics of these flows, but it provides an important overview of the bulk-flow behaviour, which can be compared with integral model predictions.

Integrated cross sectional profiles from the line momentum puff experiments are shown in Figure 3-4 and Figure 3-5. On the vertical axis the ratio of the integrated tracer concentration, c_{iy}, c_{iz}, and the initial integrated centreline tracer concentration, C_{iy}, C_{iz} are depicted. The non-dimensional radius, r/b_c is shown on the horizontal axis (Equation 3-17, 3-18). The data in both figures are compared with best fit Gaussian or double Gaussian profiles (shown as solid line) as appropriate and the 95% confidence prediction bounds are also included (shown as dotted lines). Figure 3-4 shows the integrated momentum puff concentrated profiles as viewed from the side (*y*-integrated). The negative radial values correspond to the lower portion of the descending flow and the positive values the upper portion of the flow. The profiles are presented at non-dimensional distances, z/L_{jmp}, ranging from 2.74 until 4.17, where L_{jmp} is the jet to momentum puff length scale. The profiles show that, compared to the single Gaussian profile, the top side of the flow data (on the left) is somewhat over represented while the bottom side is under represented. The 95% bounds do however catch most of the data so it is clear that the data is reasonably consistent with the single Gaussian distribution and is self-similar.

Figure 3-5 shows the integrated momentum puff concentrated profiles viewed from the top (*z*-integrated). The profiles are presented at non-dimensional distances, z/L_{jmp}, ranging from 2.93 until 4.42. Kikkert et al.'s data (2007) has been added and shows good resemblance to present data. The profiles also show self-similarity which in this case is consistent with a double Gaussian distribution.

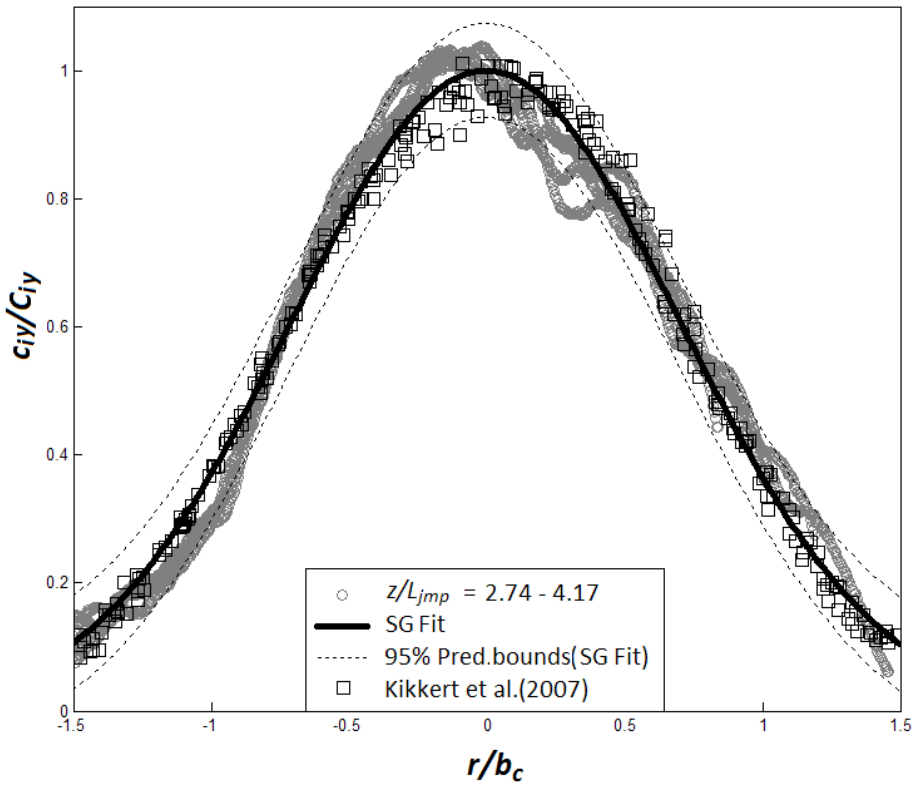

Figure 3-4: Momentum puff *y*-integrated concentration cross profiles. The negative r/b_c values on the left and the positive values for r/b_c on the right side of the figure correspond respectively with the top and bottom side of the flow.

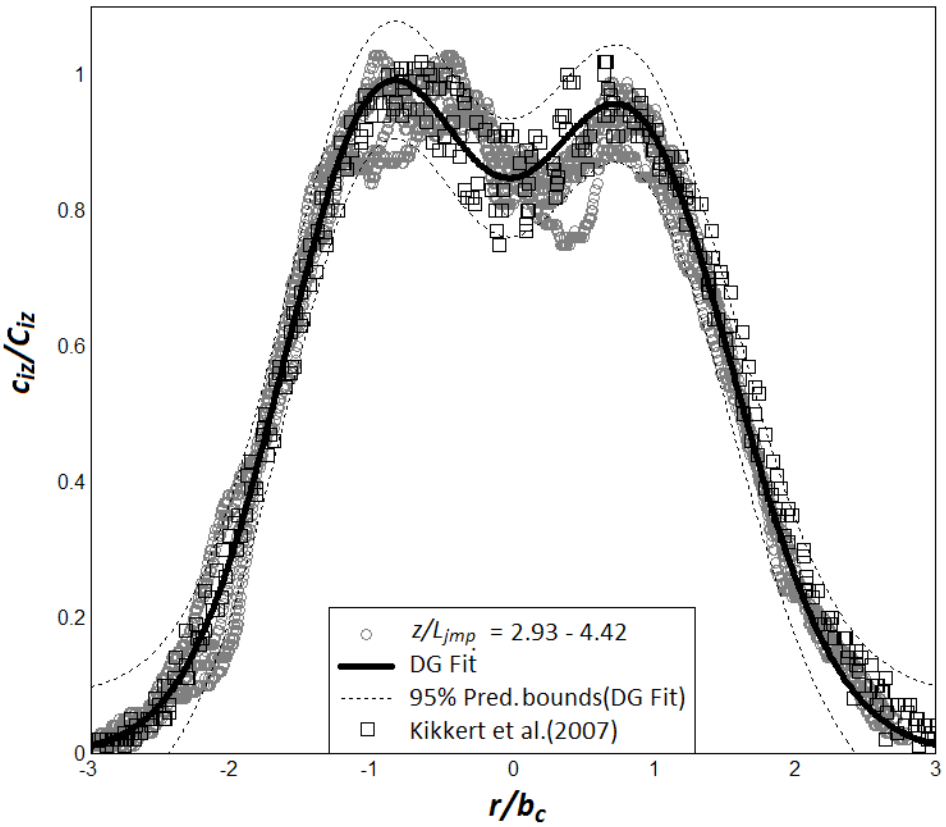

Figure 3-5: Momentum puff *z*-integrated concentration cross sectional profiles.

Integrated concentration profiles from line advected thermals are shown in Figure 3-6 and Figure 3-7. The cross sectional profiles were extracted at different distances from the source and these have been converted to a non-dimensional form using the plume to thermal transition length scale, Z_{pt}. There is clearly more distortion of the integrated profiles shown in Figure 3-6, when compared to those in Figure 3-4 and the single Gaussian distribution is a less satisfactory approximation. The increased distortion indicating notable differences in the form of the cross sectional profiles, which are possibly indicative of the different mechanisms that drive the flow, buoyancy in the case of the thermal and initial momentum flux for the line momentum puffs. Further evidence of this is seen in Figure 3-7, where the double peak form differs significantly from that shown in Figure 3-5. However, the distributions are self-similar and the double-Gaussian approximately provides a reasonable approximation of the integrated distributions. It is worth noting that in the case of the thermal the ratio of the integrated maximum concentration (C_{im}) to the maximum centreline value (C_{ic}) is 0.59, whereas in the case of the puff it is 0.85. This is consistent with the greater non-dimensional peak separation of the advected thermal profiles when compared to those of the line momentum puffs. When interpreting these profiles, it is important to recall that the cross-sectional form of these flows is "kidney shaped", whereas the analysis assumes the flows are symmetric. The increased peak separation for the buoyancy driven flow, appears to enhance this kidney form and hence there is greater distortion in the y-integrated profiles (Figure 3-6), when compared to the equivalent non-buoyant form (Figure 3-4).

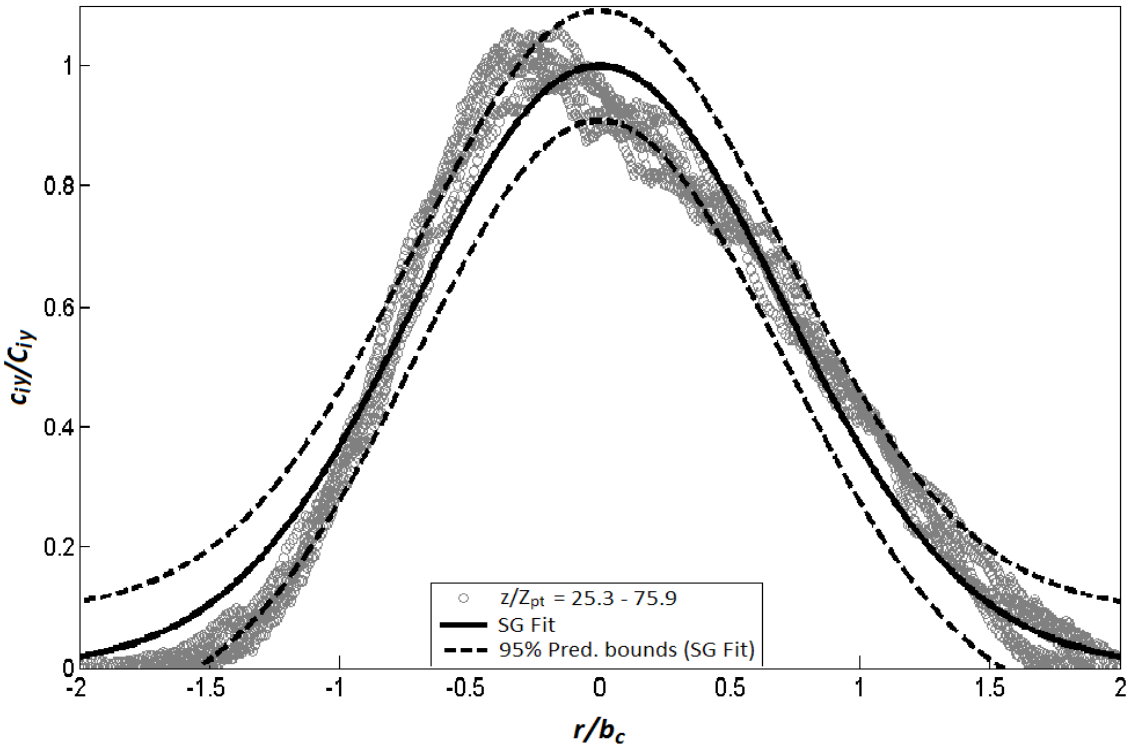

Figure 3-6: Line advected thermal *y*-integrated cross sectional profiles. The negative r/b_c values on the left and the positive values for r/b_c on the right side of the figure correspond respectively with the top and bottom side of the flow.

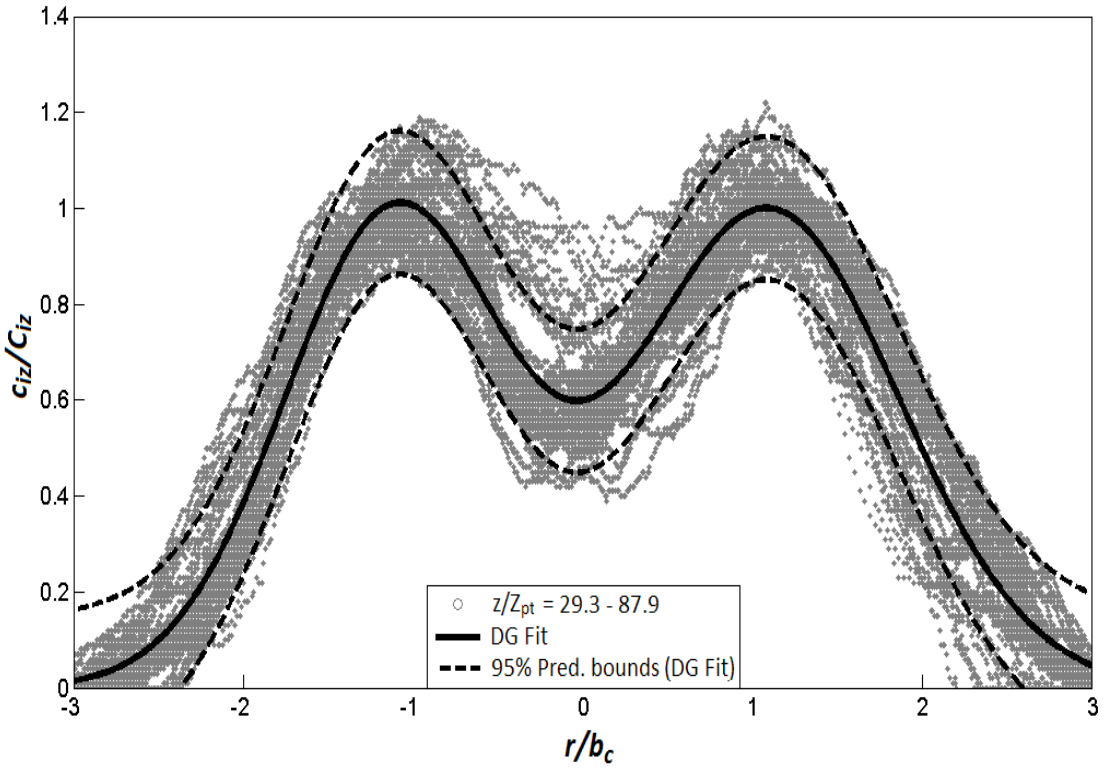

Figure 3-7: Line advected thermal *z*-integrated cross sectional profiles.

The non-dimensional parameter *f* provides a direct measure of this peak separation and its variation with non-dimensional vertical distance for the line momentum puff is shown in Figure 3-8. Five experiments from the present study are shown along with data from Kikkert et al. (2007). There is considerably more scatter in the new data, which reflects the increased detail available because of the more sophisticated relationship employed to characterise the cross sectional profiles. Whereas Kikkert et al. employed a symmetrical profile to fit the data, the present analysis has the ability to capture asymmetries in individual profiles and hence there is increased variability in the new *f* values. The *f* values presented are the average for each of the two vortices per flow experiment. However, despite this more detailed analysis, most of the new data is scattered between 0.85 and 1.15 and the *f* value calculated from an ensemble average in the region where the puff has become established is 0.89. This value is very similar to that deduced from Kikkert et al.'s experiments (0.88). Kikkert's analysis of Chu's (1996) data suggests a value of 0.86 for this parameter. It is also worth noting that *f* typically increases in the transition region as the vortex pair forms, but then reduces to the established values (above) once the vortex pair has formed. Thus in the transitional phase the relationship between the peak separation and scale of the vortices differs from that in the established flow.

In Figure 3-9 values of the *f* parameter for a horizontally discharged line advected thermal are presented and the *f* resulting from puff experiments from Kikkert et al. (2007) is included for comparative purposes.

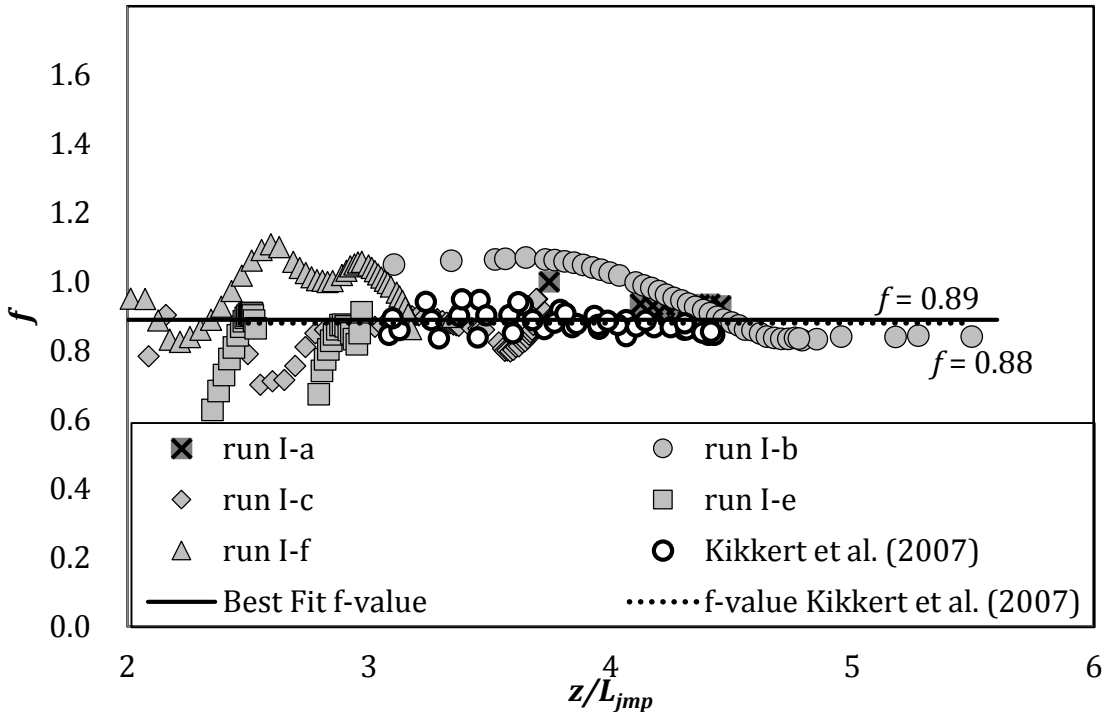

Figure 3-8: *f* values of momentum puff experiments compared with previous results. For more information on the details per experiment, see

Table 3-4.

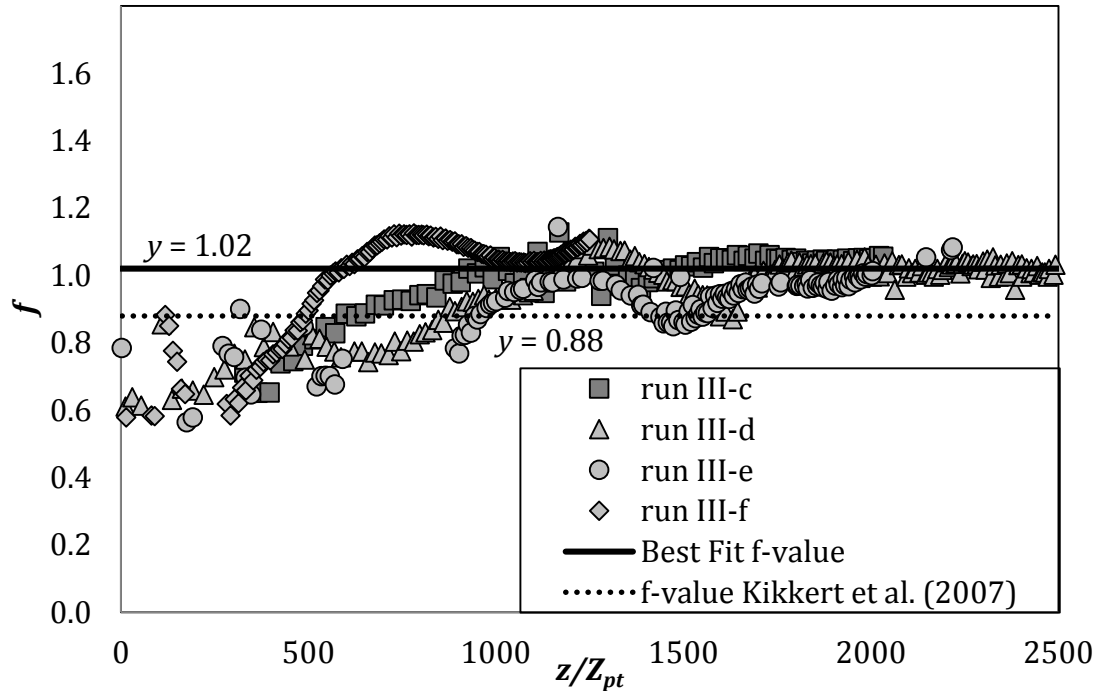

Figure 3-9: *f* values of a line advected thermal. The displayed runs are all horizontally discharged.

Initially *f* increases rapidly indicating that the distance between the peaks separate more rapidly than the associated growth of the vortices. After a distance this trend reverses as the relative peak separation and vortex growth change such that *f* reduces with distance from the source, tending towards a constant value in the region where the thermals are fully established. An ensemble average in this region suggests this established value is 1.02, which is significantly larger than that of an established momentum puff. This larger value of *f* is consistent with the increased ratio of peak to centreline integrated concentrations noted with reference to Figure 3-7**.**

In Figure 3-10, values of the *h* parameter from the momentum puff experiments are shown. This parameter represents the ratio of the spreading rates in the *z* and *y* directions. Where $h = 1$ the mean individual profiles (vortices) are circular and a value larger than 1 indicates that these vortices are elongated in the *z* direction (see Figure 3-1). The values presented in Figure 3-10 are the average of the values for the individual vortices, at specified locations, for each experiment, h_1 and h_2 (equation 3-10). As was evident in Figure 3-6, and Figure 3-7, the individual experiments show significant variability, but an ensemble average of the data once the puffs have become fully established yields a value of 1.49 for *h*. This value is consistent with Kikkert et al. (2007) value of 1.46 and Chu's (1996) estimate of 1.56. Prior to the flow becoming strongly advected and the formation of the vortex pair, the flow is theoretically circular in the mean (single Gaussian) and $h = 1$. In the transition this value increases and then becomes approximately constant as the vortex pair becomes established. In the figure the horizontal scale z/L_{jmp} is shown from 2 until 5 as for values under 2 the flow is in transition, and not self-similar. Kikkert (2006) noted that the transition to strongly advected behaviour occurred over approximately three transition length scales (L_{jmp}); results from the present experiments are generally consistent with this, but in some experiments this transition length was extended to approximately 4 length scales.

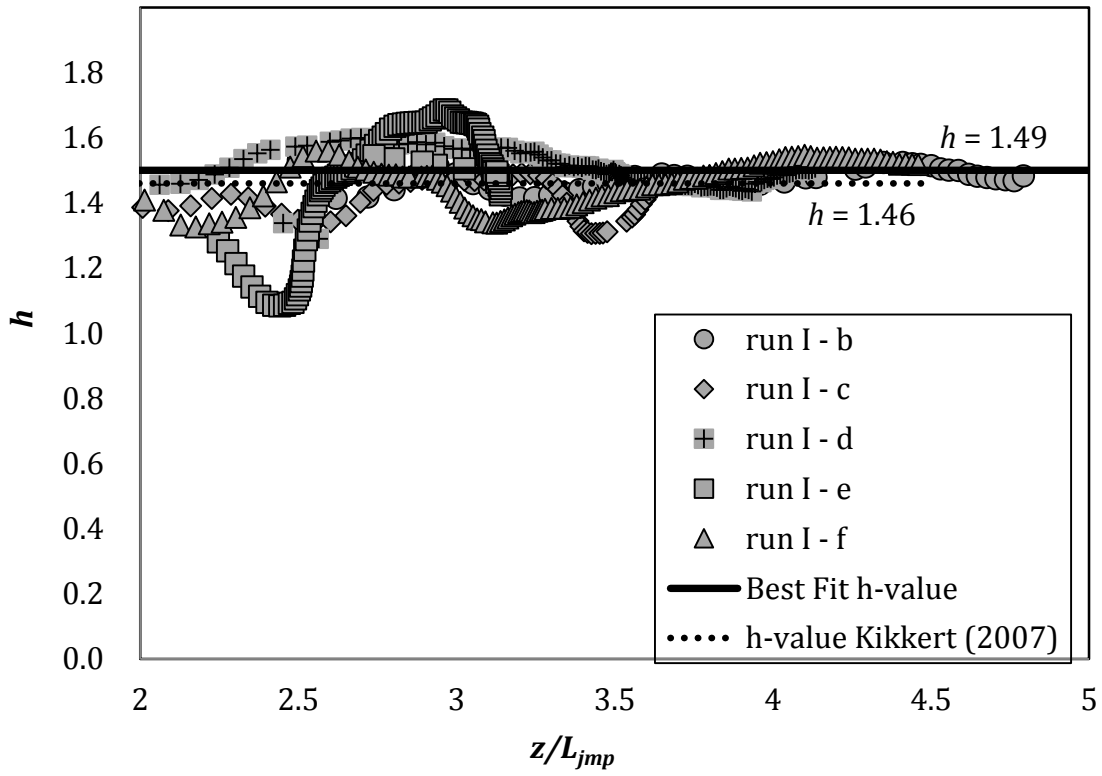

Figure 3-10: *h* values from the momentum puff experiments.

Figure 3-11 shows the values of the *h* parameter for vertically and horizontally discharged line advected thermals respectively. As with the momentum puff the presented *h* values are the average of h_1 and h_2 in equation 3-10. Similar to the momentum puff the *h* value varies significantly during the transition, but then settles towards a consistent value as the strongly advected flow becomes established. The horizontally and vertically discharged thermal ensemble average values in the established region give a value of 1.56 for *h.* These values are similar to those obtained from the puff experiments. It is worth noting that there is more variability in the data from the vertically discharged experiments. Two experiments are particularly inconsistent; one (data run II-D) starts with a high value of *h* that only reduces near the edge of the observed behaviour, possible reasons for this are discussed in section 3.5.1. In contrast the second experiment (data run II-C) has an initially low value of h, which then increases near the edge of the observed region. This is consistent with the delayed development of the vortex pair, given that lower values of *h* are expected in the weakly-advected region. It was noted in reference to Table 3-3, the transitional behaviour of the horizontally and vertically discharged experiments is quite different, with the potential for line momentum puffs to form prior to the development of line advected thermals in the case of vertical discharges whereas such transitions are not possible in the horizontal discharge case. The formation of puffs prior to the

development of advected thermals appears to introduce additional variability into the form of the mean concentration profiles.

As with *f*, variability in *h* is significant, particularly during the transitional phases of the flow. While the more sophisticated form of the double-Gaussian approximation employed here has highlighted this variability, it has also shown that the scale of the mean concentration profiles of the vortex pair integrated in the horizontal direction (along the *y* axis) is approximately 1.6 times that of the profile scale integrated in the *z* direction. It is interesting to note that this value is consistent for thermals evolving from both vertical and horizontal discharges. The values for puffs are approximately 5% smaller, thus the thermals appear to be slightly more elongated than the puffs.

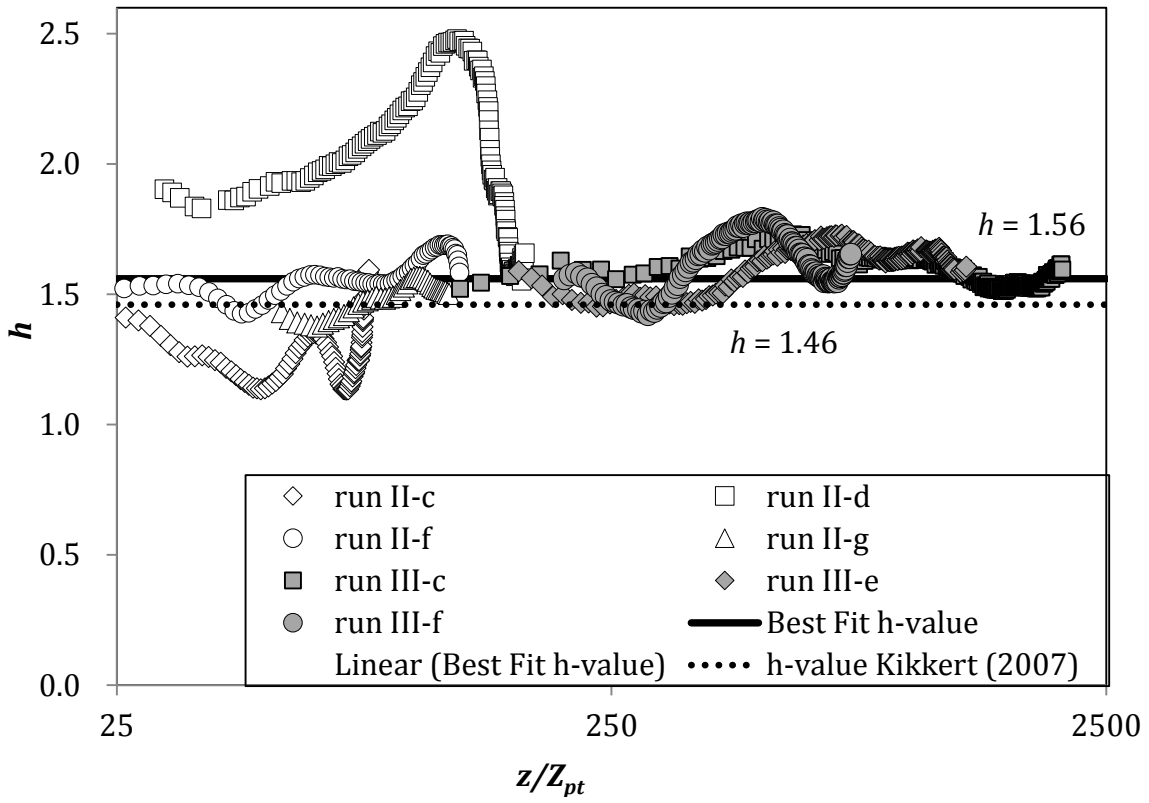

Figure 3-11: *h* values of the line-advected thermal experiments. Displayed are vertically discharged (Run II) and horizontally discharged (Run III) experiments.

Figure 3-12, Figure 3-13 and Figure 3-14 present trajectory data from momentum puffs and line advected thermals. Analytical solutions can be employed to define the expected path of these flows and based on this approach equation 3-2 defines the trajectory of a line advected thermal whereas the trajectory of a line momentum puff is given by equation 3-3.

In Figure 3-12 trajectory data from the momentum puff experiments are presented along with data from previous authors and predictions from Visjet and Corjet. Previous data has largely been limited to weakly-advected and transition regions of these flows and hence there has been limited data available that is within the strongly-advected momentum puff region. Data from the present study is focussed in this strongly-advected region and extends beyond previously obtained data. In general the new data show good agreement with previously obtained values, although there is considerably more scatter in the latter with the exception of Kikkert's (2006) data, which was also obtained with similar optical systems to the present study. Indeed one of the experiments (ref. Run 1-a) from the present study is consistent with Kikkert's (2006) experiments and also follows the predicted line of Corjet. Both this run and Kikkert's experiments used Reynolds numbers on the lower end of the turbulent scale (approximately 3000). However, in the remaining experiments from the present study the puffs did not rise quite as rapidly. Interestingly these experiments are consistent with Visjet predictions. The reasons for this small discrepancy in the trajectories of these flows are not clear, but may be associated with the mentioned variation in the initial conditions. It is worth noting that the transition to the strongly-advected behaviour occurs over approximately three transitional length scales, L_{jmp}, and this is consistent again with Kikkert's observations.

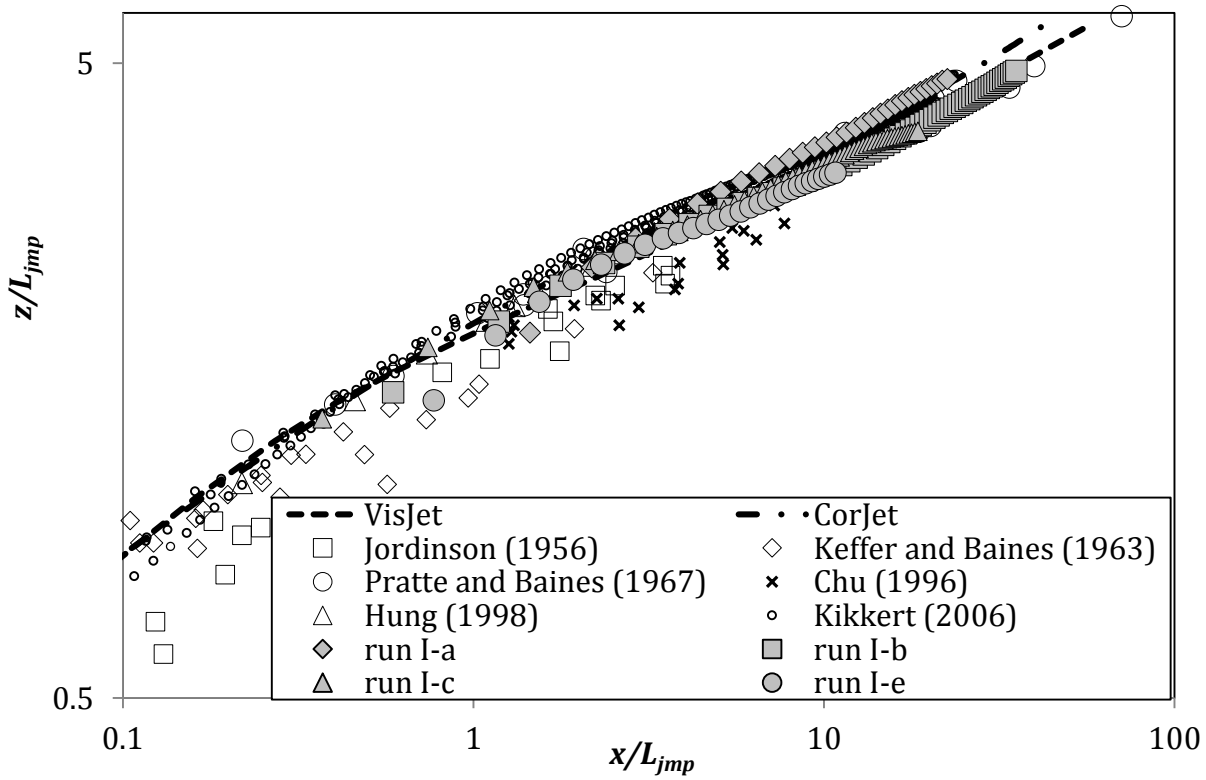

Figure 3-12: Trajectory data and model predictions for advected line momentum puffs. Reynolds numbers for runs I-a and I-b are 2930 and 4749 respectively, the Reynolds numbers for the other experiments are in excess of 8000.

In Figure 3-13, the trajectories of both vertically discharged and horizontally discharged buoyant discharges are presented, along with relevant data from previous studies and predictions from the Corjet and Visjet models. The development of the self-similar line advected thermal region within these flows can be clearly identified as the trajectories approach the line $z \sim x^{2/3}$ (see equation 3-2). As with the puff data, there is a general consistency with previous experimental data, but again significant scatter associated with experiments where data was obtained with less sophisticated techniques. With so much data in a single figure it is more difficult to interpret the flow behaviour, so Figure 3-14 presents just the newly obtained data in the same format. The reference line in this figure was calculated using an m_T of 0.73 and this is clearly consistent with the data from all 24 experiments. Hence the trajectory data provides an estimate of the "top-hat" spreading rate for line advected thermals, which differs significantly from that obtained for line momentum puffs, 0.61 (Kikkert et al. 2007).

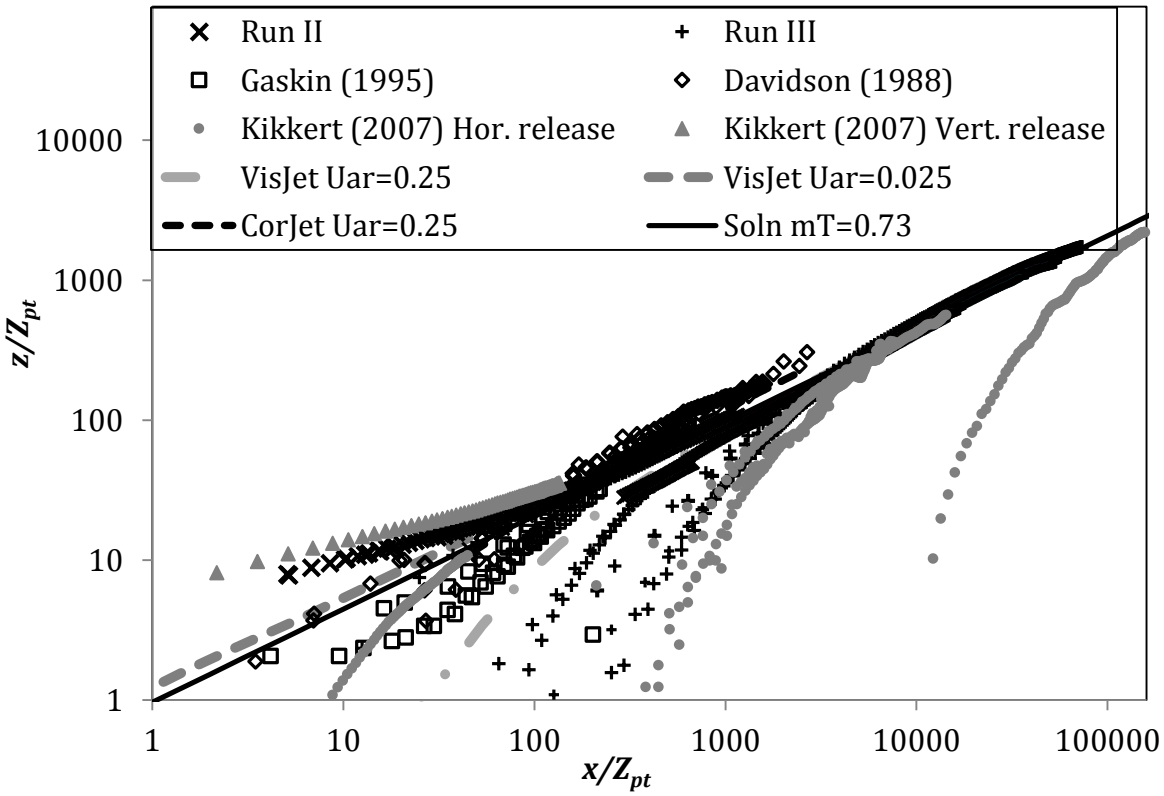

Figure 3-13: Trajectories of horizontally discharged (Run III) and vertically discharged (Run II) line advected thermals compared with previous results.

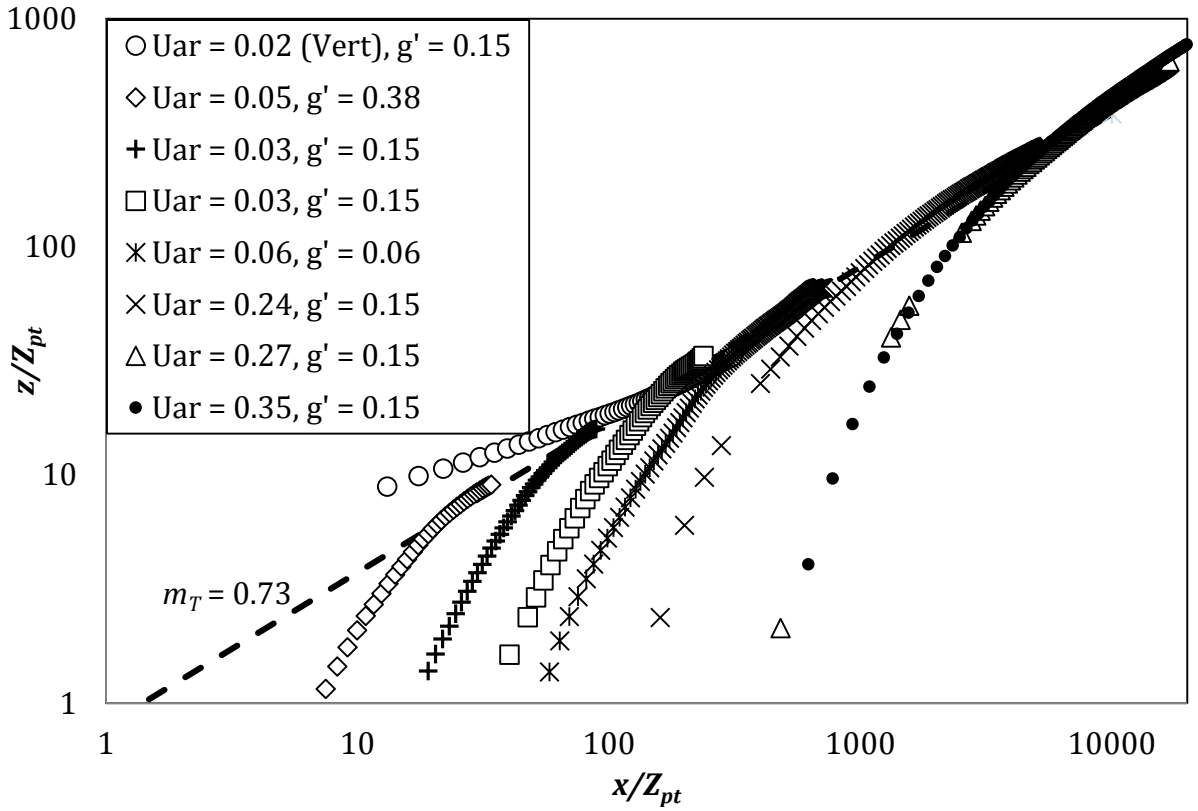

Figure 3-14: Trajectories of line advected thermals. One vertically discharged thermal trajectory (Vert) from Run II, data with U_{ar} of 0.24, 0.27 and 0.35 belong to Run III. Remaining 4 trajectories are from prior experiments (Scheepbouwer et al. 2008).

Spread data is presented in Figure 3-15 to Figure 3-18, starting initially with line momentum puff data that can be compared directly with previous data. This is followed by data from vertically and horizontally discharged line advected thermals. Figure 3-15 shows line momentum puff spread data obtained from *y*-integrated concentration profiles plotted against dimensionless vertical distance. A best fit line after the transition zone has the form 0.36(*z*-0.65), which is similar to the relationship obtained by Kikkert et al. (2007). This relationship is also shown for comparison along with data from Kikkert's study. The spreading rate is the same as that of Kikkert et al. (2007) and Knudsen (1988) and is consistent with Gaskin's (1995) value of 0.41. In Figure 3-16 spread data obtained from the vertical view is presented, that is data obtained from *z*-integrated mean concentration profiles, where the double Gaussian approximation provides a reasonable representation of these profiles. This data can be characterised by a linear trend line, with the same virtual source location as in Figure 3-17, but with a slope of 0.24. Again these values are consistent with those obtained in Kikkert et al.'s study, and the spread ratio of 1.5 is in agreement with the *h* value shown in Figure 3-10.

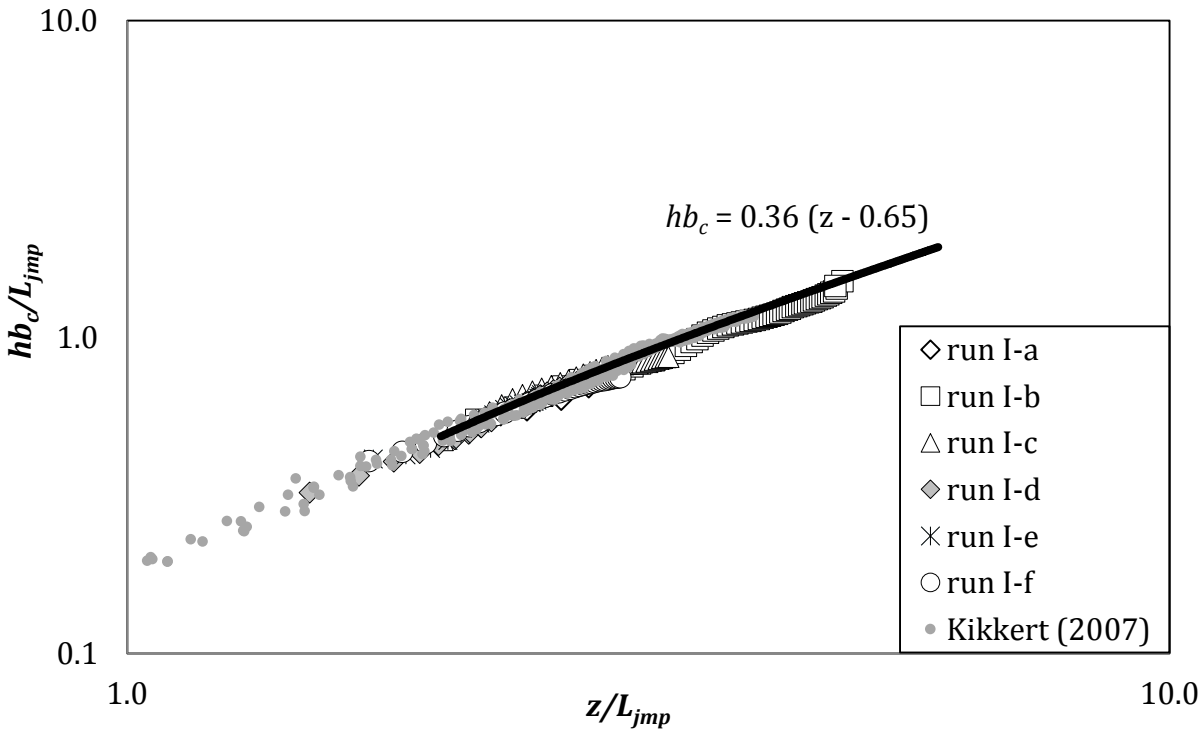

Figure 3-15: Spread of the best fit Gaussian profiles of the *y*-integrated momentum puff experiments. U_{ar} varies from 0.008 (Run I-f) to 0.027 (Run I-a), for more details see table 3-4. Data from Kikkert et al. (2007) has been added for comparison.

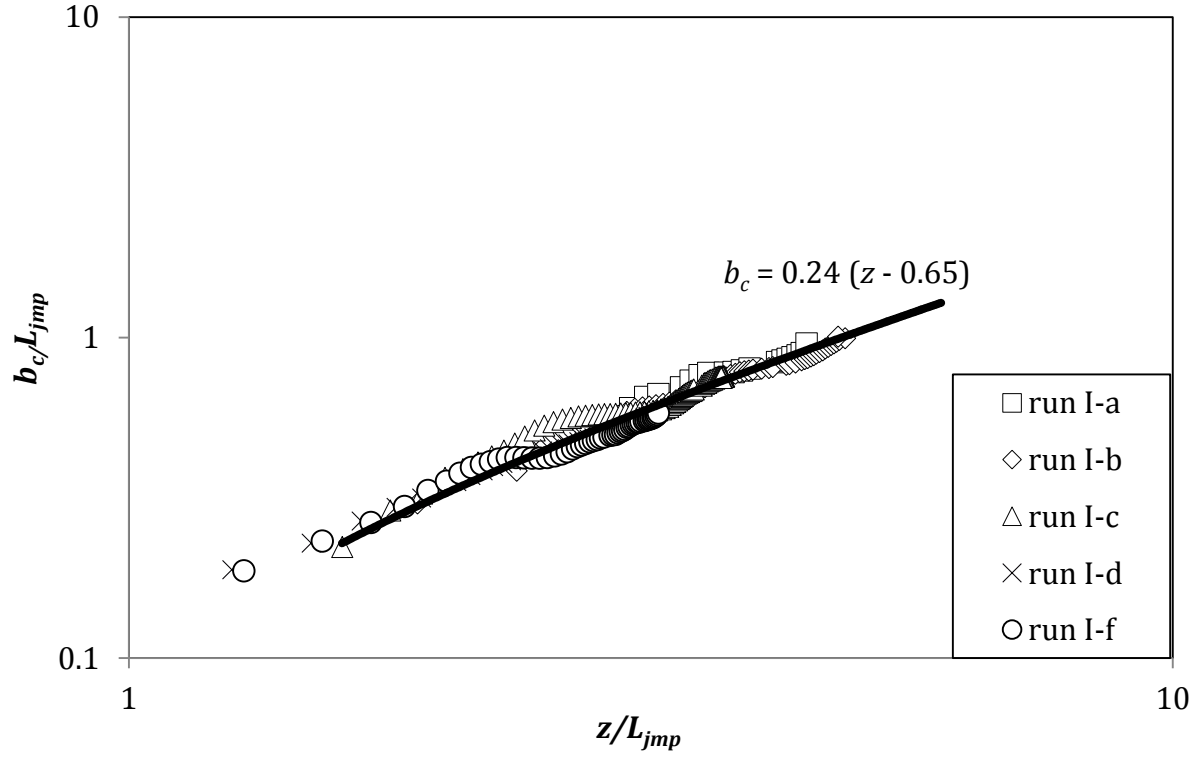

Figure 3-16: Spread of momentum puff experiments, the average spread of the double Gaussian widths of the vertically integrated concentration profiles.

Moving now to the line advected thermals, spread data from horizontally and vertically discharged thermals are presented in Figure 3-17 and Figure 3-18. In Figure 3-17 the *y*-integrated flow spread in the strongly advected region of both horizontally and vertically discharged flows can be represented by linear relationships with a gradient of 0.40. However, in the case of the vertical discharge there is the need for a virtual source, z_{vs}, because of the vertical displacement associated with regimes that form prior to the line advected thermals. This displacement also introduced additional scatter into the data, which is not evident in the case of horizontally discharged flows. Note for horizontal discharges z_{vs}=0 and for vertical discharges z_{vs}= 3. A similar influence is also evident in Figure 3-18, where spread data from the z-integrated concentration profiles are presented. Again a virtual source of 3 is required to collapse the data from vertically discharged flows with that from those discharged horizontally. A spreading rate of 0.25 is consistent with both sets of data and the corresponding spread ratio of 1.6 is then consistent with the data in Figure 3-11, as expected. It is interesting to note the similarities in the spreading rates of the puffs and thermals, with the lateral (*y*) spreading rates being very similar and the vertical (*z*) differing by approximately 10%, which is then evident in differences in the spread ratios (*h* values). These subtle differences are a reflection of more significant differences in the cross sectional forms of the flows, which are evident in the different values of the *f* parameter and more significantly the differences in the top-hat spreading rates.

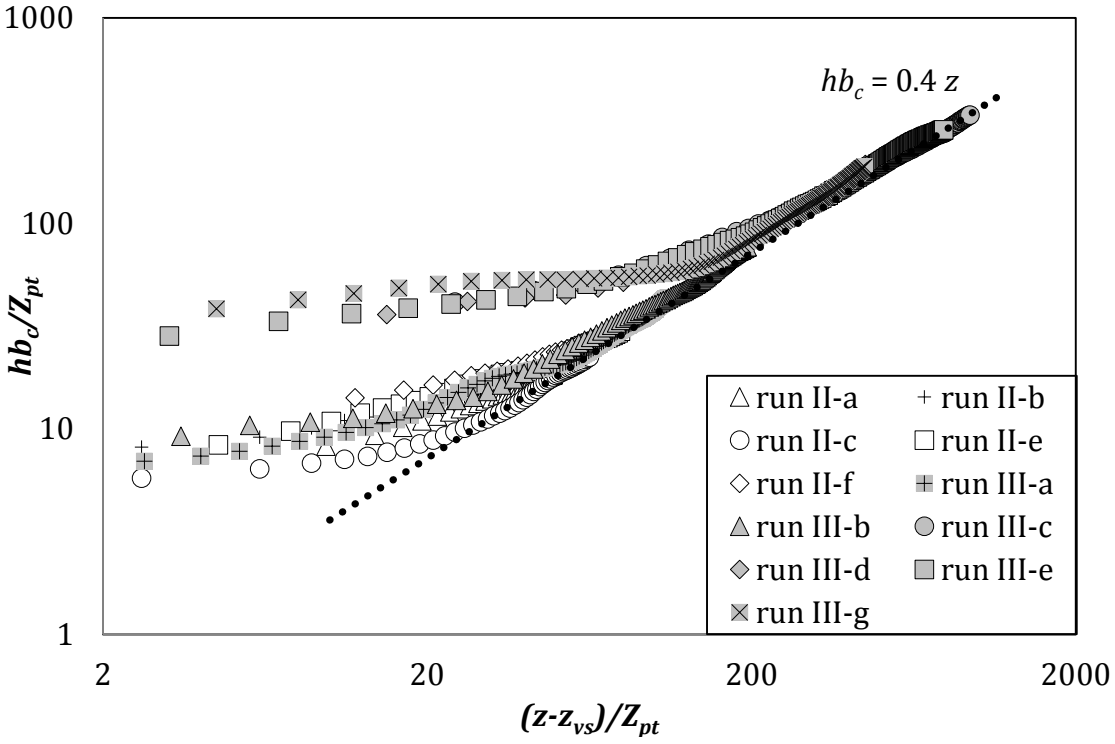

Figure 3-17: Spread of *y*-integrated horizontally (Run III) and vertically discharged (Run II) line advected thermal experiments.

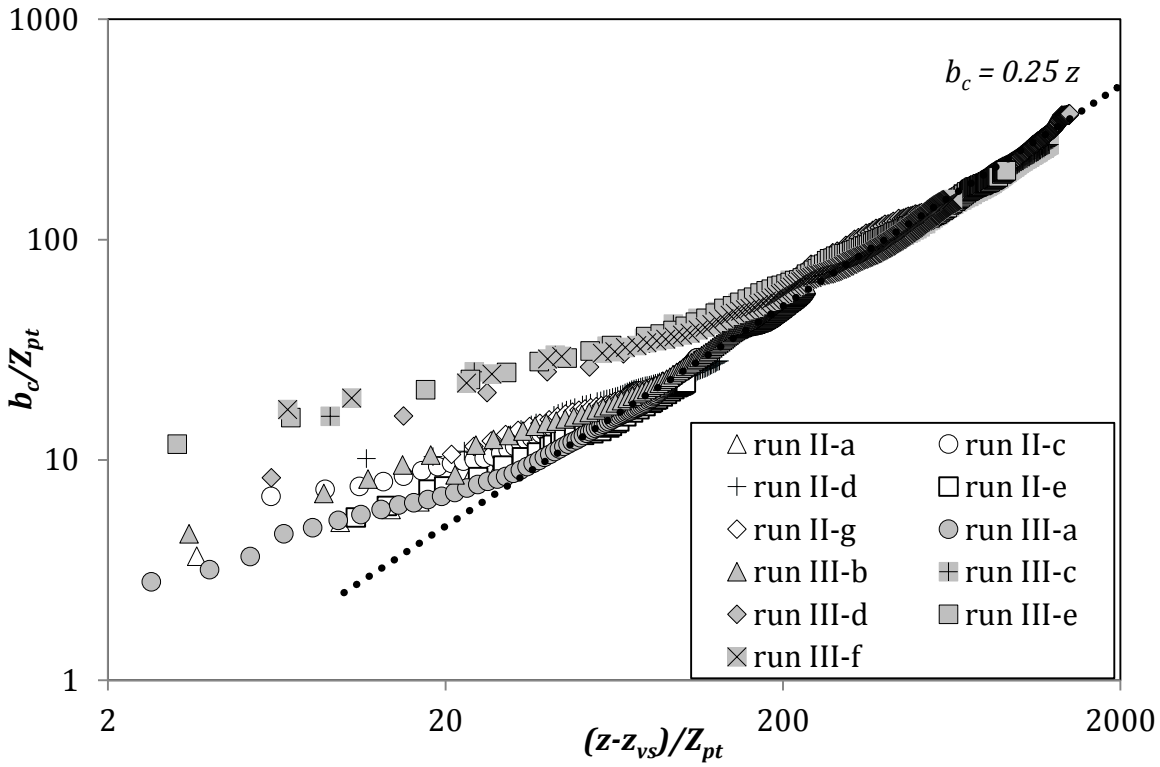

Figure 3-18: Spread of *z*-integrated horizontally (Run III) and vertically discharged (Run II) line advected thermal experiments.

Cross sectional integrated dilution data from horizontal and vertical buoyant discharges are presented in Figure 3-20 and Figure 3-21. Here variations of integrated-dilution with vertical distance from the source are shown. Figure 3-20 presents dilution data from cross sectional profiles integrated in the *y* direction, and Figure 3-21 presents dilution from profiles integrated in the *z* direction, where two peaks were evident the average value is shown. The data sets converge to a trend line with a slope of 0.86 and 0.67 respectively. The ratio between these slopes is 2/*h* (Equation 3-19 and 3-20). However, as with the spread data, in the case of the vertically discharged flow the virtual source concept is employed because of displacements associated with the regions preceding the formation of the advected thermal regime and there is a corresponding increase the scatter of the data.

It is possible to convert the integrated dilution data in Figure 3-20 and Figure 3-21 into centreline minimum dilution by combining it with the respective spread data. This is shown in Figure 3-19. The *h* value has been set to 1.56. The data shows good agreement with the analytical solution (when using m_t=0.73). 5 Sets from the horizontally discharged thermals have been displayed, the others have been omitted for clarity. For each of the shown experiments the centreline dilutions are calculated from the *y*-integrated data (y-int) and from the *z*-integrated data (z-int) to give the dilutions. For the experiments the dilutions in both directions are consistent.

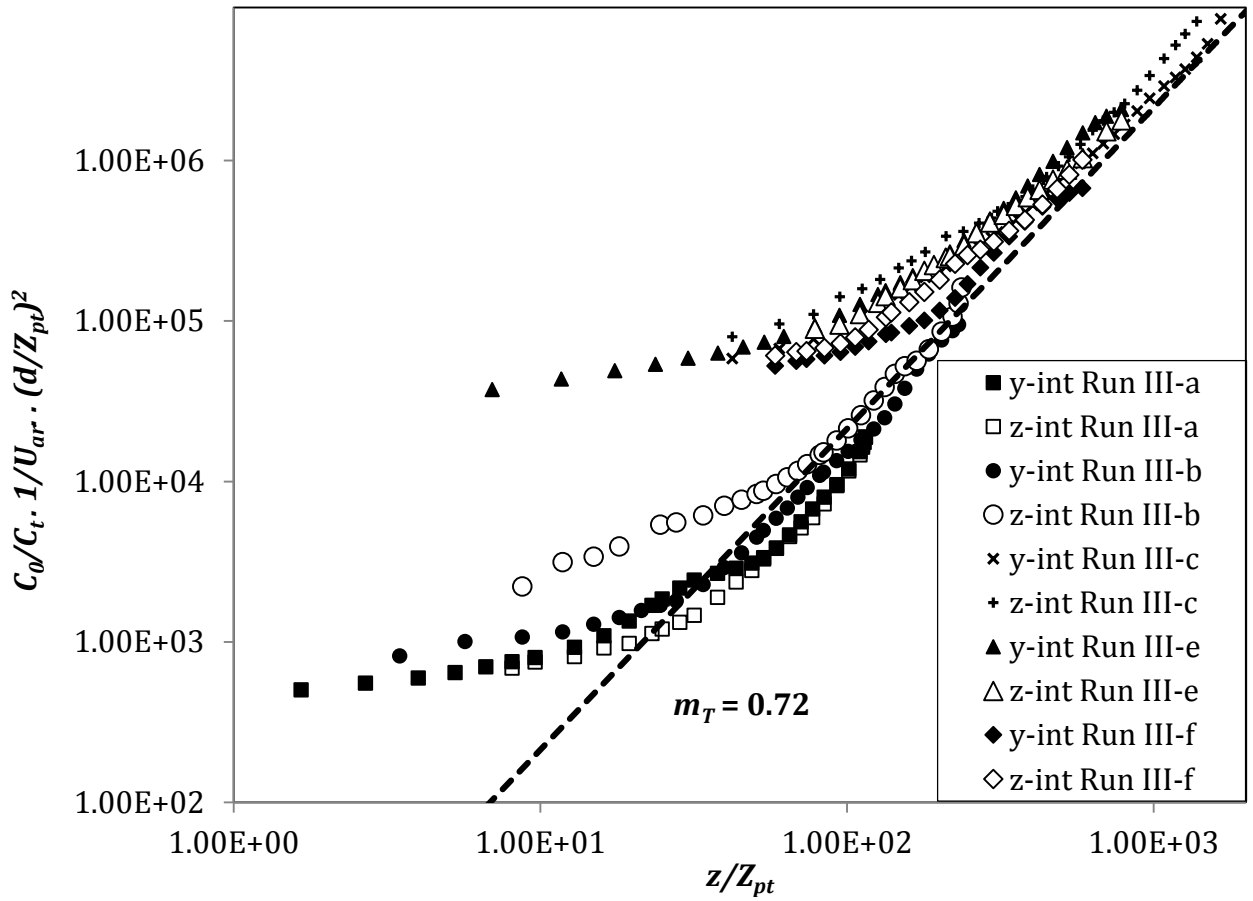

Figure 3-19: Minimum centreline dilution data for the horizontally discharged advected thermals.

Data obtained from *y*-integrated and *z*-integrated mean concentration profiles are consistent and the minimum dilution data is also in good agreement with prediction from the analytical solutions for advected thermals. Agreement with the analytical solutions is based on a top-hat to minimum dilution conversion factor of 3.3 and the significance of this is discussed in Section 3.4.1.

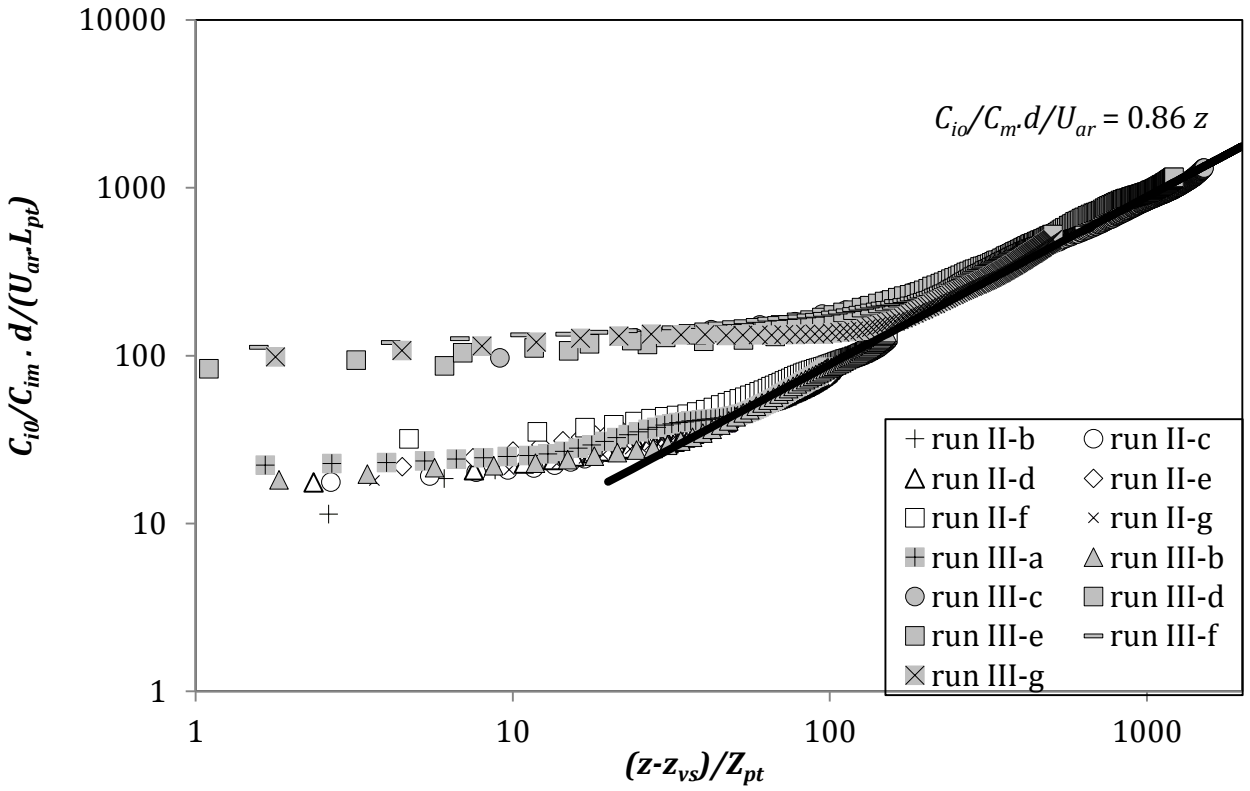

Figure 3-20: *y*-integrated dilution results of horizontally (Run III) and vertically (Run II) discharged line-advected thermals. The horizontally discharged experiments are depicted with the grey symbols.

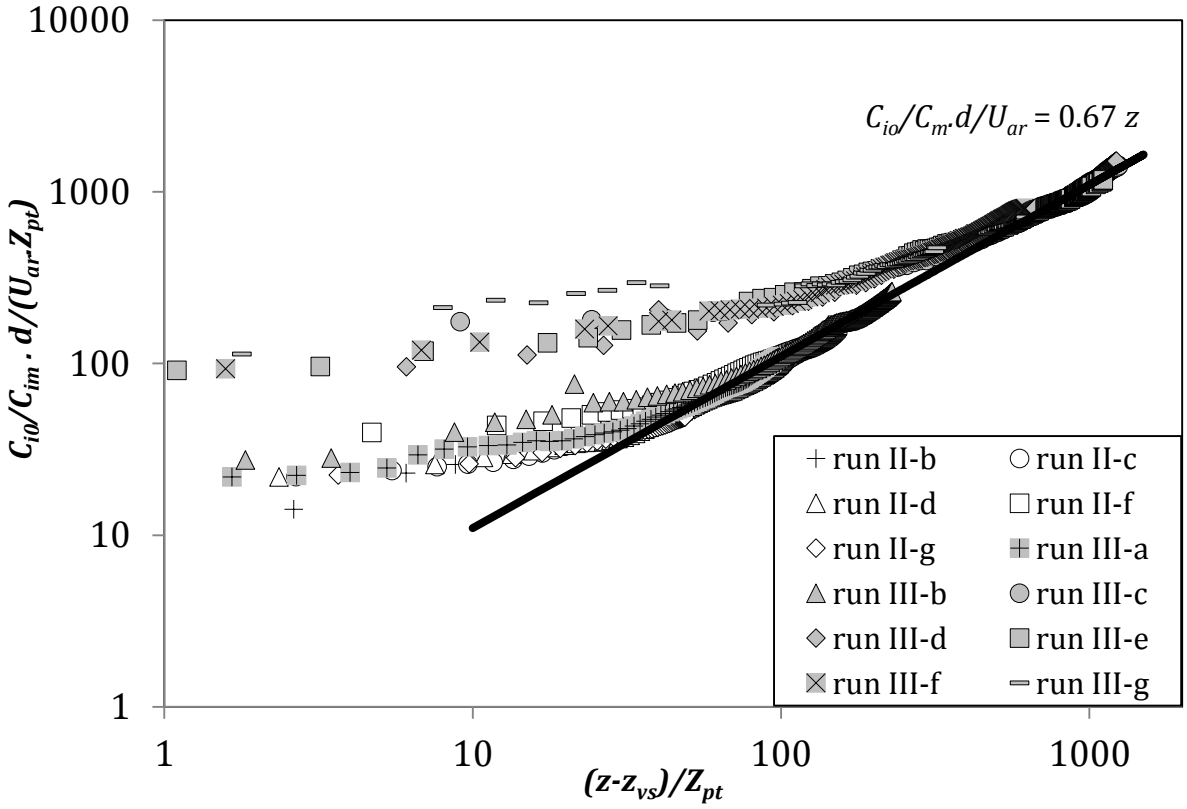

Figure 3-21: *z*-integrated dilution results of (Run III) and vertically (Run II) discharged line-advected thermals.

Figure 3-22 and Figure 3-23 show the non-dimensionalised peak distance, this is the total peak distance, extracted from *z*-integrated mean concentration profiles for both puffs and thermals. Note, in the case of thermals data from horizontal and vertical buoyant discharges is presented. The increase in peak separation in both cases is linear, with the thermal data having a gradient of 0.51 and the puff data a gradient of approximately 0.4. This data highlights a difference in mean form of the profiles, which is also evident in differences in the *f* parameter, that is, peaks of the self-similar advected thermal profiles move apart more rapidly than those of the line momentum puffs.

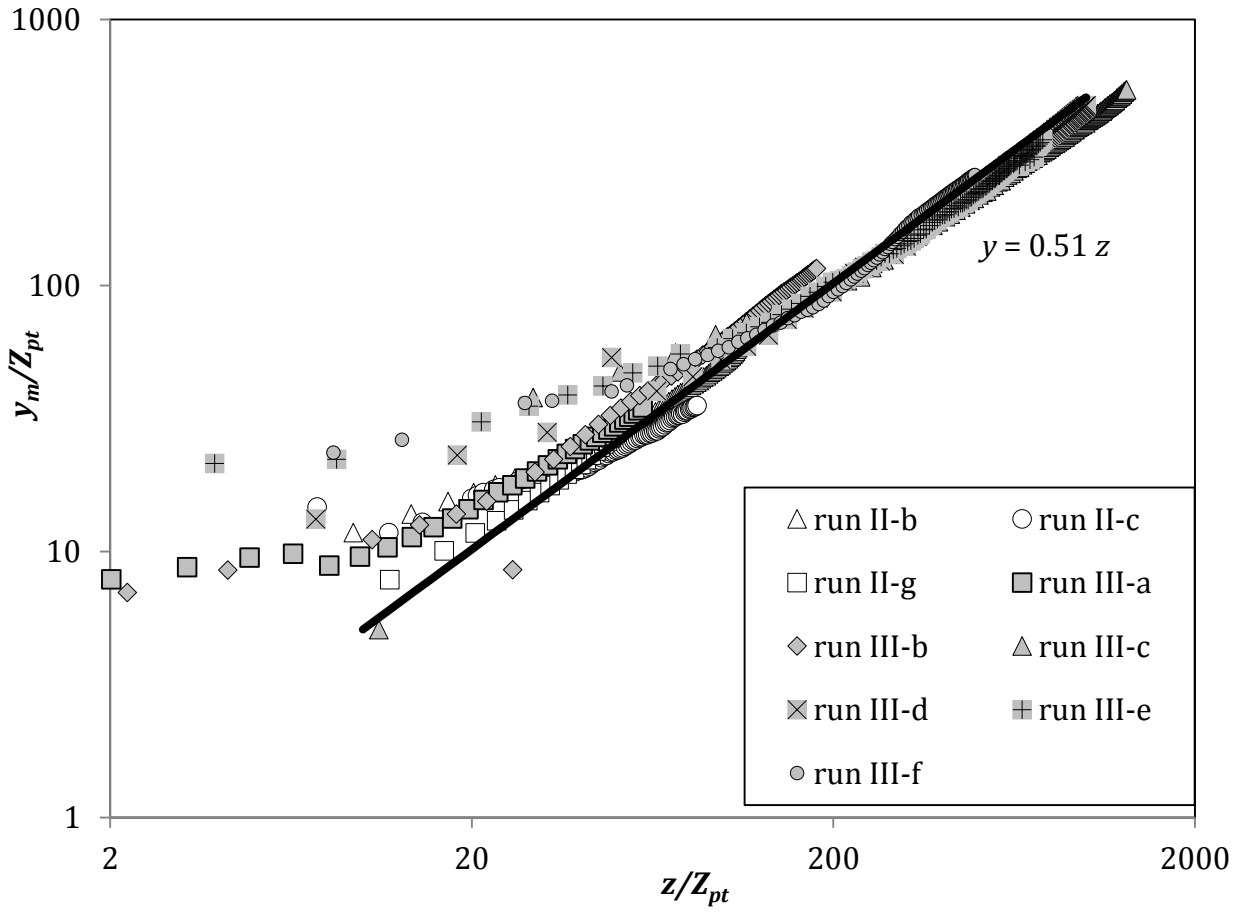

Figure 3-22: Non-dimensionalised distance between points of maximum concentration of the *z*-integrated data from line advected thermals.

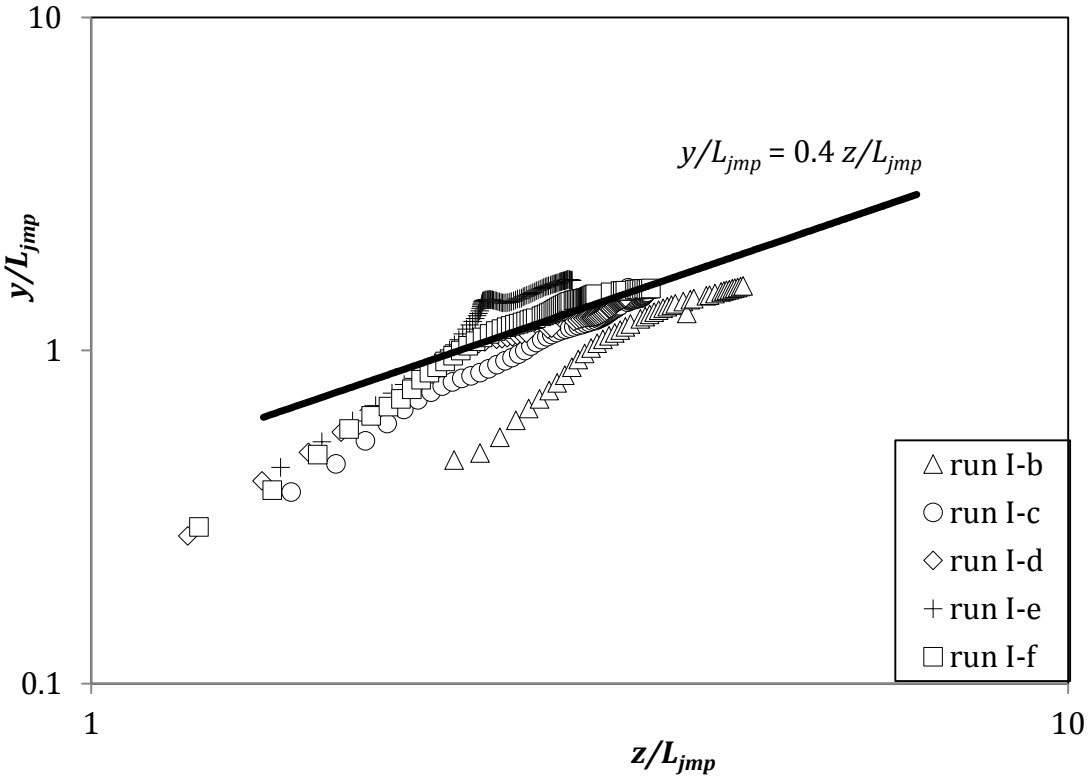

Figure 3-23: Non-dimensionalised distance between points of maximum concentration of the *z*-integrated momentum puffs.

3.4.1 Line Momentum Puffs, Line Advected Thermals and Conversion Factors

Table 3-5 gives a summary of the parameters determined from the present study for the puffs and thermals. The table highlights key differences and similarities between these two strongly advected flow regimes. Initially it is worth noting that the discharge direction has no significant effect on the self-similar form of advected thermals, although there is more inherent scatter in the behaviour of advected thermals that originate from vertical discharges. As noted previously while the spreading rates of the puff and thermals are similar, their cross sectional forms differ and this is highlighted in Figure 3-24 and Figure 3-25 where characteristic mean concentration profiles are depicted. Clearly the relationship between the peak and centreline concentrations differ for these flows and this difference in form also has potentially significant implications for the conversion factors that are required to convert predicted values from integral models, typically based on assumed simplified mean cross sectional profiles, to values that are representative of the actual profiles. In this context the relatively small differences in the spread ratio (*h*) also become important.

Table 3-5: Summary of key results from line momentum puff (M.Puff), vertically (V.Therm) and horizontally (H.Therm) discharged advected thermal experiments.

	f	Dilution horizontally integrated	Dilution vertically integrated	h	Spread horizontally integrated hk_c	Spread vertically integrated k_c	Trajectory	Peak distance, y
M.Puff	0.89	*	*	1.49	0.36	0.24	m_T=0.62	0.42
V.Therm	*	0.67	0.86	1.54	0.40	0.25	*	0.51
H.Therm	1.02	0.67	0.86	1.60	0.40	0.25	m_T=0.73	0.51

Note *, the data for these values for the vertically discharged thermals have not been depicted in a figure.

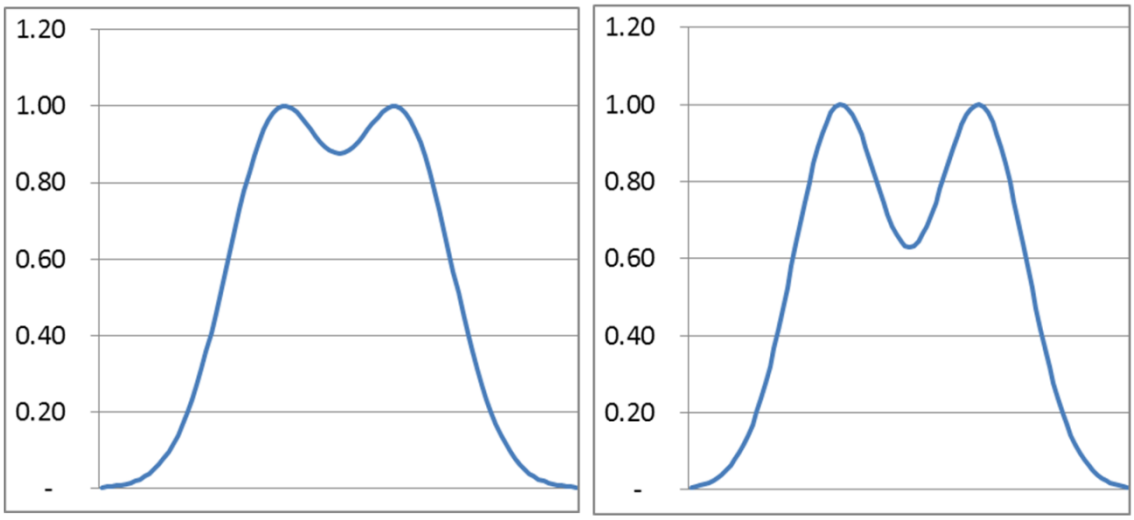

Figure 3-24: Vertically integrated concentration profiles of a momentum puff (left) and a line advected thermal (right).

Figure 3-25 shows a 3D image of the cross sectional average concentration profiles, based on the double-Gaussian assumption, for a puff (left side) and a thermal (right side) using the parameters from Table 3-5.

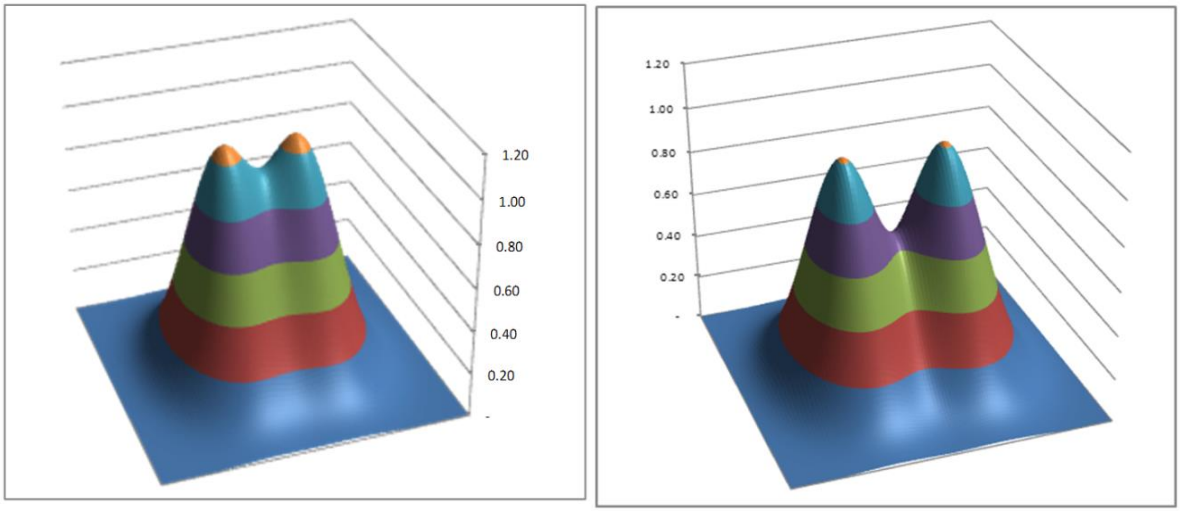

Figure 3-25: Integrated concentration profiles of a momentum puff (left) and a line advected thermal (right) in 3D.

As noted previously the Corjet and Visjet Integral models are commonly used in practice to predict the behaviour of wastewater discharges for design and environmental impact assessment purposes. In the case of Visjet top-hat or uniform cross sectional velocity and density/tracer profiles are assumed, whereas in Corjet these mean profiles are assumed to have a single Gaussian form. While these assumptions simplify the development and implementation of integral models, they do not provide accurate representations of the measured mean profiles in the strongly-advected regions of the flow and in the case of Visjet this is also true of the weakly-advected flow regions. The assumed profiles are self-similar as are the measured profiles within specific flow regions and thus conversion factors can be employed to convert characteristics of the assumed profiles to those of the measured profiles, so the integral models can provide more accurate predictions. Kikkert et al. (2007) determined conversion factors for line momentum puffs by matching volume and mass fluxes associated with the assumed and measured distributions. Characteristic parameters from the present experiments for puffs differ slightly from his (f=0.89 and h=1.49), and this suggests the maximum to centreline concentration ratio of 1.15 (combining Equations (3-12) and (3-13)), which is consistent with Kikkert et al.'s value of 1.13. Similarly, making use of Equations (3-8) and (3-15), these values suggest that the ratio of top-hat concentration spread, to the velocity profile spread (b/b_{Tc}) is 0.27. Note λ is assumed to have a value of 1.20 for non-buoyant discharges. The concentration spreading rate (k_c) of puffs from the present data is 0.24 and thus the equivalent velocity spreading rate is 0.20. These values suggest top-hat spreading rates of 0.61 (k_T) and 0.73 (k_{Tc}) for velocity and concentration profiles respectively. Combining Equations (3-9), (3-12), (3-14) and (3-16) gives the ratio of centreline maximum concentration (C_m) to the top-hat concentration (C_{Tc}) as 3.21 and the ratio of Cm to the equivalent top-hat concentration (C_T), based on the top-hat velocity spreading rate, as 2.23. As expected, equivalent values from Kikkert et al. (2007) for puffs are similar, with top-hat spreading

rates of 0.60 and 0.72 and concentration ratios 3.22 and 2.24. Kikkert et al. also analysed the conversion factors employed by Visjet and Corjet in the context of the double-Gaussian characteristic profile. They noted in the case of Visjet, that k_T = 0.64, which gives a top-hat concentration spreading rate of 0.77 (k_{Tc}). Thus the ratio of the b/b_{Tc} = 0.26 and this suggested I_q = 47.5 (Equation 3-8) and from Equation 3-16 η must then equal 2.16. This value of η then implied a concentration ratio C_m/C_{Tc} of 3.67, based on internal consistency of the model. They note that Visjet uses a conversion factor of 2.3 for C_m/C_T and thus based on Kikkert's analysis, Visjet underestimates the peak concentration of line momentum puffs by approximately 12%. Using present data gives a value for η of 2.13, I_q of 46.4 and implied concentration ratios C_m/C_{Tc} and C_m/C_T of 3.58 and 2.49 respectively. This suggests that Visjet underestimates the peak concentration of line momentum puffs by approximately 8%.

A similar analysis was conducted for Corjet where a single-Gaussian assumption is employed in the line momentum puff region. The spreading rate employed in the model is 0.25 and the flow scale at a given cross section is $b\sqrt{2}$, for a single-Gaussian distribution this then gives $b/b_{Tc} = 1/\lambda\sqrt{2} = 0.59$. The equivalent top-hat spreading rate is therefore 0.42, which is substantially lower than the data suggests. However, Kikkert et al. note that the definition of the top-hat profile is not unique, but that there should be internal consistency based on a reasonable representation of the actual mean concentration profiles. With a top-hat spreading rate of 0.42, the double-Gaussian approximation suggests the concentration ratios required for internal consistency are C_m/C_{Tc} and C_m/C_T of 1.07 and 0.74 respectively (using present values). Corjet assumes the ratio of C_m/C_T = 1.4, but C_m is matched to available data so that the error is associated with estimates of the "bulk" or top-hat values for the line momentum puff.

Interestingly both the Visjet and the Corjet model make no distinction between line momentum puffs and advected thermals in the application of parameters associated with these strongly advected flows. The new data obtained in the advected thermal region provides an important opportunity to explore the implications of this assumption. While the rate of concentration spread is similar to that of the puff at 0.25 (k_c), the associated velocity spreading rate is 0.23 (k) because of differing λ (1.07) values. The characteristic profile parameters also differ in that h=1.56 and f=1.02, so that the ratio of b/b_{Tc} then becomes 0.29 (assuming η=2). This then implies that the top-hat concentration spreading rate (k_{Tc}) should be 0.78 and the equivalent top-hat velocity spreading rate 0.73 (k_T), the latter being the same as that obtained independently from the trajectory data. The corresponding concentration conversion factors are C_m/C_{Tc}, C_m/C_T are 3.29 and 2.87. It is also worth noting that the ratio of peak

to centreline concentration for the thermal profiles is 1.44, in contrast to 1.15 for the characteristic puff profiles.

In the context of the measured mean concentration profiles for advected thermals, the Visjet model again assumes at top spreading rate of 0.64 (k_T) and the associated top-hat concentration spreading rate is then 0.68 (k_{Tc}). Maintenance of mass and volume fluxes at a given cross section then dictates that the concentration ratios of C_m/C_{Tc} and C_m/C_T have values of 2.54 and 2.22 respectively. Noting again that Visjet employs a conversion factor of 2.3 for the ratio C_m/C_T, it is evident that in the case of advected thermals the model overestimates the peak concentrations by just 4%. In contrast for the Corjet model these ratios cannot be defined, because based on Kikkert et al.'s method the associated top-hat concentration spreading rate (k_{Tc}) of 0.42 suggests a spread ratio (b/b_{Tc} = 0.55), but the maximum value of this ratio is obtained when $\eta = f = 1.02$. At this value b/b_{Tc} = 0.51 and the concentration ratios are (C_m/C_{Tc} and C_m/C_T) 1.06 and 0.92 respectively. It is sufficient to note that in the Corjet model the combination of assuming a single-Gaussian profile with a spreading rate of 0.25 is incompatible with the measured mean concentration profiles in the advected thermal region, if volume and mass fluxes are to be maintained at a given cross section. In Figure 3-26 the variation of the concentration ratios with concentration top-hat spreading rate (k_{Tc}) are shown. It is worth noting that the values of k_{Tc} are directly linked to specific η values, because the measured spreading rate (k_c) has a constant value and η alters the ratio of these two spreading rates.

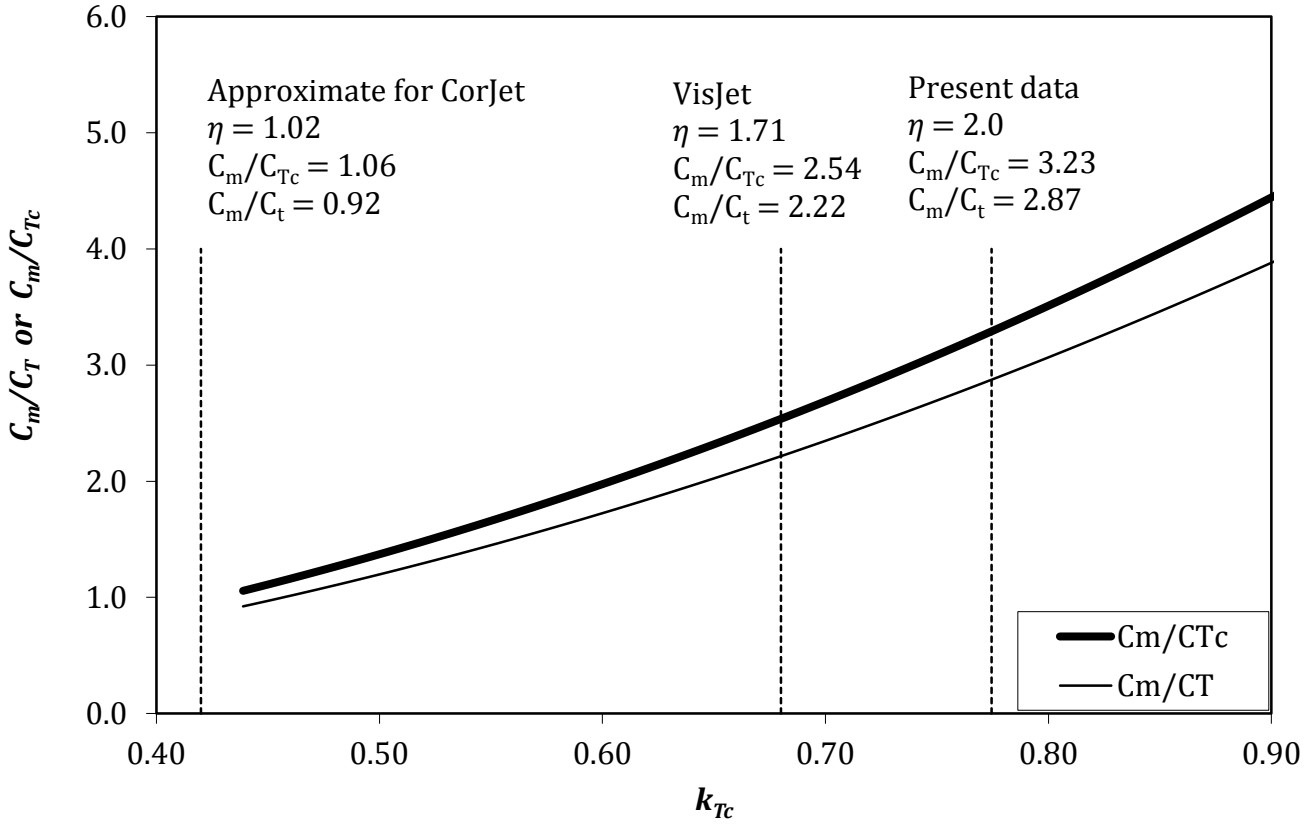

Figure 3-26: Conversion factors between experimental line advected thermal data and models.

3.5 Summary

In this chapter two set of momentum puff experiments and two sets of line advected thermals with a range of initial conditions have been described. The momentum puff flows were released vertically, perpendicular to the ambient flow. One of the thermal sets was also released in this fashion while the other was released horizontally in the same direction as the ambient flow. The flows were designed so that the transition from weakly-advected jet to a strongly-advected behaviour, (momentum puff and advected thermal) occurred happened relatively quickly. The vertically released advected thermal experiments were designed so that after a transition to a momentum puff, the transition to thermal occurred within the experimental range and could therefore be observed. The initial Reynolds numbers for the momentum puff experiments exceeded 2930. The line advected thermal sets contained two experiments that had a Reynolds number below 2000, but for the remainder it exceeded 3000 or higher. Each experimental set contained four or five experiments (momentum puffs) or 7 experiments (advected thermals) to allow representative data to be gathered.

The primary aim of this chapter was to measure and describe important differences between the flow behaviour in the momentum puff and line advected thermal regimes. The *y*-integrated and *z*-integrated mean concentration cross profiles taken at various distances from the source, demonstrated the flow is self-similar within these regimes. These mean profiles also clearly indicated the presence of a 'double-vortex' flow structure for puffs and thermals. However, these profiles also provided evidence of important differences between the two regimes. Most obviously the separation between the peaks in the integrated concentration profiles of the advected thermals was significantly larger than that of the advected momentum puff profiles. A double-Gaussian approximation enabled the cross sectional form of the tracer distributions to be characterized in a consistent manner. From the momentum puff experiments a value of 0.89 was obtained for the f parameter, which is indicative of the peak separation and compared well with results from previous authors. In contrast a value for the f parameter of 1.02 was obtained from the advected thermal experiments. In addition the h parameter, which represents the ratio of the vertical and horizontal width of the vortices, was 1.49 for the momentum puffs, and 1.56 for the advected thermals, again emphasising notable differences in the cross sectional forms for these flows.

While these differences in the cross sectional mean profiles appear to be subtle, they are significant when mapping the assumed mean cross sectional profiles to the measured profiles to determine peak values. An analysis of the mapping coefficients for the Visjet and Corjet models indicates that the

coefficient employed by Visjet underestimates the peak concentrations for line momentum puffs by approximately 8% and overestimates the peak concentrations of advected thermals by just 4%. It was also noted that mapping coefficients employed in the Corjet model are not consistent with conserving fluxes in the flow cross section, but are instead determined so they provide reasonable predictions of peak values. Interestingly the measuring spreading rates for the two flow types are similar. However, the distinctive forms of the puff and thermal profiles require significantly different spreading rates for the equivalent "top-hat" model, if fluxes are to be maintained between the "top-hat" and measured cross sectional forms. The "top-hat" spreading rates obtained from this analysis are consistent with those obtained directly from comparisons between trajectory data and relevant analytical solutions. Thus the experimental results confirm the inherently similar mean structure of advected line thermals and advected line momentum puffs, but they also highlight subtle differences, which must be treated with some care when modeling these flows.

Chapter 4 - Non-Buoyant Oblique discharges

4.1 Introduction

In order to better understand the dilution of waste fluids released into the environment, it is necessary to study the mixing processes near and far from the source. The reduction in concentration of pollutants in the far field is dominated by both mixing and decay processes, while the dilution in the near field is governed by the mixing processes alone. Near source mixing processes depend on the initial momentum of the source flow, the entrained ambient momentum flux and the buoyancy generated by the source fluid. In reality most jet discharges are buoyant as there are generally density differences between the discharged and ambient fluids, which are caused by differences in temperature and/or contaminant concentrations such as salt. However in some cases, buoyancy is less significant because the density differences are relatively small or the initial momentum flux relatively large and hence non-buoyant behaviour near the source can be of practical interest.

The way in which a jet interacts with its environment is generally well understood. Upon leaving the source the ejected fluid interacts with the ambient fluid and after an initial establishment region a self-similar flow develops. The initial momentum drives the mixing and in the mean a linearly widening axisymmetric cone is observed. If the jet is discharged into a moving ambient, where this ambient velocity is relatively small compared to the initial velocity of the jet flow, the influence of the ambient motion is limited to transportation of the mixing jet and the flow is classified as weakly advected. However, the entrained ambient momentum flux increases with distance from the source and when it becomes relatively large compared to the initial momentum flux, the influence of the ambient motion on the mixing processes becomes significant and the flow classification changes to strongly-advected.

As noted in chapter 1, the direction of the discharge relative to the ambient motion can have a significant influence on the strongly-advected behaviour. Typical configurations of interest include discharges in the same, opposite or a perpendicular direction to the ambient motion. These flows are respectively referred to as a jet in a coflow, counterflow, or crossflow. The counterflowing configuration is not dealt with here, instead the focus is on the contrast between the strongly-advected behaviour for the coflow and crossflow discharge configurations. In the case of the crossflow the strongly-advected behaviour is referred to as an advected line

momentum puff (Figure 4-1a) whereas in the coflowing case a strongly-advected jet (weak jet) forms in this region (Figure 4-1b).

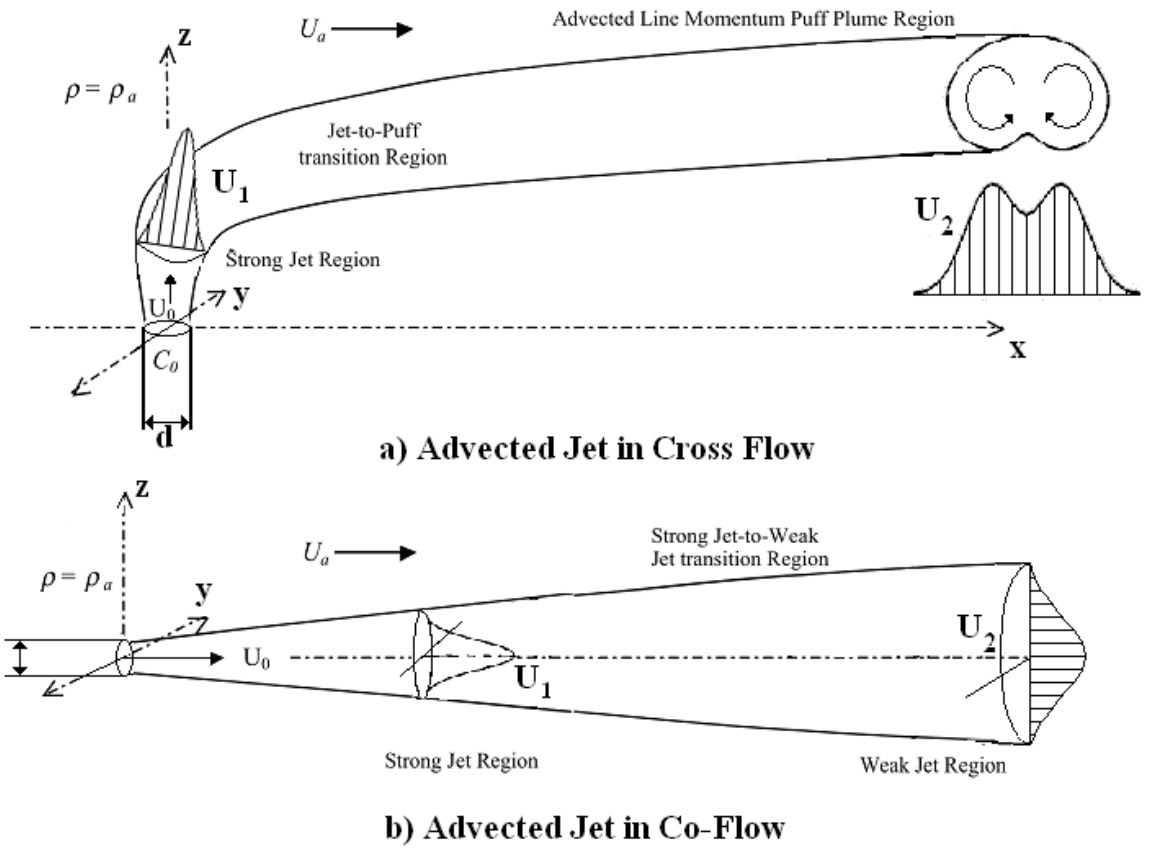

Figure 4-1: Different flow regions of advected jet. Note the similar form of the velocity profiles, U_1, and the different form of velocity profiles, U_2, of an advected jet in cross flow and an advected jet in co-flow.

The differences between these two strongly-advected flows are significant. In the strongly-advected jet region (coflowing configuration) the velocity and concentration profiles have a relatively simple, single peak, Gaussian form that is similar to the profiles in the weakly advected region of the flow (Davidson et al. 2002). In contrast, within the advected line momentum puff region the velocity and concentration profiles resemble those of a self-similar line vortex pair (Chu et al. 1974, Chu 1996, Kikkert et al. 2007, Scheepbouwer et al. 2007). It has been shown that the concentration distributions of this line vortex pair can be approximated with a double-Gaussian distribution (Kikkert et al. 2007); where there are concentration peaks associated with the centres of the two vortices. Logically the above implies that between the initial discharge angles of 0° (co-flow) and 90° (cross-flow) a change in strongly-advected behaviour occurs, from strongly advected jet to line momentum puff. The transition between these different strongly-advected behaviours is thus controlled by the angle of discharge.

Experimental studies have been carried out with initial discharge angles lying between both cases (oblique discharges). Margason (1968) studied flows with an initial discharge angle of 60° and 120°. Platten and Keffer (1971) investigated the angles between 45° and 135° with 15° increments, Chu (1975) studied the same range but with 22.5° intervals. While line advected momentum puffs were evident in the strongly-advected regions of these flows, none of the above studies focused on the transition angle, or transitional range of angles, between the two forms of strongly-advected behaviour. More recently Kikkert et al. (2009) carried out an experimental investigation into the behaviour of oblique discharges and their data suggested that for initial discharge angles greater than 40° line momentum puffs formed in the strongly-advected region, whereas for discharge angles less than 20° strongly-advected jets formed in this region. However, for discharge angles between 20° and 40° they were unable to clearly identify which type of flow formed. The authors noted difficulties in observing the strongly-advected behaviour because of the lengthy transitions from weakly- to strongly-advected behaviour. The experiments were also conducted with a single camera to view the flow, which made it more difficult to clearly identify behaviour in the strongly-advected flow region.

In this chapter the findings of an extension to previous studies are presented. Here a more sophisticated set of experiments is carried out with a focus on oblique discharges with initial discharge angles ranging from 29 to 53°. As Kikkert (2006) had shown, the lower discharge angles (up to 20°) were acting as weak jets, so the discharge angles have been selected such that two discharges were expected to act as momentum puffs (47.6 and 52.7°) and one discharge was expected, based on a set of preliminary experiments, to act as strongly-advected jet (28.9°). The remaining three discharge angles (32.4°, 35.9° and 39.0°) were chosen to more precisely establish the position of the transitional angle between a weak jet and a momentum puff.

4.2 Analytical solutions

Following Kikkert et al. (2007, 2009), data presentation and interpretation is aided by a relatively simple framework based on relevant analytical solutions and a double-Gaussian approximation. These analytical solutions are developed within each of three possible flow regimes, weakly-advected jet, strongly-advected jet and line momentum puff. The solutions are presented in Table 4-1, Table 4-2 and Table 4-3, and have been developed for a discharge released through a port of diameter, d, with velocity, U_0, at an angle θ_0 to the horizontal ambient current of strength U_a (Figure 4-2). The fluid is released into an ambient fluid of equal density ρ_0 and with negligible

temperature difference. Consistent with previous definitions, the initial volume flow rate, Q_0, of the discharge is given by $\pi/4\ U_0 d^2$. The initial excess velocity, U_{e0}, is defined as the difference between the discharge velocity and the component of the ambient velocity that is parallel to the discharge velocity, $U_a cos\ \theta_0$. The initial excess momentum flux, M_{e0}, of the discharge per unit density is then $U_{e0}Q_0$, whereas the initial momentum flux per unit density $M_0 = U_0 Q_0$. A convenient coordinate system is defined such that the discharge lies in the x-z plane, where the x coordinate is aligned with the ambient current and z coordinate is orthogonal to it. The y coordinate is then perpendicular to the x-z plane and the origin of the system is located at the point of discharge (Figure 4-2).

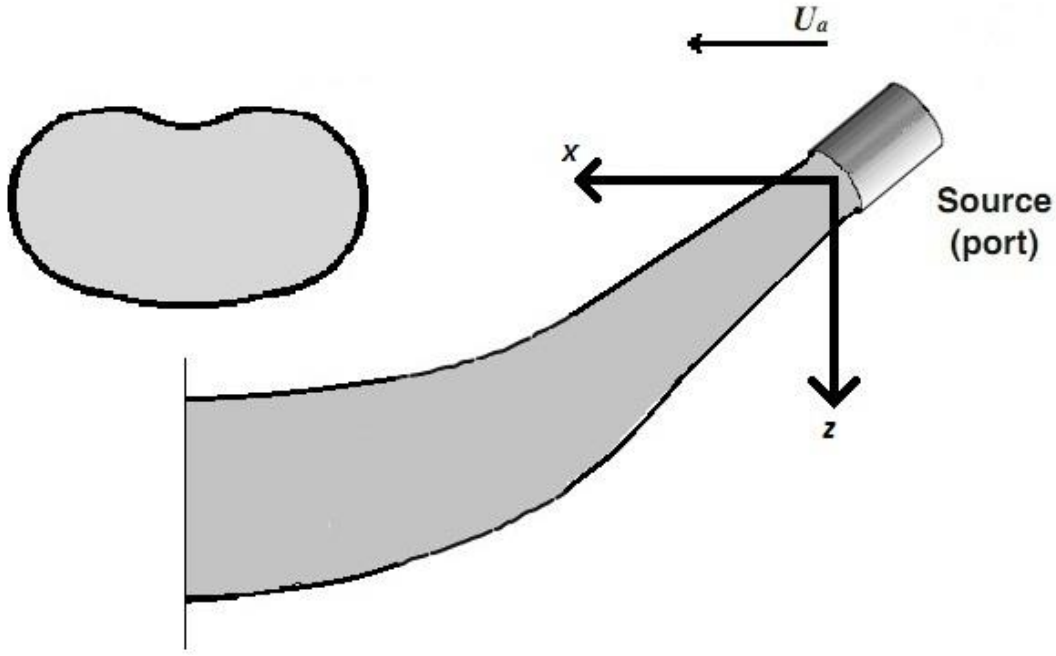

Figure 4-2: Schematic diagram of discharge configuration, the *y* axis comes out of the page. A cross section of the profile is depicted at the top left of the figure.

The solutions are written in the context of the relevant transition length scales, which for these flows are:

Weakly-Advected Jet to Strongly-Advected Jet, l_{jwj}

$$l_{jwj} = \frac{M_{e0}^{1/2}|cos\theta_0|}{U_a} \tag{4-1}$$

Weakly-Advected Jet to Advected Line Momentum Puff, l_{jmp}

$$l_{jmp} = \frac{M_{e0}^{1/2}|sin\theta_0|}{U_a} \quad (4\text{-}2)$$

In the following three subsections the important relationships that define the expected mean flow behaviour in the strongly-advected jet, advected-line momentum puff and weakly-advected jet are listed. These relationships will provide the framework for analysing the new experimental data.

Strongly-advected Jet

As noted above, within the strongly-advected regions the ambient velocity is relatively large when compared to the mean excess centerline velocity and it therefore plays an important role in defining the mixing and motion of the effluent. The entrained ambient momentum flux here exceeds the initial excess momentum flux and the governing parameter is the ratio of the root of the initial excess momentum (per unit density) to the ambient velocity, $M_{e0}^{1/2}/U_a$. Where the discharge angle is small, a strongly-advected jet forms and the flow moves predominantly in the *x* direction, but the component of excess momentum flux perpendicular to the ambient motion, deflects the flow in this direction, which here is taken as the *z* direction. The velocity and concentration retain a single-Gaussian form and the behaviour of the bulk parameters are defined with the relationships listed in Table 4-1 (Davidson et al. 2002, Kikkert et al. 2009).

Table 4-1: Strongly-advected jet equations.

Parameter	Equation	Reference
Dilution (Davidson et al. 2002)	$\frac{1}{cos\theta_0{}^{2/3}}\frac{U_{ar}}{1-U_{ar}}\frac{C_0}{C}=I_c\left(\frac{3k}{C_{jk}I_q}\right)^{2/3}\left(\frac{x}{l_{jwj}}\right)^{2/3}$	(4-3)
Integrated dilution	$\frac{1}{cos\theta_0{}^{1/3}}\left(\frac{U_{ar}}{1-U_{ar}}\right)^{1/2}\frac{C_{i0}}{C_{iy}}=\left(\frac{3k}{C_{jk}I_q}\right)^{2/3}\left(\frac{x}{l_{jwj}}\right)^{1/3}$	(4-4)
Spread (Davidson et al. 2002)	$cos^{2/3}\theta_0\frac{b}{l_{jwj}}=\left(\frac{3k}{C_{Jk}I_q}\right)^{1/3}\left(\frac{x}{l_{jwj}}\right)^{1/3}$	(4-5)
Trajectory	$\frac{1}{tan\theta_0 cos^{1/3}\theta_0}\frac{z}{l_{jwj}}=\frac{4}{3\pi^2\left(\frac{3k}{C_{Jk}I_q}\right)^{2/3}}\left(\frac{x}{l_{jwj}}\right)^{1/3}$	(4-6)

In Table 4-1, θ_0 represents the initial discharge angle relative to the ambient current. U_{ar} is the ambient to initial velocity ratio, C_0 is the initial concentration and C centerline mean concentration, k is the spread constant with a value of 0.104 and C_{jk} the integration constant that has a value of 2 (Davidson et al. 2002). The constant I_c is described by:

$$I_c=\iint_{-\infty}^{\infty}\frac{c}{C}\frac{dy}{b}\frac{dz}{b} \tag{4-7}$$

Which, for a single-Gaussian distribution equals,

$$I_c=\lambda^2\pi \tag{4-8}$$

Note the value of I_c is dependent on the ratio of tracer to velocity spread λ, which has a value of 1.20 in the weakly advected region (Fischer et al. 1979, chapter 3). Assuming this value remains unchanged in the strongly-advected region gives a value of 4.52 for I_c. The integral constant I_q equals π for a single-Gaussian flow. Making use of the Light Attenuation capture system provides dilution data that is integrated in the camera direction. Thus relationships for integrated dilutions have been listed in Table 4-1. In Equation 4-4 C_{iy} is the maximum integrated concentration along the y axis, and C_{io} is the initial integrated concentration. As the concentration distribution is single-Gaussian, the integrated dilution remains the same for every integration direction

perpendicular to the *x* direction. In Equation 4-4 the ratio C_{io}/C_{iy} can be substituted with C_{io}/C_{in} in which n-represents an integration direction that is perpendicular to the *x* axis.

Momentum Puff

Where the initial discharge angle is larger, a line double vortex forms in the strongly-advected region, and the cross sectional profiles of the line momentum puff are quite distinct from strongly-advected jets. The spread, trajectory and concentration equations therefore differ and are shown in Table 4-2 (Davidson et al. 1998, Kikkert et al. 2007).

Table 4-2: Momentum puff equations.

Parameter	Equation	Reference
Trajectory	$sin^{1/3}\theta_0 \frac{z}{l_{jmp}} = \left(\frac{3}{\pi k_{sg}^2 I_q}\right)^{1/3} \left(\frac{x}{l_{jmp}}\right)^{1/3}$	(4-9)
Concentration in the cross profile	$\frac{c}{C} = e^{-\left(\frac{z}{hb_c}\right)^2} \left[e^{-\left(\frac{y}{b_{c1}} - f_1\right)^2} + e^{-\left(\frac{y}{b_{c2}} + f_2\right)^2}\right]$	(4-10)
z-integrated concentration in the cross profile	$\frac{c_{iz}}{C} = \sqrt{\pi} h b_c \left(1 + e^{-4f^2}\right)$	(4-11)
y-integrated concentration in the cross profile	$\frac{c_{iy}}{C} = 2\sqrt{\pi} b_c$	(4-12)
Relation between dilution and distance from the source	$\frac{U_a}{U_0}\frac{C_0}{C} = I_{cdg} k_{sg}^2 \left(\frac{z}{l_{jmp}}\right)^2$	(4-13)
y-integrated dilution	$\frac{1}{sin\theta_0}\left(\frac{U_0}{U_{e0}}\right)^{1/2} \frac{C_{i0}}{C_{iy}} = 2h\lambda k_{sg} \frac{z}{l_{jmp}}$	(4-14)
z-integrated dilution	$\frac{1}{sin\theta_0}\left(\frac{U_0}{U_{e0}}\right)^{1/2} \frac{C_{i0}}{C_{iz}} = h^2 \lambda k_{sg} \frac{z}{l_{jmp}}$	(4-15)
Spread	$\frac{b_c}{l_{jmp}} = \lambda k_{sg} \frac{z}{l_{jmp}}$	(4-16)

Where k_{sg} is the concentration spread rate for the single-Gaussian divided by λ, I_{cdg} a shape constant (defined in chapter 3) that equals $2h\lambda^2\pi$, c is the local concentration, b_c is tracer spread

(λb), $2fb_c$ is the distance between the peaks of the individual Gaussians and h is the ratio of spreads in the z and y directions. The y- and z-integrated dilutions are respectively C_{io}/C_{iy}, and C_{io}/C_{iz}.

Weakly-Advected Jet

In the weakly-advected region, the initial excess momentum flux is dominant and for completeness the equations that describe the bulk behavior in this region are listed in Table 4-3. The cross sectional profiles in the weakly-advected jet region have Gaussian form, resembling those of a jet discharged into a still ambient fluid. However, the motion of the flow is deflected by the presence of the ambient current as it entrains ambient momentum; z is taken as the initial discharge direction.

Table 4-3: Weakly-advected jet equations.

Parameter	Equation	Reference
spread	$b = k\frac{z}{sin\theta_0}$	(4-17)
Dilution	$\frac{U_{ar}}{(1-U_{ar}cos\theta_0)}\frac{C_0}{C} = \frac{I_{qc}k_g}{I_m^{1/2}}\frac{z}{l_{jmp}}$	(4-18)
Trajectory	$\frac{x}{l_{jmp}} = \left(\frac{I_m^{1/2}k}{2C_{Ju}}\right)^{1/2}\left(\frac{z}{l_{jmp}}\right)^2$	(4-19)

Where k is the spread constant for a jet, I_{qc} is a shape constant that equals 1.99 for single-Gaussian distributed concentration and velocity profiles (Davidson et al. 1999), C_{Ju} is a trajectory constant with value 1.0, for more information on this constant see Davidson and Pun 1999. Finally I_m represents a shape constant that equals 1.74 (Davidson et al. 2002).

In Table 4-4 the scaling is based on the analytical solutions (Table 4-1, 4-2, 4-3) for different measured parameters are listed. To help identify characteristic momentum puff, strongly- or weakly-advected jet behaviour, the data is scaled using these different approaches. The data that collapses under a specific approach provides evidence of the existence of the associated flow regime. Given that the primary focus of this chapter is the determination of the form of the flow within the strongly-advected region; the experimental data will be primarily scaled based on the

strongly-advected jet and advected line momentum puff solutions. In Table 4-4 appropriate dimensionless forms for the measured parameters are shown in terms of graphical representations of the trajectory, spread and integrated dilution data. In addition parameters employed to characterise the cross-sectional profiles of the flows are included for completeness.

Table 4-4: Overview scaling of the parameters

#	**Parameters**	**Scale x axis**	**Scale y axis**
1	*z*-integrated cross profile	r/b_c	C_{iz}/C_{i0}
2	*y*-integrated cross profiles	r/b_c	C_{iy}/C_{i0}
3	*y*-integrated spread, strongly-advected jet scaling	$\frac{x}{l_{jwj}}$	$cos^{2/3}\theta_0 \frac{b_c}{l_{jwj}}$
4	*y*-integrated spread, momentum puff scaling	$\frac{z}{l_{jmp}}$	$\frac{hb_c}{l_{jmp}}$
5	*z*-integrated spread, strongly-advected jet scaling	$\frac{x}{l_{jwj}}$	$cos^{2/3}\theta_0 \frac{b_c}{l_{jwj}}$
6	*z*-integrated spread, momentum puff scaling	$\frac{z}{l_{jmp}}$	$\frac{b_c}{l_{jmp}}$
7	Trajectory, strongly-advected jet scaling	$\frac{x}{l_{jwj}}$	$\frac{1}{tan\phi_0 cos^{1/3}\theta_0}\frac{z}{l_{jwj}}$
8	Trajectory, weakly advected jet scaling	$\frac{x}{l_{jmp}}$	$\frac{z}{l_{jmp}}$
9	Trajectory, momentum puff scaling	$\frac{x}{l_{jmp}}$	$sin^{1/3}\theta_0 \frac{z}{l_{jmp}}$
10	*y*-integrated dilution, strongly-advected jet scaling	$\frac{x}{l_{jwj}}$	$\frac{1}{cos\phi_0{}^{1/3}}\left(\frac{U_0}{U_{e0}}\right)^{1/2}\frac{C_{i0}}{C_{iy}}$
11	*y*-integrated dilution, momentum puff scaling	$\frac{z}{l_{jmp}}$	$\frac{1}{sin\theta_0}\left(\frac{U_0}{U_{e0}}\right)^{1/2}\frac{C_{i0}}{C_{iy}}$
12	*z*-integrated dilution, strongly-advected jet scaling	$\frac{x}{l_{jwj}}$	$\frac{1}{cos\theta_0{}^{1/3}}\left(\frac{U_0}{U_{e0}}\right)^{1/2}\frac{C_{i0}}{C_{iz}}$
13	*z*-integrated dilution, momentum puff scaling	$\frac{z}{l_{jmp}}$	$\frac{1}{sin\theta_0}\left(\frac{U_0}{U_{e0}}\right)^{1/2}\frac{C_{i0}}{C_{iz}}$
14	f	$\frac{z}{l_{jmp}}$	None
15	h	$\frac{z}{l_{jmp}}$	None

4.3 Model

While the abovementioned analytical solutions provide an important framework for interpreting the experimental data, given the extended length of the transitions it is also important to have a more general model that provides the capability of predicting this transitional behaviour. The model outlined below is developed for a steady discharge into a uniform ambient cross-flow. For simplicity the model makes use of "top hat" parameters within a Lagrangian framework.

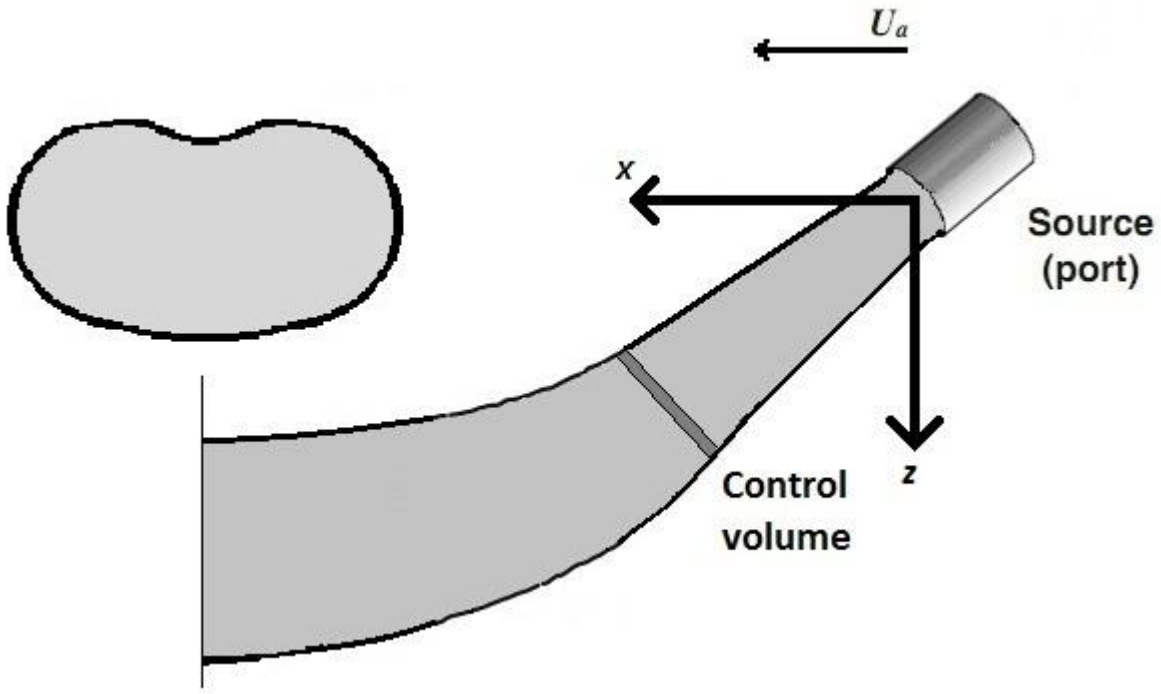

Figure 4-3: Diagram with control volume, showing key parameters for the model.

The horizontal momentum flux associated with the control volume changes because the entrained fluid is moving in the horizontal direction, thus the horizontal momentum flux relationship can be written as:

$$\frac{dM_{h*}}{dt_*} = U_{ar}\frac{dQ_*}{dt_*} \tag{4-20}$$

In which U_{ar}, represents the non-dimensional ambient velocity, U_a/U_0. M_{h*} is the non-dimensional horizontal momentum flux and Q_* the non-dimensional volume flux. Note the subscript "$*$" denotes a dimensionless parameter, where velocities, momentum fluxes, volumes fluxes and lengths are scaled on the relevant source values (U_0, M_0, Q_0 and d respectively). The selected time scale is the ratio of the source diameter, d, and the initial velocity, U_0.

Similarly the vertical momentum flux associated with the control volume changes when buoyancy forces are present and its variation with time can be written as:

$$\frac{dM_{v*}}{dt_*} = \frac{1}{Fr_0^2} \tag{4-21}$$

Where M_{v*} is the non-dimensional vertical momentum flux. Clearly in non-buoyant cases the initial densimetric Froude number is infinite and hence the vertical momentum flux is constant.

The geometric relationships can then be written as:

$$\frac{dz_*}{dt_*} = \frac{M_{v*}}{Q_*} \tag{4-22}$$

$$\frac{dx_*}{dt_*} = \frac{M_{h*}}{Q_*} \tag{4-23}$$

Closure is gained through the spread relationship, which can be written in the following form:

$$\frac{db_{T*}}{dt_*} = k_T u_{T*} \tag{4-24}$$

Where u_T represents the velocity in excess of the ambient velocity (Figure 4-4) and hence drives the mixing processes.

In order to solve the system of equations, it is convenient to write u_T in terms of the relevant momentum fluxes. Noting

$$M_h = (U_a + u_T \cos\theta)Q \tag{4-25}$$

$$M_v = u_T \, \mathrm{Q} \sin\theta \tag{4-26}$$

And letting

$$M_e = u_T Q \tag{4-27}$$

Equation 4-24 can then be written as:

$$\frac{db_{T*}}{dt_*} = k_T \frac{M_{e*}}{Q_*} \tag{4-28}$$

In which M_{e*} represents the excess momentum. Now (4-27 can be re-arranged to give:

$$M_e cos\theta = M_h - U_a Q \tag{4-29}$$

If Equation 4-25 is differentiated and combined with Equation 4-29 it is clear that the excess horizontal momentum is a constant and given that the flow is non-buoyant the vertical component of the total flux is also constant and thus M_e remains constant throughout the flow.

A relationship for the time rate of change of volume flux can be developed by combining relationships for the total momentum and volume fluxes to give:

$$M_s = Q * u_s = u_s^2 \pi b_T^2 \tag{4-30}$$

Where M_s stands for the total momentum flux and u_s the total velocity. Differentiating this relationship gives:

$$Q_* \frac{dQ_*}{dt_*} = 2b_{T*}^2 \frac{dM_{s*}}{dt_*} + 4M_{s*} b_{T*} \frac{db_{T*}}{ds_*} \tag{4-31}$$

Noting the time rate of change of the total momentum flux is given by:

$$\frac{dM_{s*}}{dt_*} = \frac{M_{v*}}{M_{s*}} \frac{dM_{v*}}{dt_*} + \frac{M_{h*}}{M_{s*}} \frac{dM_{h*}}{dt_*} \tag{4-32}$$

And that $dM_{v*}/dt_* = 0$. Equation 4-20, Equation 4-31 and Equation 4-32 can be combined to give an explicit relationship for the time rate of change of volume flux:

$$\frac{dQ_*}{dt_*} = \frac{\frac{2b_{T*}^2}{Q_*} \frac{M_{v*}}{M_{s*}} \frac{dM_{v*}}{dt_*} + \frac{4M_{s*} b_{T*}}{Q_*} \frac{db_{T*}}{ds_*}}{1 - \frac{2b_{T*}^2}{Q_*} U_{a*} \frac{M_{h*}}{M_{s*}}} \tag{4-33}$$

The spreading rate, k_T, of the weakly-advected jets differs significantly from that of advected line momentum puffs. Kikkert (2006) suggest a value 0.145 for the former and 0.61 for latter. Kikkert et al. (2009) also noted that while Wang (2000) suggests the spreading rate in the strongly-advected jet region also differs from the weakly-advected jet region, this variation can effectively be taken into account by relating the spread to the excess "top hat" velocity as opposed to the centerline velocity and thus the spreading rates in the two regions are essentially the same at 0.145. Therefore the transition from weakly- to strongly-advected jet behaviour is incorporated into the model as it stands, however the transition from weakly-advected jet to advected line momentum puff requires a specific definition. For simplicity the change in spreading rates

between these two regions is assumed to occur at a point, which is defined by the relative magnitudes of the initial and entrained ambient momentum fluxes.

The initial discharge angle dictates whether or not a line momentum puff or a strongly-advected jet forms as the flow evolves. However, the angle(s) at which the strongly-advected behaviour changes have not been clearly identified and are a focus of the present study. Thus rather than arbitrarily defining the transition angle, two separate models have been developed, one that evolves into a strongly-advected jet (SAJ) model and the other evolves into an advected line momentum (ALMP) model. These models will be employed to help identify the characteristic behaviour of these flows within the new data sets.

The initial conditions for the model are defined based on the velocity diagram shown in Figure 4-4. The initial excess velocity (U_{e0}) is given by the difference between initial discharge velocity (U_0) and the component of ambient velocity parallel to it ($Ua\ cos(\theta_0)$). The initial excess momentum flux (M_{eo}) is then $U_{e0}Q_0$ .The initial vertical momentum flux, M_{vo}, is then the vertical component of the excess momentum flux, $M_{e0}*sin(\theta_0)$ and the initial horizontal momentum flux (M_{ho}) is the sum of the entrainment ambient momentum flux (U_aQ_0) and the horizontal component of the excess momentum flux ($M_{eo}\ cos(\theta_0)$). The magnitude of the total initial momentum flux, M_{so}, is then determined from the horizontal and vertical momentum fluxes as $\sqrt{(M_{vo}^2+M_{ho}^2)}$. The spread at source, b_{To} approaches 0 and the initial non-dimensional volume flux is 1. All spatial coordinates are initially set to 0.

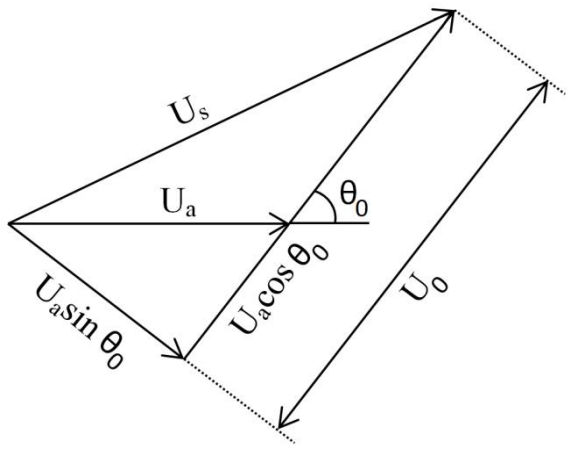

Figure 4-4: Oblique discharge velocity diagram.

4.4 Results

In total 50 experiments have been conducted with six initial discharge angles, three of these angles are expected to create transitional behaviour in the strongly-advected region (32.4°, 35.9° and 39.0°) and the remainder are expected to create a line momentum puff (47.6° and 52.4°) or a strongly-advected jet (28.9°) in the strongly-advected region. Table 4-5 lists the initial conditions for the experiments. Apart from variations in the initial discharge angle, the initial conditions for each of the experiments are very similar. The initial Reynolds number (Re_0) is based on the initial source fluid velocity, the source diameter and viscosity of the source fluid. The initial conditions were selected such that the flow was fully turbulent and that the transition from weakly-advected to strongly-advected behaviour was expected to occur within the captured spatial range (Scheepbouwer et al. 2007).

Table 4-5: Initial conditions for the non-buoyant experiments. The inclination angle is measured from the horizontal, relative to the direction of the ambient velocity, thus 0° represents a coflowing jet and 90° a jet in crossflow.

Experiments	Inclination Angle (θ_0)	Re_0	U_{ar}	d [mm]
Set 1	28.9°	6184-9302	0.028 ± 4%	2.45
Set 2	32.4°	6381-6394		
Set 3	35.9°	6184-6496		
Set 4	39.0°	6231-6496		
Set 5	47.6°	5924-6600		
Set 6	52.7°	5769-7120		

Table 4-6 contains the non-dimensionalised length-scales for the weakly-advected jet to strongly-advected jet. In determining these lengths scales, coefficients of 1 have been introduced to Equation 4-1 and Equation 4-2, so that the transition locations become apparent based on comparisons with the experimental data. It is worth noting that Kikkert et al. (2007) recently suggested a coefficient of 3 for weakly-advected jet to line momentum puff transition.

Table 4-6: Transitional length scales for the various experiments.

Experiments	Inclination Angle (θ_0)	l_{jwj}/d	l_{jmp}/d
Set 1	28.9°	26.6	14.7
Set 2	32.4°	25.7	16.3
Set 3	35.9°	26.1	16.2
Set 4	39.0°	25.6	20.6
Set 5	47.6°	20.7	22.6
Set 6	52.7°	18.7	24.5

In Table 4-6 the transitional length scales of the transition from weakly- to strongly-advected are depicted. As noted previously, whether a weakly advected jet transforms into a strongly-advected jet or a momentum puff is expected to depend on the inclination angle, not on the relative magnitude of the presented length scales.

Images from a single experiment are shown in Figure 4-5, where the initial discharge angle is 47.6° and hence an advected line momentum puff is expected to form in the strongly-advected region of the flow. The top image (Figure 4-5a) represents the integrated concentration as viewed along the *z* axis. The bottom image (Figure 4-5b) shows the integrated concentration for the same discharge viewed along the *y* axis. Although the flow is asymmetrical, in the top image the formation of two peaks in the integrated concentration is evident. This indicates that a double vortex pair is forming. In contrast, in the bottom image the integrated concentration shows no signs of a formation of a double peak distribution. It is possible therefore to approximate the *y*-integrated concentration with a single-Gaussian distribution, while the *z*-integrated concentration profiles are better suited to a double-Gaussian distribution.

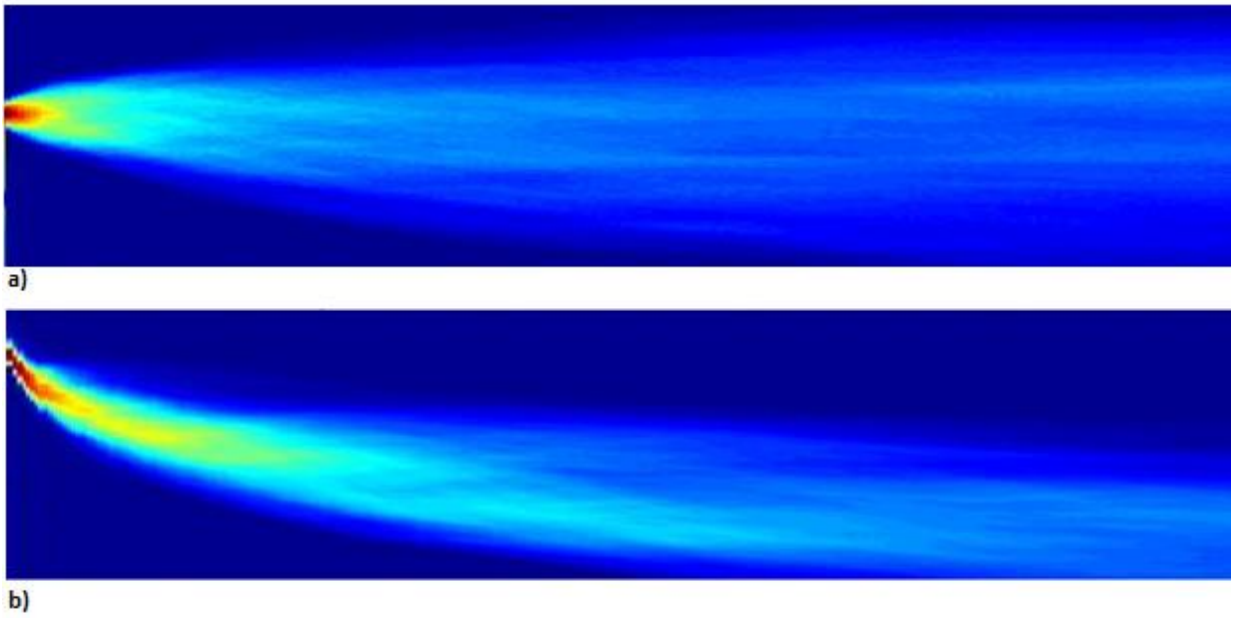

Figure 4-5: Images from an experiment with an initial inclination of 47.6º. Figure (a), represents the integrated concentrations viewed parallel to the *z* axis, whereas Figure (b) represents integrated concentrations of the same discharge viewed parallel to the *y* axis.

A series of integrated concentration profiles, extracted perpendicularly to the flow trajectory, are shown in Figure 4-6. The data in these profiles has been integrated in the *z* direction (that is, viewed parallel to the *z* axis in Figure 4-2). The profiles were extracted from an experiment from set 4 (Table 4-5), where the initial discharge angle was 39.0˚. The data is averaged over a period of approximately 15 seconds. The horizontal axis shows the *y* coordinate non-dimensionalised by the source diameter, and the vertical axis the local integrated concentration (C_{il}) divided by the initial integrated concentration (C_{i0}). Five distinct integrated concentration profiles are depicted at non-dimensional distances ranging from 1.8 to 4.1, where these ranges are non-dimensionalised with the jet to puff length scale, L_{jmp} (Equation 4-2). In this figure only 1 in 10 of the available data points is shown for the sake of clarity. Least-squares fits of the more general double-Gaussian distribution, details of which are given in chapter 3 (Equation 4-10), are also shown for each integrated concentration profile. Figure 4-6 demonstrates the ability of this more general double-Gaussian distribution to capture the main features of the integrated concentration profiles, including asymmetries in the flow. Initially the integrated concentration profiles have a single peak, which is typical of the weakly-advected (jet-like) region of the flow. As the flow develops these profiles broaden and a double peak distribution begins to form, which is consistent with the development of a vortex pair as the flow becomes strongly-advected and an advected line momentum puff forms. However, further into the strongly-advected region the peaks of the

vortex pair are less distinct, which is inconsistent with previous observations in the advected line momentum puff region (Kikkert et al. 2007).

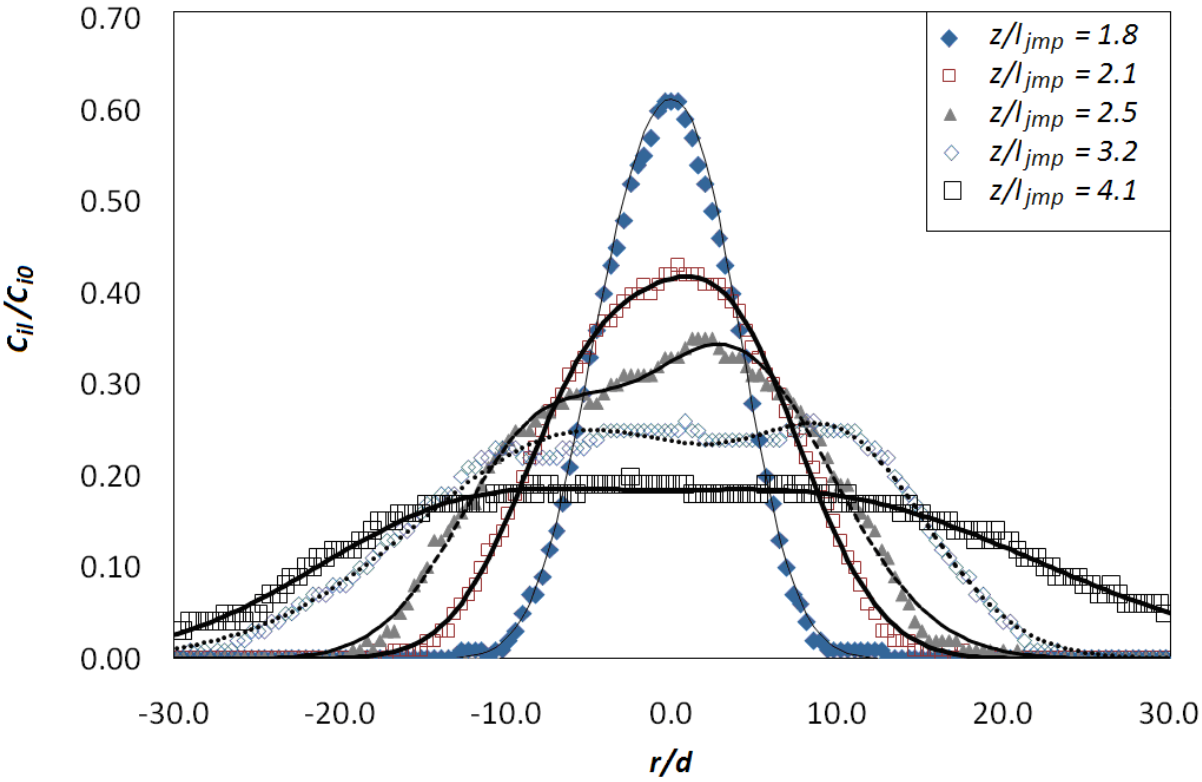

Figure 4-6: Integrated concentration profiles viewed along the *z* axis (figure 1) at several locations downstream from the source, non-dimensionalised with the jet to puff length scale. These profiles have been extracted from Experiment 4 (Table 4-5). The solid lines represent least-squares double-Gaussian fits to the concentration data.

Figure 4-7, Figure 4-8 and Figure 4-9 show the least square fits to the integrated concentration profiles for three initial discharge angles (28.9°, 39.0 and 47.6° to the horizontal). In contrast to Figure 4-6, these figures are created from ensemble averages of all the data obtained for a particular initial discharge angle. The data for the initial discharge angles are (ensemble) averaged over approximately 90 seconds. In Figure 4-7 (28.9°) it is evident that a double peak does not form, which indicates that a vortex pair is unlikely to be present and suggests that some form of strongly-advected jet has formed within the strongly-advected region. Figure 4-8 (39.0°) presents data from the same initial conditions as Figure 4-6, but in Figure 4-8 the data is averaged over an ensemble of 5 experiments. This averaging process has clearly reduced the asymmetry in the profiles. While there is some evidence of the development of the line vortex pair as the flow becomes strongly-advected (double peaked profiles), this double-peaked form is not sustained. However the single peaked distribution that subsequently forms is much broader near

the peak than is typical of a single-Gaussian distribution. Thus the profiles do not necessarily suggest the formation of a strongly-advected jet as the flow develops. Indeed the broad nature of the profiles suggests that a relatively closely spaced vortex pair may exist in the strongly-advected region**.** In contrast, in Figure 4-9 (47.6°) the formation of the double peak distribution is clearly evident and this double peak form is sustained as the flow continues to develop.

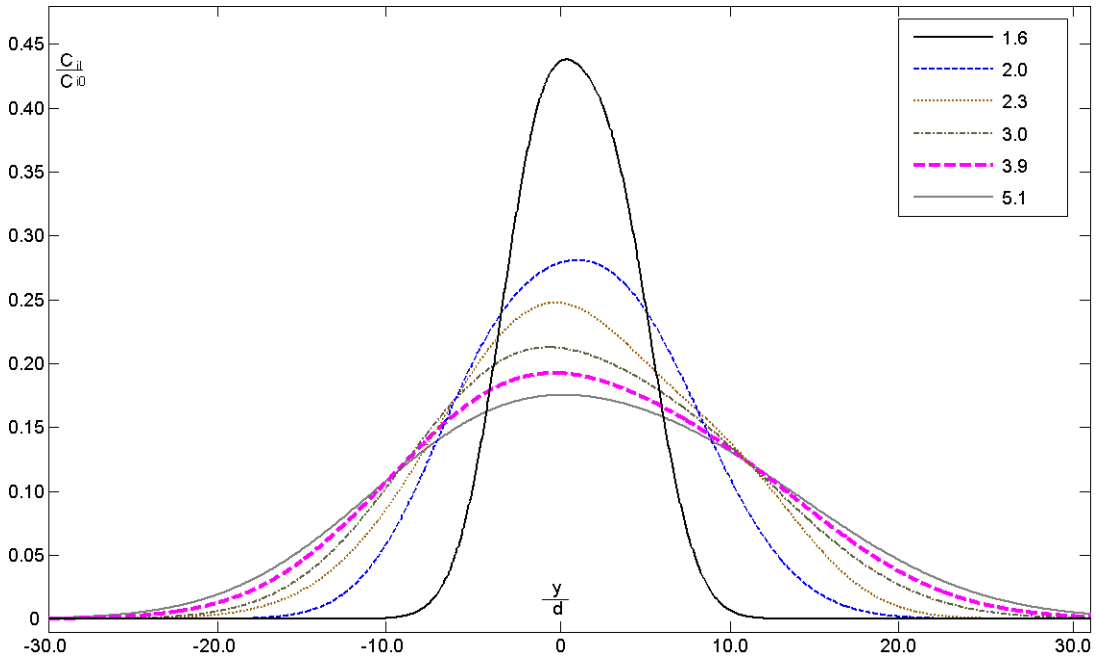

Figure 4-7: Profiles from ensemble averages of the *z*-integrated concentration data for a source with inclination 28.9° at different distances from the source, non-dimensionalised with l_{jmp}.

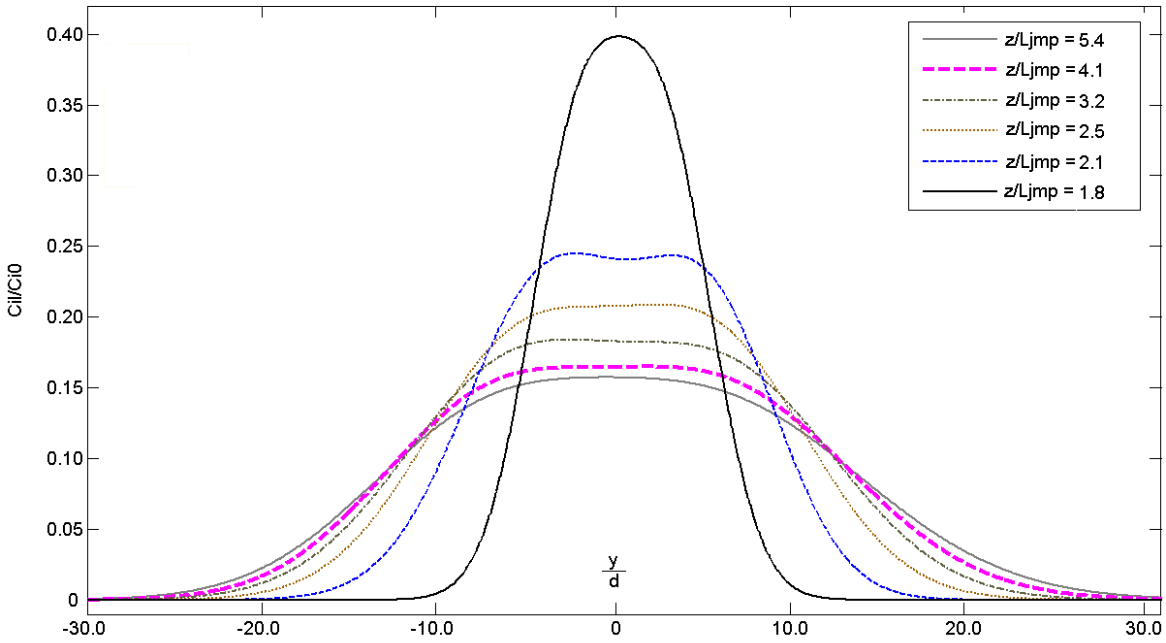

Figure 4-8: Profiles from ensemble averages of the *z*-integrated concentration data for a source with inclination 39.0°.

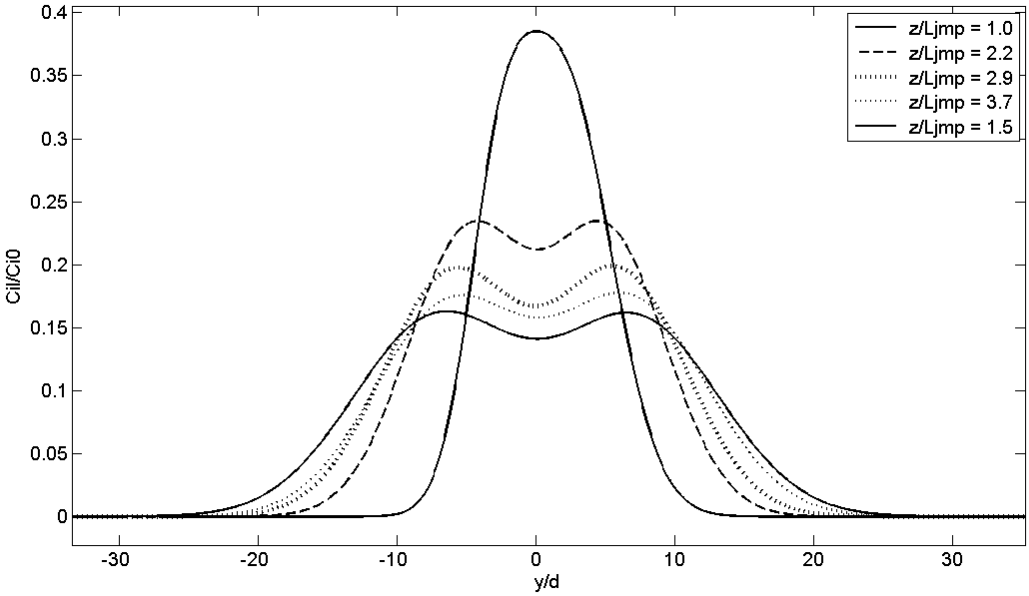

Figure 4-9: Double-Gaussian profiles from ensemble averages of the *z*-integrated concentration data for a source with inclination 47.6°.

In the following three sections the trajectory, spread and dilution data of these oblique discharges is presented. Strongly-advected jet and advected line momentum scaling (Table 4-6) is employed to provide further guidance as to the characteristic nature of the flow within the strongly-advected jet region for differing initial discharge angles.

4.4.1 Trajectory data

The trajectory data is shown in three different ways in Figures 4-10 to 4-12. In Figure 4-10 the trajectory data is scaled based on Equation 4-19. Figure 4-11 is scaled based on Equation 4-6 so that data in the strongly-advected jet region becomes evident and finally Figure 4-12 is scaled based on Equation 4-9 so that advected line momentum puff data collapses. This approach provides the basis for identifying which regimes are evident in the various data sets.

In the weakly-advected jet region of Figure 4-10, near the source, the trajectory data collapses as expected and then diverges as strongly-advected flows develop. The data remains collapsed until approximately 10 length scales, indicating that some form of transitional behaviour occurs beyond this non-dimensional distance. The analytical solution is also shown for comparison. It is evident that the transitions to strongly-advected behaviour occur closer to the source for higher initial discharge angles. This is consistent with transitions to strongly-advected behaviour occurring closer to the source when advected line momentum puffs form, which is evident in the length scale coefficients selected for Table 4-6.

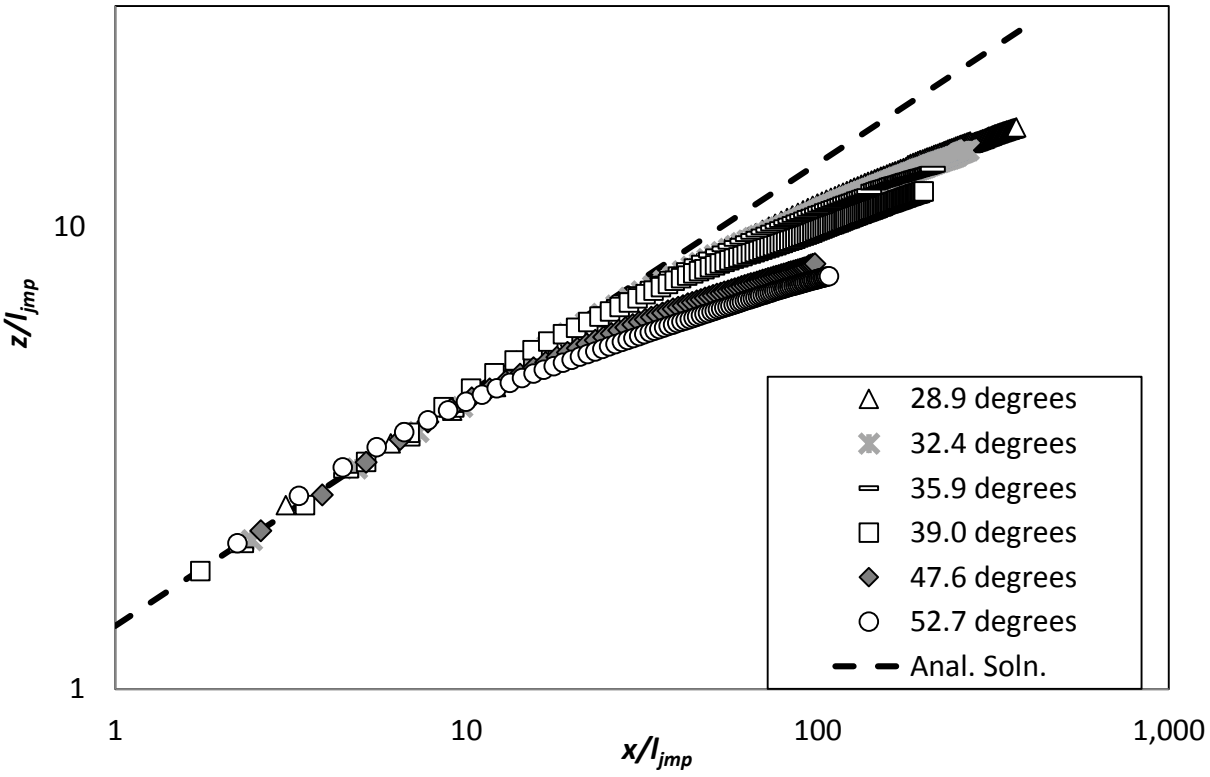

Figure 4-10: Trajectory compared to weakly advected jet analytical solution.

In Figure 4-11, experimental data from sets 1, 2, 3 and 6 are displayed. Set 4 (39.0°) and set 5 (47.6°) collapsed onto respectively sets 3 and 6 and have been left out for clarity reasons. Also included are data sets from Kikkert (2006), which contain data from experiments, conducted at shallower angles (10°, 12° and 17.5°). Three model predictions have been added, the strongly-advected (SAJ) model prediction and the advected line momentum puff (ALMP) model prediction at angles 52.7° and 28.9°. The scaling of the axes is based on the analytical solution for a strongly-advected jet so the SAJ model predictions collapse whereas the ALMP predictions do not. The data from Kikkert's study and for initial discharges angles of 28.9° and 32.4° from the present study is consistent with the SAJ model, indicating that strongly-advected jets have formed in these experiments. The remaining data sets diverge from the SAJ model and from each other, suggesting that strongly-advected jets are not forming in these cases.

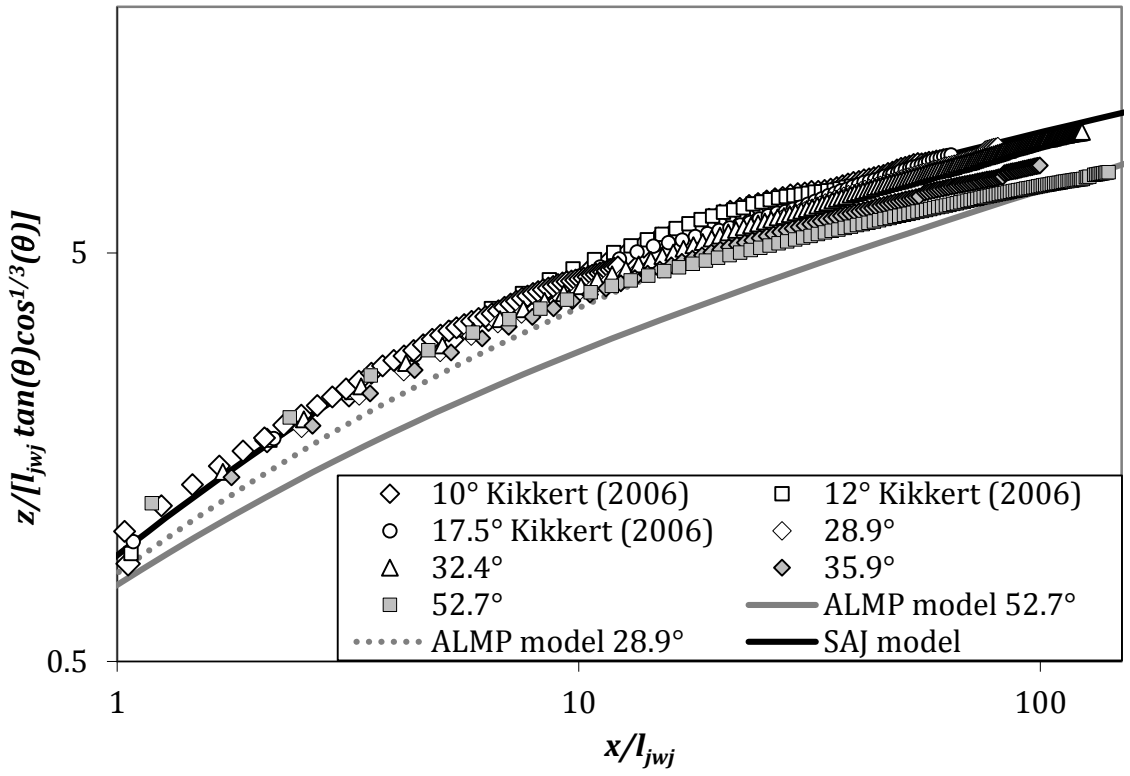

Figure 4-11: Experimental trajectory data, including data from Kikkert (10°, 12°and 17.5°) and strongly-advected jet (SAJ) model and advected line momentum puff (ALMP) model predictions.

Scaling of the data and models based on the analytical trajectory solution for a line momentum puff is presented in Figure 4-12. In addition to the new data, line momentum puff data from Kikkert (2006) is also shown for comparison, as are relevant model solutions. Note for clarity data set 2 has not been included. Data from flows released perpendicularly to the ambient current

and the numerical solution for the same initial conditions are seen to collapse in the strongly-advected region where line momentum puffs have clearly formed. It is evident that the trajectory data from the oblique discharges are also converging to this collapsed form, however, the initial displacement due to the weakly advected behaviour is significant and hence it is a considerable distance from the source before the line momentum puff behaviour becomes evident. The data from the present set of experiments is presented along with numerical model predictions that assume a momentum puff forms in the strongly-advected region of the flow (the ALMP model). There is very good agreement between data and model predictions in the weakly advected region of the flow, but as the flow develops this consistency is less evident for lower discharge angles (28.9° and 35.9°) suggesting that a line momentum puff has not formed. Data from the higher initial angle discharges (39.0°, 47.6° and 52.7°) remain consistent with the ALMP model predictions and collapse as the flows develop, indicating advected line momentum puffs have formed.

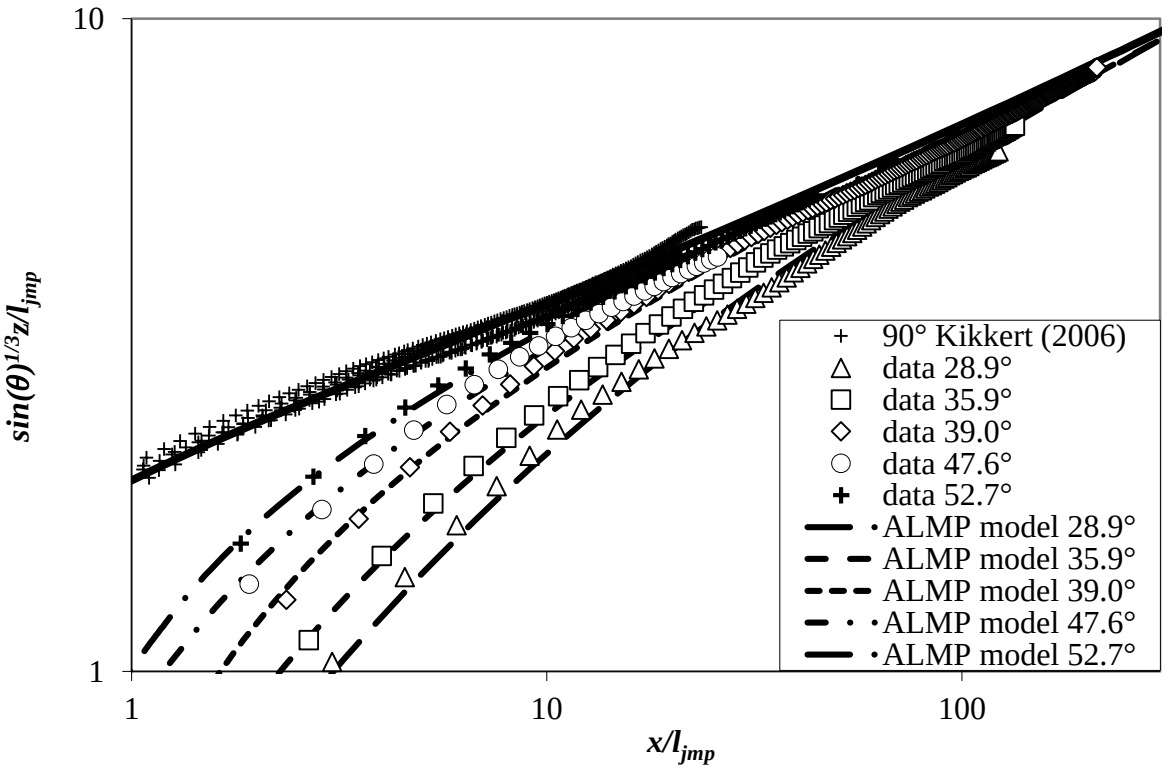

Figure 4-12: Momentum puff trajectories including a 90° discharge from Kikkert (2006) and model predictions for sets 1, 3 through to 6.

4.4.2 Spread data

In the following figures the development of spread data with the distance from the source is presented. The twin camera system provides spread data from mean concentration profiles integrated along a line parallel to the *y* and *z* axes and this data is presented separately for clarity. When assessing the spread data it is important to note that, as with the trajectory data, the dependence on distance from the source is the same for both strongly-advected jets and line momentum puffs and the differences are only evident in the equation coefficients. In Figure 4-13, where the *y*-integrated spread data is scaled based on Equation 4-5; data that collapse provide evidence of strongly-advected jet behaviour. Coflowing jet data from Wang (2000) and oblique jet from Kikkert (2006) have also been added for comparison. As expected Wang's data collapse with predictions from the SAJ model. Data from Kikkert's 30° discharges also collapse with this model. The results from the 28.9° and 32.4° discharges from the present study lie within the scatter of data from these experiments and are consistent with the model. The other four sets of new data do not follow the strongly-advected jet predictions. Data sets 4 and 5 collapses onto set 6 and are not included for clarity. It is worth noting that data from Kikkert's 35° discharge collapses with the 35.9° discharge from the present experiments and both data sets deviate from the strongly-advected jet predictions. In Figure 4-14 the *z*-integrated spread information is shown. Again data from the 28.9° and 32.4° discharges collapse onto the SAJ model. Interestingly the discharge at 35.9° appears to also coincide with the model predictions, but does show significant scatter. The higher angle discharges do not coincide with the SAJ model (only the 39.0° and 52.7° discharges shown for clarity). In Figure 4-14, the *z*-integrated data from experiments with larger discharge angles fall above the SAJ model, while in Figure 4-13 the respective *y*-integrated data falls below the same model. The SAJ model predictions are based on an assumed axisymmetric single-Gaussian profile.

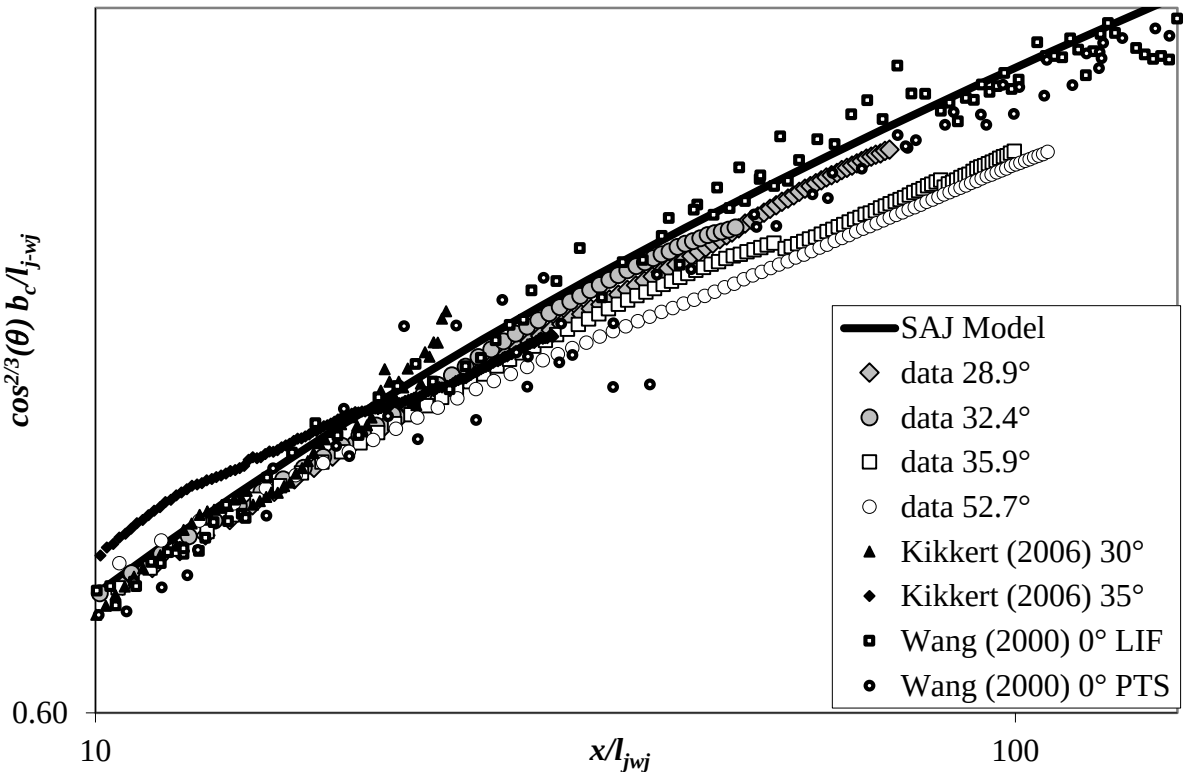

Figure 4-13: Oblique discharge *y*-integrated spread data compared with SAJ model. Data from Wang (2000) and Kikkert (2006) are added for comparison.

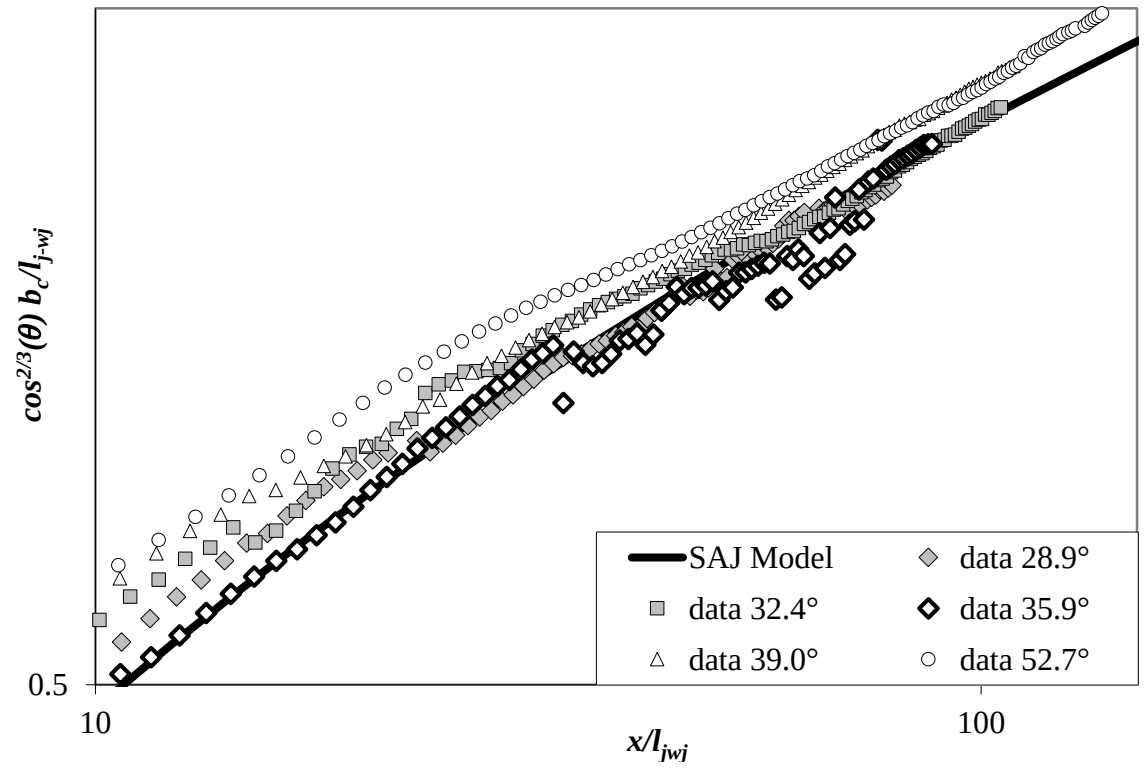

Figure 4-14: Oblique discharge *z*-integrated spread data compared with SAJ model. The spread data concerns widths of single-Gaussian fits.

In Figures 4-16 to 4-18 the same spread data is presented with appropriate scaling to identify line momentum puff behaviour (Equation 4-16). In Figure 4-15 the spread from profiles integrated along line parallel to *y* axis are shown in combination with predictions from the ALMP model. Data from the sets 1 and 2 (initial discharge angles of 28.9° and 32.4°) increases beyond the limit provided by the ALMP model, indicating line momentum puffs have not formed in these cases. The ALMP model provides a reasonable approximation of the spread results for the remaining experiments that is for discharge angles of 35.9° and above. An alternative way to present the evolution for this spread data is in terms of horizontal distances from the source. The scaling is obtained by combining Equation 4-9 with Equation 4-17 and the data is presented in this form in Figure 4-16 where the horizontal scale is now $(x/l_{jmp})^{1/3}$. An advantage of this alternative approach is that the horizontal coordinate is determined from the trolley speed (U_a) and hence it has less variability than the measured z-coordinate. Three model predictions have been added, 28.9°, 35.9° and 52.7°. Again, the experiments with discharge angles of 35.9° and above collapse onto the model predictions as the flow develops, whereas the data from the two more acute angles does not. Whereas the ALMP model does not accurately predict the behaviour of the 28.9° and 32.4° discharges as these flows develop.

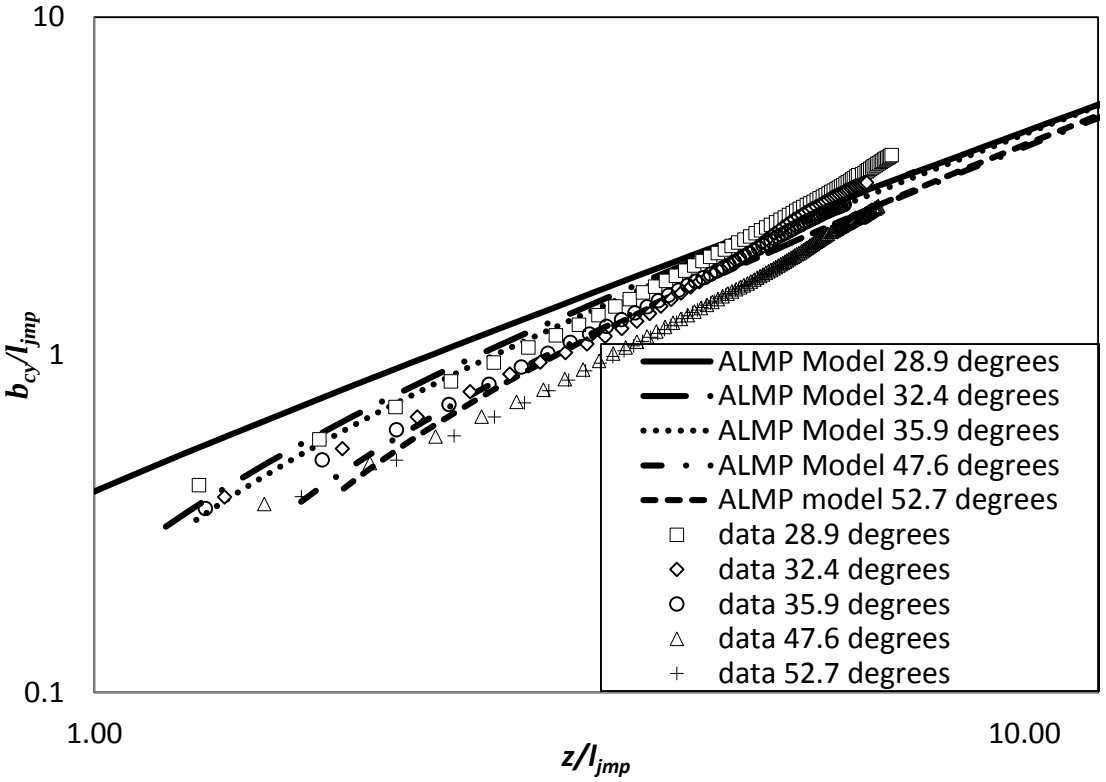

Figure 4-15: Oblique discharge *y*-integrated spread data compared with ALMP model.

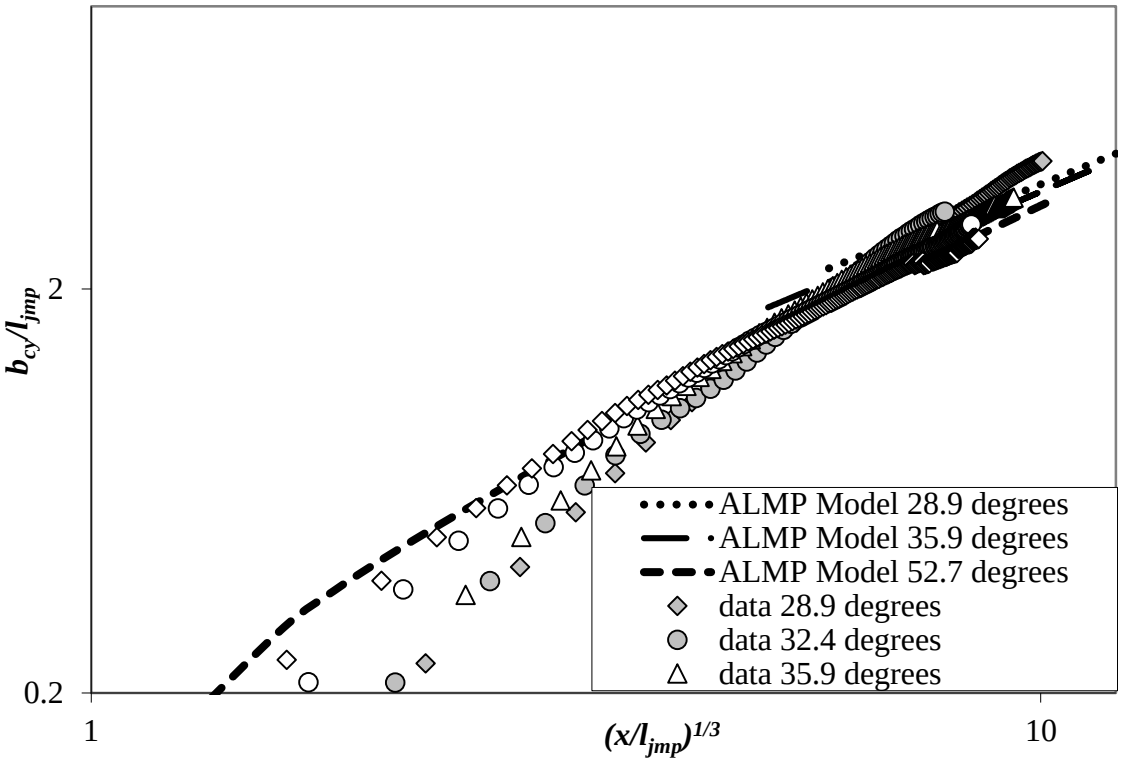

Figure 4-16: Oblique discharge *y*-integrated spread data (same as Figure 4-15) displayed versus $(x/l_{jmp})^{1/3}$ compared with ALMP.

In Figure 4-17, spread data extracted from profiles integrated parallel to the *z* axis is presented under line momentum puff scaling (Equation 4-16). The spread data in this case is taken as the average of the spreads of the individual Gaussian that make up the double-Gaussian profile. Consistent with the data extracted from profiles integrated parallel to *y* axis, the data sets with discharge angles of 35.9° and above collapse onto the puff model predictions, whereas as those at more acute angles do not.

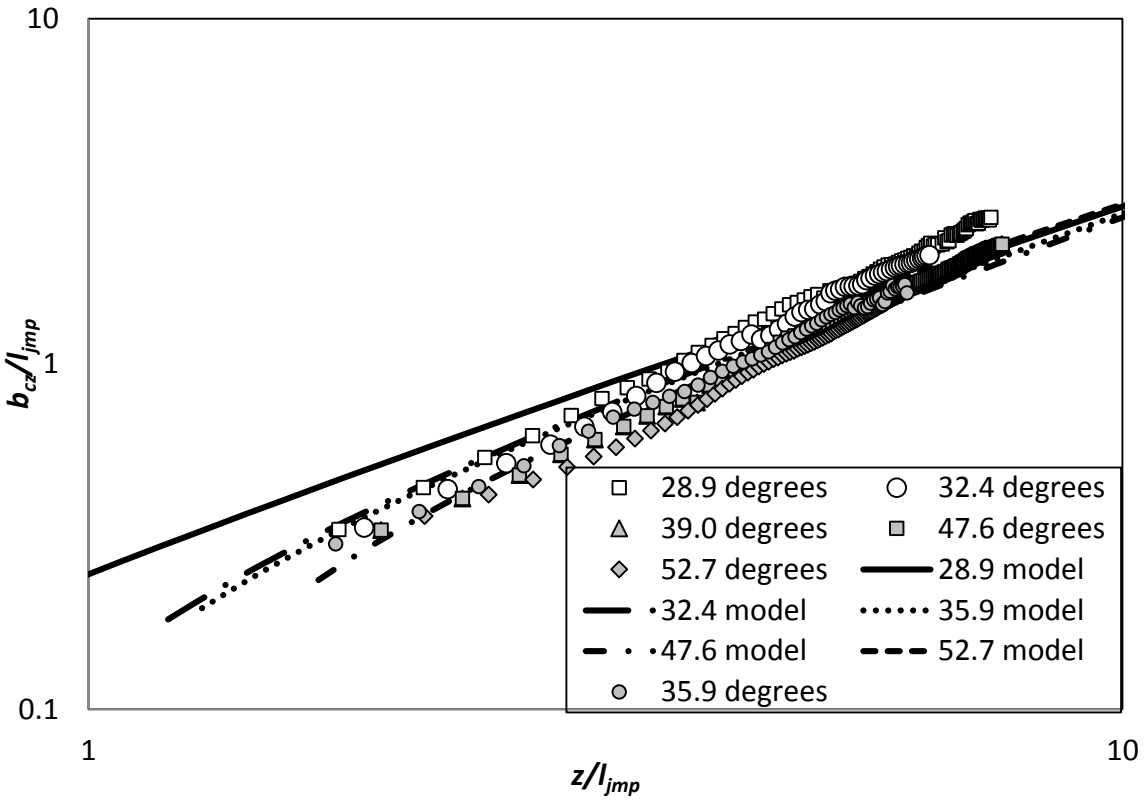

Figure 4-17: Oblique discharge *z*-integrated spread data non-dimensionalised with the momentum puff length scale.

4.4.3 Dilution data

The following four graphs portray the evolution of the dilution with distance from the source. Adopting the same approach, the first two figures show *y*-integrated and *z*-integrated dilution data scaled on the strongly-advected jet solutions (Equation 4-4), whereas the second two figures contain the same data scaled based on the momentum puff solutions (Equation 4-14 and Equation 4-15). In Figure 4-18 and Figure 4-19, predictions from the SAJ model have been added for comparison. Strongly-advected jet behaviour is clearly evident in the *y* and *z*-integrated dilution data for the 28.9° and the 32.4° discharge angles. This data collapses and becomes very consistent with the SAJ model predictions as the flow develops. In contrast the 39.0°, 47.6°, and 52.4° discharges sets collapse at larger *x*-distances, but become increasingly inconsistent with the SAJ model predictions, confirming again that strongly-advected jets do not form for these flows. Interestingly the *z*-integrated dilution data from the 35.9° appears to coincide with the SAJ model; whereas the *y*-integrated dilution data does not.

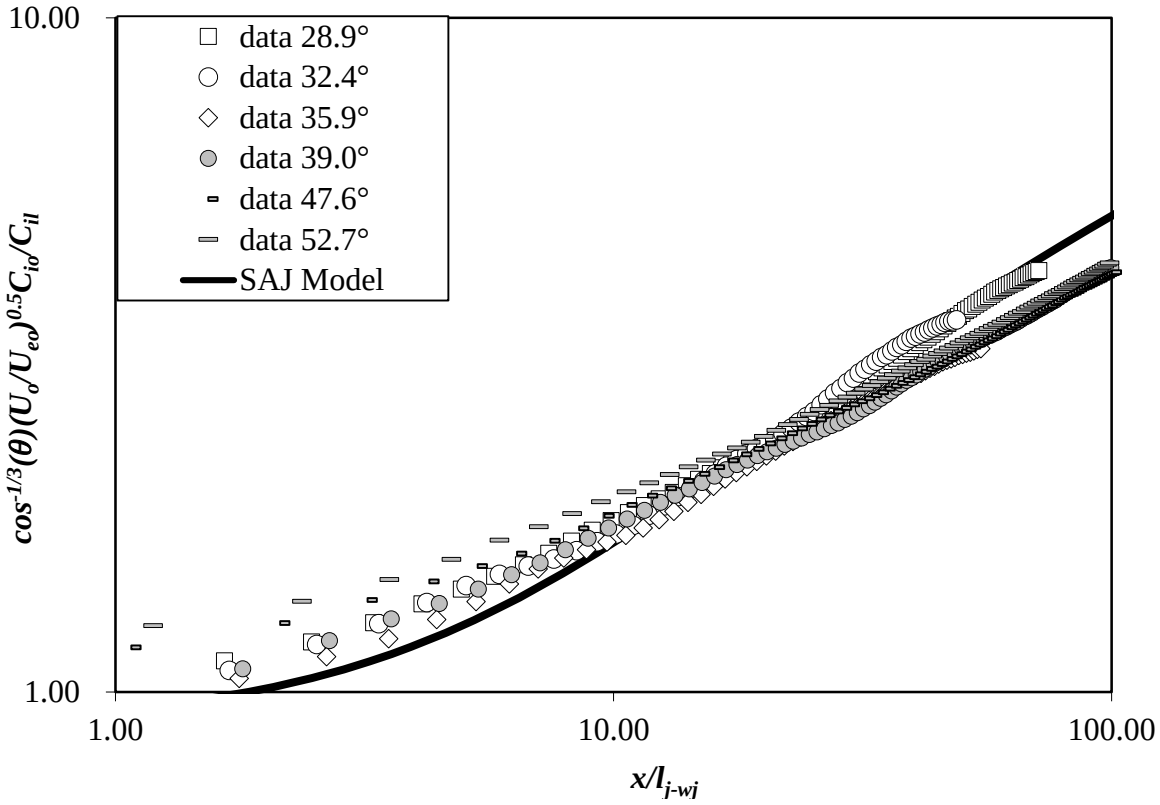

Figure 4-18: *y*-integrated dilution non-dimensionalised with the strongly-advected jet length scale.

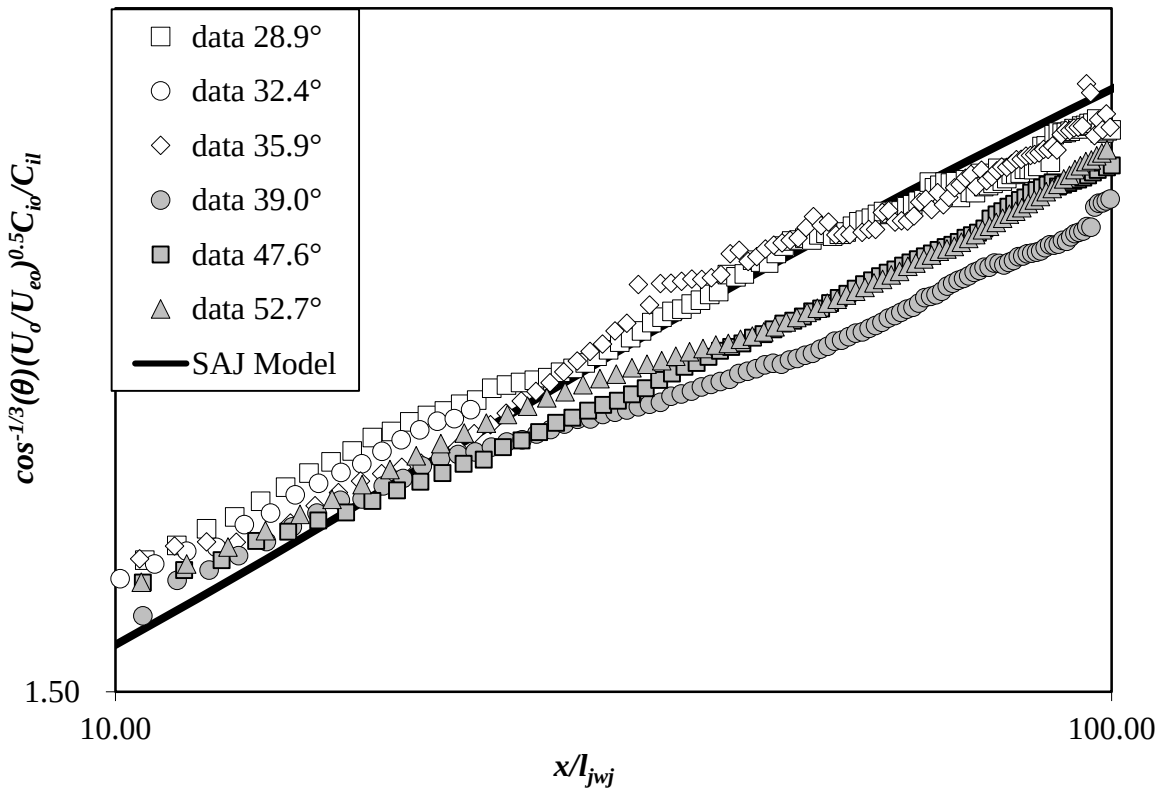

Figure 4-19: Oblique discharge *z*-integrated and averaged dilution non-dimensionalised with the strongly-advected jet length scale.

Figure 4-20 and Figure 4-21 present the same integrated dilution scaled based on the advected line momentum puff solution. Reference data has been added to the *y*-integrated dilution data (Figure 4-20), that is, Kikkert's data for a 35° and 40° discharge. Here Kikkert's data for 35° coincides with the 35.9° data from the present study as do the 40° and 39.0° data sets from the two studies. In this presentation the 28.9° and the 32.4° sets follows a path, which is some distance away from the ALMP model prediction. Whereas the 39.0°, 47.6° and 52.7° integrated dilution data sets eventually collapse and coincide with predictions from the ALMP model, dilution data from the 28.9° , 32.4° and 35.9° discharges does not collapse under this scaling and is not consistent with the ALMP model predictions. This behaviour is also evident for the dilution data from profiles integrated parallel to the *z* axis (Figure 4-21). The dilution data confirming line momentum puff behaviour for initial discharge angles of 39.0°, 47.6°, and 52.7° and strongly-advected jet behaviour for the 28.9° and 32.4° initial discharge angles.

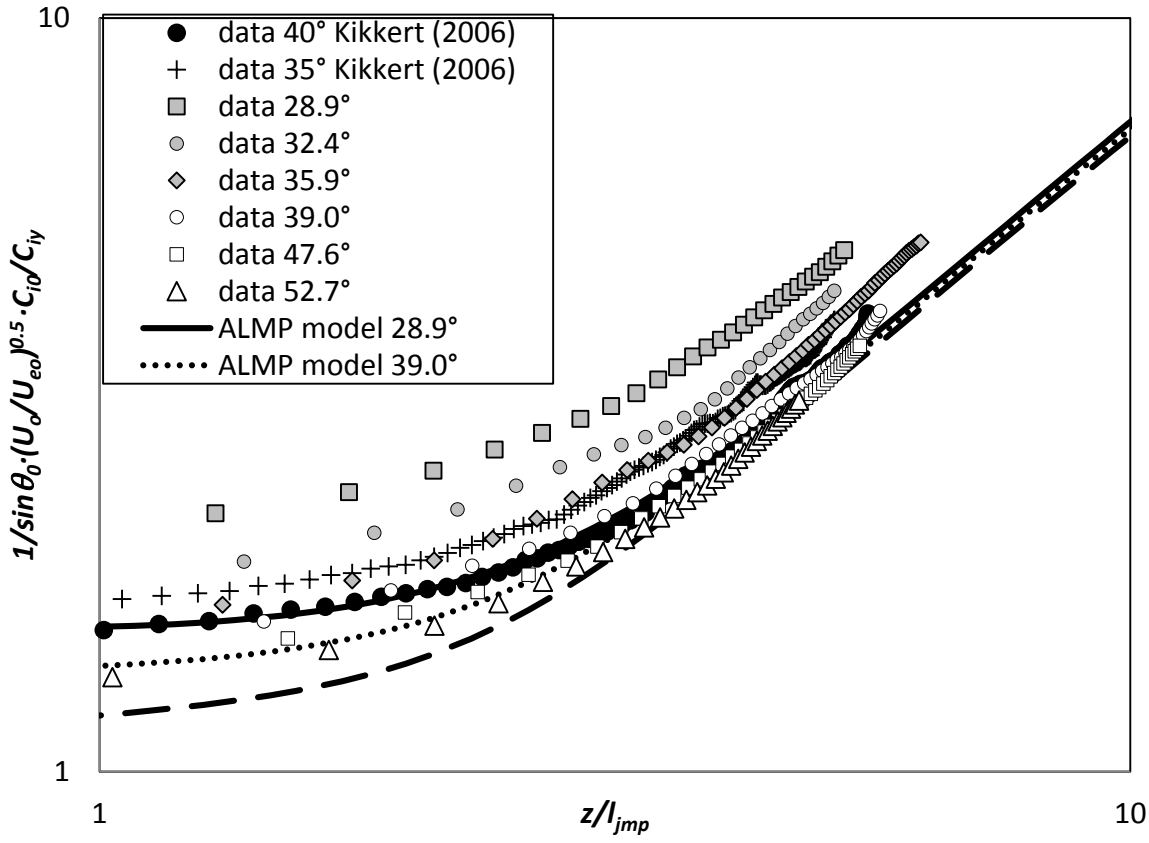

Figure 4-20: *y*-integrated dilution data non-dimensionalised with the puff length scale. Used model is the advected line momentum puff (ALMP) model.

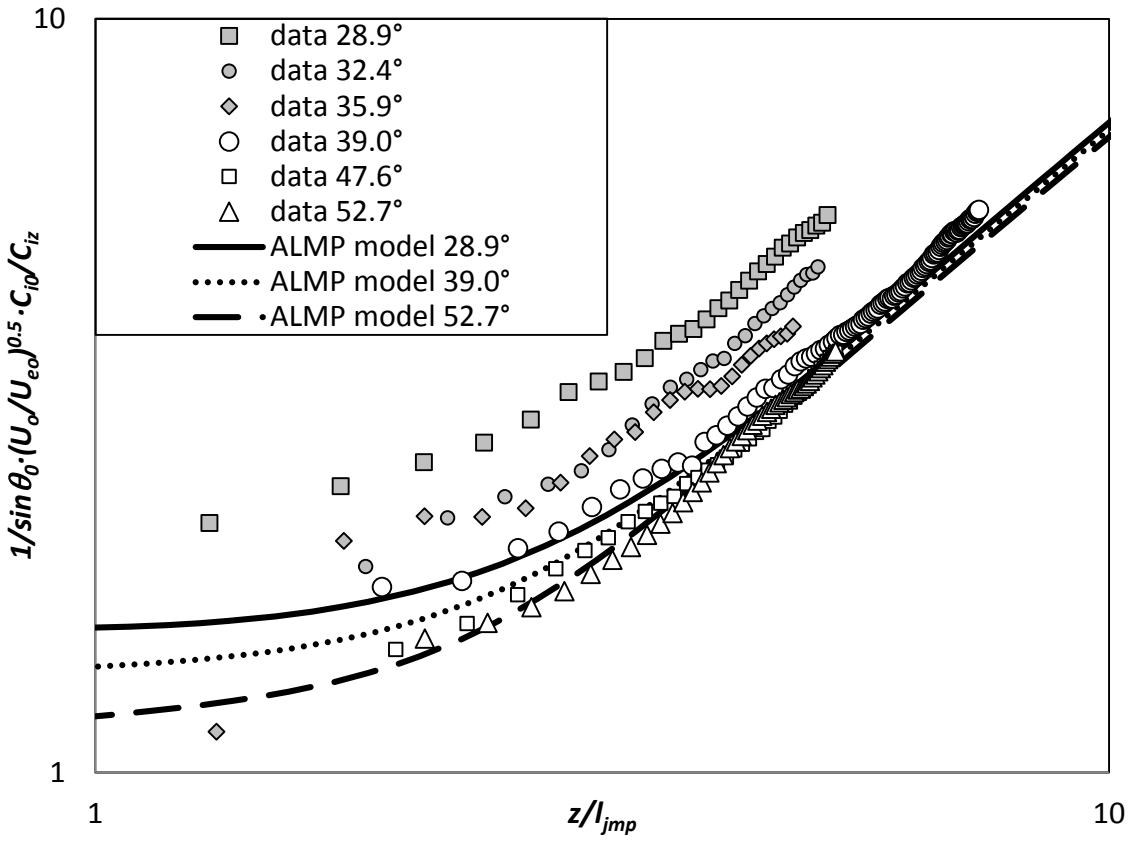

Figure 4-21: *z*-integrated dilution non-dimensionalised with the puff length scale.

4.4.4 Trajectory, spread and dilution results summary

A summary of observations made with regards to the behaviour of the bulk parameters for the oblique discharges investigated here is given in Table 4-7. The division between strongly-advected jet and advected line momentum puff behaviour, in the strongly-advected region of these flow, lies near the discharge angle of 35.9°, or specifically between 32.4° and 39.0°, based on the spread, trajectory and dilution results. The results for the 35.9° discharge are more scattered than other discharge angles and give therefore at times an unclear picture. Some results point to 35.9° discharge being an advected line momentum puff result, that is the trajectory and *y*-integrated spread results. Other results, the *z*-integrated spread and *z*-integrated dilution results, point to this flow acting as a strongly-advected jet. The *y*-integrated dilution results for the initial discharge angle of 35.9° are not consistent with expected strongly-advected jet or advected line momentum puff behaviour. The behaviour of higher angle discharges can be predicted with line momentum puff solutions and for lower angle discharges strongly-advected jet solutions can be employed to predict flow behaviour.

Table 4-7: Summary from observations from the trajectory, spread and dilution data.

Experiments	Inclination Angle (θ_0)	Trajectory	Spread	Dilution
Set 1	28.9°	Consistent with data from previous strongly-advected jet experiments; collapses onto SAJ model predictions; not consistent ALMP predictions	Consistent with data from previous strongly-advected jet experiments; collapses onto SAJ model predictions;	Collapses onto SAJ model predictions;
Set 2	32.4°			
Set 3	35.9°	Data inconsistent with data from previous strongly-advected jet experiments; collapses onto ALMP model predictions	*y*-integrated data collapses onto ALMP predictions. *z*-integrated data is scattered, but appears to collapse onto SAJ model predictions.	*y*-integrated data does not collapse on ALMP or SAJ model predictions. *z*-integrated data is scattered but collapses onto SAJ model predictions.
Set 4	39.0°		Data collapses onto ALMP model predictions	Data collapses onto ALMP model predictions
Set 5	47.6°			
Set 6	52.7°			

4.4.5 Profile Characteristics (f and h parameters)

Two additional parameters have the potential to provide further insight into the form of the cross-sectional profiles as these flows develop. Recalling that the *f* parameter essentially represents the distance from the profile centreline to the peaks of the double-Gaussian distribution, scaled by the width of the individual spreads of the two vortices that make up the distribution. The *h* parameter represents the ratio of the spread of the integrated (along lines parallel to the *y* axis) mean concentration profiles (single-Gaussian) to the spread of the individual Gaussian

components that make up the double-Gaussian profiles evident in the mean concentrations integrated along lines parallel to the *z* axis. The *h* value therefore provides an indication of orthogonal profile distortion.

The figures in this section show values of the f and h parameters for the six datasets as functions of non-dimensional distance from the source. The jet to momentum puff length scale has been used to scale distances from the source, because more significant variations in these parameters are expected as the double vortex forms. Starting with the f parameter, representative values are shown in Figure 4-22, Figure 4-23 and Figure 4-24. Figure 4-22 displays f for all sets. Figure 4-23 shows more detailed data from the 28.9° experiments, including the average. Figure 4-24 presents the f values for the 52.7° experiments, and again includes the average.

It is important to note that the double-Gaussian approximation can also be applied to single peak distributions. For symmetrical double-Gaussian distributions if the *f* value is less than 0.72, then only a single peak is evident. Thus the formation of a symmetrical double peak distribution can be inferred from the *f* values. However, there is some sensitivity of this reference value to changes in profile symmetry. For example, with an asymmetrical profile in which the smaller peak is 80% of the larger peak, and the spread of the smaller peak is 10% smaller than the larger peak, the reference value *f* value for double-peak formation becomes 0.75. As the asymmetry of the profiles increases further, so does this reference value.

Figure 4-22 shows that the *f* values the larger initial discharge angles of 39.0°, 47.6° and 52.7° eventually exceed 0.8 and move towards a value of 0.89, which is the average value measured in the puff region of perpendicular discharges. These changes in *f* values suggesting the formation of a vortex pair as the flow becomes strongly-advected. Interestingly the location of the transition varies significantly with initial discharge angle. The transition at 52.7° occurs at approximately 3 length scales from the source, whereas the transitions at 39.0 and 47.6° occur after a distance of 4 lengths scales from the source. The values of *f* extracted from discharges at shallow angles (28.9° ,32.4° and 35.9°) do show some increase as the flows evolve but tend to remain constant at approximately 0.7, which is consistent with the continued existence of single peaked distributions and the formation of strongly-advected jets.

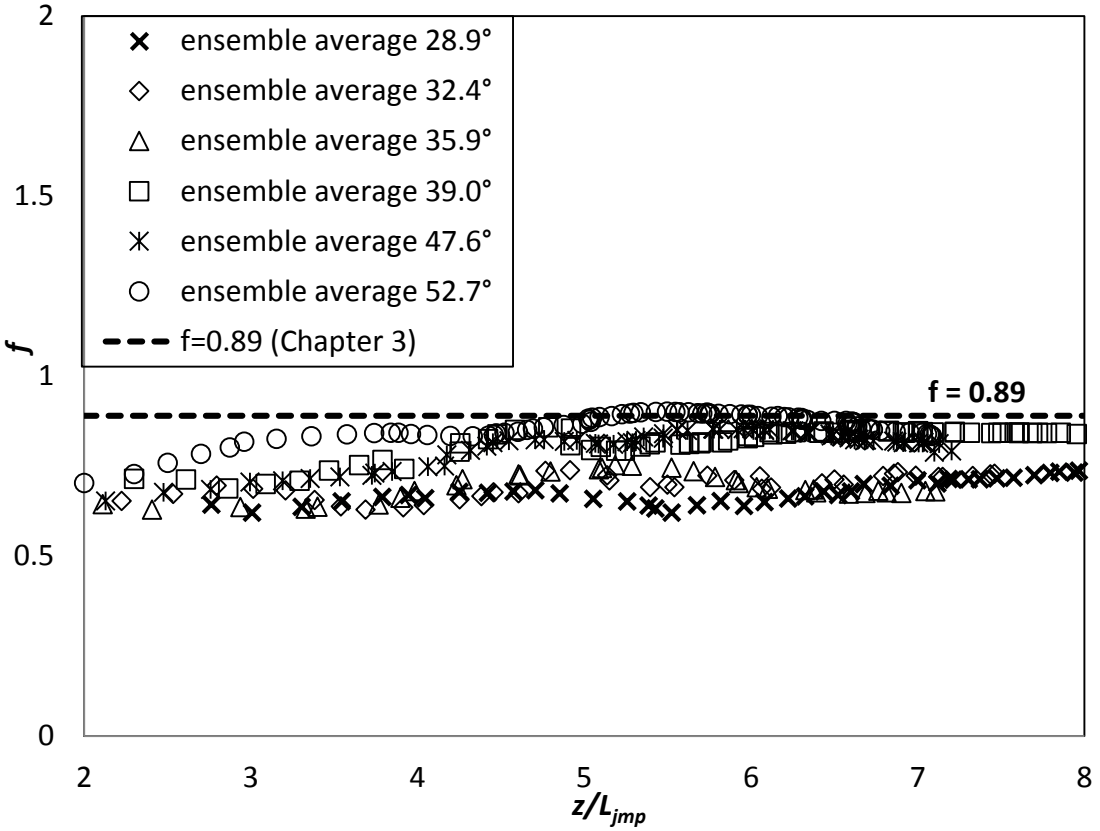

Figure 4-22: The evolution of *f* values with distance from the source for all initial discharge angles investigated. Data presented are ensemble averages from multiple experiments non-dimensionalised with the puff length scale.

In Figure 4-23, all of the f values from the experiments with an initial angle of 28.9° are shown, along with the averaged values presented in Figure 4-22. There is significant scatter in this data, which is expected given the relatively short averaging times for each experiment, but the data rests between 0.62 and 0.74 indicating that double peak distributions are unlikely, even with asymmetries present in the profiles. Similar data is presented for the 52.7° initial discharge angle experiments in Figure 4-24, where the data generally falls between 0.84 and 0.90 indicating that a double vortex is likely to exist at all points. The overall variability of the data appears to have reduced at this larger discharge angle.

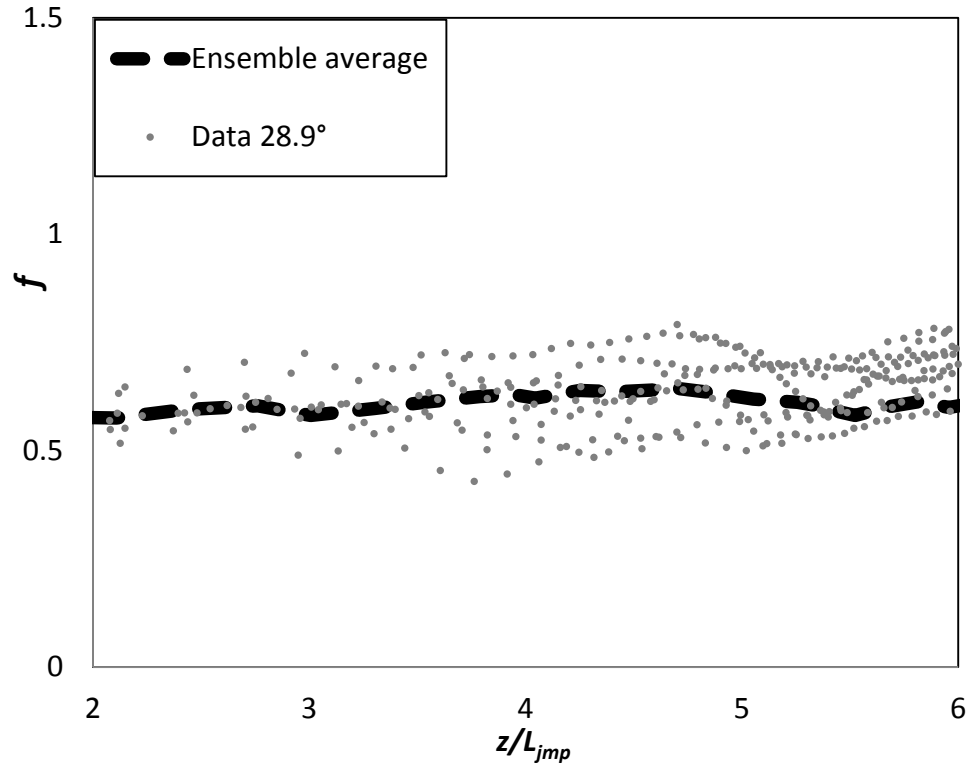

Figure 4-23: *f* values for the 28.9° discharges, with the average values also shown.

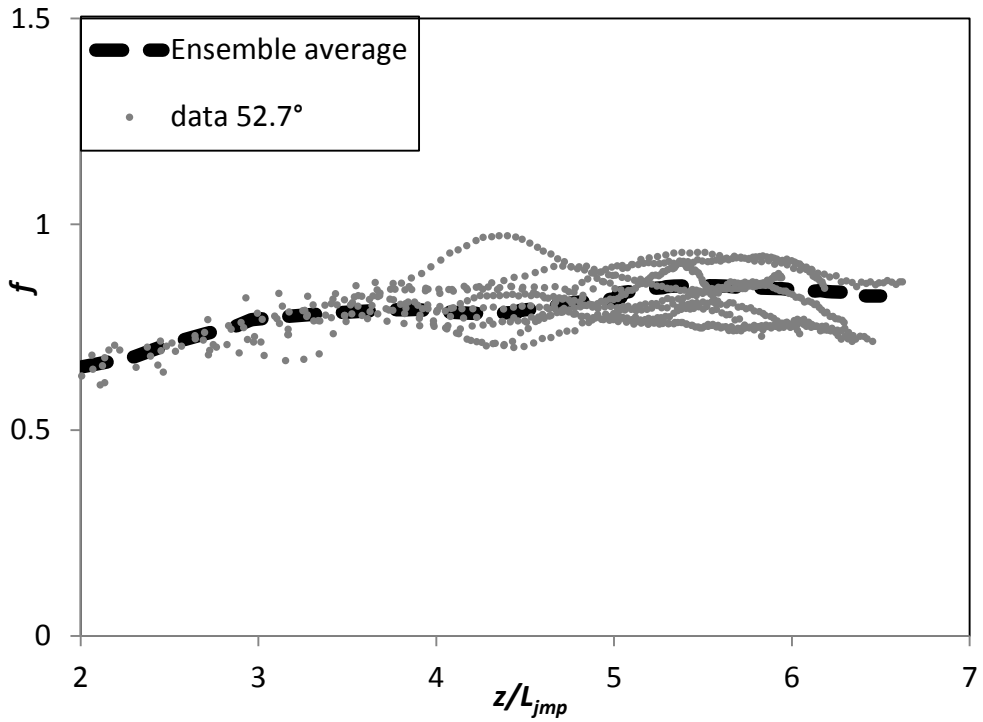

Figure 4-24: *f* values for the 52.7° discharges, with the average values also shown.

Variations in the *h* parameter with distance from the source for the six initial discharge configurations are shown in Figure 4 25. Here the ensemble averages of this parameter for each of the initial discharge angles are presented. In Figure 4 25 the ensemble average and data from all individual experiments of the 52.7° discharge flow are shown. The data shows some scatter around the value of 1.46.

Where previously the *z*-integrated profiles had been fitted with a double-Gaussian, and the *y*-integrated profile with a single-Gaussian profile, for the following figures the *z*-integrated data from all experiments has also been fitted with a single-Gaussian profile. The ratios of the *y*-integrated and *z*-integrated concentration spreads for all experiments have been calculated and are shown in Figure 4-27. If the flow is axisymmetric a value of 1 will result, however if the flow is vortex shaped the value will tend towards a lower value (*h/2* for symmetrical distributions). Figure 4-28 shows the data from individual experiments that make up the ensemble average (along with this average) for the 28.9° set of experiments.

In Figure 4-25, there is no clear distinction between the parameter values for the different discharge angles. This is initially surprising given that the single-Gaussian discharges at shallower angles (28.9° and 32.4°) are not expected to suffer significant distortion. The *h* value for the 52.7° set is relatively low with an end value of 1.40, while the 47.6°, 39.0°, 35.4°, 32.4° are higher with a value of approximately 1.46 which is consistent with chapter 3 and Kikkert (2006), the 28.9° set lies below the 1.46 line at approximately 1.35. In Figure 4-27, the 28.9° discharge is shown to be almost axisymmetric. The ratio of the 39.0° and more obtuse discharge angles collapse on an approximate value of 0.69. The 32.4° and 35.9° discharge angles can be seen to lie in-between. This indicates that these two acute angles 32.4° and 35.9° are more elongated than the 28.9° discharge but not quite as wide in the horizontal as the more obtuse discharge angles. In Figure 4-28 the ratios of the widths of the fitted single-Gaussian profiles of the horizontally and vertically integrated concentration data are depicted for the 28.9° discharge angle. There is some scatter visible but all data lies around the 1.0 value while none of the data goes as low as 0.69. Similar variability about the average *h* value for a line momentum puff can be seen in Figure 4-28, where the individual realisations are presented along with the average value. As noted above this average value is approximately 4% less than that expected based on results from chapter 3, however, the reasons for this reduced value are not clear.

In fitting a generic double-Gaussian distribution to a single-Gaussian flow, the result can be that the best fitting two Gaussian profiles are placed with their maxima at the same or virtually the

same location. This would result in wrong spread values that then result in an inappropriate *h* value. Calculation of the *h* value is therefore not a good method to establish whether a flow has a double- or single-Gaussian concentration distribution. Rather, with the assumption that a flow is double-Gaussian, it describes the elongation of the separate vortices.

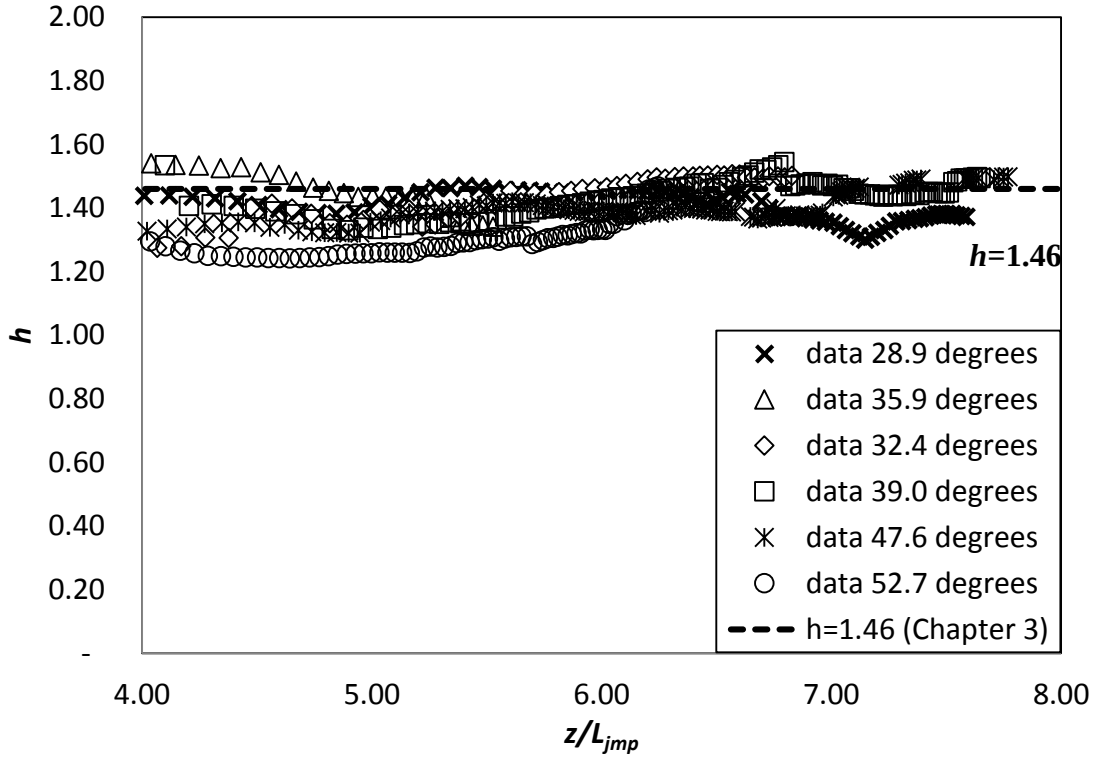

Figure 4-25: The evolution of *h* values with distance from the source for all initial discharge angles. Data presented are ensemble averages from multiple experiments.

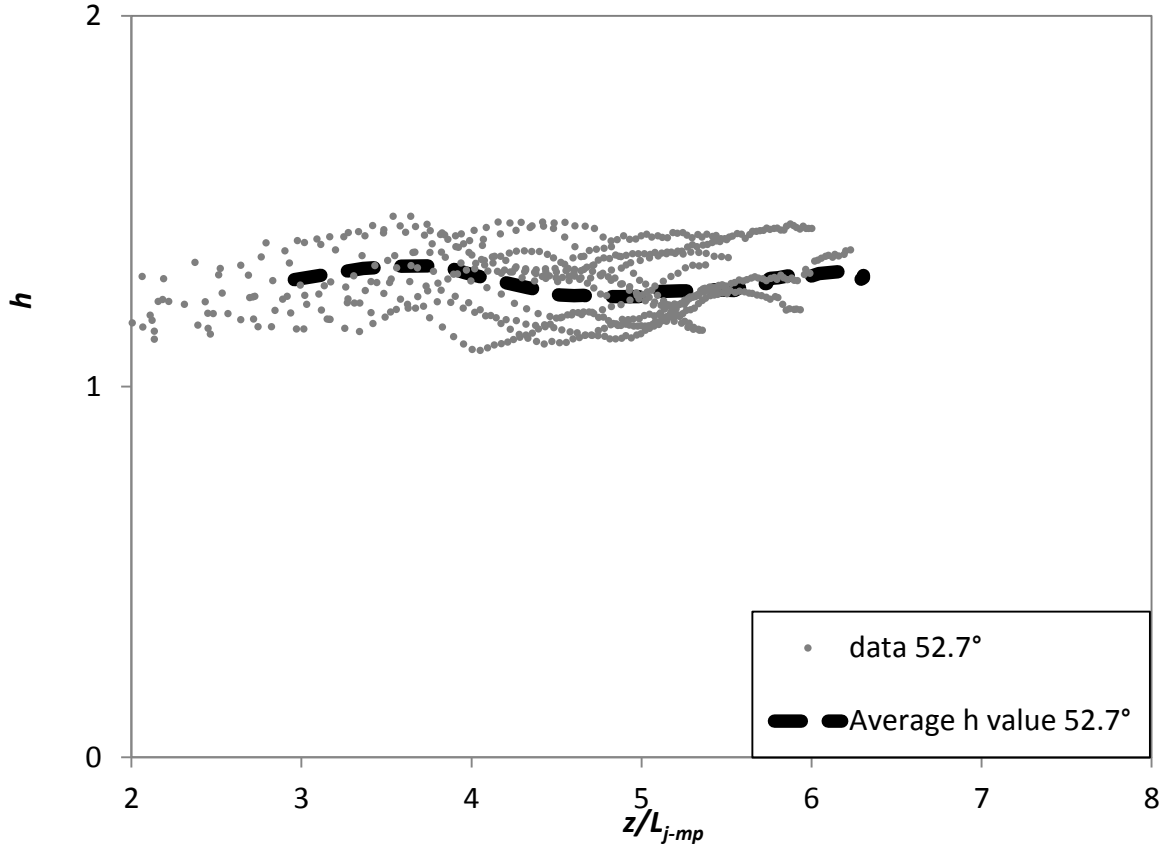

Figure 4-26: The evolution of the *h* value for 52.7° discharge plus average *h* value for 52.7°.

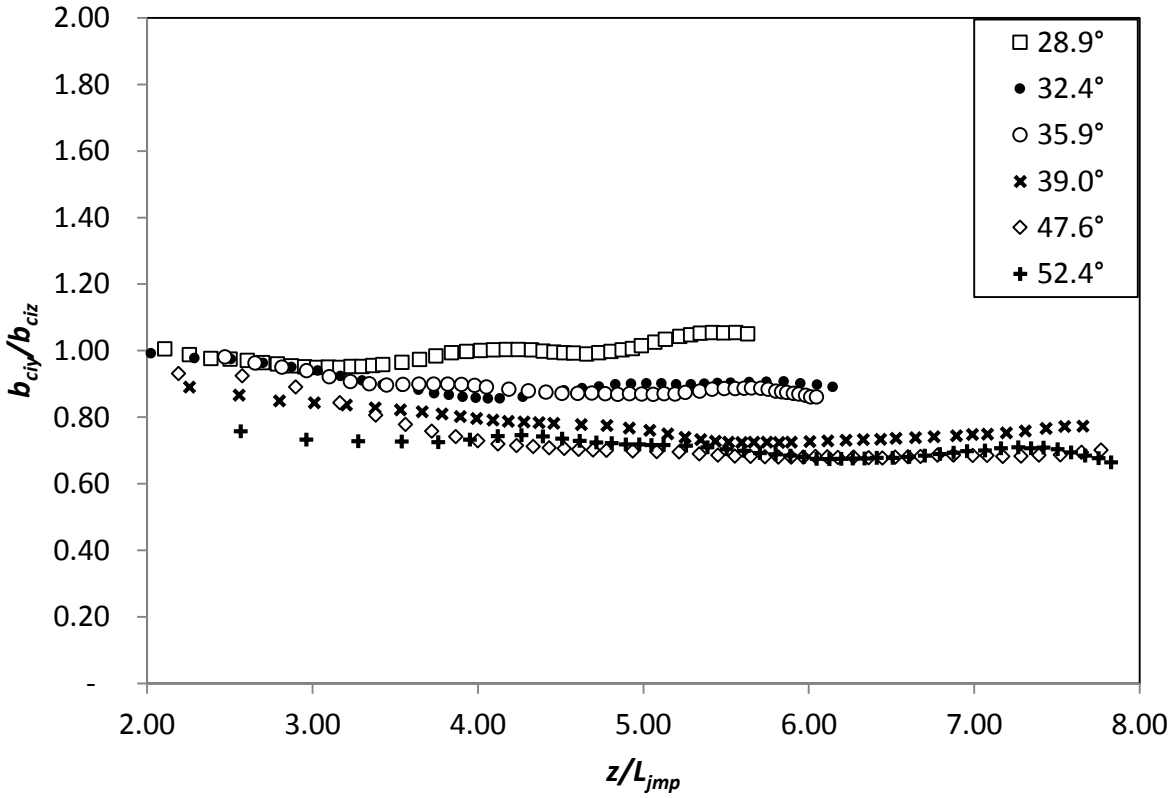

Figure 4-27: The evolution of the average ratios of the widths of the horizontally and vertically integrated concentration profiles. Widths are based on single-Gaussian widths.

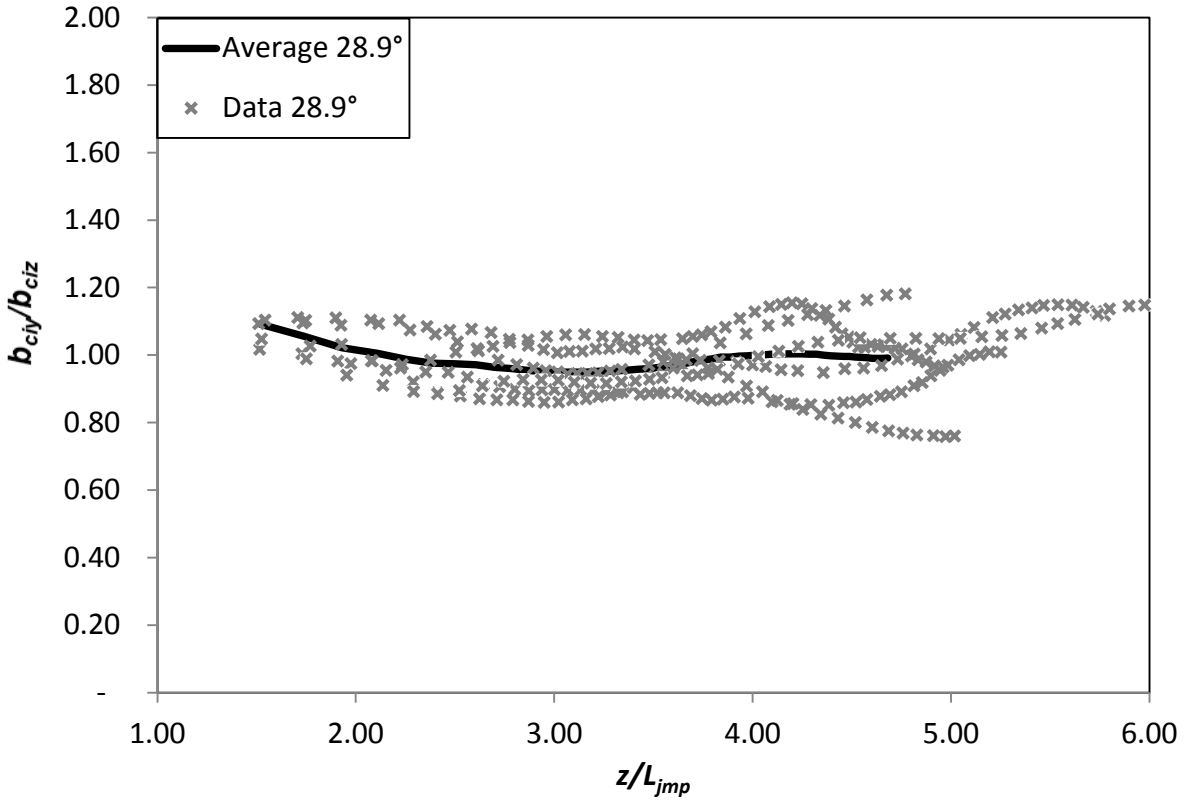

Figure 4-28: Evolution of b_{ciy}/b_{ciz} for the 28.9° discharges. The average ratio is included.

In Table 4-8 a summary of observations made with regards to the profile and shape factors for the oblique discharges investigated is given. The division between strongly-advected jet and advected line momentum puff behaviour, in the strongly-advected region of these flow, lies again near the discharge angle of 35.9° (section 4.4.4). The two most obtuse sets (47.6° and 52.7° are seen to have the traits of a double-Gaussian distribution. The concentration profiles show a double peak and the *f* value is 0.89 as expected based on chapter 3 and Kikkert (2006). Fitting these flows with single-Gaussian distributions for both directions shows that the vertically integrated profile is more elongated, as expected with a double vortex structure. The *h* values finally are 1.40-1.49 which is consistent with the 1.46 as found for double peak distributions in chapter 3. In contrast the 28.9° discharge shows no indication of a double peak profile and has been shown to be axisymmetric. In between lie the 32.4°, the 35.9° and the 39.0° discharges. The 39.0° discharge conforms almost to the more obtuse angles, the difference here is small and as both the *h* and *f* parameters are as expected it stands to reason that this discharge transforms into a momentum puff. The remaining two discharges both have no double peak profile, and lower *f* values. The ratio of concentration spreads indicates an elongation in the horizontal plane but not to such an extent that a fully formed momentum puff can be found. On the other hand the flows are not axisymmetric and hence can be classified as transitional flows.

Table 4-8: Summary of results on profile and shape factors.

<table>
<tr><th>Exp.</th><th>Discharge Angle (θ_0)</th><th>Cross-sectional profile</th><th>f value</th><th>C_{iy}/C_{iz}</th><th>h value</th></tr>
<tr><td>Set 1</td><td>28.9°</td><td rowspan="3">No sustained development of a double peak profile.</td><td rowspan="2">f values lower than larger angles</td><td>Single-Gaussian width ratios are close to 1.</td><td rowspan="3">Double-Gaussian h values are not relevant as there is no (sustained) double peak present.
Double-Gaussian h values are not relevant as there is no (sustained) double peak present.</td></tr>
<tr><td>Set 2</td><td>32.4°</td><td rowspan="3">Single-Gaussian widths ratios are lower than 1, but do not collapse on the more obtuse angles.</td></tr>
<tr><td>Set 3</td><td>35.9°</td></tr>
<tr><td>Set 4</td><td>39.0°</td><td rowspan="3">f values close to the perpendicular f value of 0.89</td></tr>
<tr><td>Set 5</td><td>47.6°</td><td rowspan="2">Double peak profile.</td><td rowspan="2">Single-Gaussian width ratios collapse and are approximately 0.69.</td><td>h value ends at approximately 1.49</td></tr>
<tr><td>Set 6</td><td>52.7°</td><td>h value somewhat lower than expected, ending around 1.40</td></tr>
</table>

4.4.6 Detailed Profile

In this section the integrated profiles for different initial discharge angles are presented and discussed in more detail. Three representative discharge angles are selected, the most acute, the most obtuse and the intermediate discharge angle of 35.9°. Figure 4-29 shows values of the *f* parameter of three experiments with an initial discharge angle of 28.9°. The displayed information is a selection of individual experiments. The three runs have been selected as they produced the most extreme f values during the flow evolution. The ensemble average for all 28.9° experiments is also shown for reference. The vertical dotted lines represent the locations where concentration profiles (integrated along lines parallel to the *z* axis) have been extracted and these profiles are presented in Figures 4-30, 4-31 and 4-32.

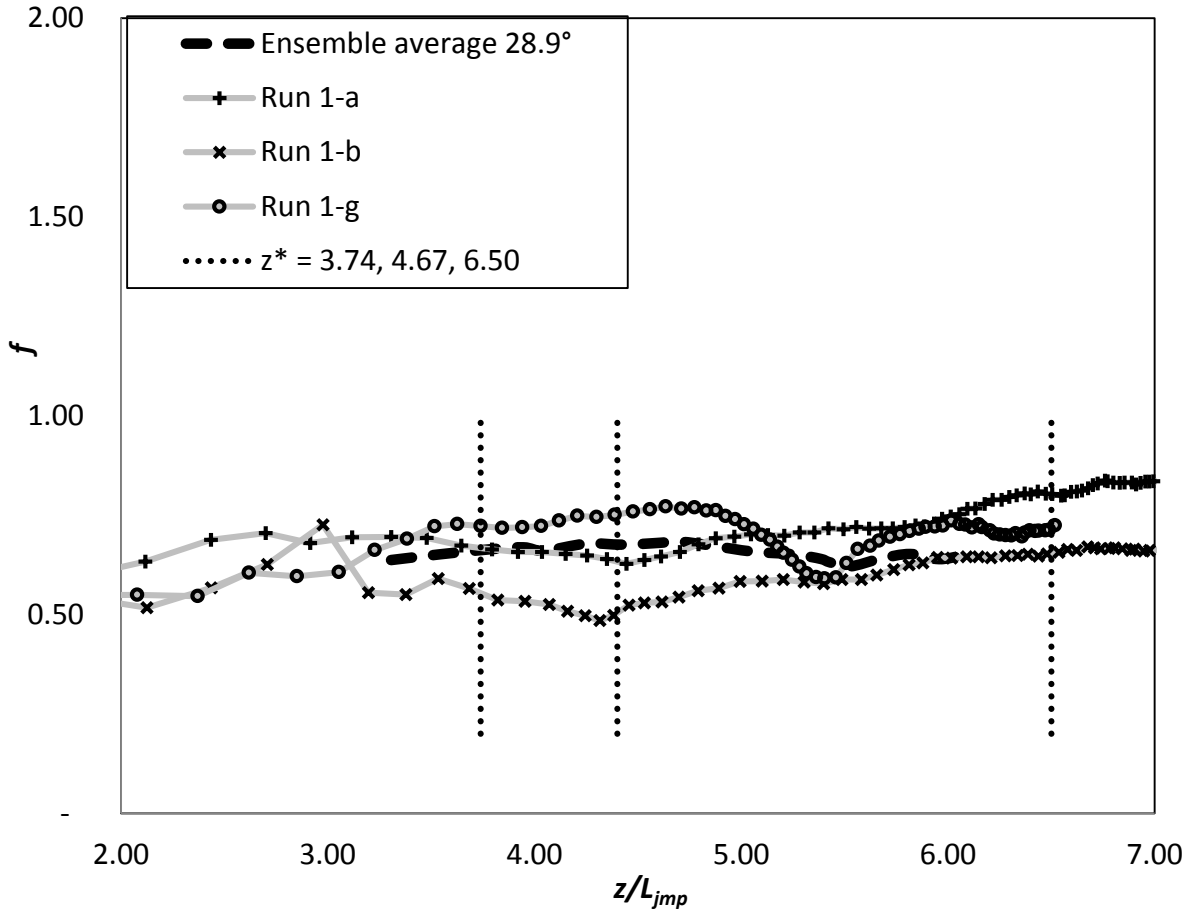

Figure 4-29: *f* values for the 28.9° discharge angle for three experiments along with the ensemble average of all experiments at this discharge angle. The dotted lines show the distances at which the cross-sectional profiles have been extracted and presented in Figure 4-30, Figure 4-31, and Figure 4-32.

Figure 4-30 shows three profiles extracted from a single experiment (Run 1a), where the *f* values for the profiles are seen generally increasing, reaching a value of 0.80 at the 3rd reference location, z^* ($=z/l_{jmp}$) = 6.50. However, there is no evidence of a double peak forming in the experimental data. Another example of an individual experiment at this initial discharge angle is shown in Figure 4-31 (Run 1-g). Here the *f* values remain reasonably constant at all three locations, respectively 0.72, 0.77, and 0.71 and again there is no evidence of the formation of a double peak distribution in the data or the profile approximating the data. The third example from an individual experiment (Run 1b) making up the ensemble values is shown in Figure 4-32. This run has the lowest values of the *f* parameter of all the 28.9° initial discharge angle experiments, with values of 0.54, 0.51, and 0.61 at the three reference locations. Interestingly the last profile, z^*=6.50 shows some evidence of a double peak form, although the profile is asymmetric. These

profiles provide some indication of the degree of variability of the integrated mean concentration profiles as the flows evolve and although this variability can be removed to a large extent through ensemble averages, it is an important feature of these flows. However, it is also evident from these profiles that in general the profiles have a single-Gaussian form, which is consistent with earlier observations associated with the evolution of the bulk parameters for these flows.

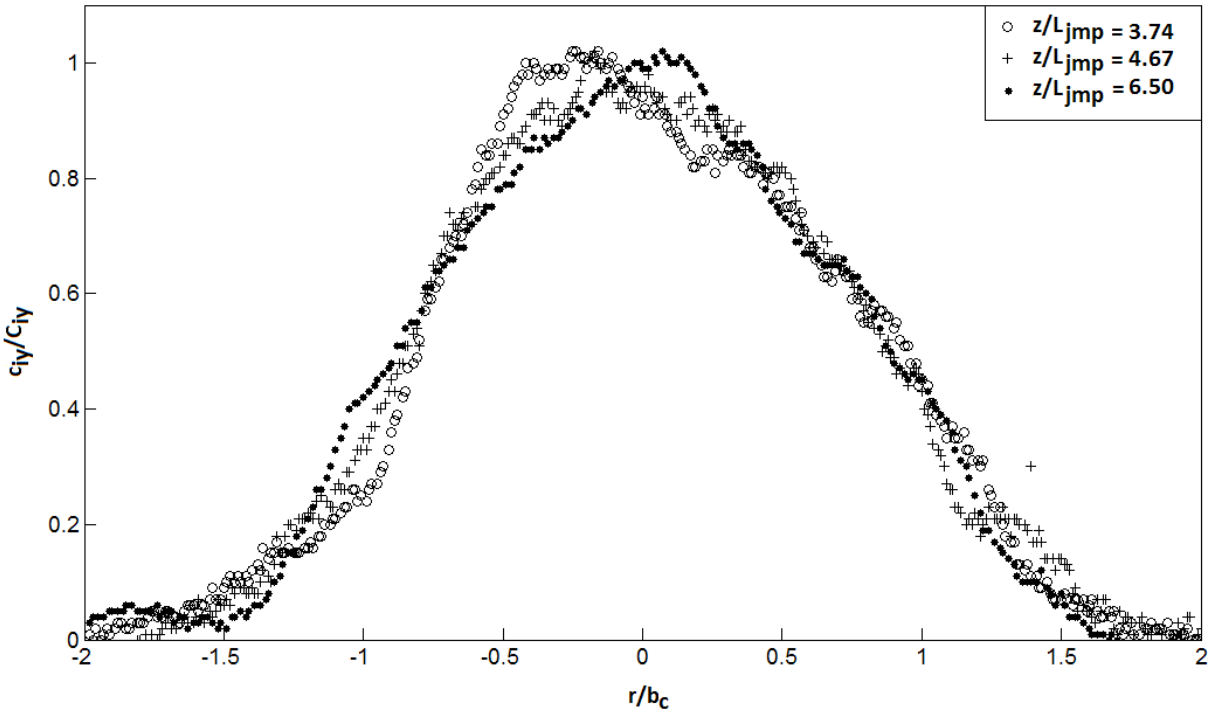

Figure 4-30: Run 1-a cross-sectional profiles at 3 non-dimensional distances from the 28.9° discharge angle, respective *f* values are 0.65, 0.64, and 0.80.

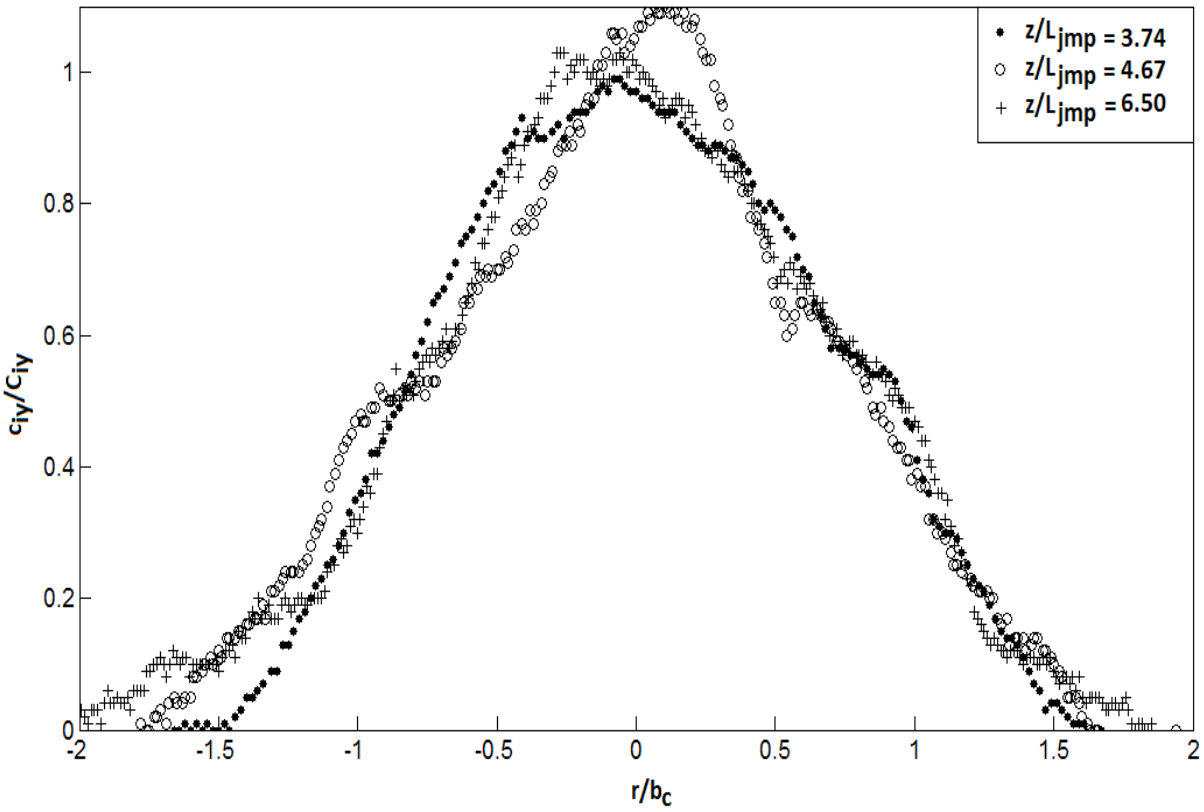

Figure 4-31: Run 1-g cross-sectional profiles at 3 non-dimensional distances from the 28.9° discharge angle, respective *f* values are 0.72, 0.77, and 0.71.

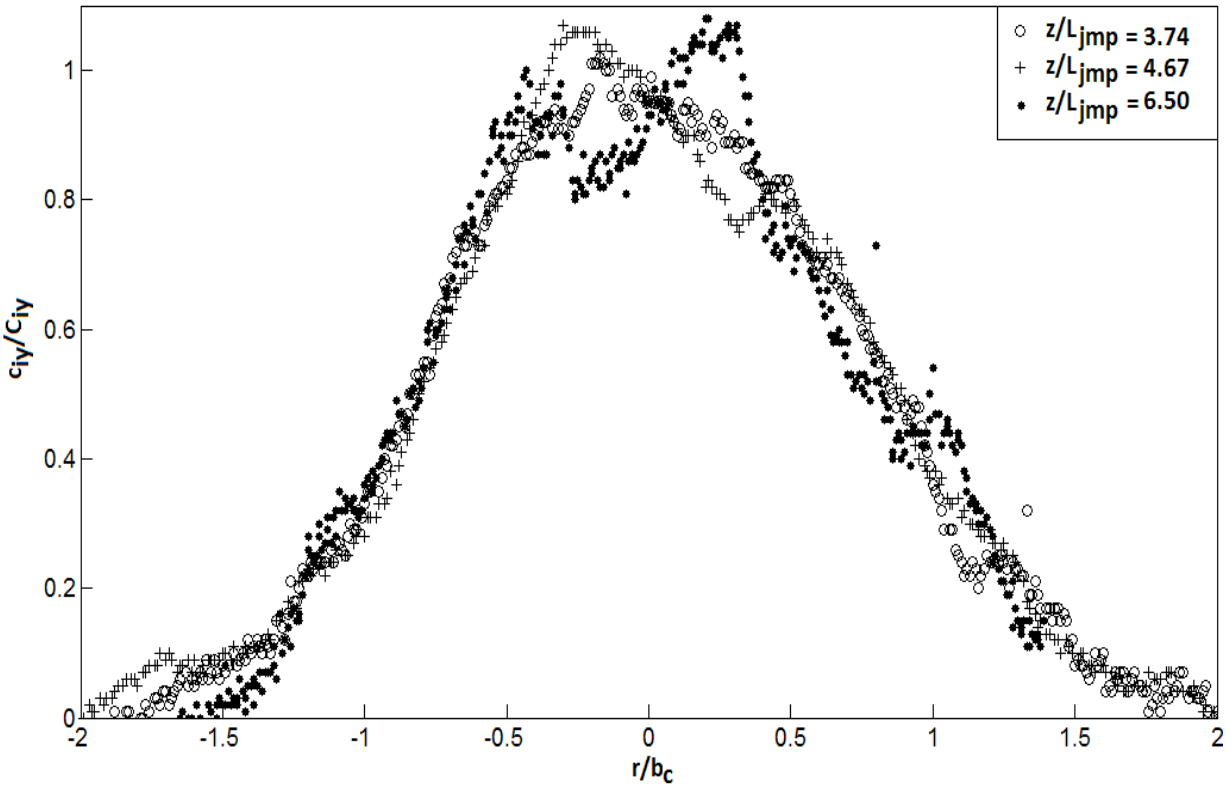

Figure 4-32: Run 1-b cross-sectional profiles at 3 non-dimensional distances from the 28.9° discharge angle, respective *f* values are 0.54, 0.51, and 0.61.

In Figure 4-33 values of the *f* parameter from a selection of experiments for the largest initial discharge angle considered are shown, that is, 52.7°. The ensemble average of all experiments is also shown for reference. As with the most acute discharge angle, the selected experiments demonstrate the most extreme values of this parameter. Mean concentration profiles (integrated along line parallel to the *z* axis) have been extracted at three locations from the source, which represent these extremes and these are indicated with the dotted lines. These cross-sectional profiles are presented in Figure 4-34, Figure 4-35, and Figure 4-36. Figure 4-34 shows experiment Run 6-d, the fourth experiment of set 6. The *f* values from this run are 0.87, 0.75 and 0.85 at source distances, z^* of respectively 3.1, 4.4 and 5.2. The experimental data shows a double peak at all three distances. In Figure 4-35 the experiment Run 6-g is shown. Run 6-g seems to have fairly constant *f* values at the three distances, respectively values 0.79, 0.80, 0.84. The experimental data shows a double peak at all three distances, albeit that at the middle distance the trough is less pronounced. The third figure (Run 6-l) shows *f* values of 0.71, 1.01, and 0.86. Here the cross-sectional profiles are more asymmetric with significant variations in the peak values on one side of the flow.

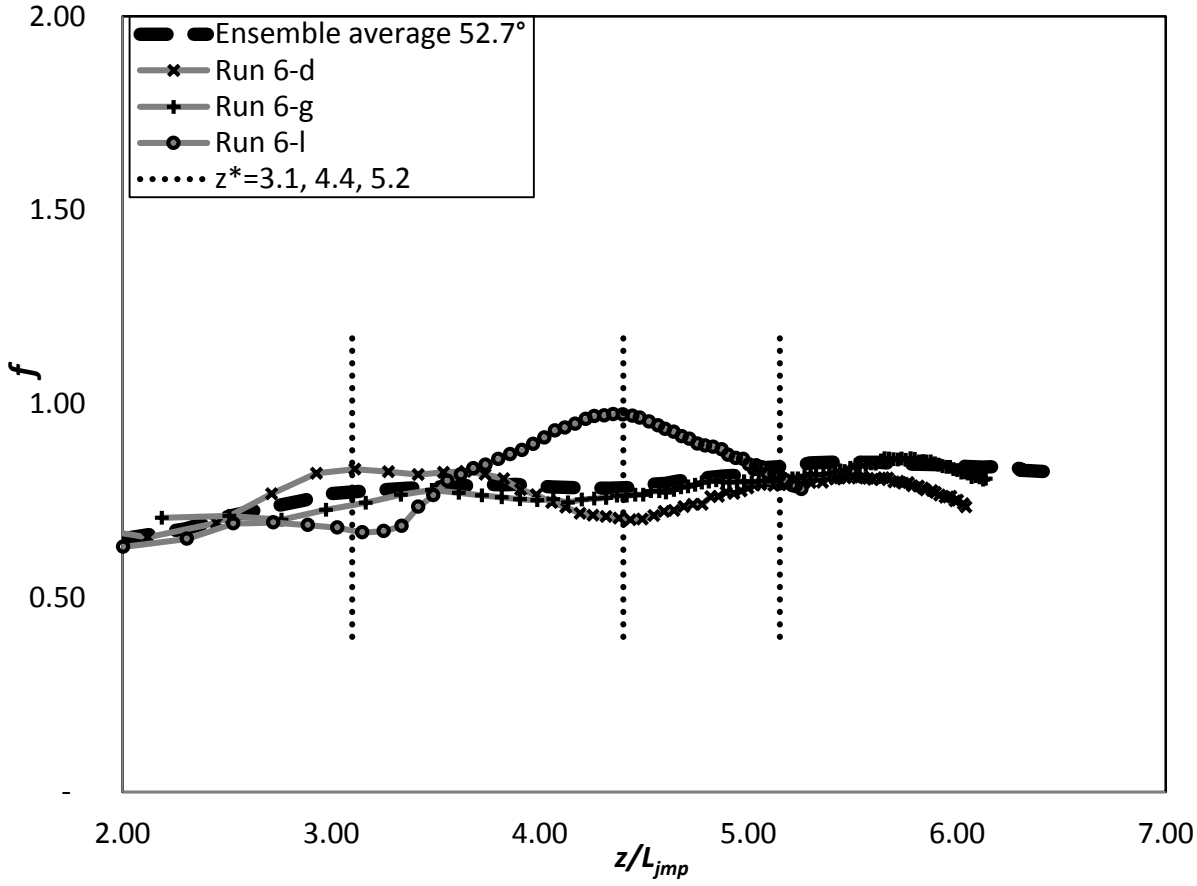

Figure 4-33: *f* values for the 52.7° discharge angle for three experiments along with the ensemble average of all experiments at this discharge angle. The dotted lines show the distances at which the cross-sectional profiles have been extracted and presented in Figure 4-34, Figure 4-35, and Figure 4-36.

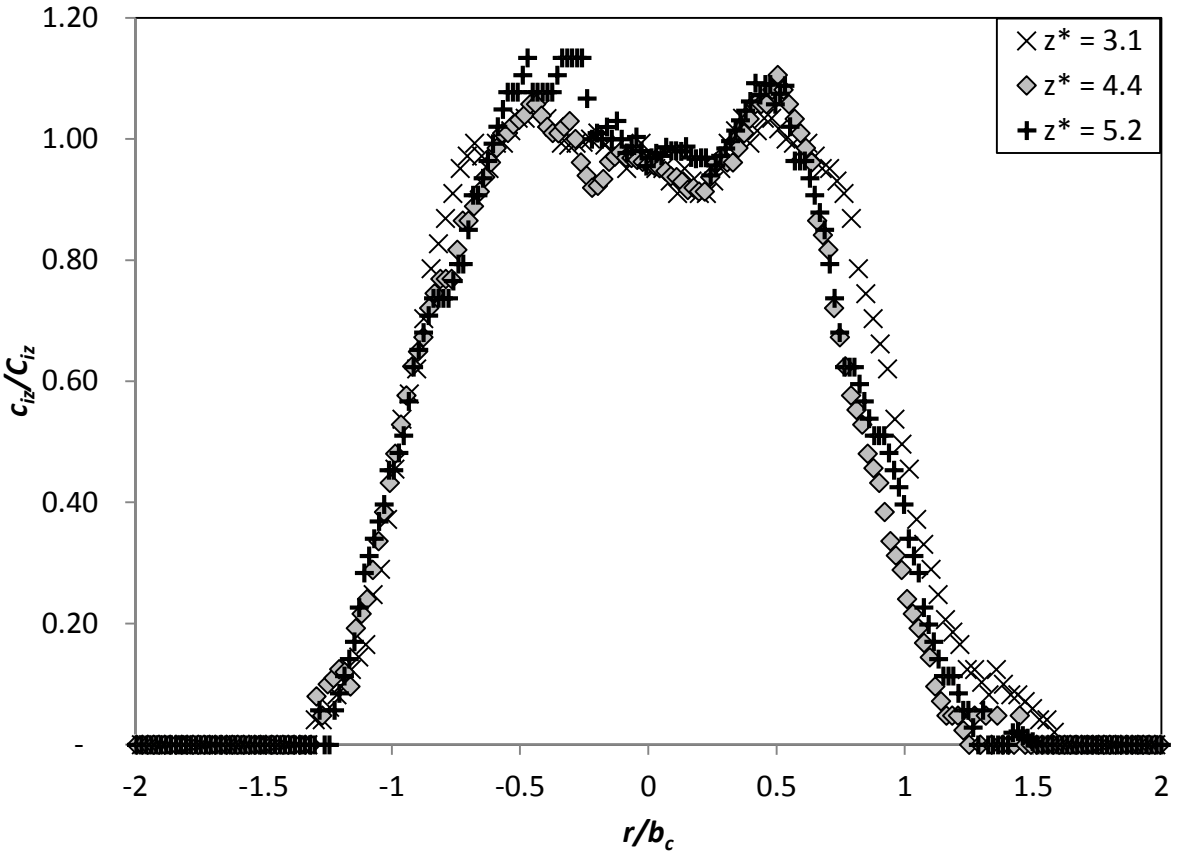

Figure 4-34: Run 6-d cross profiles at 3 distances, left the experimental data, right the best fit double-Gaussian distribution, *f* values 0.87, 0.75, 0.85.

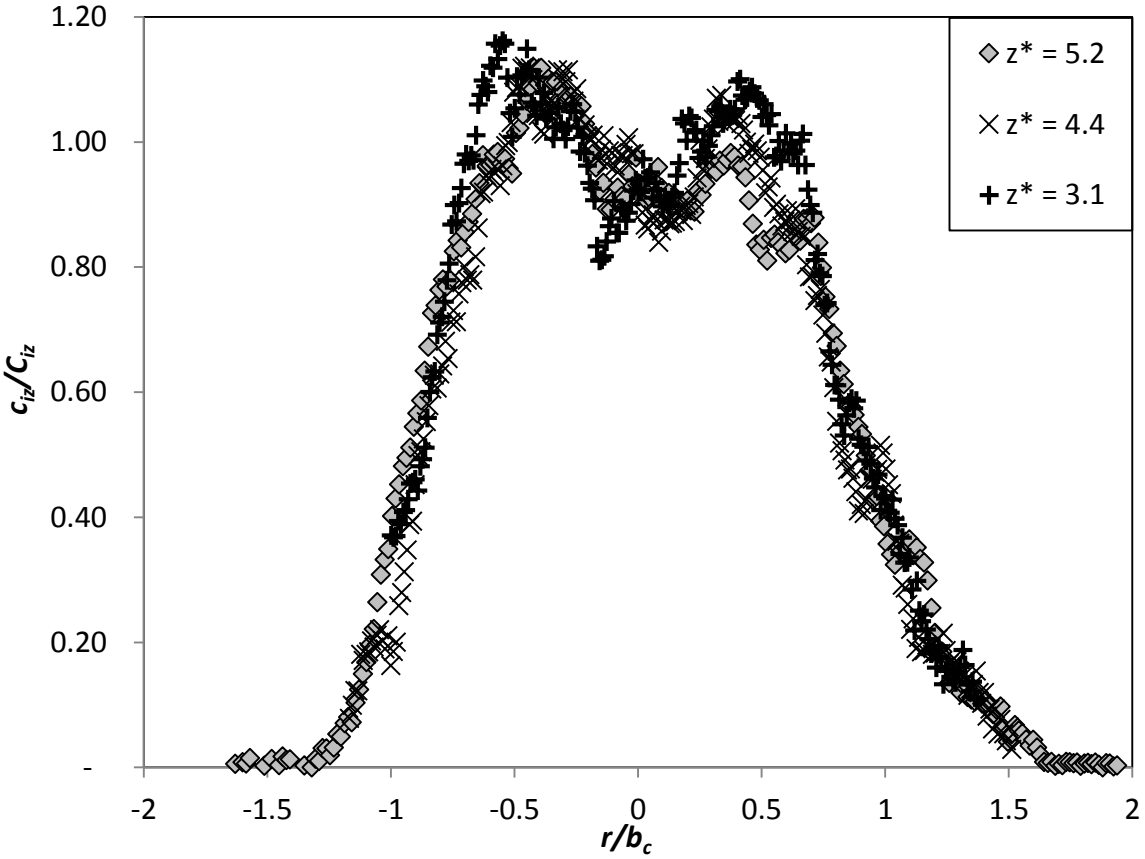

Figure 4-35: Run 6-g cross profiles at 3 distances, left the experimental data, right the best fit double-Gaussian distribution, *f* values 0.79, 0.80, 0.84.

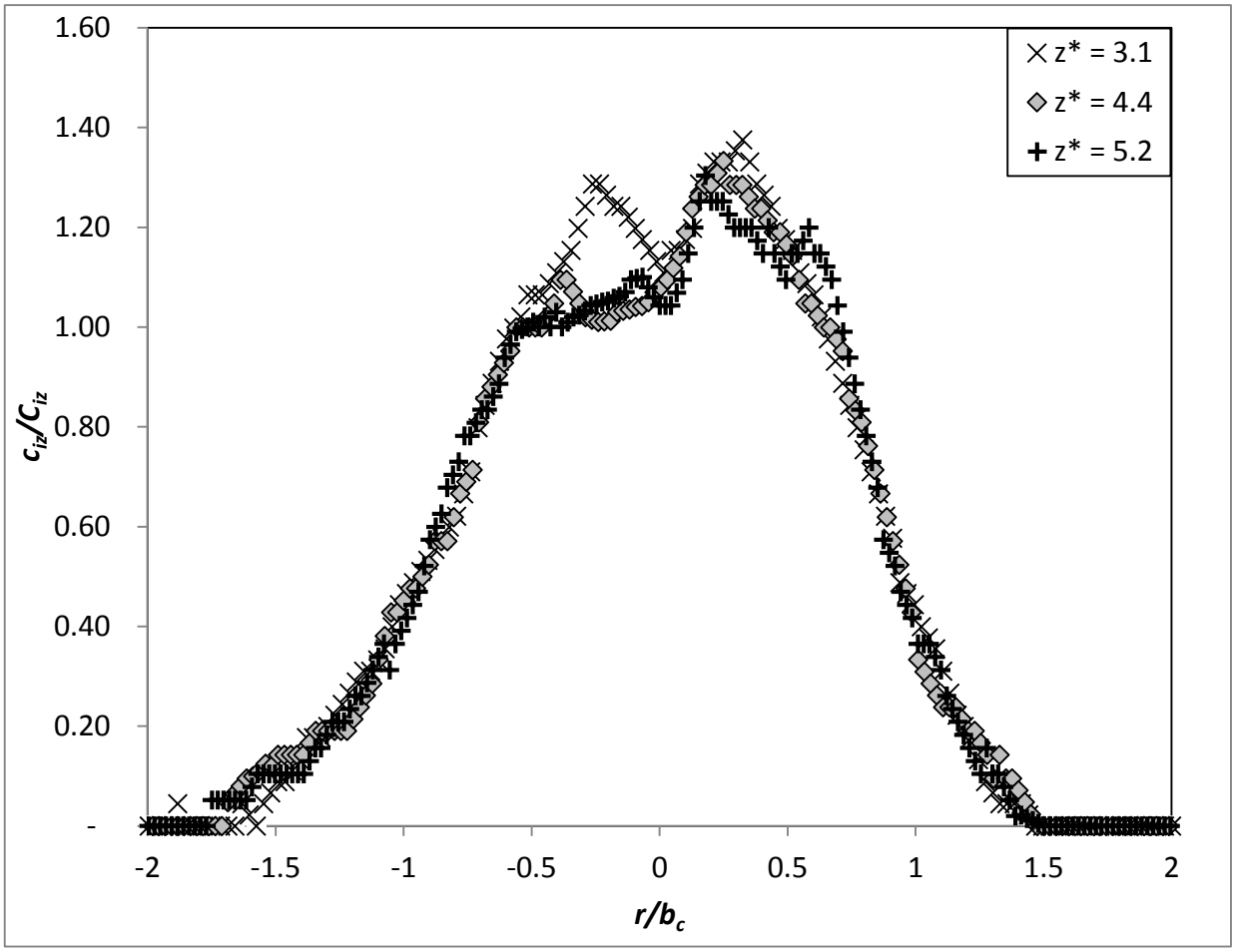

Figure 4-36: Run 6-l cross profiles at 3 distances, left the experimental data, right the best fit double-Gaussian distribution, *f* values 0.71, 1.01, 0.86.

The 35.9° initial discharge angle represents the intermediate angle for the present investigation. Based on the summary in section 4.4.4 and Table 4-8, the trajectory, dilution and spread results along with the profile and shape factors, suggest this angle displays characteristics of both momentum puff and strongly-advected jets. Figure 4-37 shows a selection of experiments that demonstrate the range of *f* values measured for this discharge angle and integrated concentration cross-sectional profiles have been extracted at three different locations (indicated with the dotted lines). These cross-sectional profiles are presented in Figure 4-38, Figure 4-39, and Figure 4-40.

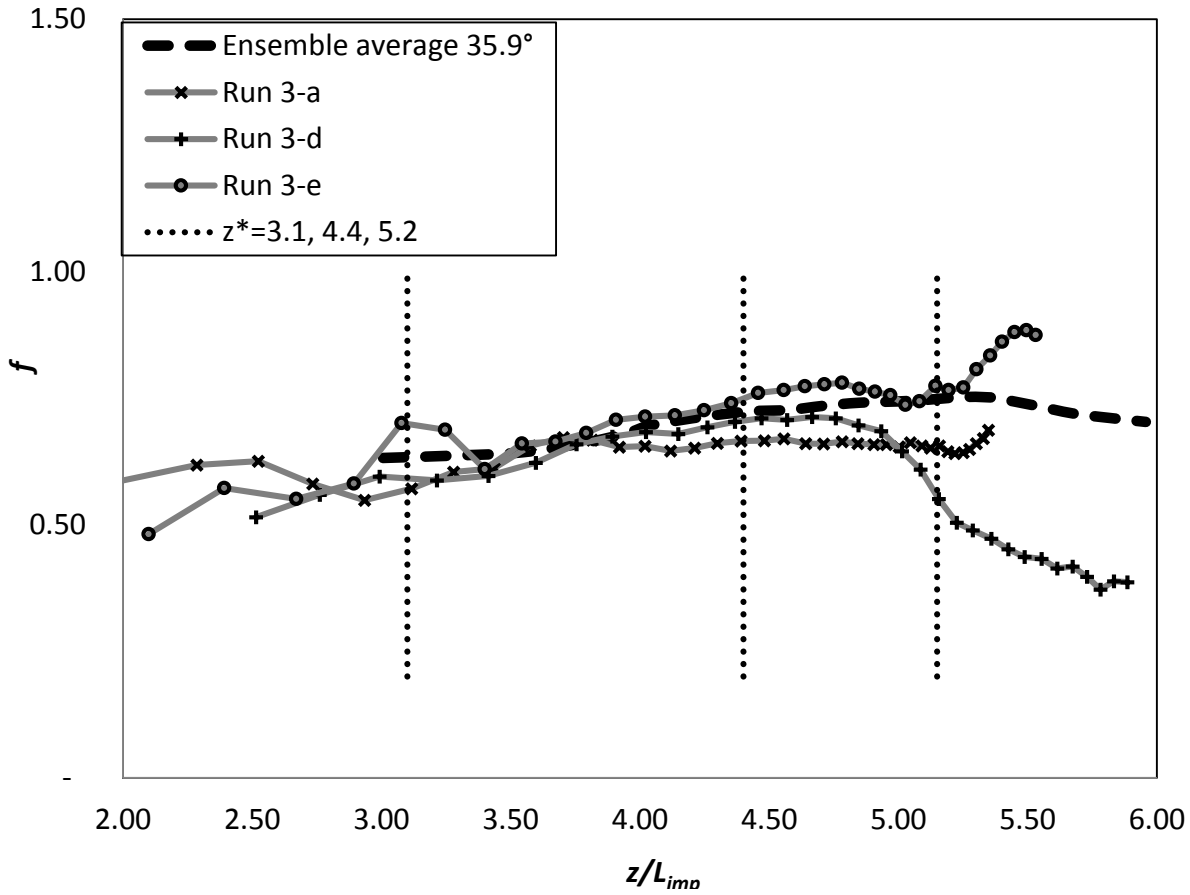

Figure 4-37: *f* values for the 35.9° discharge angle for three experiments along with the ensemble average of all experiments at this discharge angle. The dotted lines show the distances at which the cross-sectional profiles have been extracted and presented Figure 4-38, Figure 4-39, and Figure 4-40.

Figure 4-38 shows profiles with *f* values of 0.59, 0.66, 0.66 at non-dimensional distances from the source, *z**, of respectively 3.1, 4.4, and 5.2. While the derived parameters, particularly the low *f* values, do not indicate the presence of a double peak, the measured profiles show there is some evidence of a double peak. However, the twin peaks are very close together and it is unlikely that a double vortex, typical of a line momentum puff, has formed.

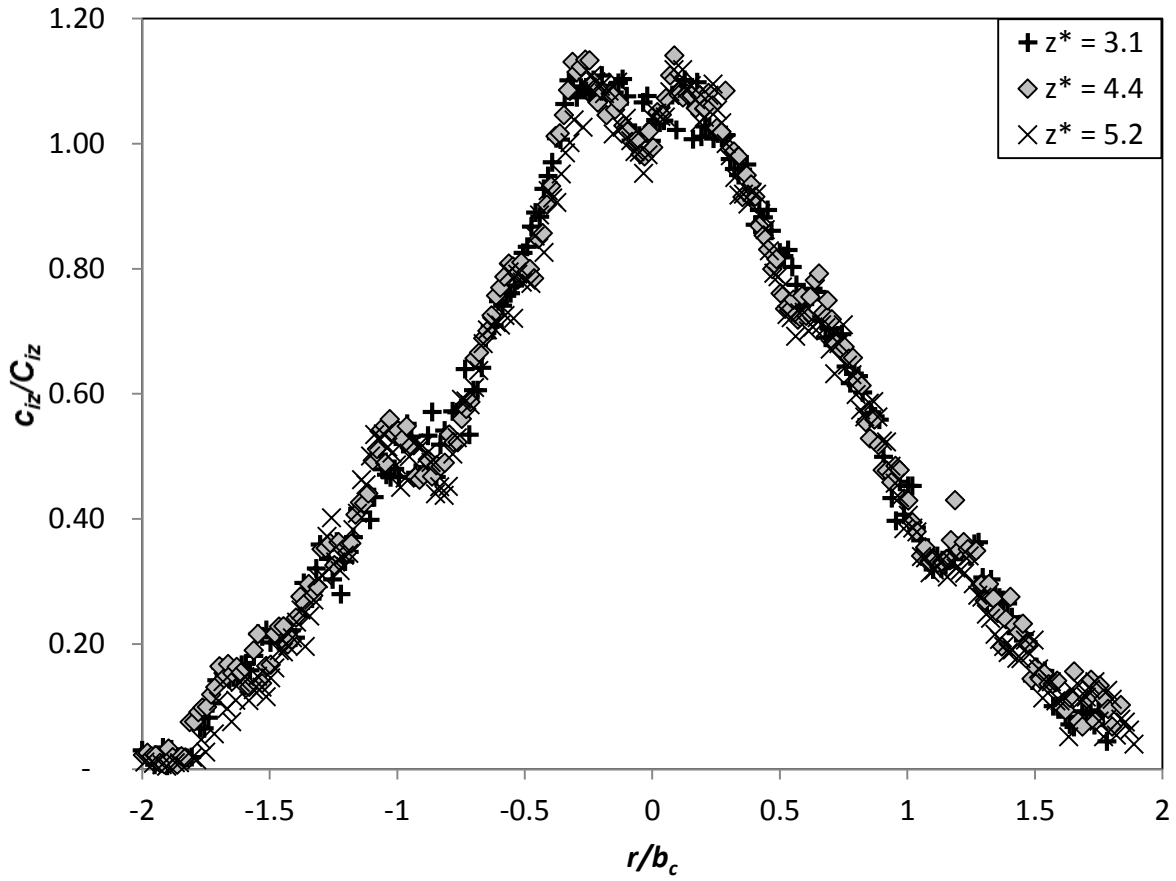

Figure 4-38: Run 3-a cross profiles at 3 distances, left the experimental data, right the best fit double-Gaussian distribution, *f* values 0.59, 0.66, 0.66.

In contrast, in Figure 4-39 where the *f* values range from 0.60 to 0.74 to 0.55, the experimental data shows a more distinct double peak form at all three distances, but there is significant asymmetry in these profiles with one peak being substantially smaller than the other. Figure 4-41, shows data from another experiment (Run 3-e), where the *f* values that are very close to the ensemble average values, that is, 0.70, 0.76, and 0.74. Here there is little evidence of a double peak distribution in the mean concentration profiles and there associate double-Gaussian forms.

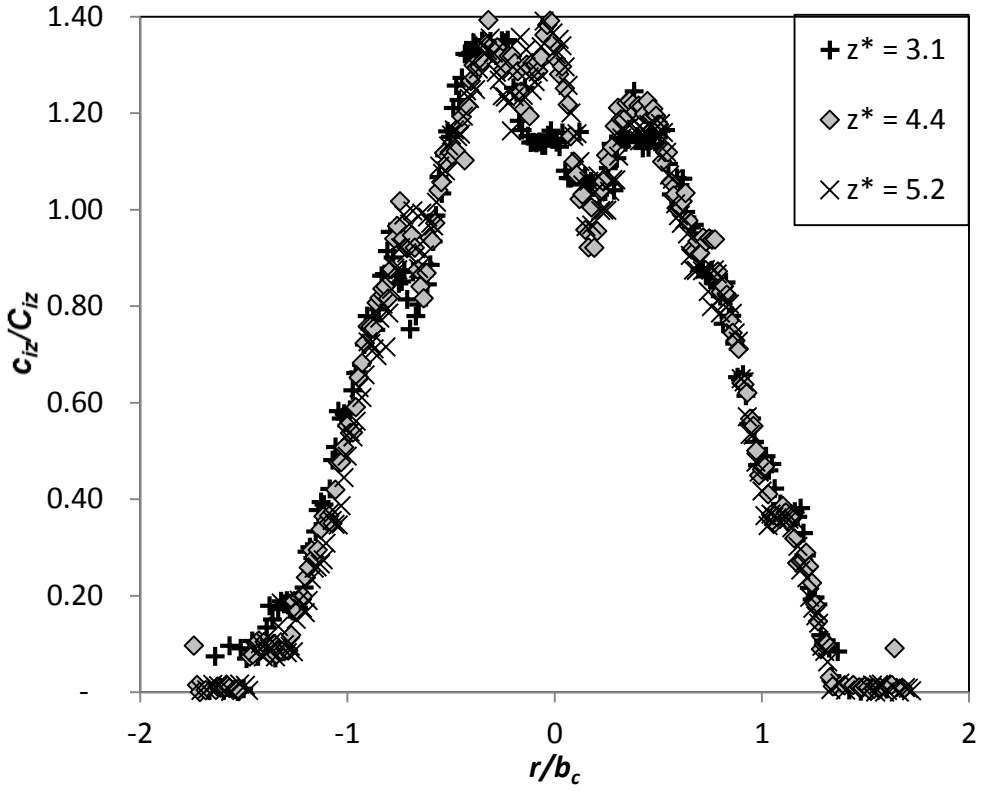

Figure 4-39: Run 3-d cross profiles at 3 distances, left the experimental data, right the best fit double-Gaussian distribution, *f* values 0.60, 0.74, 0.55.

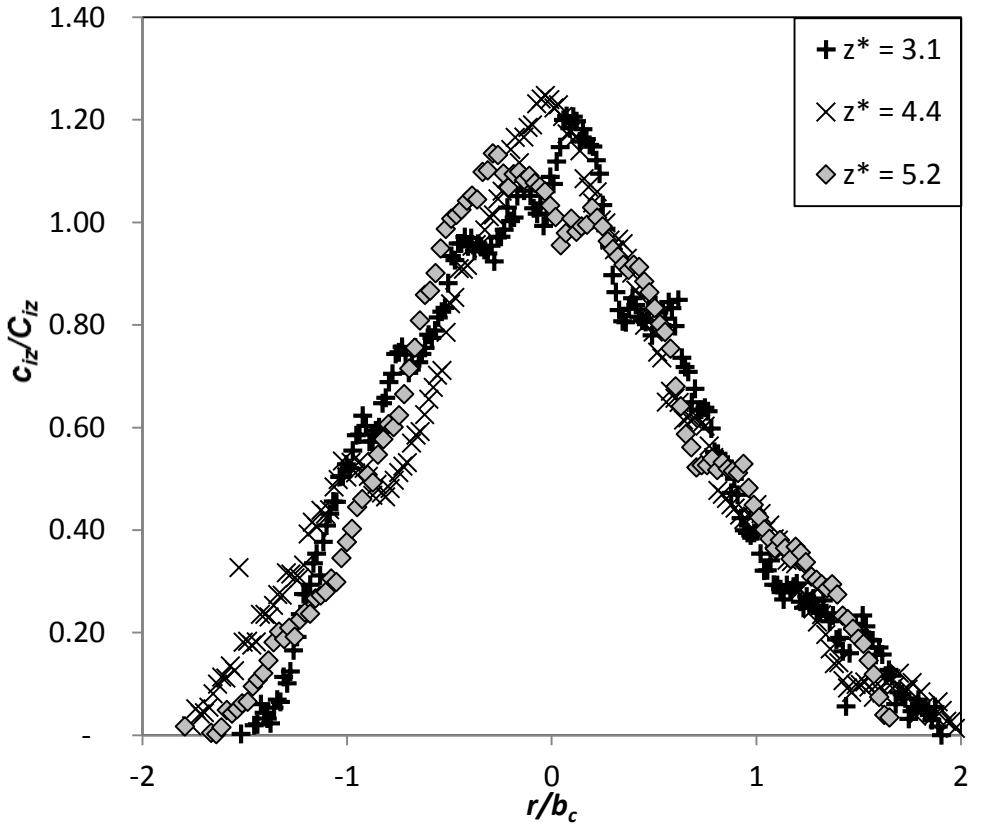

Figure 4-40: Run 3-e cross profiles at 3 distances, left the experimental data, right the best fit double-Gaussian distribution, *f* values 0.70, 0.76, 0.74.

In summary the more detailed look at the mean concentration profiles paints a picture that is consistent with the information presented in section 4.4.4 (the trajectory, spread and dilution results summary) and Table 4-8. For the 28.9° discharge angle, there is little evidence of a double peak distribution, suggesting strongly-advected jets generally form once the ambient motion dominates the flow behaviour. In contrast at 52.7° double-peak distributions are generally present, supporting the conclusion that advected line momentum puffs have formed once the flow becomes strongly-advected. There is however, significant variability associated with individual experiments and the more general observations require an extended averaging time to become clearly evident. Of particular interest is the intermediate angle of 35.9°, where the flow does not exhibit behaviour that is typical of either an advected line momentum puff or strongly-advected jet. The mean concentration profiles for individual experiments showing the presence of a double peak form for some experiments, but not for others. The ensemble average of these experiments removes any direct evidence of the presence of these double peaks, but this process generates a broad single peak mean concentration distribution that is not consistent with a single-Gaussian form.

4.5 Summary

In this chapter results from an experimental investigation into the behaviour of non-buoyant oblique discharges in a moving ambient fluid have been presented. Light Attenuation techniques were again employed to measure integrated concentration profiles and trajectory data. The experiments focussed on determining the nature of the discharge in the strongly-advected region and its dependence on the initial discharge angle. While previous investigations have highlighted the significance of the initial discharge angle in defining the strongly-advected behaviour, the focus had largely been on the extremes where the strongly-advected behaviour is clearly defined. That is, where either a strongly-advected jet or an advected line momentum puff clearly forms in the strongly-advected region (co-flowing and/or cross-flowing jets). Here, however, the focus was on the initial discharge angles where the expected strongly-advected behaviour is not as clear. A series of experiments has been conducted with initial discharge angles, relative to the ambient velocity direction, of 28.9, 32.4°, 35.9°, 39.0°, 47.6° and 52.7°.

For higher initial angles of 39.0°, 47.6°and 52.7° a double peak distribution, typical of an advected line momentum puff, is evident and for the lower angle discharges, 28.9° and 32.4°, a single peak distribution, more typical of a strongly-advected jet, is evident. The angle in between

(35.9°) shows behaviour that sometimes appears to be a single peak and at other times a double peak. Ensemble averages of these profiles results in a broad single peak profile suggesting that the integrated concentration profiles (viewed along the *z* axis) do not form a stable profile, single-Gaussian nor double-Gaussian. Whether this broad profile is evidence of two closely spaced double vortices cannot accurately be determined with the present LA method and needs further investigation with other techniques (for example PTV or LIF).

The reason why the value of 35.9° is critical is not clear from the present experiments. Below this value the shear from the cross flow is apparently not of sufficient strength, when compared to the shear associated with the initial momentum flux, to disrupt the 'standard' jet structure. However above this value the cross flow shear dominates and the double peak structure is clearly evident. The reason why some parameters at 35.9° are more consistent with the double vortex structure and others adhere to the jet-like behaviour could be explained by an intermittent behaviour, where the double vortex starts to form but collapses again. However, as noted above, further detailed experiments are required to determine the exact form of this behaviour.

The observations based on the integrated mean concentration profiles are consistent with those based on the evolution of the bulk parameters (spread, trajectory and integrated dilution) of these flows with distance from the source. Data from the higher discharge angles (39.0° to 52.7°) collapsed under scaling based on analytical solutions of line momentum puffs and were consistent with predictions based on the ALMP model. Similarly data from experiments with initial discharges angles of 28.9° and 32.4° collapsed under scaling based on the strongly-advected jet analytical solutions and were consistent with predictions from the SAJ model. In contrast data from the 35.9° discharge did not demonstrate consistent behaviour under either form of scaling and was not generally consistent with either of the integral models.

Chapter 5 - Buoyant Jets Evolving Along Three-Dimensional Paths

5.1 Introduction

As discussed previously, wastewater is commonly discharged into the receiving water via a diffuser located on the seabed. The wastewater has a different density than the receiving water and there are usually ambient motions present, for example tidal motions. The behaviour of the released effluent can be altered significantly by the presence of these motions. In general, with a relatively small density difference between the ambient and effluent, it is expected that the flow exits the diffuser in a jet-like manner, but this flow is then altered by the presence of buoyancy forces and entrained ambient momentum. Ultimately the ambient motions dominate and a strongly advected flow forms where buoyancy effects continue to drive mixing processes and the initial momentum flux of the discharge that formed the jet-like flow is no longer significant. Where the directions of the initial momentum flux, buoyancy forces and ambient motions are all different the flow is more complex, because it is moving along a time dependent three-dimensional path.

Three-dimensional paths are more difficult to investigate in the laboratory, because the measuring systems are typically planar and it is more difficult and cumbersome to gain a detailed overview of the flow that moves through the planar system. This is a situation where the LA system has significant advantages (see chapter 2), because it enables the evolution of flow behaviour to be captured without the need for the laborious process of capturing large numbers of individual planar flow cross-sections or alternatively scanning the planar sheet in an attempt to capture the overall flow behaviour. Cheung (1991) and more recently Lai and Lee (2012) employed LIF to record detailed cross-sectional information for discharges that follow three-dimensional paths. These profiles were only recorded perpendicular to the ambient motion and this limits there value near the source, where the predominant motion is not aligned with the ambient motion. In order to capture the behaviour near the source a large number of cross-sectional profiles are required at a variety of angles and this limits the practicality of employing most planar measuring systems to study the evolution of flows with three-dimensional trajectories. This issue can be overcome to some extent by using a 3D LIF system. The 3D LIF system consists of two rotating mirrors that direct a continuous laser beam through a flow in a

programmed pattern. One mirror sweeps the beam up and down while the camera shutter is open and the second mirror moves the beam a small distance horizontally while the camera shutter is closed in between subsequent frames. As the cameras are capable of capturing up to 260 frames per second, multiple slices of the flow are taken almost simultaneously creating a 3D image (Tian and Roberts 2003; Tian et al. 2004). However this system is considerably more complex than the LA system employed here and to date its application to study discharges that follow three-dimensional paths has been limited.

Kikkert et al. (2009) explored the application of the LA technique to discharges with three-dimensional trajectories. They employed a similar system to that utilised here to investigate five discharge configurations that differed significantly from each other in either initial horizontal or vertical discharge angles. This research gave valuable indications of the variability of the three dimensional trajectories and dilution data, but the transition between different strongly advected regions was not consistently observed or for some cases could not be accurately measured. Specifically, Kikkert et al. noted that for two of the five discharge configurations a line vortex pair did not form in the strongly-advected region of the flow. They concluded that the increased flow complexities associated with discharges following three dimensional paths made it difficult to employ relatively simple conceptual models to interpret and predict their behaviour, particularly when such models are developed based on limited data from less complex (two-dimensional) discharge configurations.

However accurate predictions of the behaviour of three-dimensional discharges are a critical tool when assessing potential environmental impacts and defining appropriate mixing zones for regulatory purposes. Integral models like CorJet (Jirka 2004) and VisJet (Lee et al. 2000) are used to forecast the dilution and trajectory, and these models have been extensively validated against existing laboratory and, where possible, field data. For two-dimensional cases extensive data sets are available and have enabled the models to be calibrated and validated. However validation for the more complex three-dimensional discharges is seriously compromised by a lack of detailed experimental data, because of the issues outlined above. Therefore the models extrapolate the behaviour observed for two-dimensional trajectory cases to more complex three dimensional trajectory flows (Wood 1993). The extrapolation of flow behaviour is also supported by Jirka (2004); who compared CorJet predictions with Ayoub's (1971) three-dimensional trajectory data and found the match to be reasonable. Cheung (1991) and Lai and Lee (2012)

compared predictions from VisJet with their experimental data and also concluded that the model predictions were reasonably consistent in the strongly-advected regions of these flows.

Previous experimental data for discharges with three-dimensional trajectories provides limited information about the transitional behaviour of these flows and therefore it was not possible to adequately describe the mechanisms involved. The experimental program outlined in this chapter provides additional insight into the transitional behaviour of these discharges and their consistency with expected behaviour based on our understanding of discharges that following two-dimensional paths. In addition the variability of the flow behaviour is explored through the extensive repetition of specific discharge configurations. The model utilised in chapters 3 and 4 is also expanded to a three dimensional model to, along with the analytical solutions, provide a framework for interpreting the flow behaviour.

5.2 Methods

The camera LA system is used to investigate the development of buoyant jets that follow three-dimensional paths. The method employed to capture the evolution of these flows is similar to that described by Kikkert et al. (2009). The technique consists of capturing sequences of images, from two perpendicular directions to the ambient motion, of the discharged fluid as it mixes with the ambient. The ambient motion is simulated by towing the flow source through stationary receiving water. The images are recorded on cameras that remain stationary and thus the whole flow is observed, from the source to the point where the flow begins interacting with a boundary. The calibrated images provide integrated concentrations of the flow at various times and locations, which are then stitched together and averaged using the Imagestream software (Nokes 2009). This process creates a single image from each camera of the integrated concentration field from the source to the point of boundary interaction. The width of each of these images was approximately 700 mm and with an ambient velocity of 50 mm/s or larger, an individual experiment provided data for at least 14 seconds at a given cross section. To increase the observation time per cross section, where necessary, the experiments were repeated a number of times and this provided the basis for creating ensemble averages.

The present study extends the earlier work of Kikkert et al. (2009) by measuring the flow behaviour over extended distances downstream from the source and providing more detailed

spread and dilution data over this extended range. In addition a wider range of initial conditions are also investigated. Enhancements to the dual-camera light-attenuation system have been incorporated, which include the use of multiple dyes, improvements in temperature and flow control of the source, improvements to the capture system and an increase in size and stability of the light sources (see chapter 2). The LA system provides the ability to clearly identify the development of a line vortex pair as the flow becomes strongly advected, that is, the entrained ambient momentum dominates the flow behaviour. In this region the rates of spread and dilution change dramatically and its development is therefore of practical significance. Importantly, as previously noted, Kikkert et al. observed that for two of their five discharge configurations a line vortex pair did not form in the strongly-advected region of the flow, which is inconsistent with expectations based on experiments with discharges following two-dimensional paths. Here this unexpected result is investigated further.

5.3 Setup

5.3.1 Experimental setup

The experimental setup is similar to that described for the advected thermal and oblique discharges experiments described in chapters 3 and 4. The source for the three-dimensional trajectory experiments was discharged horizontally at initial angles of 22°, 45° or 90° to the ambient (Figure 5-1). The initial motion is therefore predominantly in the *x*-*y* plane, but buoyancy effects drive the motion in the *z*-direction, thus creating a three dimensional trajectory. The LA system captures the flow behaviour in both *x*-*y* and *x*-*z* planes. These views enabling the formation of double peak distributions, indicative of the formation of a vortex pair, to be clearly identified as the flow evolves. Figure 5-1 shows a schematic of the setup, along with schematics of the views from the two different cameras.

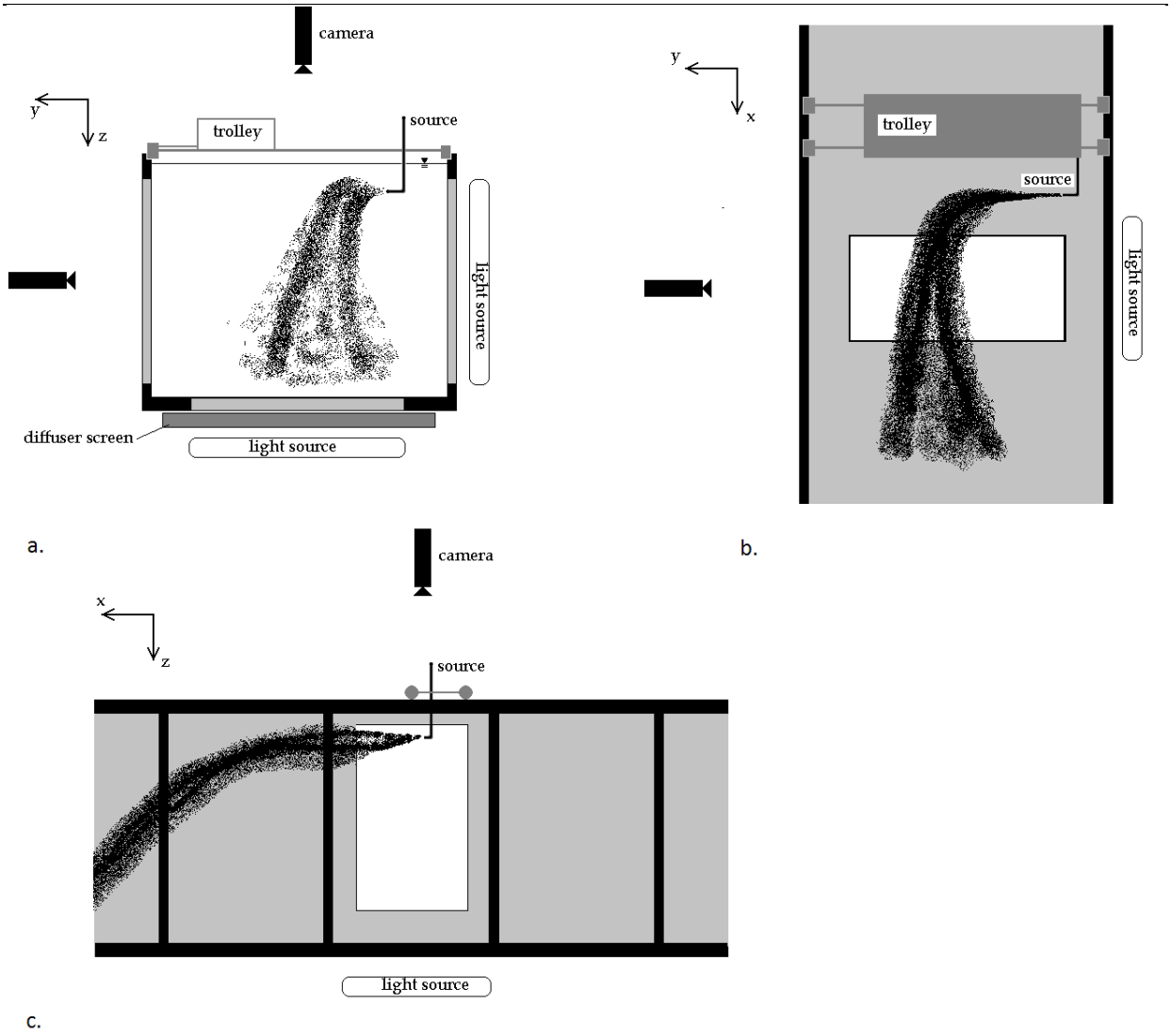

Figure 5-1: A schematic of the dual-camera LA system. On the top left (a.), the view along the *x* axis is shown, the trolley is pulled in the x direction (into the page) and this figure shows the position of the two cameras. On the top right (b.), the setup as seen from the top is shown. Here the tank walls, the trolley (moving towards the top of the figure), and the *z*-integrated discharge can be seen. On the bottom (c.), the view from the side is shown.

The experiments on discharges with three-dimensional trajectories were conducted in two phases. In the initial phase the variability of the flows was explored by selecting two discharge configurations (45° and 90°) and fixing the initial conditions for those configurations (shown in Table 5-1), so that all relevant flow regimes could be clearly observed. Experiments for these specific conditions were then repeated (11 for one configuration and 16 for other) to obtain more extensive data sets, which provided the basis for exploring the variability of these flow in terms of their bulk parameters and the evolution of the various flow regimes. For the 45° configuration, where 16 experiments have been conducted, a total of 224 seconds of data was available at each

pixel, whereas for the 90° discharge configuration 154 seconds was available. These relatively long sampling times also provide the basis for exploring the time scales necessary to obtain representative information for these flows. Previous research indicates (Scheepbouwer et al. 2008) that for Reynolds numbers lower than approximately 3500 there is increased variability in the establishment of the self-similar double vortex structure. Therefore relatively large initial Reynolds numbers have been used to remove this effect. The reduced gravity of the discharge flow for these experiments was 0.40 (Table 5-1).

Table 5-1: Initial conditions for the experiments of phase I.

Set	*Fr*	*Re*	Number of experiments used in ensemble	Horizontal discharge angle	Ambient to initial velocity ratio U_{ar} ±2%
Set 1	95	6600 – 7639	16	45	0.0178
Set 2	93	6964 – 7432	11	90	0.0175

In the second phase a third discharge angle was added (22°), because based on the experiments described in chapter 4, this was expected to change the intermediate flow regime from an advected line puff, to a strongly advected jet. Experiments where then conducted for a range of initial conditions for each discharge configuration, focusing in particular on variations in the ambient velocity ratio. Experiments were repeated to provide ensemble averages, but not as extensively as in the first phase of these experiments because of the time involved. Details of the initial conditions for second phase of the experiments are given in Table 5-2. Eight sets of experiments were conducted, with 1, 2 or 3 discharge angles per set. The three discharge angles were 90, 45 and 22 degrees from the ambient velocity in the horizontal plane (*x*-*y* plane). The 90° experiments provided the extreme case for creating a line momentum puff, before the formation of a line advected thermal. Whereas experimental results on discharges that following two-dimensional paths suggest that for a 22° initial discharge angle a line momentum puff will not form (as noted above). The 45° angle provides an intermediate angle where the line momentum puff is expected to form, this was the angle where Kikkert et al. (2009) did not observe the formation of a double-peak distribution in either the advected line momentum or advected thermal regions of the flow.

Table 5-2: Initial conditions for the experiments of phase II.

Set	Horizontal discharge angle	Ambient to initial velocity ratio, U_{ar} ±2%	*Fr*	*Re*	*g'*
Set 1	90	0.0042	87 – 97	6860 – 7432	0.42 – 0.43
Set 2	90	0.0054			
Set 3 a	90	0.0088			
Set 3 b	45				
Set 4 a	90	0.0130			
Set 4 b	45				
Set 4 c	22				
Set 5 a	90	0.0180			
Set 5 b	45				
Set 6 a	90	0.0280			
Set 6 b	45				
Set 6 c	22				
Set 7 a	90	0.0420			
Set 7 b	45				
Set 7 c	22				
Set 8 a	90	0.0570			
Set 8 b	45				
Set 8 c	22				

Note, the *Re* and *Fr* numbers differed only slightly between sets and between experiments in a set and have therefore been grouped together.

5.3.2 Phase I: Flow development

After leaving the source, beyond the initial zone, the flow establishes a self-similar form. The nature of this flow is defined by the relative magnitudes of the initial excess momentum flux, the buoyancy generated momentum flux, and the entrained ambient momentum flux. In the case of the Phase I experiments, four flow regions are possible (Figure 5-2) for a discharge in an ambient flow of different density. First the initial excess momentum flux (M_{e0}) will govern because both the entrained ambient and buoyancy generated momentum fluxes start at zero. As the flow evolves the initial excess momentum flux remains constant, but the density difference between the discharge and the ambient generates buoyancy forces. These forces give rise to an increasing buoyancy generated momentum flux, M_B, which can potentially dominate the flow and create plume like behaviour. However, in addition to this the flow is also entraining ambient momentum

flux, M_a, and this will ultimately dominate the flow behaviour creating a line advected thermal. It is possible for the entrained momentum flux to dominate the flow behaviour before the plume forms and in this case the formation of a line momentum puff will precede the formation of the line advected thermal, instead of the plume. Figure 5-2 shows the four possible flow regions and the two possible flow paths from jet to advected thermal. Whether the flow undergoes transitions 1 and 3 or 2 and 4 (Figure 5-2), is dependent on whether or not the buoyancy generated momentum governs before the entrained ambient momentum flux.

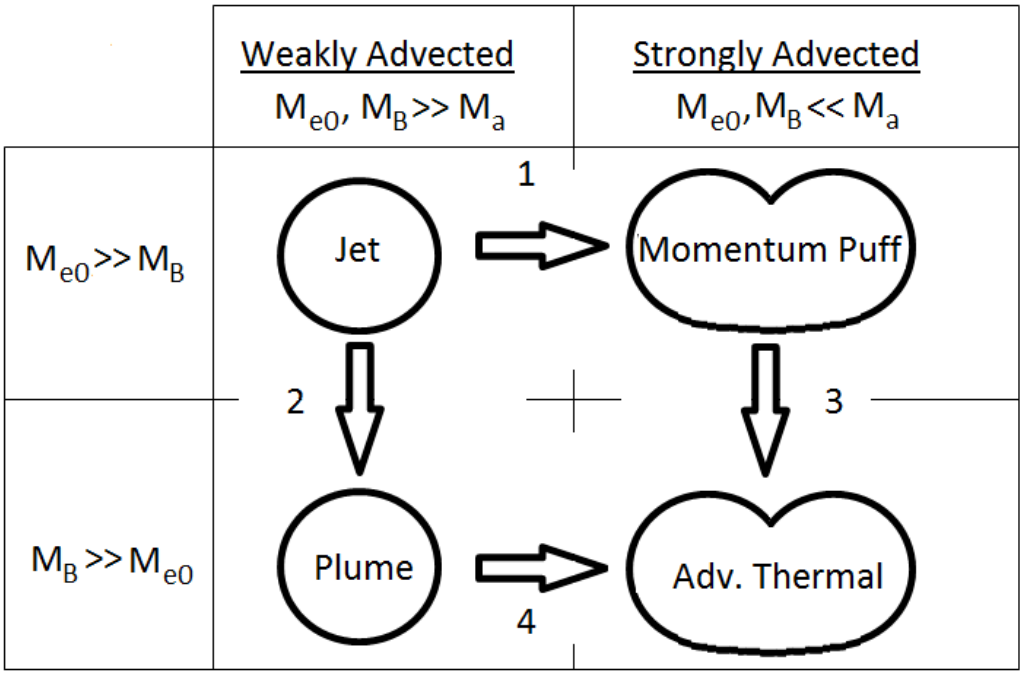

Figure 5-2: The four possible flow regions for the Phase I of the experiments. The regions are shown in their self-similar cross sectional form. The numbers represent the transitions between the flows. M_{e0}, M_B, and M_a represent respectively the initial excess momentum, the buoyancy generated momentum, and the ambient momentum [Scheepbouwer et al. 2010].

Estimates of the location of the transitions between the various flow regimes can be obtained through comparisons of the three components of the total momentum flux, that is, the initial, buoyancy generated and entrained ambient momentum fluxes. When two of these fluxes become comparable in size, the flow transitions from one region to another. While such comparisons provide approximate locations for these transitions, comparisons with experimental data enable them to be refined through the introduction of a transition constant. Kikkert at al. (2009) adopted this approach to estimating the location of the transitions and the relevant relationships are shown in Table 5-3.

Table 5-3: The more general forms of the transition length scales relevant to the present investigation.

Flow Region Transition and Transition constants	Length Scale
Strong Jet to Plume (K_{JP} =0.68)	$\frac{S_{JP}}{d} = \sqrt{\frac{K_{JP}}{k_T}}\left(\frac{4}{\pi}\right)^{1/4}\frac{M_{eo}^{3/4}}{(Q_0\Delta_0)^{1/2}d}$
Strong Jet to Advected Line Momentum Puff (K_{JM} =0.26)	$\frac{S_{JM}}{d} = \frac{K_{JM}}{\pi^{1/2}k_T}\frac{M_{e0}^{1/2}\lvert sin\phi_0\rvert}{U_a d}$
Strong Jet to Strongly Advected Jet (K_{JWJ} = 8.9)	$\frac{S_{JWJ}}{d} = K_{JWJ}\frac{M_{e0}^{1/2}\lvert cos\phi_0\rvert}{U_a d}$
Strong Jet to Advected Plume (K_{sp} = 2.3)	$\frac{S_{sp}}{d} = K_{sp}\frac{M_{eo}^{3/4}}{Q_0\Delta_0 d}$
Plume to Thermal (K_{PT} =0.35)	$\frac{Z_{PT}}{d} = K_{PT}^3\frac{3}{4\pi}\frac{1}{k_T^2}\frac{\Delta_0 Q_0}{U_a^3 d}$
Advected Line Momentum Puff to Advected Thermal (K_{MT} =2.22)	$\frac{L_{MT}}{d} = \left(\frac{3}{4\pi}K_{PT}^3\left(\frac{K_{MT}}{k_T}\right)^2\right)^{1/3}\left(\frac{\left(M_{e0}\lvert\sin\phi_0\rvert\right)^2}{Q_0\Delta_0 U_a d^3}\right)^{1/3}$
Strongly Advected Jet to Advected Thermal (K_{WJT} = 0.63)	$\frac{X_{WJT}}{d} = K_{WJT}\frac{M_{e0}U_a\lvert cos\phi_0\rvert}{Q_o\Delta_0 d}$
Advected Plume to Advected Thermal (K_{PT} = 0.1)	$\frac{Z_{PT}}{d} = K_{PT}\frac{Q_0\Delta_0}{U_a^3 d}$

Where k_T represents the top hat spread constant of 0.144, S represents the length scale measured in the direction of the initial discharge, L is the length scale measured along the projection of the initial discharge direction in the y-z plane, X and Z are the length scales in de x and z directions respectively and the various K values represent the transitional constants. The transition lengths for the Phase I experiments have been calculated based the relationships and constants listed in Table 5-3, and the magnitudes of these length scales are listed in Table 5-4. In both cases the jet to line momentum puff length scale is significantly smaller than the jet to plume length scale. It is therefore expected that the jet to puff transition occurs before the jet to plume transition for these initial conditions and thus plumes are not expected to form. The expected behaviour is jet to puff to thermal. The puff to thermal transition lengths is also more than double that of the jet to puff transition, so the formation of a distinct puff region is also expected. It is worth noting,

that it can be difficult to distinguish between puff and thermals for discharges with two-dimensional trajectories, because the double-peak distribution evident in both regimes have the same orientation. For the present experiments, however, the discharge configurations considered promote the formation of the puff and thermals with different orientations. The advected puffs are generated by the initial excess momentum flux and hence their double peak form should be evident in the *x*-*z* plane. The buoyancy generated momentum flux that is critical to the formation of the advected thermals acts orthogonally to the initial excess momentum flux and in the case the double form will be evident in the *x*-*y* plane. Thus for discharges with three-dimensional trajectories it is possible to more clearly define the formation of these flow regimes.

Table 5-4: The various transitional points for experiments of phase I, all lengths are non-dimensionalised with the source diameter *d*.

	Transition (Figure 5-2)	Set 1	Set 2
Jet to Puff	1	50.8	35.3
Jet to Plume	2	198	205
Plume to Thermal	4	1.68	1.54
Puff to Thermal	3	96.5	76.9
Puff to Thermal/Jet to Puff		1.90	2.18

The transitions in Figure 5-2 are not reversible. For example, once the entrained ambient momentum flux exceeds the initial momentum flux an advected puff forms and it is no longer possible for a plume or a jet to form. This is because the entrained ambient momentum flux increases more rapidly than the buoyancy generated momentum flux with distance from the source, and the initial momentum flux remains constant. Similarly a flow in the plume region can transition to an advected thermal, but not an advected puff because initial momentum flux remains constant; while the buoyancy generated momentum flux continues to increase. When the entrained ambient momentum exceeds this buoyancy generated momentum flux an advected thermal forms.

5.3.3 Phase II: Flow development

In the second phase of the three-dimensional trajectory experiments a third discharge angle (22°) was introduced and a broader range of initial conditions considered. The introduction of this third

angle, also introduces a fifth flow regime, that is, the strongly-advected jet (Figure 5-3). The inclusion of this fifth regime introduces two new length scales to cover the jet to strongly-advected jet and strongly-advected jet to advected thermal transitions, which are labelled as 5 and 6 respectively. Relationships for these length scales, based on the work of Kikkert et al. 2009 and Davidson et al. 1998 are shown in Table 5-3. Based on the results from chapter 4, the new length scales are only relevant to this new discharge angle and length scales relevant to the remaining discharge angles are those discussed with reference to the phase II experiments.

In the experiments the initial conditions have been chosen (Table 5-1, Table 5-2, Table 5-4, and Table 5-4) to make transitional length scale S_{jp}, the jet to plume length scale, significantly larger than S_{jmp}, the jet to momentum puff length scale, thereby making it likely that a puff forms first, which is then followed by a transition to an advected thermal. The values of relevant lengths scales for all three discharge angles and all initial conditions are listed in Table 5-5. The results from Chapter 4 suggest that for discharge angles 45° and 90° the expected behaviour is that a momentum puff forms after the initial strong jet, transitions 1 and 3 in Figure 5-3. The 22° discharge is expected to form a strongly advected jet and then transition into a line advected thermal, transitions 5 and 6. The accompanying transitional length scales (including the constants shown in Table 5-3) are depicted in the first two data columns in Table 5-4. The subsequent transitional length scales towards an advected thermal are also depicted. The length scales from jet to plume and plume to advected thermal are also given for completeness. Finally the last column contains the ratio between relevant length scales, either puff to thermal divided by jet to puff or strongly-advected jet to thermal divided by jet to strongly advected jet. These ratios provide an indication of the relative scale of the intermediate flow regime. A larger value suggesting the intermediate regime is of significant scale and a smaller value that it might be difficult to detect.

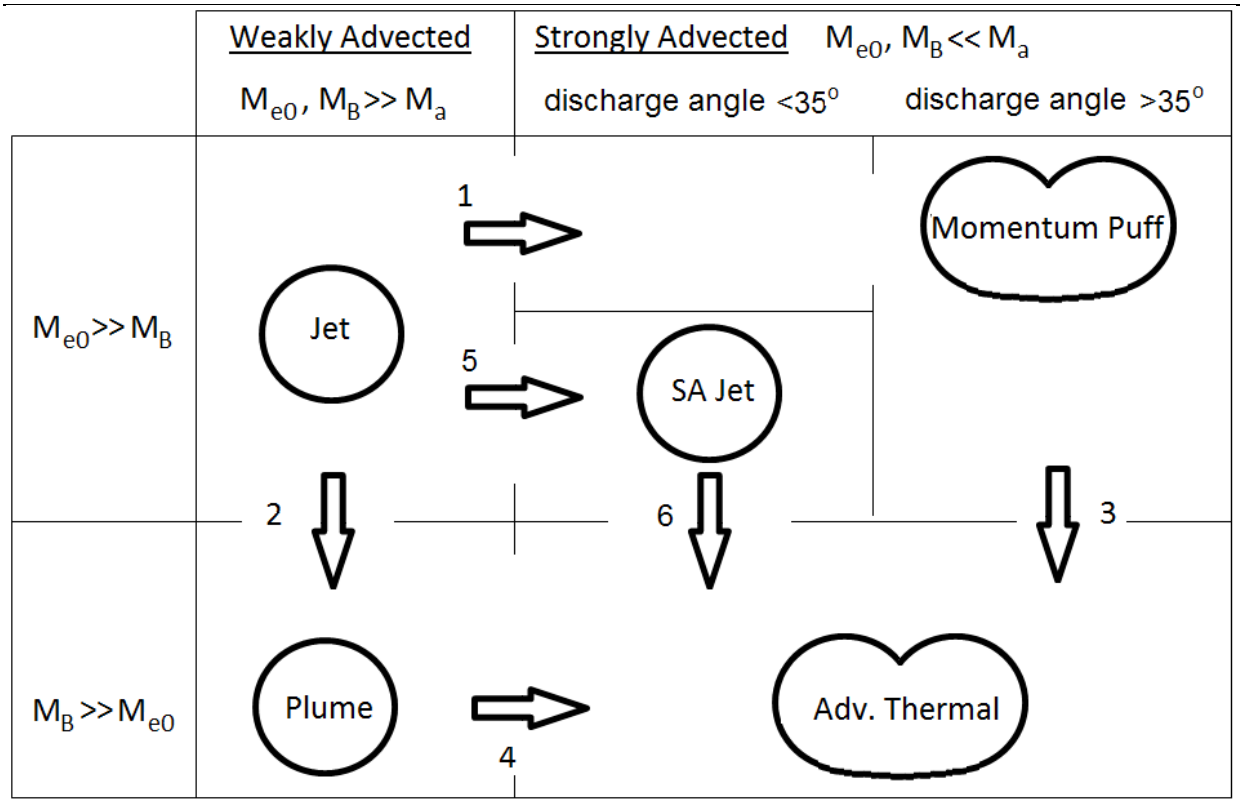

Figure 5-3: The 5 possible flow regions and transitions between them. The regions are shown in their self-similar cross sectional form. The numbers stand for the transitions between the flows. M_0, M_B, and M_a represent respectively the initial excess momentum, the buoyancy generated momentum, and the ambient momentum.

Table 5-5: The various transitional points for experiments in phase II, all lengths are non-dimensionalised with the source diameter *d*.

	Jet - Puff	Jet - SA Jet	Jet – Plume	Puff - Thermal	SA Jet - Thermal	Plume - Thermal	Puff-Thermal/Jet-Puff or SA Jet-Thermal/Jet-SA Jet
Set 1	215.5		200.1	150.6		617	0.70
Set 2	164.9		199.4	133.2		276	0.81
Set 3 a	102.7		197.2	121.7		68.7	1.19
Set 3 b	73.2		200.1	97.2		69.9	1.33
Set 4 a	72.0		200.1	109.2		23.0	1.52
Set 4 b	50.6		200.8	85.9		23.1	1.70
Set 4 c		571.9	198.6		96.3	22.8	0.17
Set 5 a	50.8		197.8	96.5		8.28	1.90
Set 5 b	35.3		205.0	76.9		7.59	2.18
Set 6 a	31.7		201.5	83.4		1.94	2.63
Set 6 b	21.7		199.4	63.7		1.92	2.94
Set 6 c		245.3	197.9		212.8	1.90	0.87
Set 7 a	21.6		200.1	73.1		0.624	3.38
Set 7 b	15.3		205.4	57.3		0.642	3.75
Set 7 c		174.7	207.2		317.2	0.646	1.82
Set 8 a	15.6		195.1	64.4		0.246	4.13
Set 8 b	10.9		200.1	49.7		0.253	4.56
Set 8 c		122.7	200.1		401.4	0.252	3.27

5.4 Model

In order to compare the experimental results with expected results, the mathematical model used in chapter 4 has been extended to include flows with three-dimensional trajectories.

The change in initial momentum flux, represented by the *y*-momentum flux equals 0,

$$\frac{dM_{y*}}{dt_*} = 0 \tag{5-1}$$

In which M_{y*} is the non-dimensional momentum in *y*-direction. The change in vertical momentum flux equals the inverse square of the initial Froude number or,

$$\frac{dM_{z*}}{dt_*} = \frac{1}{Fr_0^2} \tag{5-2}$$

In which M_{z*} is the non-dimensional vertical momentum. The change in horizontal momentum flux in the ambient or *x*-direction equals the relative ambient flow velocity times the change in flow,

$$\frac{dM_{x*}}{dt_*} = U_{a*}\frac{dQ_*}{dt_*} \tag{5-3}$$

The geometric relationships are, the change in *z*-coordinate equals the vertical momentum divided by the flow, the change in *x*-coordinate equals the horizontal momentum in *x*-direction divided by the flow, and the change in *y*-coordinate equals the horizontal momentum in *y*-direction divided by the flow or,

$$\frac{dz_*}{dt_*} = \frac{M_{z*}}{Q_*} \tag{5-4}$$

$$\frac{dy_*}{dt_*} = \frac{M_{y*}}{Q_*} \tag{5-5}$$

$$\frac{dx_*}{dt_*} = \frac{M_{x*}}{Q_*} \tag{5-6}$$

The spread, b_T, in a lagrangian system equals the top hat velocity times the constant m_T, which is, expressed in terms of momentum flux,

$$\frac{db_T}{dt_*} = m_T \frac{M_{z*}}{Q_*} \tag{5-7}$$

In which M_z represents the vertical momentum. The flow can be seen as the velocity times the cross-sectional area (both in top hat form),

$$Q = u_s \pi b_T^2 \tag{5-8}$$

Where u_s stands for the total instantaneous velocity. The total momentum flux becomes,

$$\frac{dM_{s*}}{dt_*} = \frac{M_{x*}}{M_{s*}}\frac{dM_{x*}}{dt_*} + \frac{M_{y*}}{M_{s*}}\frac{dM_{y*}}{dt_*} + \frac{M_{z*}}{M_{s*}}\frac{dM_{z*}}{dt_*} \tag{5-9}$$

Finally conform chapter 4, an explicit relationship for the change in flow, dQ_*/dt_* gives,

$$\frac{dQ_*}{dt_*} = \frac{2b_{T*}^2 \frac{M_{z*}}{M_{s*}}\frac{dM_{z*}}{dt_*} + 4M_{s*}b_{T*}\frac{db_{T*}}{dt_*}}{Q_* - 2b_{T*}^2 U_{a*}\frac{M_{x*}}{M_{s*}}} \tag{5-10}$$

The above equations can be coded into Matlab software to calculate the different parameters. The initial conditions for the present experiments are set as follows. The initial *x*-, *y*-, and *z*-coordinates are 0. The spread at source, b_{To} approaches 0 and the initial non-dimensional volume flux is 1. The initial vertical momentum flux, M_z, equals 0 as all the flows are discharged horizontally. The initial total excess momentum equals 1-U_{ar}*cos(θ). The *x*-momentum equals $Q*U_{ar} + M_{eo}*cos(\theta)$. The *y*-momentum then equals $M_{eo}*sin(\theta)$. The total momentum flux equals the square root of the sum of the squares of the momentums in *x*, *y* and *z*-direction. Finally we have the parameter m_T, which has been set as 0.72 (chapter 3), the value for a thermal. The model is therefore applied where advected thermal behaviour is expected and this removes ambiguities associated with any transitional model, enabling the advected thermal behaviour to be more clearly identified.

5.5 Results

5.5.1 Variability of the results from the Phase I experiments

In this section the variability of 3D flows is assessed. An understanding of this variability can aid the interpretation of predictions from numerical models. As the 3D flows approach a 2D form when the initial momentum becomes insignificant, the expectation is that the variability in the final flow regime will be similar to equivalent 2D experiments. The variability presented here represents the variability in the averaged integrated profiles and not the instantaneous or point concentrations. Instantaneous profiles can be measured using different visualisation techniques, such as LIF, to display the eddies through which the mixing occurs. However this is not the focus of the present study. In following sections the *f* and *h* parameters provide additional information about the mean structure of the flow cross-section.

In assessing the variability of the phase I experiments, the standard deviation has been calculated for a select number of parameters. For this the assumption has been made that the parameters or rather the variability of them, follow a normal distribution. The investigated parameters are the location of the peak concentration and the trajectory. Figures have been prepared for these parameters, where the ensemble averages are presented along with the individual experimental realisations of the flow parameter, thereby providing a qualitative impression of the variability. The standard deviations provide a quantitative assessment of that variability.

In Figure 5-4 and Figure 5-5, the location of the integrated concentration peaks viewed along the *z*-direction are depicted. On the horizontal axis the non-dimensional *x*-coordinate is show, which is measured in the direction of the ambient motion. On the vertical axis the non-dimensional *y*-coordinate is presented, which is measured perpendicular to the ambient current within a horizontal plane. In the figures the left and right peak concentration (local maximums) are shown, resulting in two data streams. Data is presented for the discharge at 90° to the ambient motion (along the *y* axis) in Figure 5-5 and the 45° to ambient current in Figure 5-4. The coordinates are non-dimensionalised with the plume-to-thermal length scale, Z_{pt}. The reasons for selecting this scaling are discussed in section 5.3.3. In the figures the ensemble average is presented as "grey-filled circles" along with the data from each experimental realisation of the flow, which is presented with series of smaller "black circles". These figures show that there is significant variability in the location of these peaks, particularly in the 45° discharge cases. For both discharge angles this variability appears to reduce once the thermal region becomes established,

but interestingly the location of the peak furthest from the source appears to be less variable than that nearer the source.

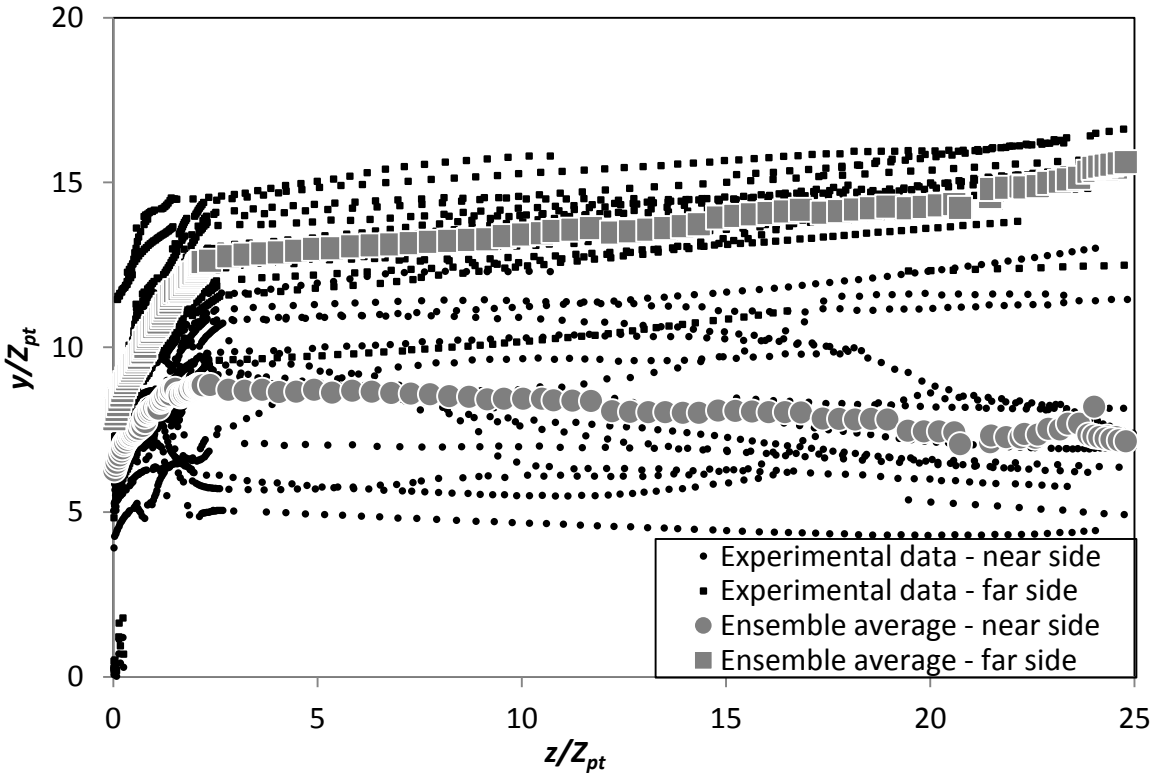

Figure 5-4: Locations of the peaks of the double vortices for the 45° discharge angle, seen in de z-direction.

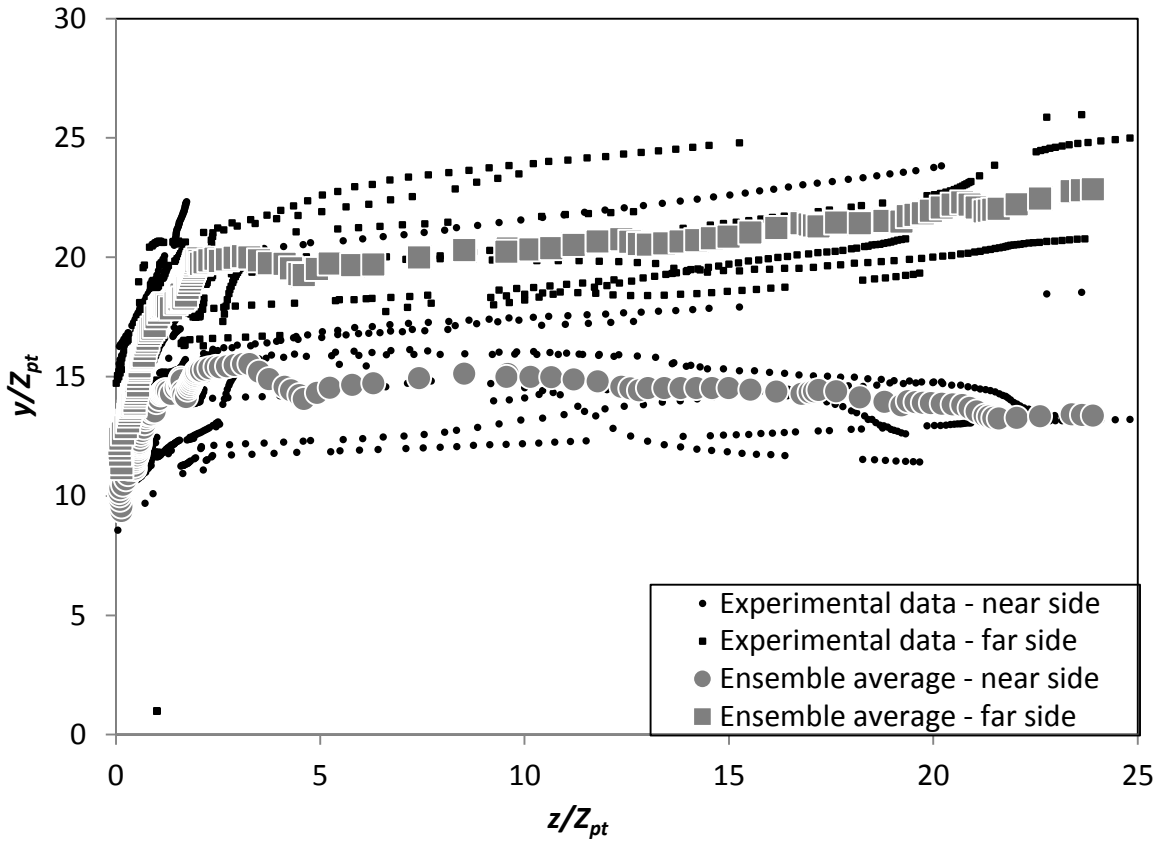

Figure 5-5: Locations of the peaks of the double vortices for the 90° discharge angle, seen in de *z* direction.

The ensemble averages from Figure 5-4 and Figure 5-5 are plotted together in Figure 5-6, without the data from the individual experiments. In Figure 5-7, the information from the 90° discharge is translated on top of the 45° discharge. It is evident that a similar behaviour is observed; although the initial movement in the *y*-direction is reduced in the 45° case, which is consistent with the reduced initial momentum flux in this direction. Conducting the experiments with a relatively small ambient to initial velocity ratio ensures that the initial momentum flux plays a significant role in defining the flow behaviour prior to the formation of the advected thermal region. Interestingly the fact that the paths collapse under the appropriate scaling suggests that the behaviour within and between these flow regimes is essentially the same for the two initial discharge angles. Thus the significant increase in the initial momentum flux component parallel to the ambient motion has little influence on the transitional behaviour of the flow, and the formation and subsequent development of the advected thermal is essentially independent of this change in the initial conditions. This result contradicts the finding of Kikkert et al. (2009) where it was observed that the double peaked distribution did not form for the 45° case. However their experiments were conducted for relatively low Reynolds numbers (3400 to 4100) in contrast to

the Reynolds numbers for the present experiments which range from 6860 to 7432. As noted previously in Scheepbouwer (2008), the formation of the double peaked distribution becomes less reliable at Reynolds numbers below 3500 and thus care must be taken when interpreting this data in context of practical applications.

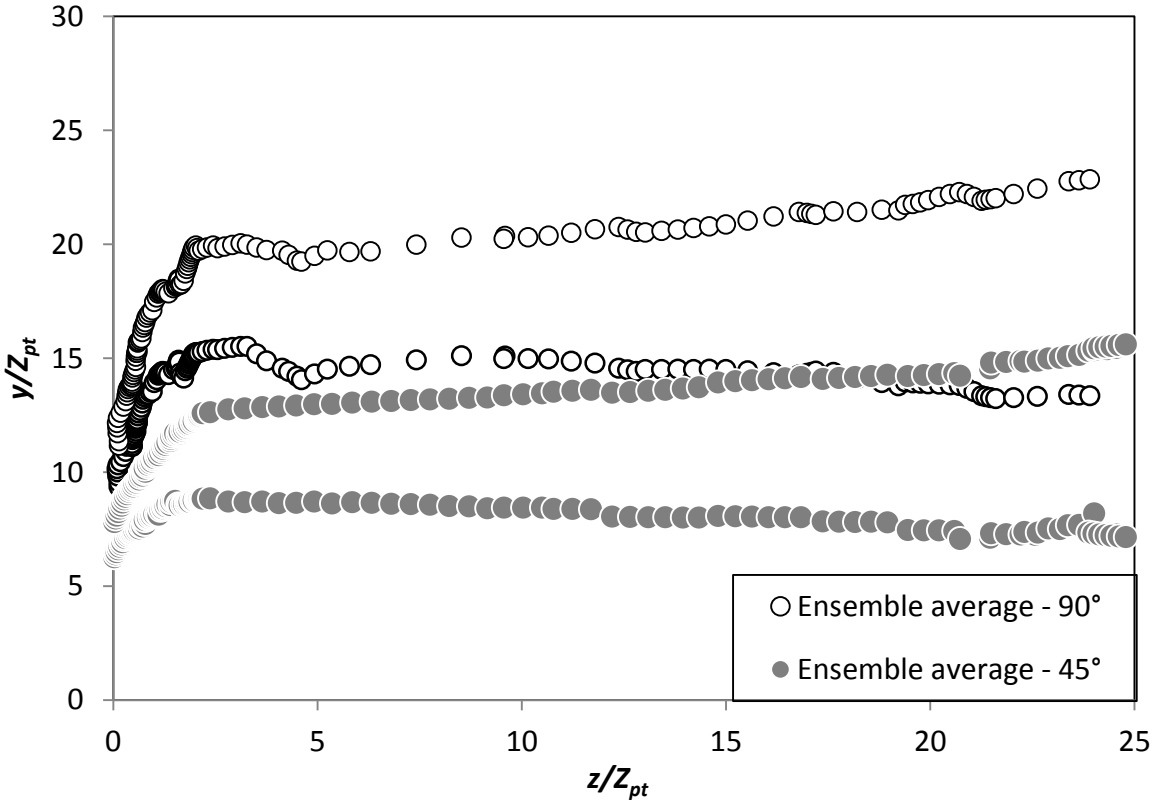

Figure 5-6: Top view (integrated *x*-*y* plane) of the locations of the ensemble averaged positions of the peaks of the double vortices for the 45° (open circles) and the 90° (grey circles) discharges.

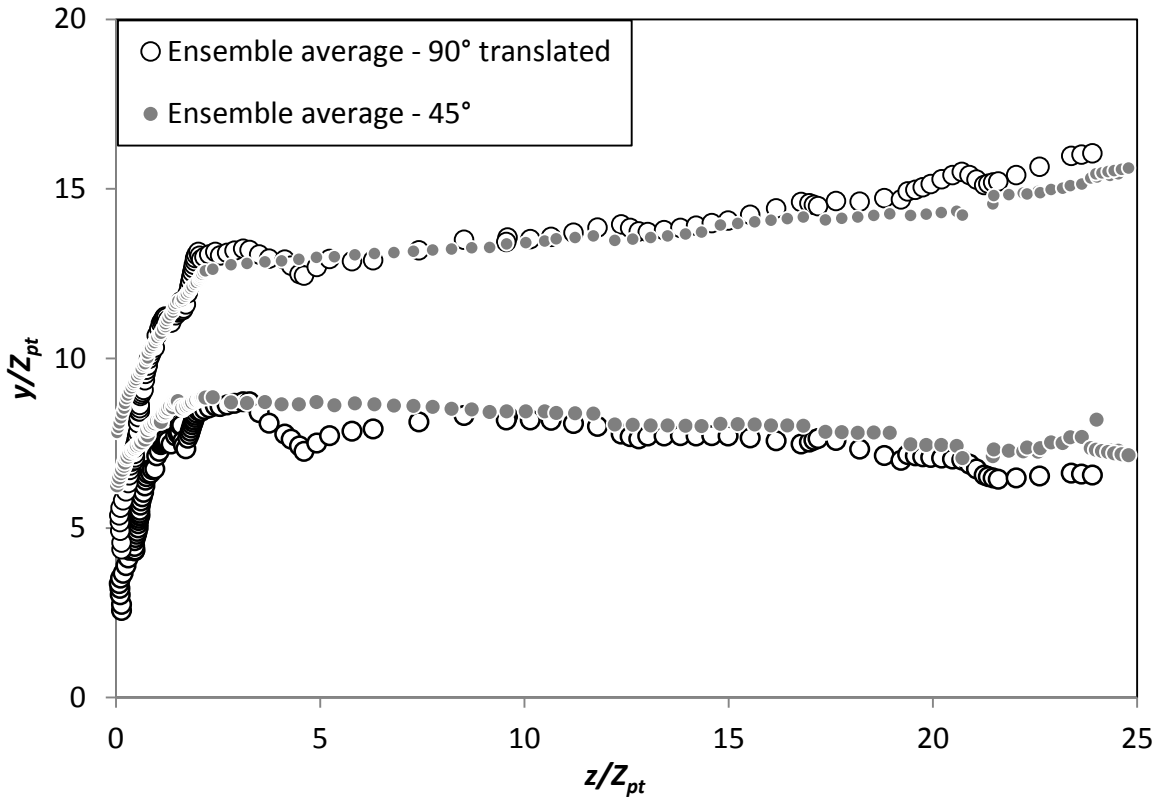

Figure 5-7: Top view (integrated *x*-*y* plane) of the locations of the ensemble averaged virtual positions of the peaks of the double vortices for the 45° (open circles) and the 90° (grey circles) discharges.

A direct measure of the variability in location of the peak concentrations is the standard deviation of the position relative to the ensemble average location. This represents the distance that the whole double vortex deviates from the average position of the double vortex as seen from the top. The ratio of the standard deviation over the average *y* location is shown in Figure 5-8. Note the movement in the *y* direction is driven by the component of the initial momentum flux in this direction, which remains constant during the evolution of the flow, during which the flows volume flux increases. The relative standard deviation settles on approximately 12% for the 90° discharge and 20% for the 45° discharge. Interestingly, although the movement in *y* direction reduces with increasing distant from the source, the variability appears to remain reasonably constant once the thermal regime is established. The uncertainty of the position of the double vortex or strongly advected flow is clearly larger in the case of a 45° discharge, which perhaps a more complex interaction between the ambient and discharged fluids.

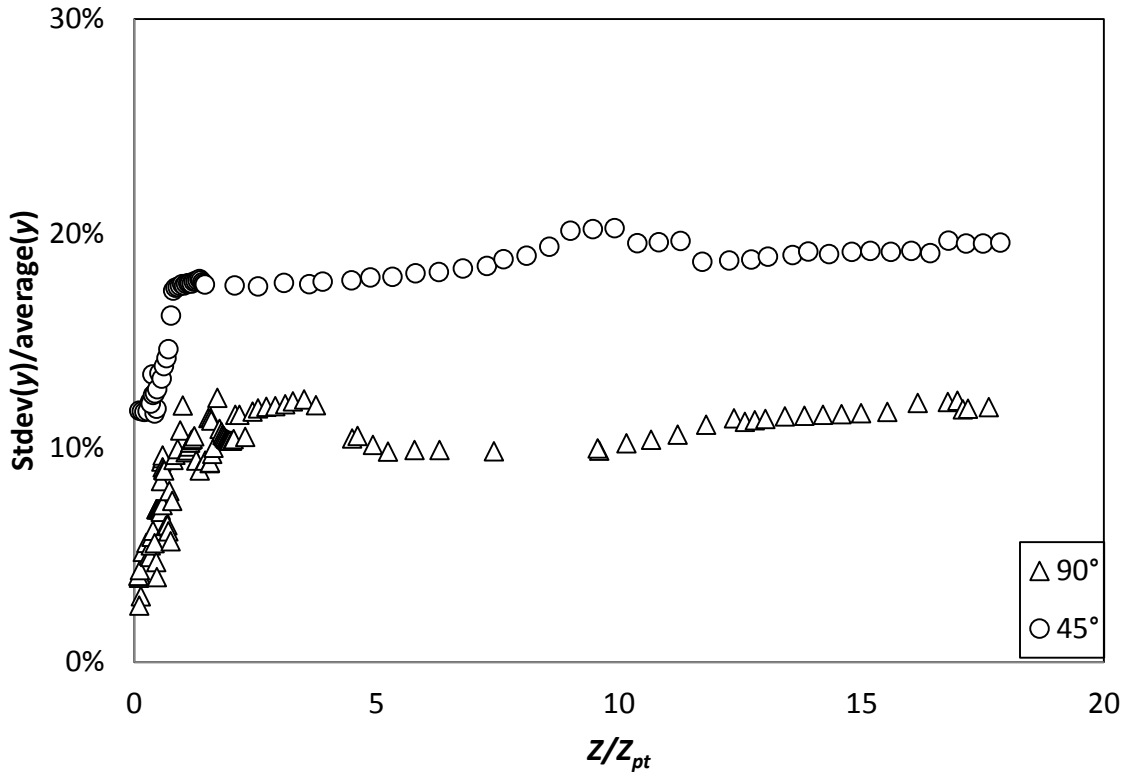

Figure 5-8: Ratio of the standard deviation of the movement in *y*-direction of the individual experiments and the average movement in *y*-direction versus the non-dimensionalised movement in the direction of the ambient flow.

In Figure 5-9 and Figure 5-10 the trajectories of the 45° and 90° discharge in the *x*-*z* plane, viewed along the *y* axis, are shown. The circles represent the peak integrated concentration locations. The small black circles represent the individual experiments; the grey circles are the ensemble averages. The vertical and horizontal axes are both non-dimensionalised by the plume to thermal length scale. Figure 5-11, shows the ensemble averages of the 45° and 90° discharges from Figure 5-9 and Figure 5-10 in one figure. Both averages are nearly identical and collapse on top of each other. From this perspective there appears to be more variability in the 90° discharge trajectories (Figure 5-9) than the 45° discharge trajectories (Figure 5-10). This is confirmed in Figure 5-12, where the relative standard deviation of the vertical centreline location is presented. In this figure the higher initial variability of the 90° discharges is evident, but once the flows have fully evolved into thermals this variability reduces to approximately 10%, which is consistent the variability in the 45° discharge trajectories.

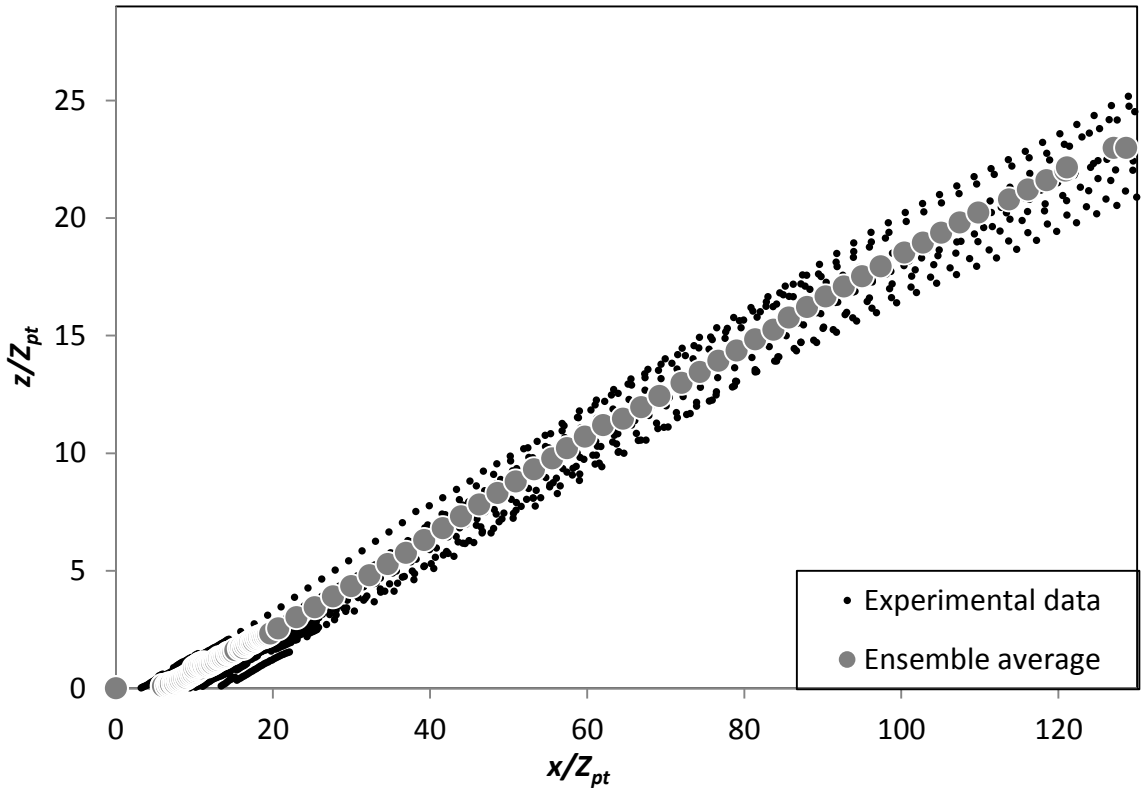

Figure 5-9: Side view of the locations of the ensemble averaged positions of the peaks of the fitted single Gaussians for the 45° (grey circles) and ensembles discharges.

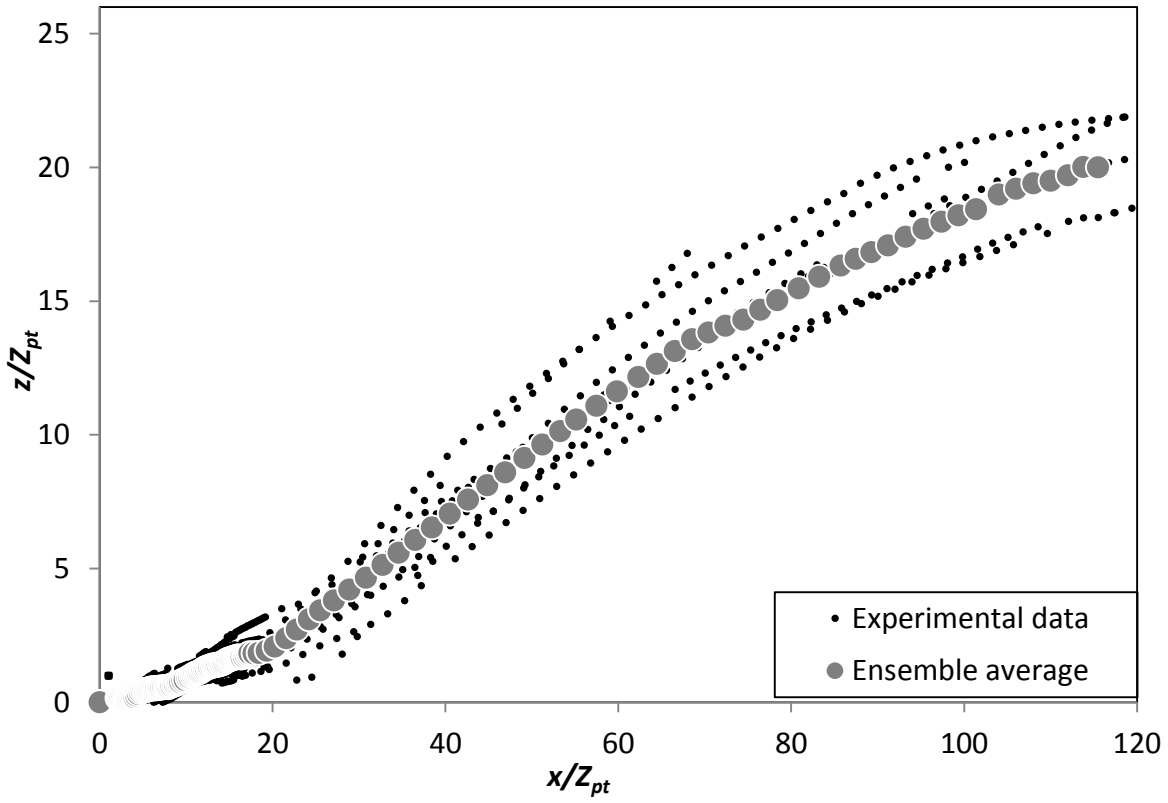

Figure 5-10: Side view of the locations of the ensemble averaged positions of the peaks of the fitted single Gaussian profiles for the 90° discharges.

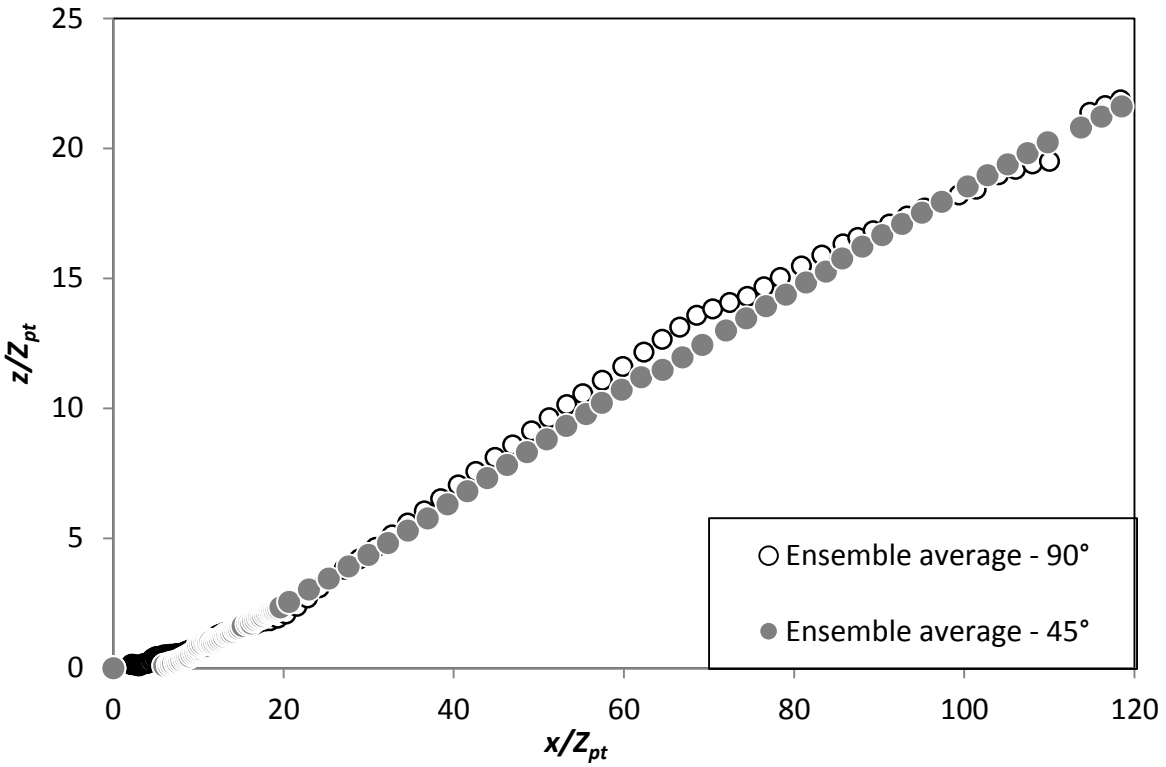

Figure 5-11: Side view of the locations of the ensemble averaged positions of the peaks of the fitted single Gaussians for the 45° (grey circles) and the 90° (open circles) discharges.

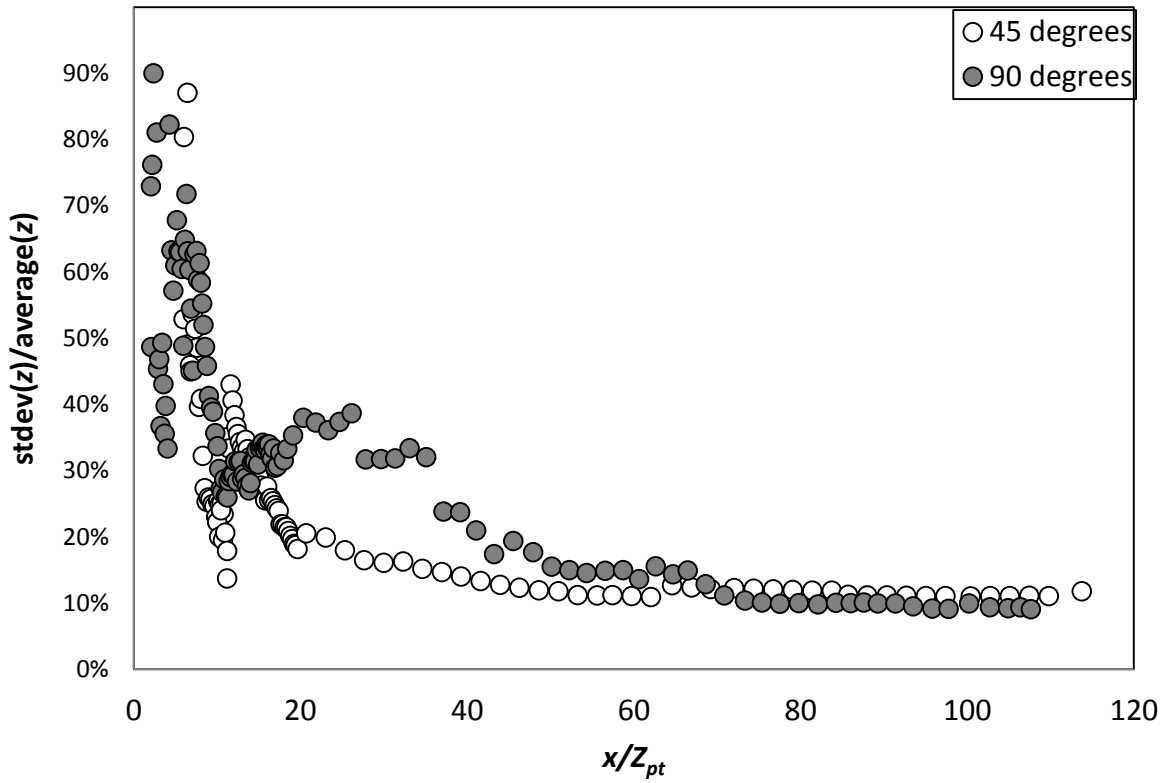

Figure 5-12: Standard deviation of the individual z-position at an x-distance from the source versus the average z-position at that distance.

In Figure 5-13, and Figure 5-14 the dilution results are shown. The integrated dilution results, C_{iy}/C_{im}, against the vertical coordinate, z, non-dimensionalised with the jet to thermal length scale, Z_{pt}. The integrated dilution results from the 45° discharge show some variability along the flow path; however they all approach the analytical solution, represented by the dashed line (chapter 3). The ensemble average summarises this consistent behaviour. The dilution results from the 90° discharge, Figure 5 14, show a similar picture. However, there appears to be a more pronounced transition to the region where the experimental data is consistent with the analytical model predictions. Compared to the 45° ensemble average, the 90° ensemble average reaches the analytical solution at a lower dilution and vertical distance from the source.

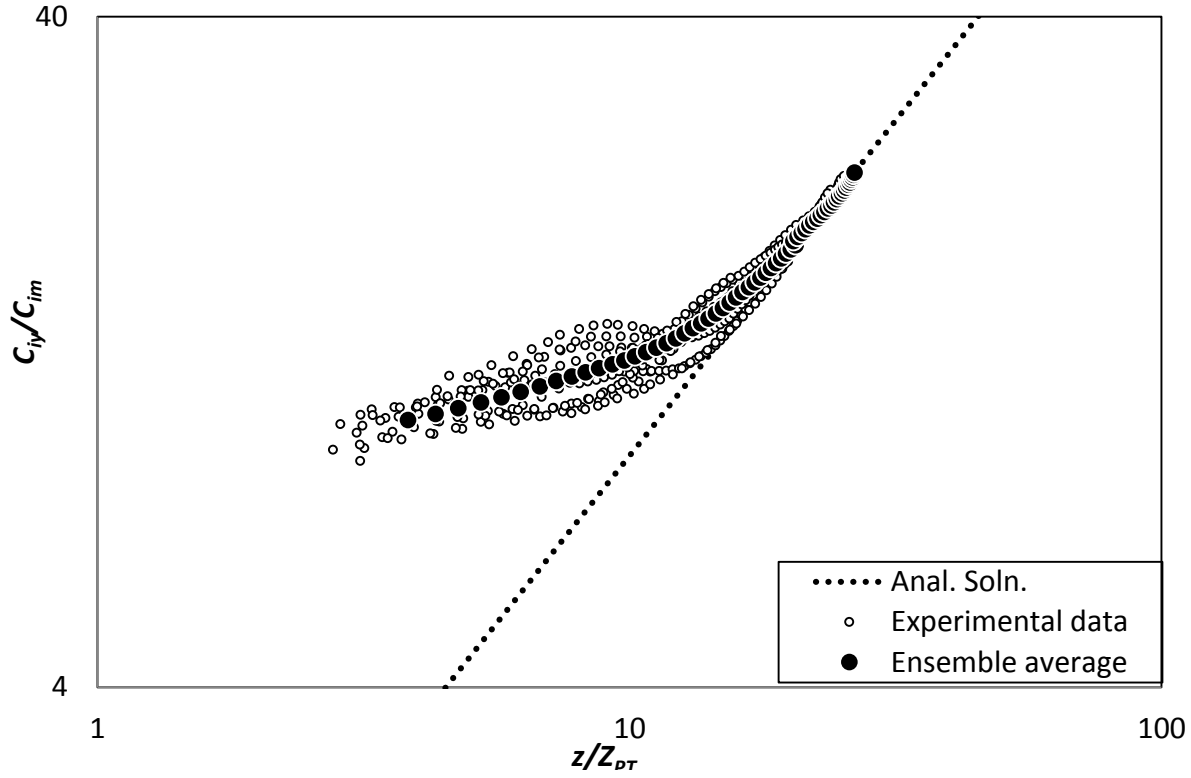

Figure 5-13: *y*-integrated dilution data from 45° discharges.

The dilution results from the 90° discharge, Figure 5-14, show a similar picture. However, there appears to be a more pronounced separation between the move towards the analytical expected line and the subsequent move along it. Compared to the 45° average, the 90° average touches the expected line at a lower dilution and *z*-coordinate.

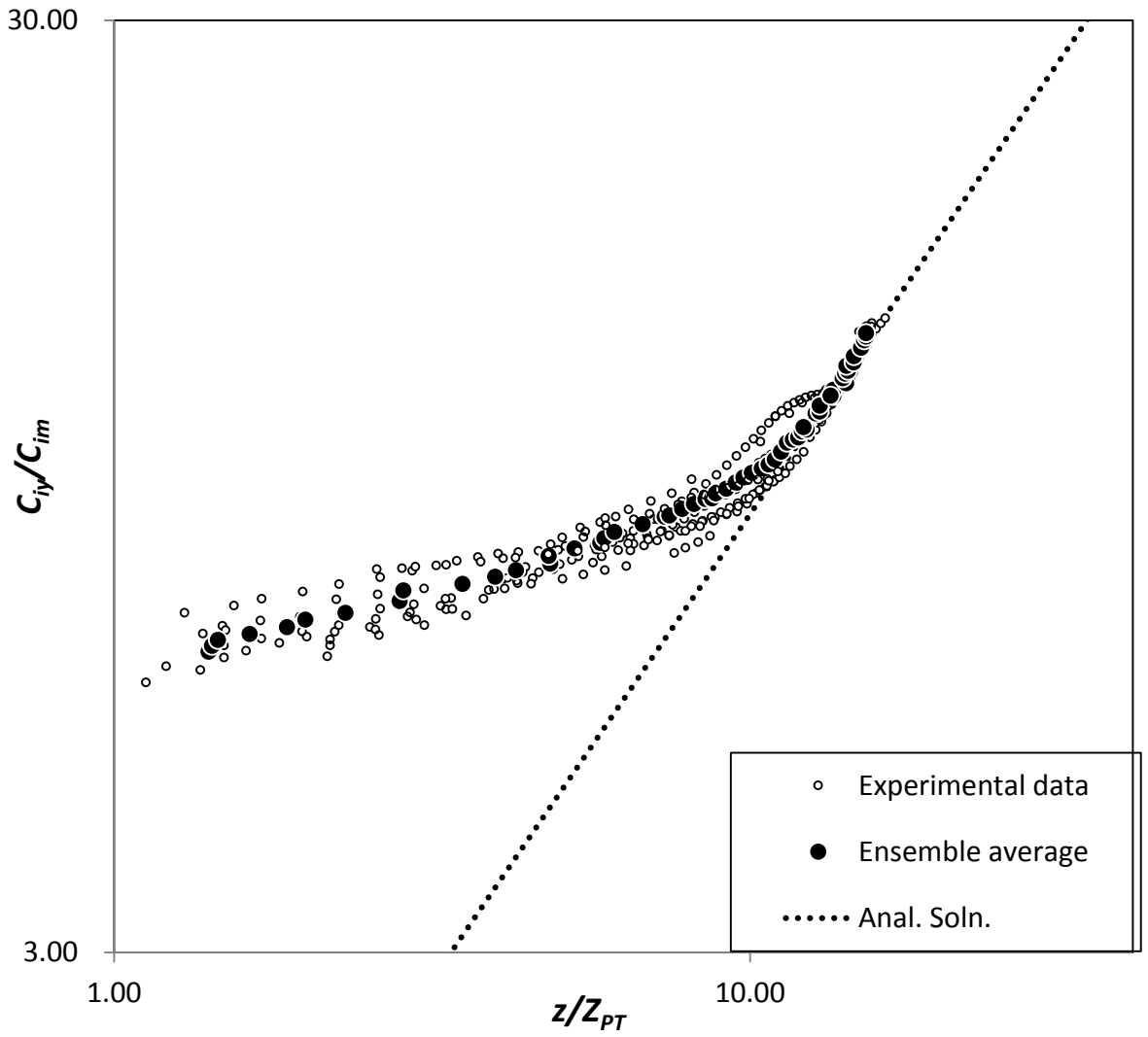

Figure 5-14: *y*-integrated dilution data from 90° discharges.

Figure 5-15 shows a three-dimensional view of the trajectory of the integrated concentration peaks from an individual experiment, where the initial discharge angle was 90°. Where two peaks are evident from the double-Gaussian fits to the measure profiles, two locations are shown at a particular cross-section, if not, a single location is shown. In this context, two peaks are defined if there is a measurable trough between the peaks. Initially, in region A, the flow has a single peak and is moving predominantly in the *y*-direction suggesting it is behaving as a weakly advected jet. At point B a double peak appears in the vertical plane as the flow becomes more progressively deflected by the ambient current, suggesting an advected line momentum puff has formed with the one counter rotating vortices located above the other. From the start the buoyancy grows in relative magnitude and apparently it starts to interfere with the double vortex structure. Between point B and C there is a growing deflection under the influence of gravity and

as the flow approaches point C it begins to fall more significantly in the vertical direction. Interestingly at point C two distinct peaks can no longer be detected and the flow can then best be approximated with a single peak distribution as it progresses through to point D. The formation of the double peak structure typical of an advected thermal occurs over a significant distance. At point D this second double peak distribution becomes evident. Here the two peaks are aligned in the horizontal plane, suggesting a line advected thermal has formed. This behaviour is generally consistent with that expected based on the length scale analysis, although the fact that there is an extended distance between the advected line puff and advected line thermal regions where a double peak distribution is not evident is unexpected. However, the lack of a double peak distribution where a line advected thermal is expected to form has been observed by Kikkert et al. (2009) and more recently by Lai and Lee (2012). The data suggesting that there is a significant transitional region where the flow structure is reorientated due to the change in the predominant driving force and during this the re-orientation the double peak distribution is lost.

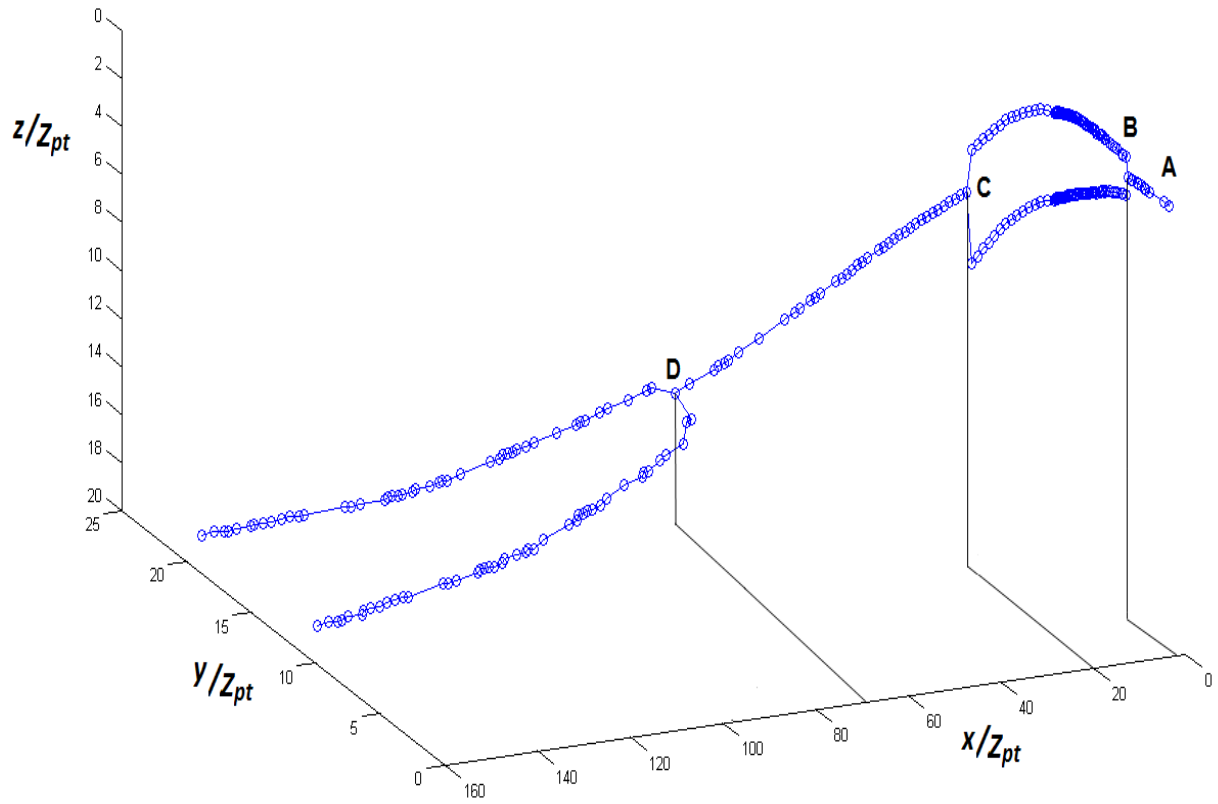

Figure 5-15: 3D view of the locations of the peaks of the fitted Gaussians for a 90° discharge.

Figure 5-16 shows in more detail the development of advected line puff from Figure 5-15, where the *z*-coordinate is shown on the vertical axis and on the s-coordinate on the horizontal axis; both

axes are non-dimensionalised with the jet to puff length scale. After the initial weakly-advected jet region, a double peak is seen to form, with the distance between the peaks increasing linearly with increasing distance from the source, as expected from chapter three. After a distance from the source of approximately nine length scales, the increase in peak distance arrests and vertical motion of the flow as a whole becomes more significant under the influence of gravity. Interestingly beyond this location the double peak does not seem to develop further in terms of peak separation, but the two peaks remain evident until approximately 25 length scales from the source.

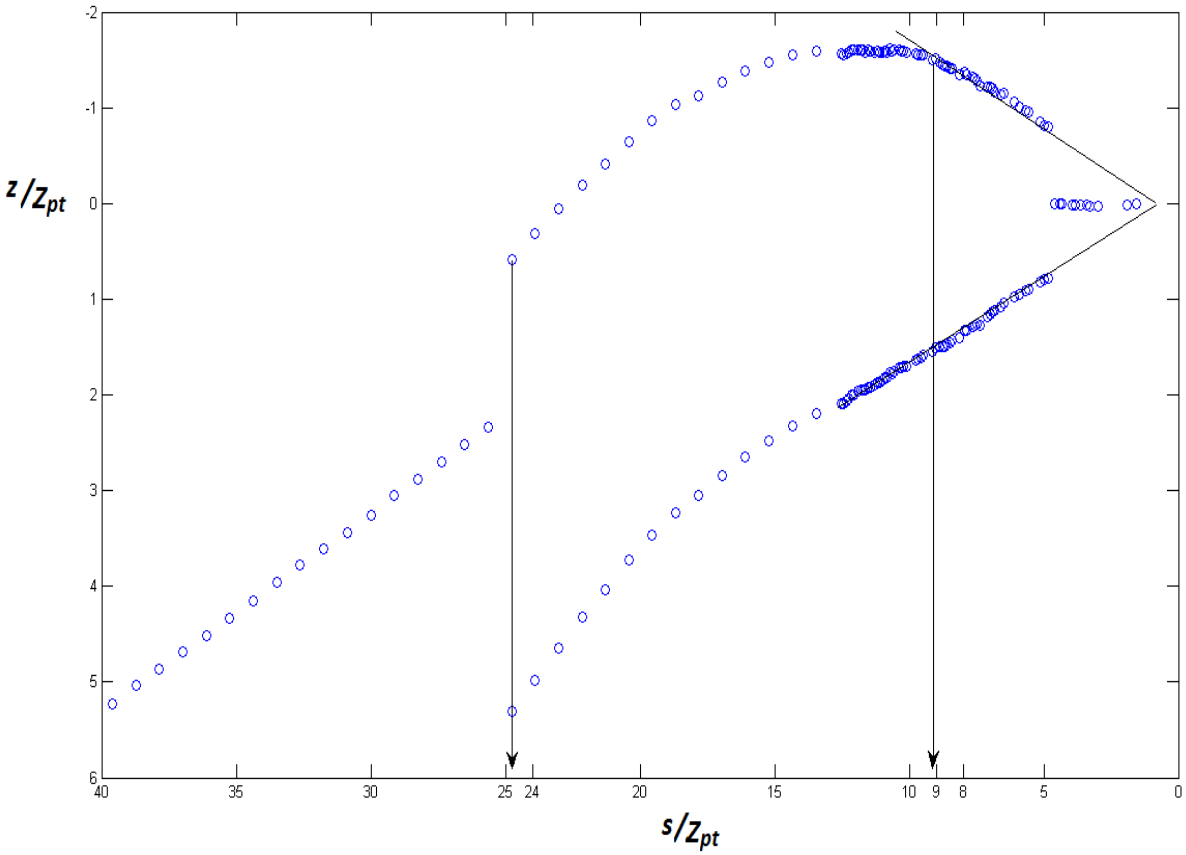

Figure 5-16: Vertical coordinates of the peak locations for a 90° discharge versus distance from the source.

In summary the results from phase I of the three-dimensional trajectory experiments shows that the trajectories of the 45° and the 90° discharges follow a similar pattern, both in *y*- and *z*-directions. However there is more variability in the location of the 45° discharges within an x-y plane, where the relative standard deviation becomes approximately 20%. In contrast the relative standard deviation for the 90° discharges is approximately 10% in an *x*-*z* plane. The variability in the location for both initial discharge angles within a vertical *x*-*z* plane is also approximately 10%. There is also variability in the integrated dilution results associated with individual

experiments, but there are no consistent trends in this variability and the behaviour is generally consistent with obtained from the ensemble average (Figure 5-13, Figure 5-14). Interestingly, the analytical solution is based on the advected thermals that follow two dimensional paths (chapter 3) and appears to provide a good approximation to the measured behaviour for these more complex three-dimensional trajectory flows, once they evolve into advected thermals.

5.5.2 Results from phase II of experimental study into discharges with three-dimensional trajectories

In this section the results from the eight sets of three-dimensional trajectory experiments (Table 5-2) into the behaviour of buoyant discharges in a moving ambient will be discussed. The aim of this section is to explore the impact of variations in the initial conditions on the evolution and final form of these flows. The experiments broaden the results obtained in phase I of the study where the flow behaviour for just two sets of initial conditions was studied in some detail through multiple repetitions of the same flow. Here fewer repetitions are carried out, so that a broader range of initial conditions can be explored. This reduction in repetitions can increase the error in the ensemble averages of the data, but comparisons between ensemble averages and varying numbers of repetitions from the phase I experiments, indicates that the variability is likely to be within 10% for trajectory results and decreasing with distance for the dilution results.

In this section the trajectory results will be shown first, followed by the dilution and spread results. After this the *f*- and *h*-values will follow. In Figure 5-17 three images of integrated concentration intensities are shown for individual realisations of the flows for initial discharge angles of 22° (top), 45° (middle), and 90° (bottom). These images are integrated along lines that are essentially parallel to the *y* axis, so that the information presented rests in the *x*-*z* plane. The flows are discharged on the top right of the image and they evolve towards the lower left in the images. Consistent with Figure 5-15 in the image for the 90° discharge a double peak profile is clearly evident (suggesting the formation of an advected puff), but the twin peaks disappear as the flow evolves, moving predominantly in *x*-direction due to ambient motion. The middles image shows data from the 45° discharge image, where two peaks are distinguishable but they disappear relatively quickly. Again suggesting that an advected line puff has formed in this case, prior to it evolving into an advected thermal. As expected in the 22° discharge case (top image)

there is no evidence of a double peak distribution and hence no evidence of the formation of an advected line puff.

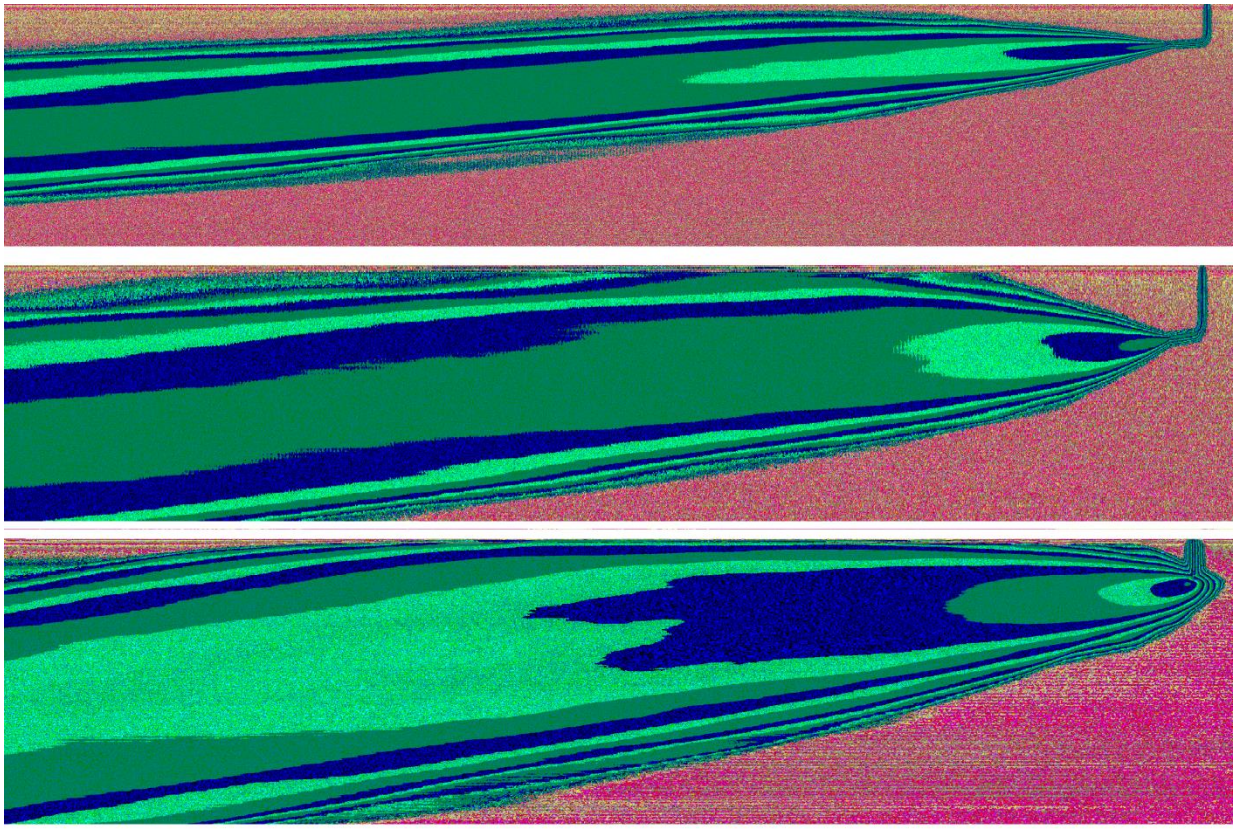

Figure 5-17: False colour images of *y*-integrated concentration profiles of a 22° discharge (top), 45° discharge (middle) and a 90° discharge (bottom).

To date the data has been scaled with the plume to thermal transition length scale (Z_{pt}), which is somewhat counterintuitive given the plume to thermal transition is not expected to occur for these flows. With the expansion of the range of initial conditions in the phase II experiments, it is possible to explore the impact of different length-scales in collapsing the data. In the following four figures the trajectories of several experiments are shown and these have been non-dimensionalised with a different length scales. The horizontal and vertical axes have been scaled with the jet to advected line momentum puff length scale, S_{JM} (Figure 5-18), the jet to advected plume length scale, S_{SP} (Figure 5-19), the advected line momentum puff to advected thermal length scale, L_{MT} (Figure 5-20), and the advected plume to advected thermal length scale, Z_{PT} (Figure 5-21). In Figure 5-18 and Figure 5-21, the analytical solution is added for comparison and sets from angles other than 90° are included. The main area of interest is further from the source, which is the region where the advected thermal is expected to form and hence buoyancy

plays an important role. The different trajectories from the experiments and the analytical solutions collapse most effectively in Figure 5-21; indicating the plume to thermal length scale is the most relevant length scale for these discharges. The implication is that buoyancy plays a more significant role than the length-scale analysis suggests in defining the transition to advected thermal behaviour, which is possibly consistent with the loss of a double peaked distribution during the transformation from line momentum puff to advected thermal evident in Figure 5-15.

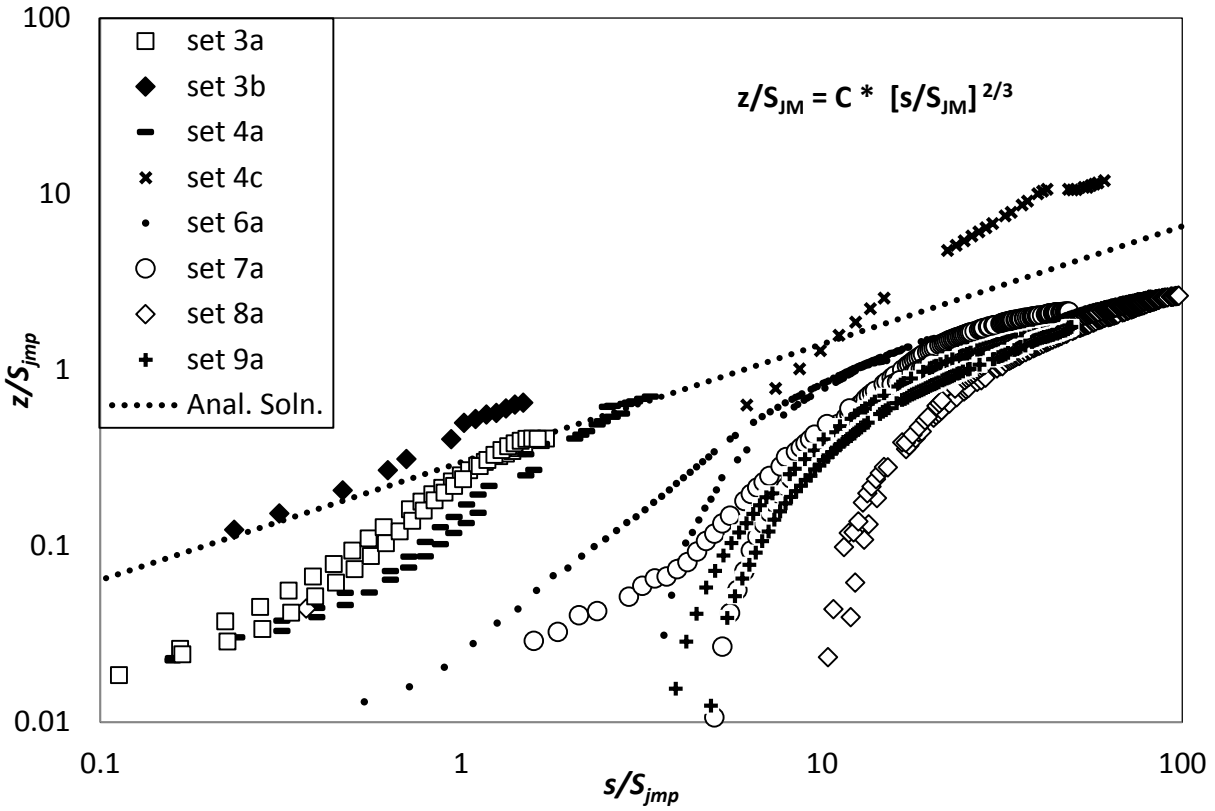

Figure 5-18: Trajectories of several 3D experiments, non-dimensionalised with the jet to momentum puff length scale. The analytical solution for a trajectory is added for reference.

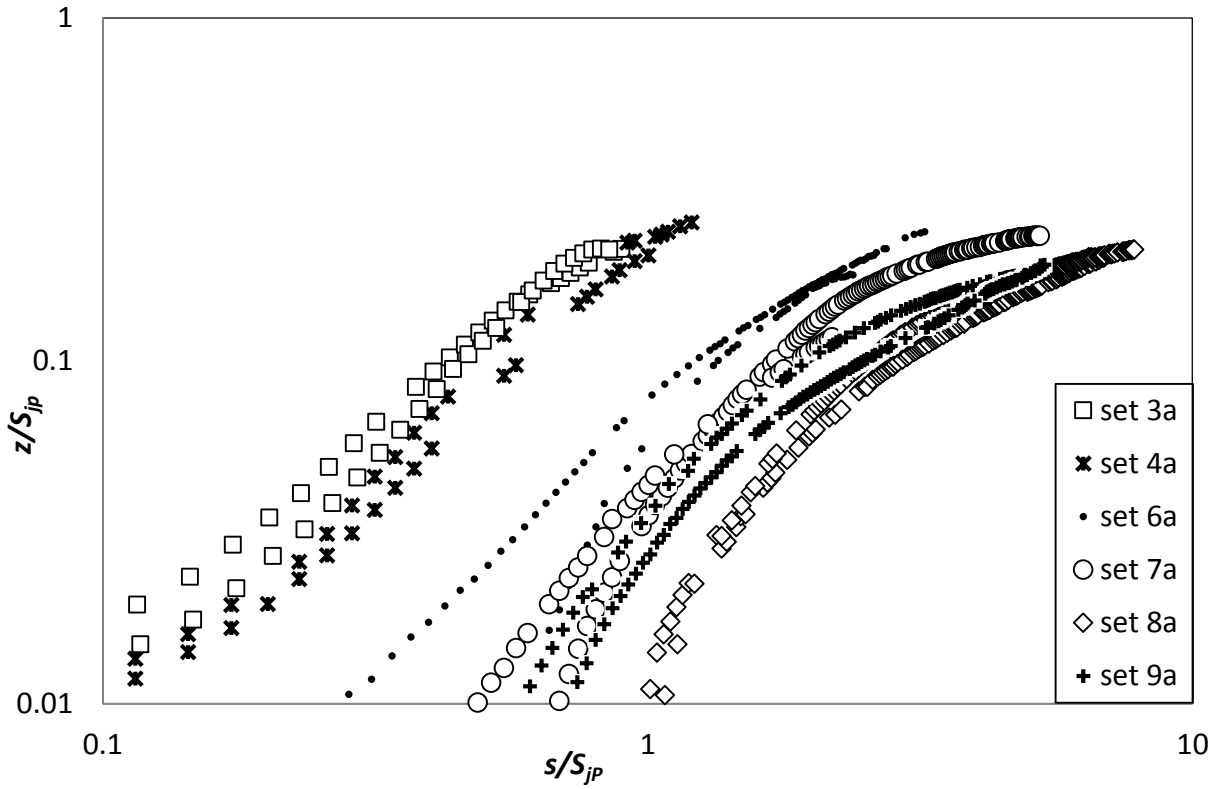

Figure 5-19: Trajectories of several 3D experiments, non-dimensionalised with the jet to advected plume length scale.

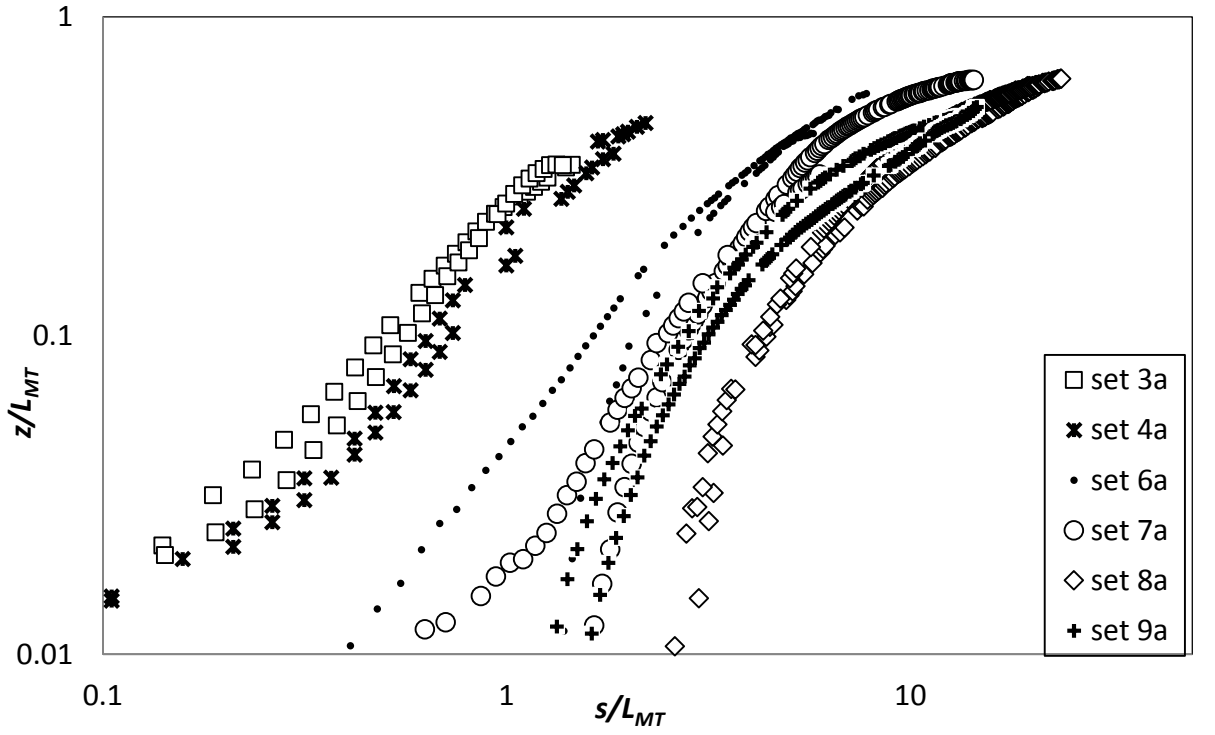

Figure 5-20: Trajectories of several 3D experiments, non-dimensionalised with the momentum puff to thermal length scale.

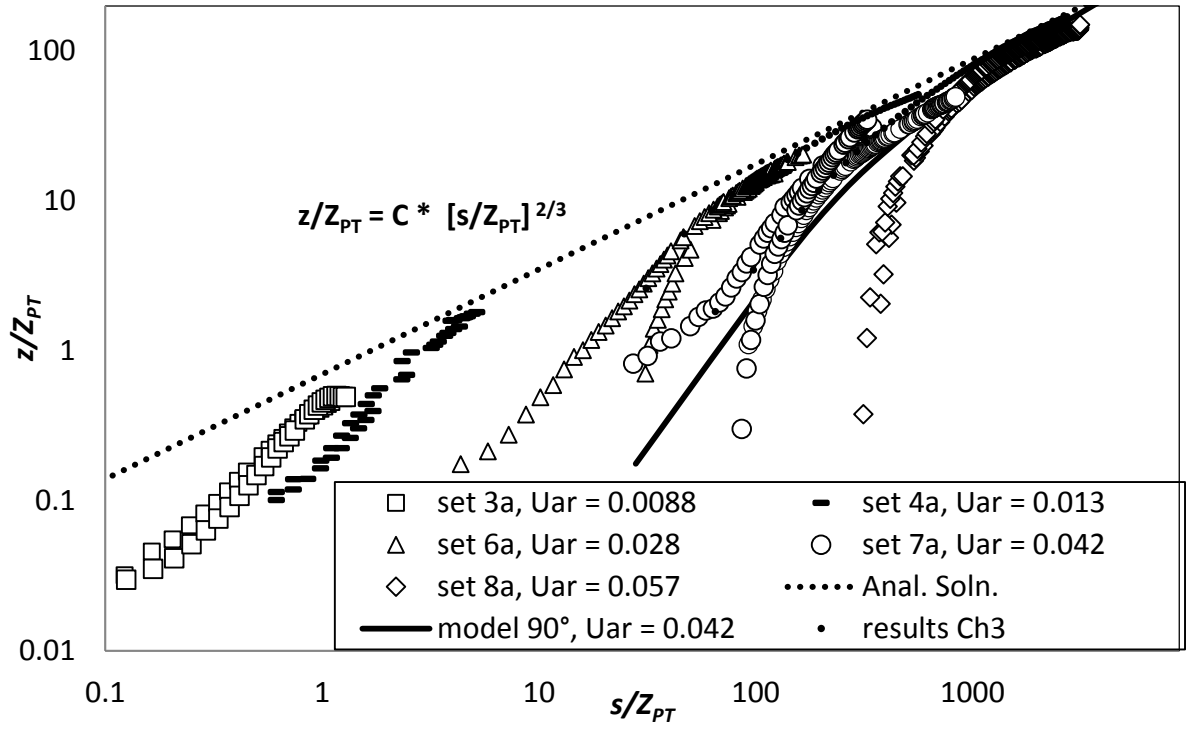

Figure 5-21: Trajectories of several 3D experiments, non-dimensionalised with the advected plume to thermal length scale. The analytical solution for a trajectory is added for reference.

Figure 5-22, Figure 5-23, and Figure 5-24 show the trajectory results from the eight sets of experiments, with discharge angles of 90°, 45° and 22°, and a relative ambient velocity ranging from 0.0042 to 0.0570 (Table 5-2). Included in the figure are results from discharges that follow a two dimensional path (chapter 3), along with analytical and numerical solutions for an advected thermal. The numerical model predictions are based on an ambient to initial velocity ratio, U_{ar}, of 0.042.

In the figure the experimental results tend towards the analytical solution, especially the results of the sets with the higher U_{ar} values and corresponding lower Z_{pt} values. These results lie more towards the right top of the graph. The data on the lower left side of the graph progresses towards the analytical solution, but does not necessarily reach it. This data belongs to experiments, both of 45° and 90°, which were discharged in a relatively slow ambient velocity. Thus only a small portion of the experiments could be used as the flows quickly suffered from boundary (side wall) effects. This progression towards the analytical solution is also evident in the numerical model predictions, which specifically models the advected thermal flow regime. It is therefore possible for the advected thermal to form prior to characteristic behaviour evident in the analytical solution becoming obvious. It is some distance beyond the transition to the advected thermal

behaviour, before evidence in the trajectories of the initial conditions or previous flow regimes is reduced to the point that consistency with the analytical solutions is achieved. However, all data sets obtained show this tendency to become progressively consistent with the advected thermal analytical solution and this suggests all flows evolve into this form, as expected based on our understanding of discharges that follow two-dimensional paths.

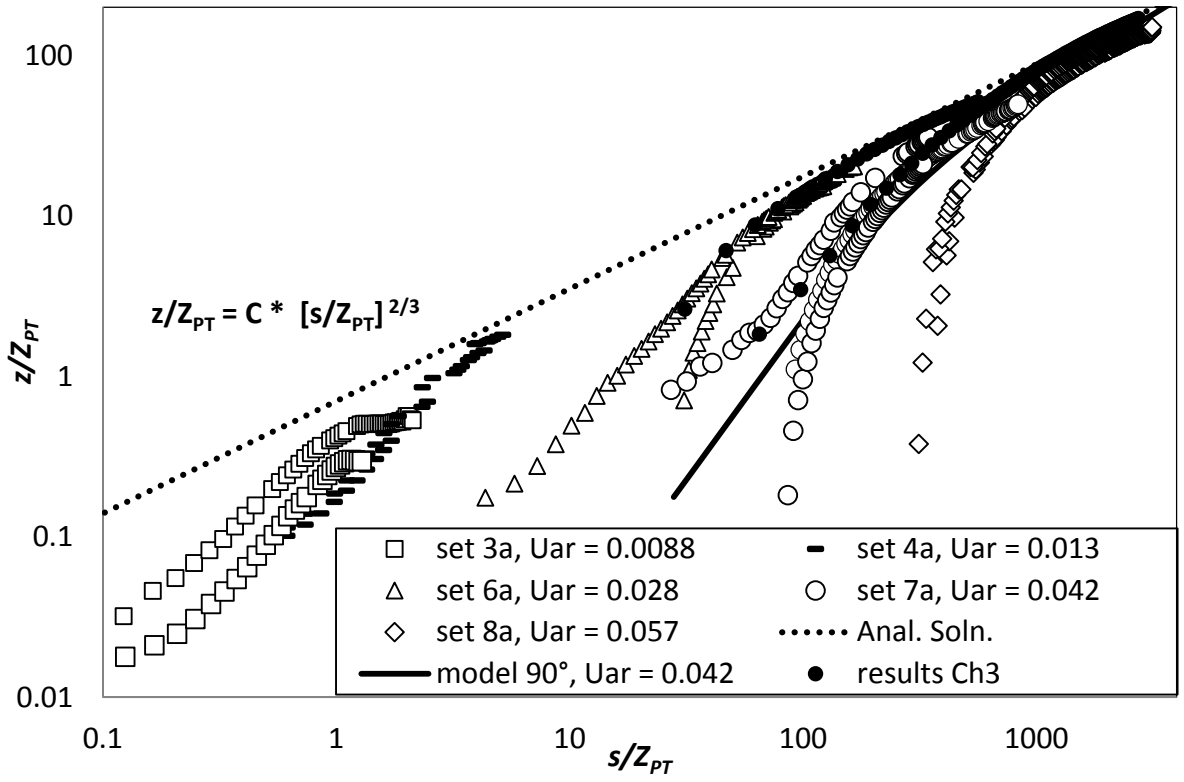

Figure 5-22: Trajectory results of 90° discharges, including the analytical solution, the model at U_{ar} of 0.0042 and results from 2D thermals from Chapter 3.

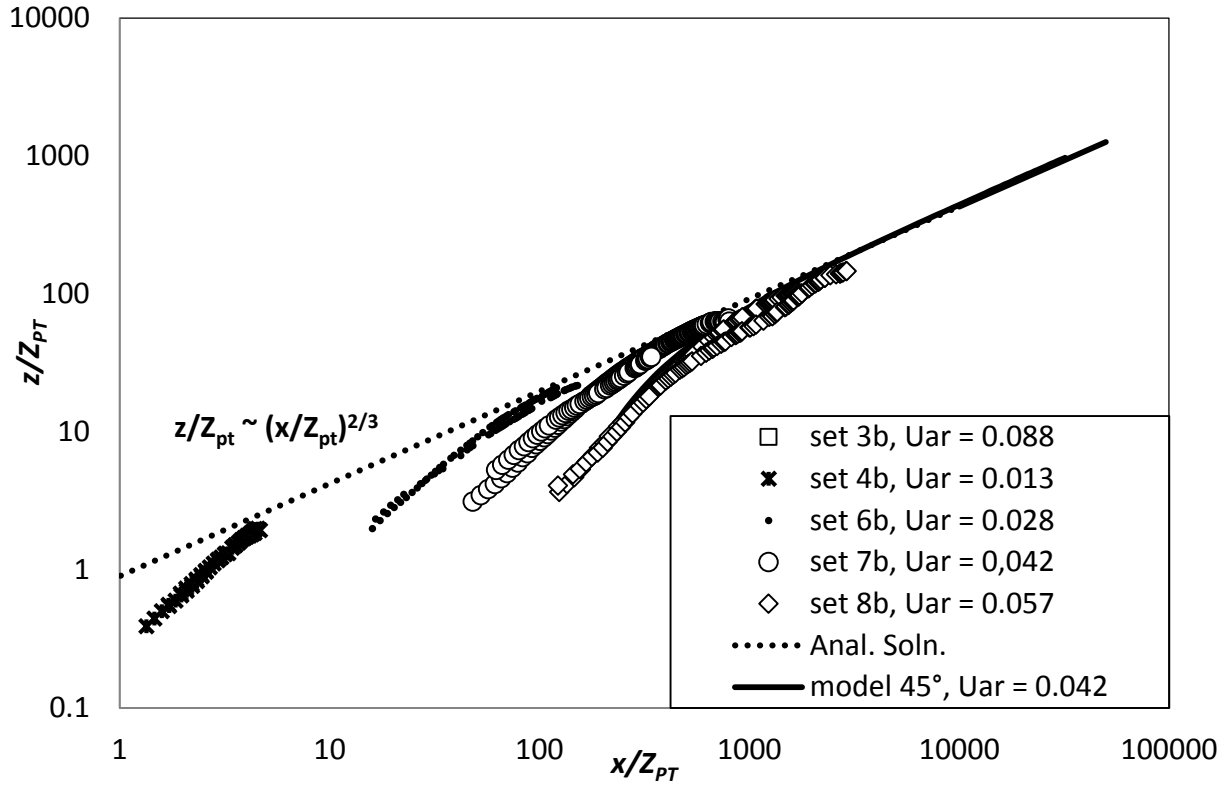

Figure 5-23: Trajectory of 45° discharges, including the analytical solution and the model at U_{ar} of 0.042.

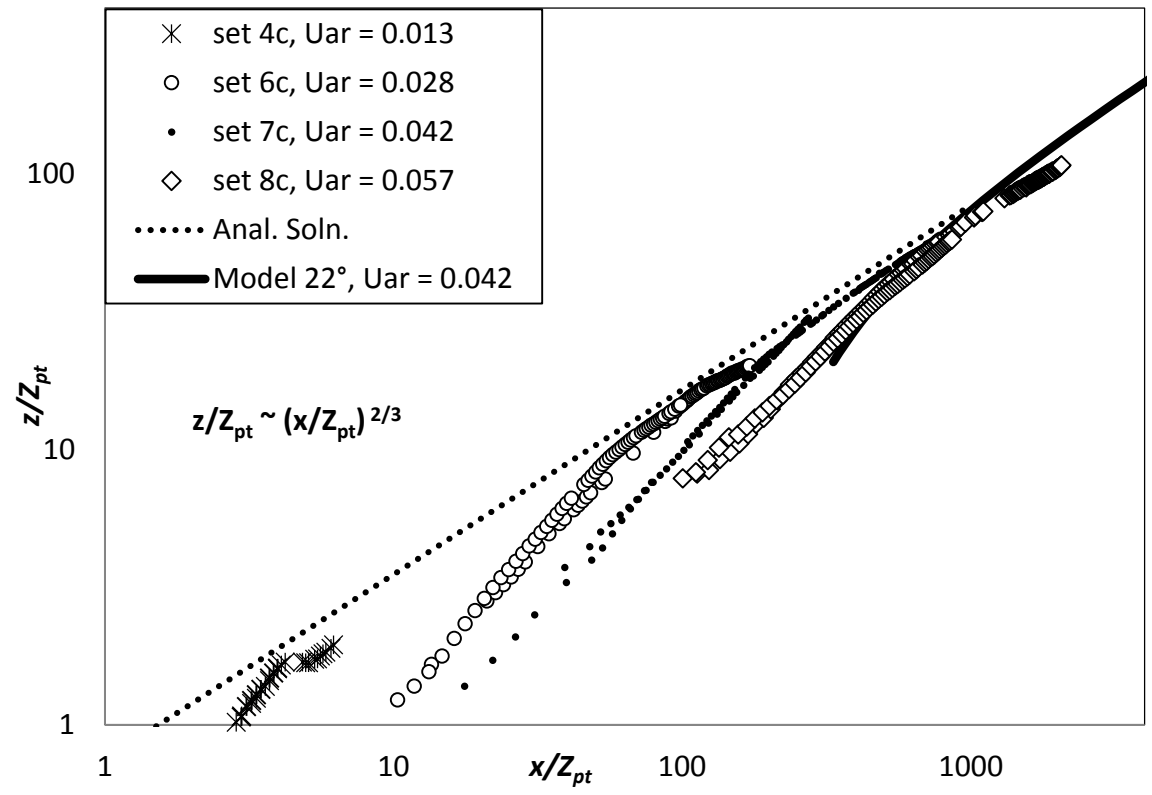

Figure 5-24: Trajectory of 22° discharge, including the analytical solution and the model at Uar of 0.042.

The cross-sectional *y*-integrated and *z*-integrated dilution results are depicted in Figure 5-25 respectively Figure 5-28. The horizontally integrated results show the maxima or peaks of the single Gaussians fits of the measured integrated dilution values, while the vertically integrated results are the average of the two maxima of the fitted double Gaussian of the measured integrated dilutions. For comparison data from 2D trajectory advected thermals (see chapter 3), the analytical solutions and the model predictions are added.

The data sets converge to a trend line with a slope of 0.86 and 0.67 respectively. The ratio between these slopes is 2/h (see chapter 3, Equation 5-17 and 5-18. Unlike some of the 2D trajectory data, there is no need for a virtual source for the 3D trajectory experiments, because the initial conditions do not create any motion in the *z*-direction. However, the differing initial conditions result in variations of the evolution of the flow, which introduced some apparent scatter in the data. However, this variation is consistent with the predicted behaviour based on the integral model. The data does not collapse perfectly with the model in the transitional area as expected.

It is possible to convert the integrated dilution data in Figure 5-25 and Figure 5-28 into centreline minimum dilution data. Like the 2D trajectory data in chapter 3, the present data from *y*-integrated and *z*-integrated mean concentration profiles are consistent with the minimum dilution data and are also in good agreement with prediction from the analytical solutions for advected thermals. Agreement with the analytical solutions is based on a top-hat to minimum dilution conversion factor of 3.3 (chapter 3).

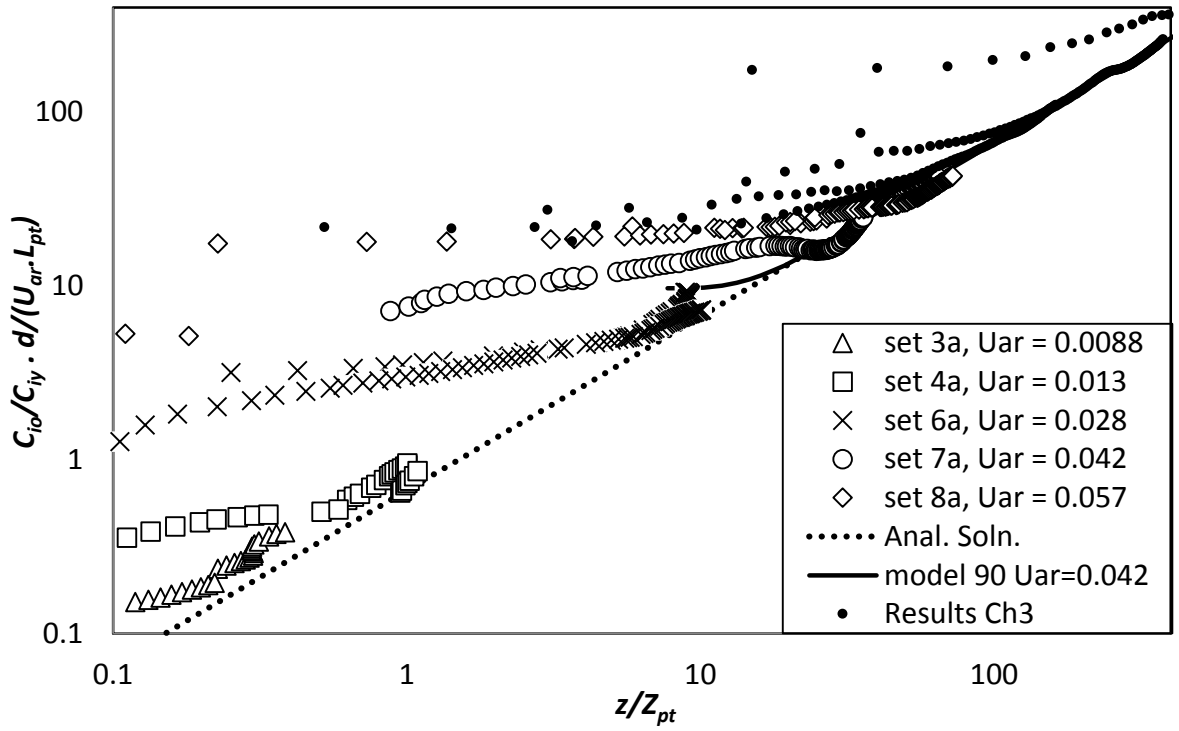

Figure 5-25: *y*-integrated dilution results from 90° discharges including the analytical solution, a model solution at U_{ar} of 0.042 and results from chapter 3.

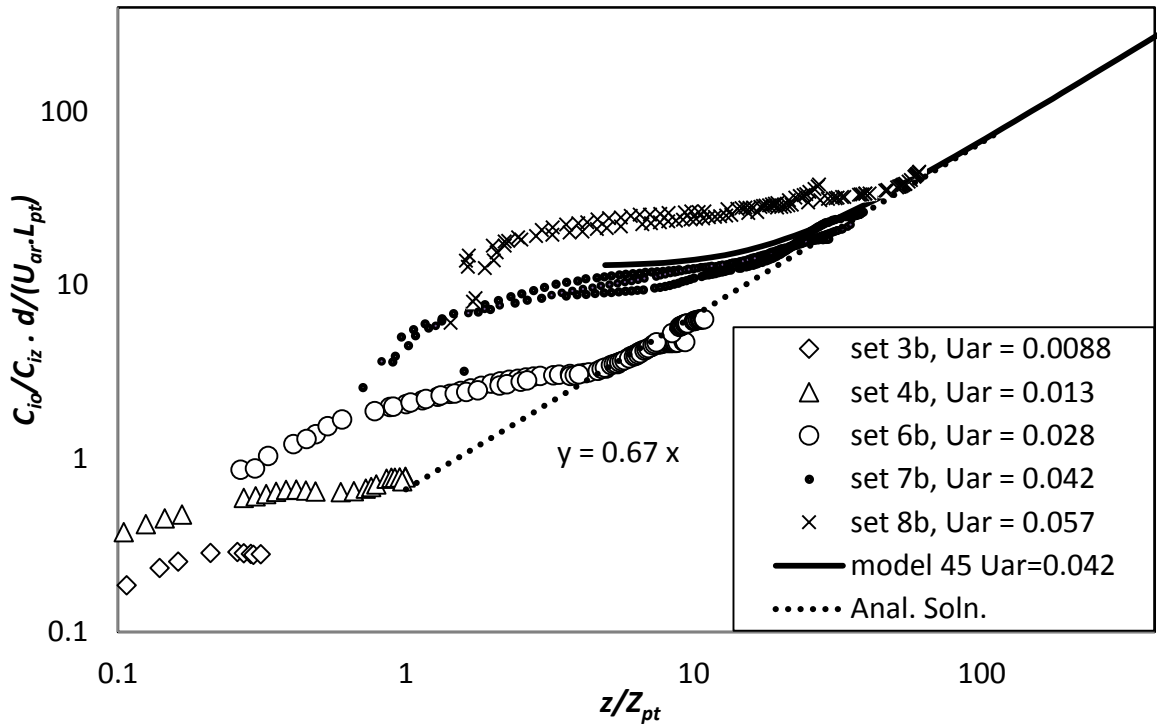

Figure 5-26: *y*-integrated dilution results from 45° discharges including the analytical solution, and a model solution at U_{ar} of 0.042.

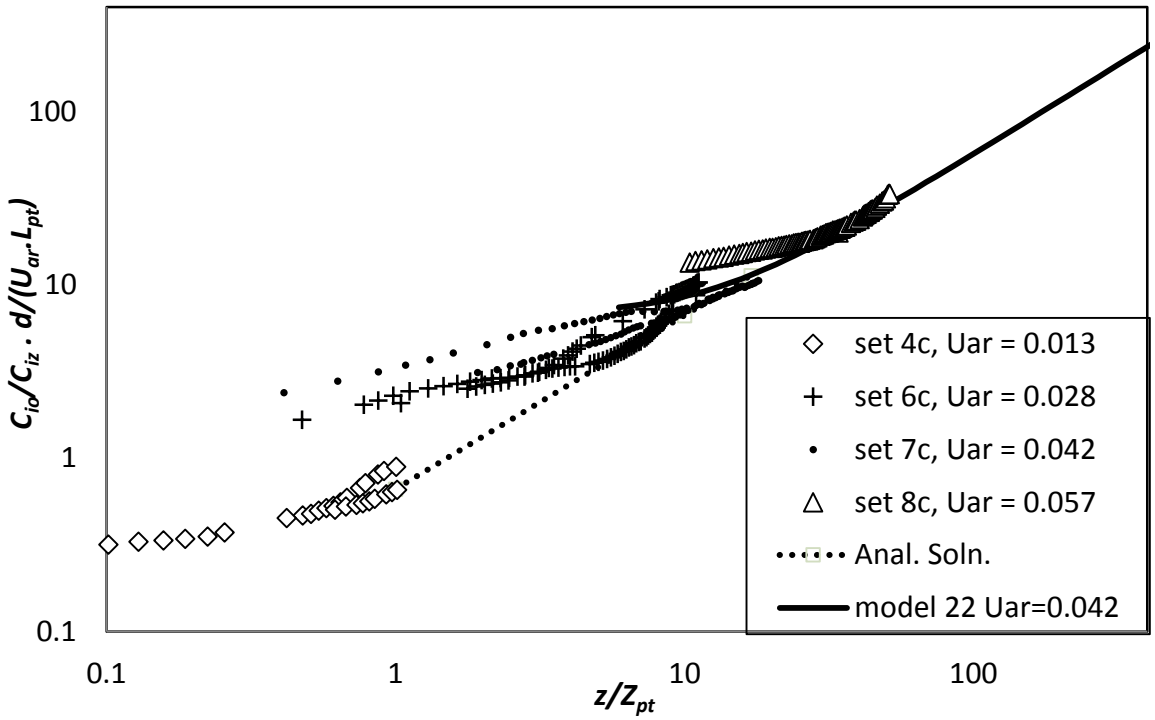

Figure 5-27: *y*-integrated dilution results from 22° discharges including the analytical solution, and a model solution at U_{ar} of 0.042.

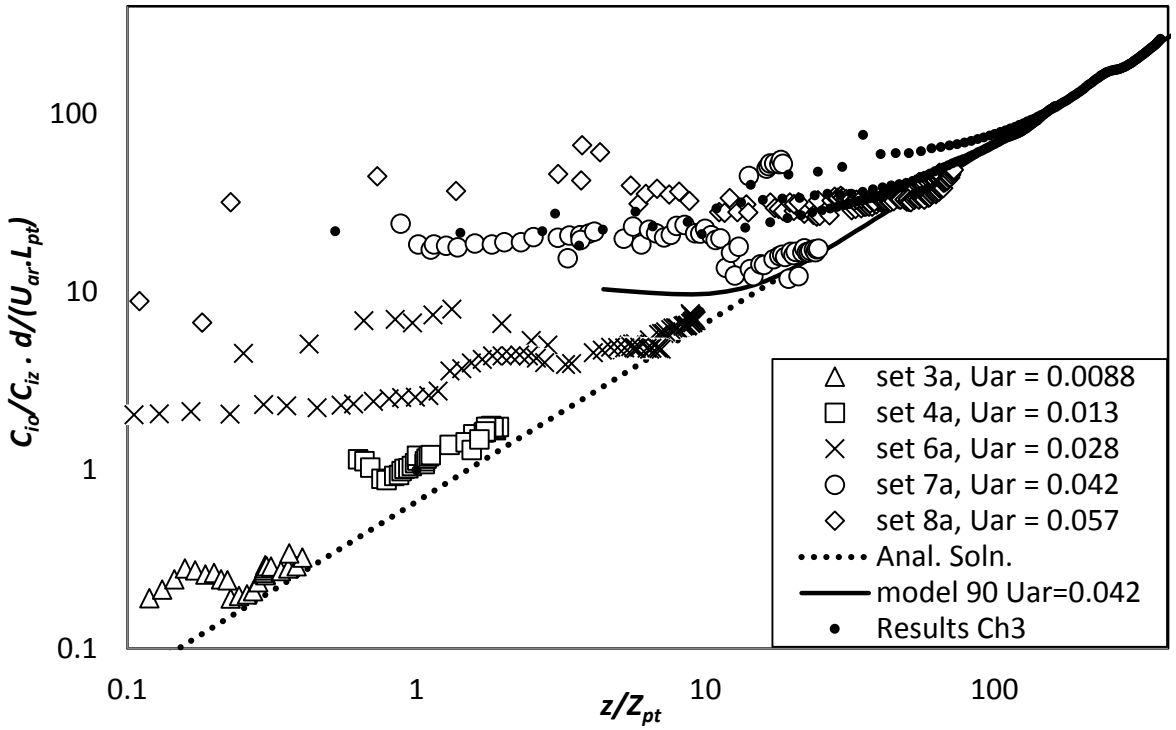

Figure 5-28: *z*-integrated dilution results from 90° discharges including the analytical solution, a model prediction at U_{ar} of 0.042 and results from chapter 3.

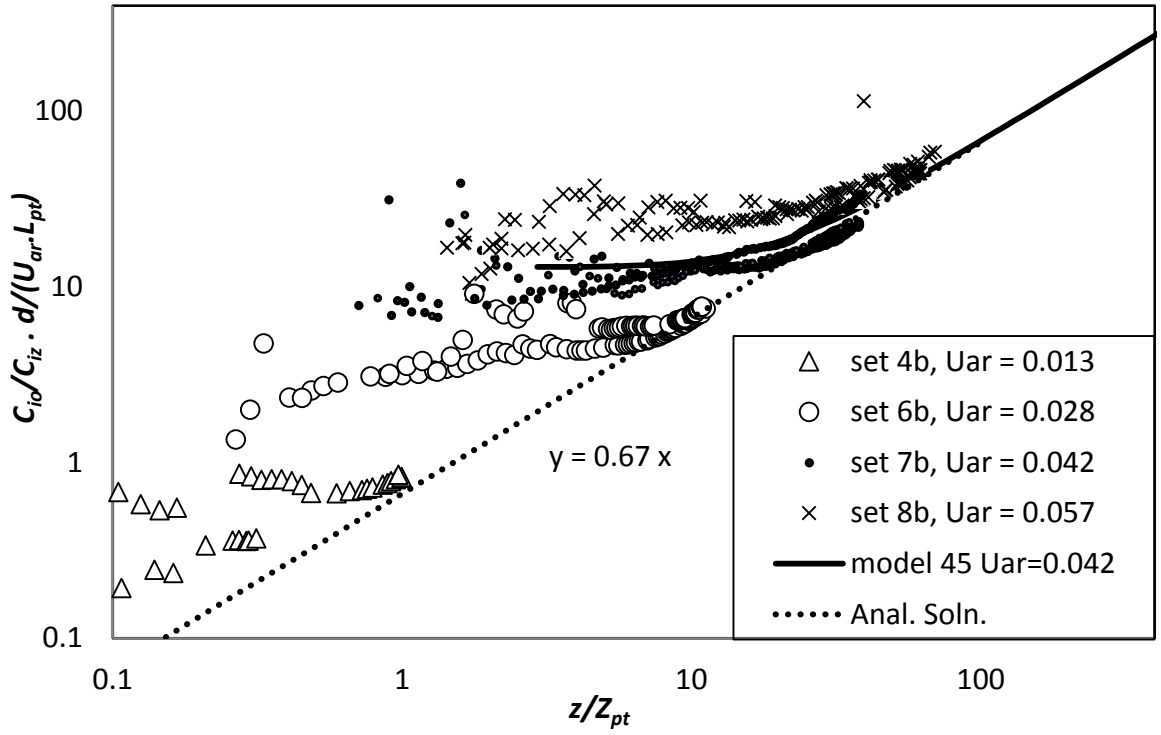

Figure 5-29: *z*-integrated dilution results from 45° discharges including the analytical solution, a model prediction at U_{ar} of 0.042 and results from chapter 3.

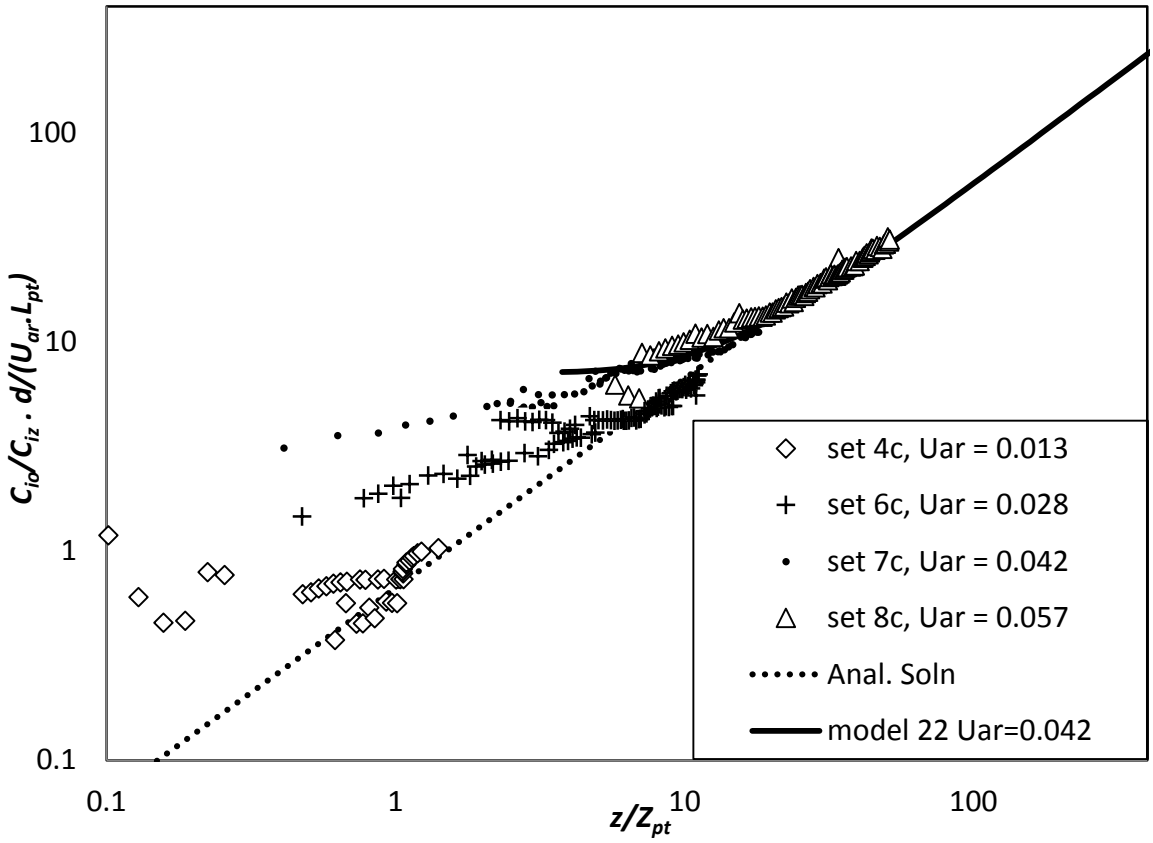

Figure 5-30: *z*-integrated dilution results from 22° discharges including the analytical solution, a model prediction at U_{ar} of 0.0042 and results from chapter 3.

The spread data from the 3D trajectory experiments are presented in Figure 5-31 through to Figure 5-36. The first three figures show the spread of the *y*-integrated profiles from respectively the 90°, 45° and the 22° discharge, the second three figures show the spread of the *z*-integrated profiles for the same initial discharge angles. The spread data from the 3D trajectory experiments are presented in Figure 5-31 through to Figure 5-36. The first three figures show *y*-integrated data from respectively the 90°, 45° and the 22° discharge, the second three figures show the same discharges integrated in *z*-direction. In Figure 5-31 the *y*-integrated flow spread in the strongly advected region can be represented by a linear relationship with gradient of 0.40, which is consistent with the 2D trajectory advected thermal experiments (chapter 3). There is additional scatter in the data because of the more complex flow evolution, but as with the dilution data there is no need for a virtual source, because the vertical displacement associated with these preceding regimes is not significant.

Integrated spread data is presented in Figure 5.31 to 5.36, starting with the *y*-integrated spread data from the 90°, 45° and 22° discharge data, followed with the respective *z*-integrated data in the last three figures. In all the figures the appropriate model predictions and the best fit lines through data from advected thermals with two-dimensional trajectories (chapter 3) have been added and the data is plotted against dimensionless vertical distance. Figure 5-31 and Figure 5-34 (90° discharges) have been supplemented with experimental data from chapter 3. The spread data obtained from *z*-integrated concentration profiles is the average spread of the separate vortices as approximated with a best fit double-Gaussian distribution and the linear trend line has a slope of 0.25. The *y*-integrated data has been approximated with a single-Gaussian distribution and the slope of the linear trend line is 0.40. The slope values are consistent with those obtained in chapter 3, which itself was consistent with data from Kikkert et al. (2007) and the spread ratio of 1.5 is in agreement with the *h*-value shown in Figures 5-40 to Figure 5-42.

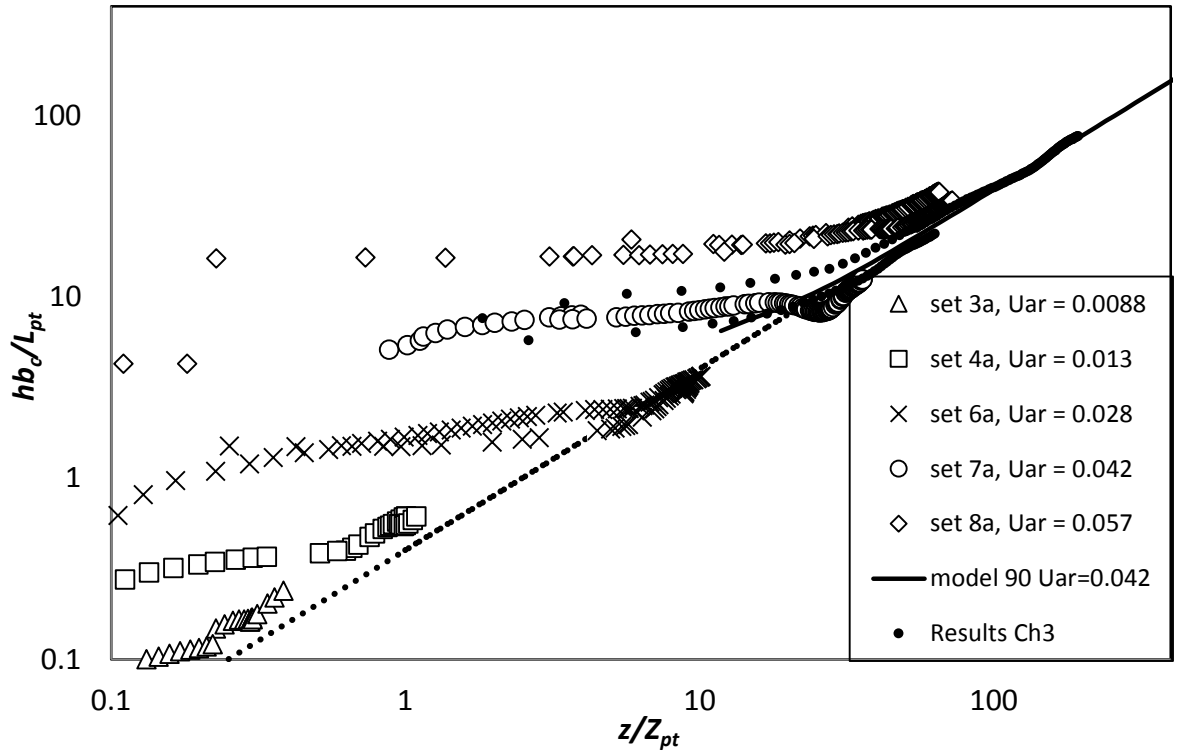

Figure 5-31: *y*-integrated spread results from 90° discharges, including results from chapter 3 and the model predictions at U_{ar} of 0.042.

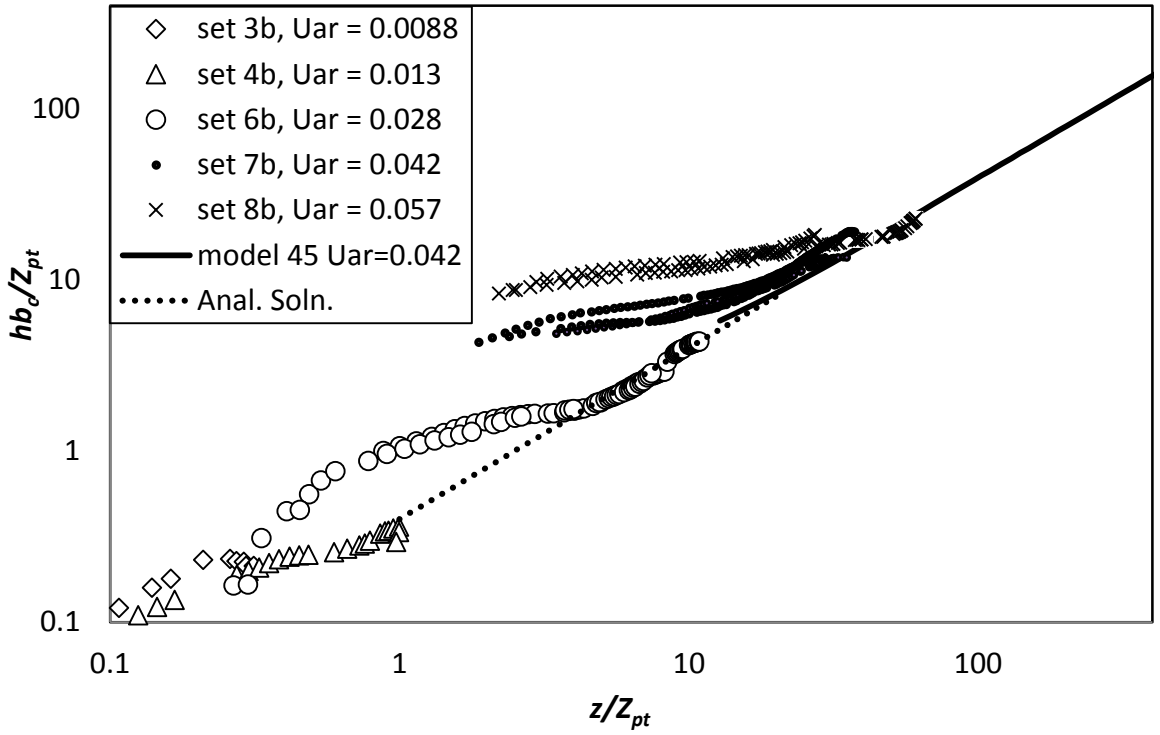

Figure 5-32: *y*-integrated spread results from 45° discharges, including results from chapter 3 and the model predictions at U_{ar} of 0.042.

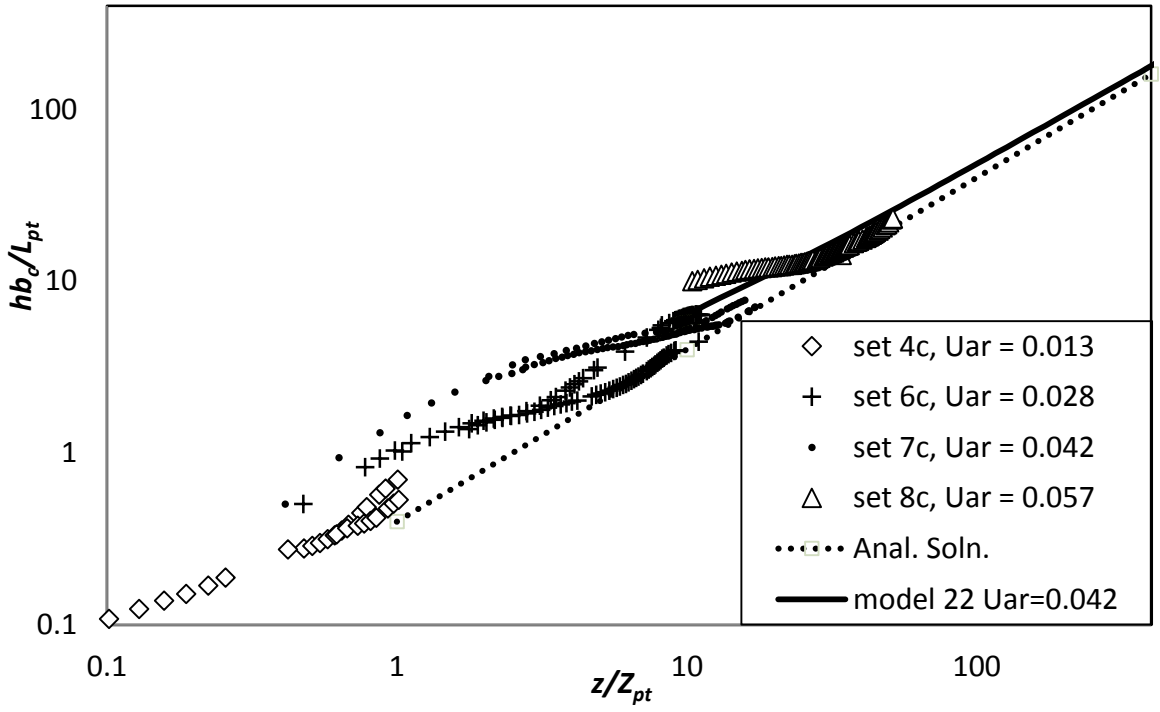

Figure 5-33: *y*-integrated spread results from 22° discharges, including results from chapter 3 and the model predictions at U_{ar} of 0.042.

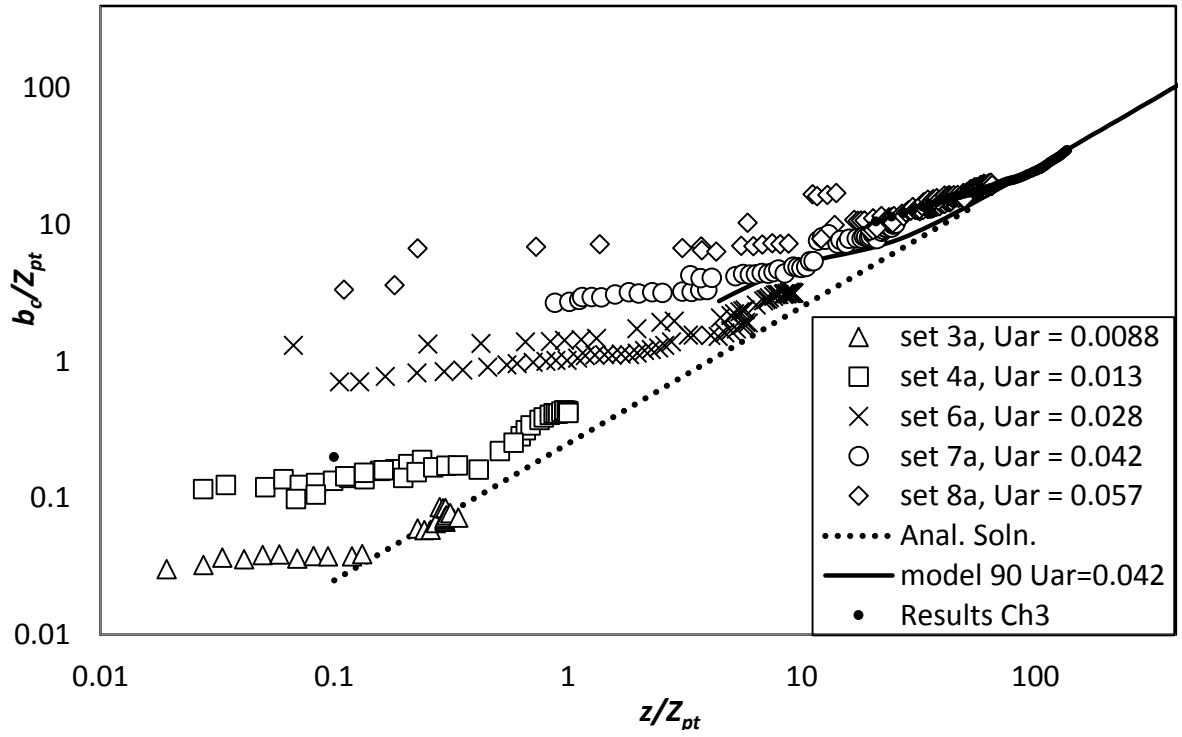

Figure 5-34: *z*-integrated spread results from 90° discharges, including results from chapter 3 and the model predictions at Uar of 0.042.

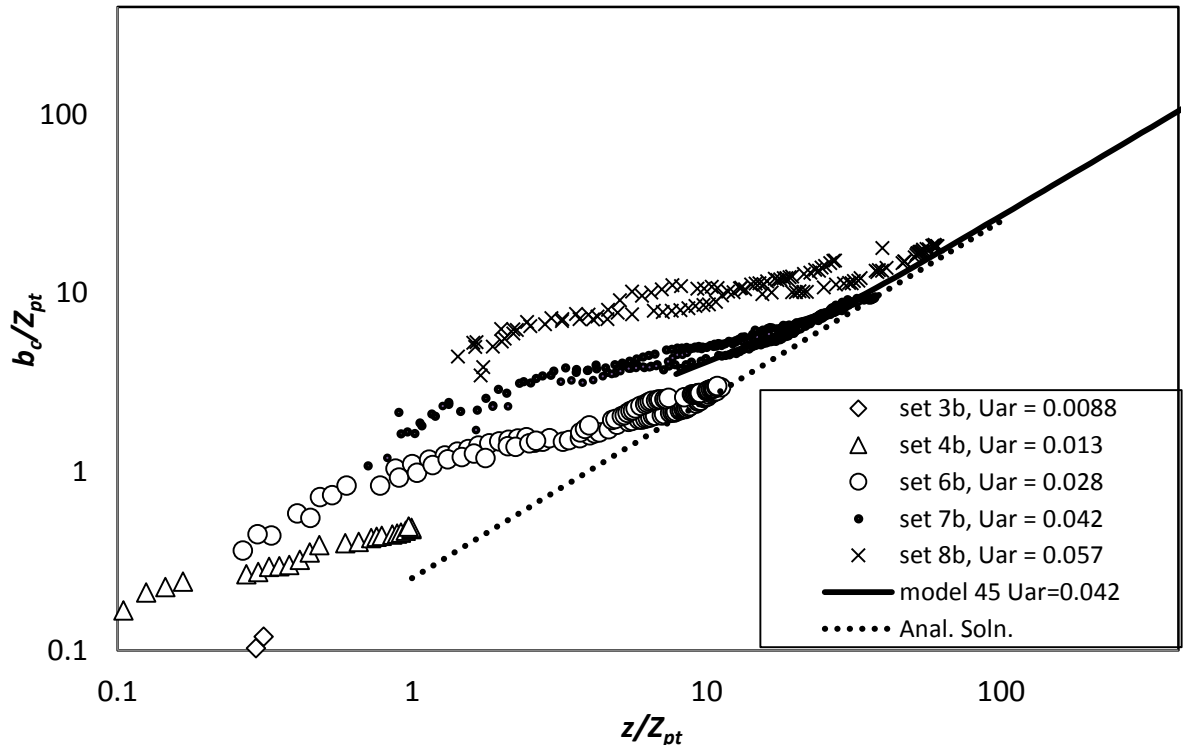

Figure 5-35: *z*-integrated spread results from 45° discharges, including the model predictions at U_{ar} of 0.042.

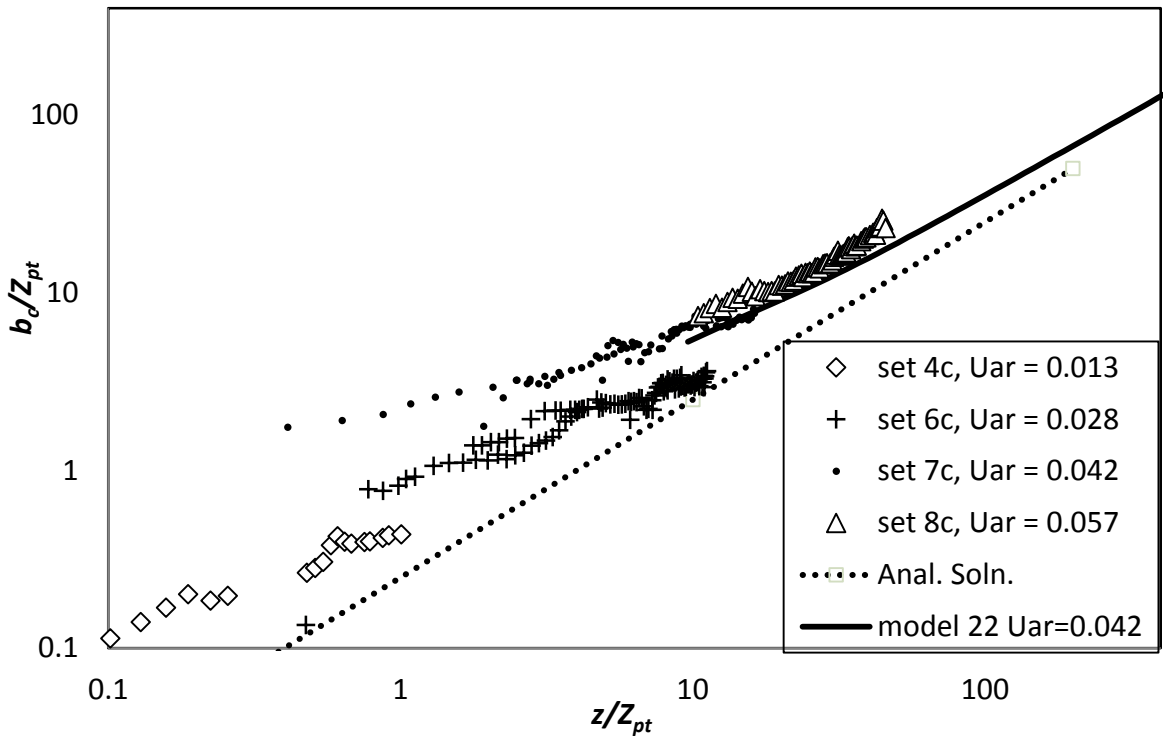

Figure 5-36: *z*-integrated spread results from 22° discharges, including the model predictions at U_{ar} of 0.042

The *f*-values for the 3D trajectory experiments are shown in Figure 5-37 (90° discharges) in Figure 5-38 (45° discharges) and in Figure 5-39 (22° discharges) and are summarised in Table 5-6. In Figure 5-39 values below 0.58 have been filtered out. The reference value from the 2D trajectory line advected thermals experiments (chapter 3) is 1.02. The 90° and the 22° discharge data are reasonably consistent with this value although a lot more scatter is present. The average *f*-value is 1.06 respectively 1.08 for the two discharges, the value 1.02 is close and falls within 1 standard deviation of these values. The 45° discharge however is not consistent with this value, showing a larger and continually increasing *f*-value. If an *f*-value is calculated from the experimental data it would be around 1.33 with a standard deviation of 0.06. The 45° discharges are more asymmetric and tilted, compared to the 90° discharges, which could attribute to the inconsistent results.

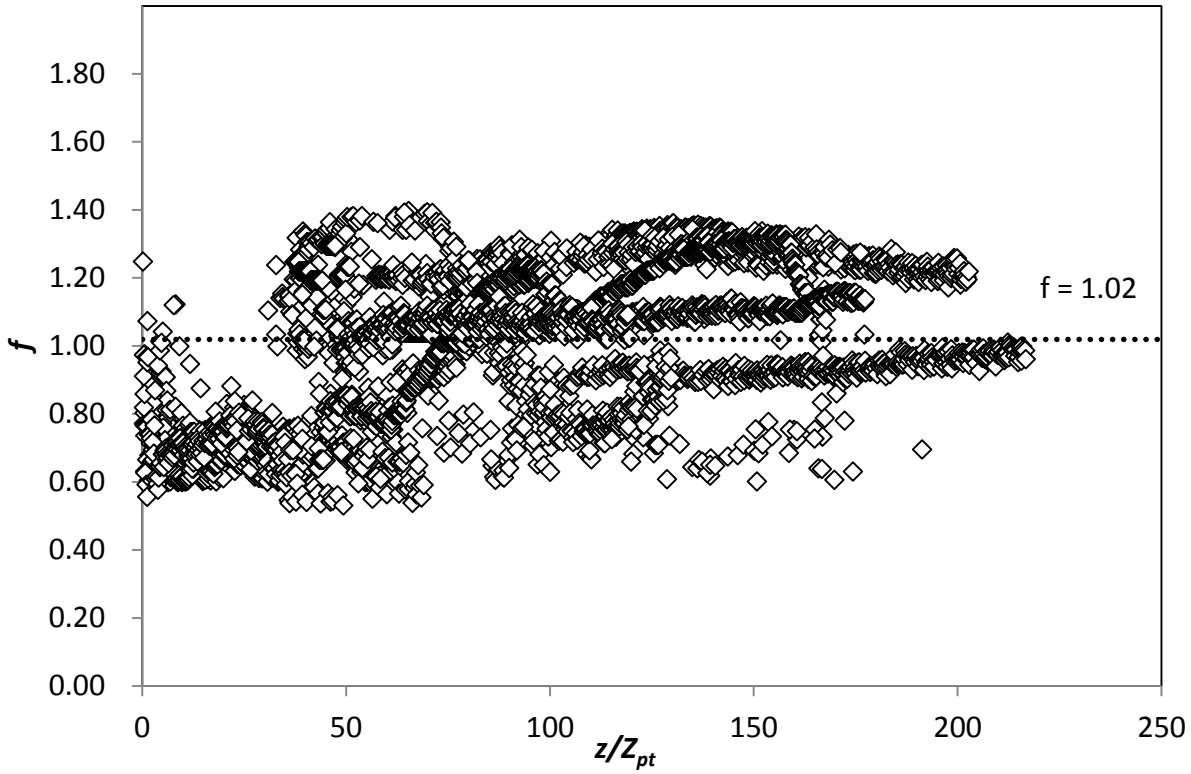

Figure 5-37: *f*-value for 90° experiments. The *f*-value from chapter 3 is included for reference.

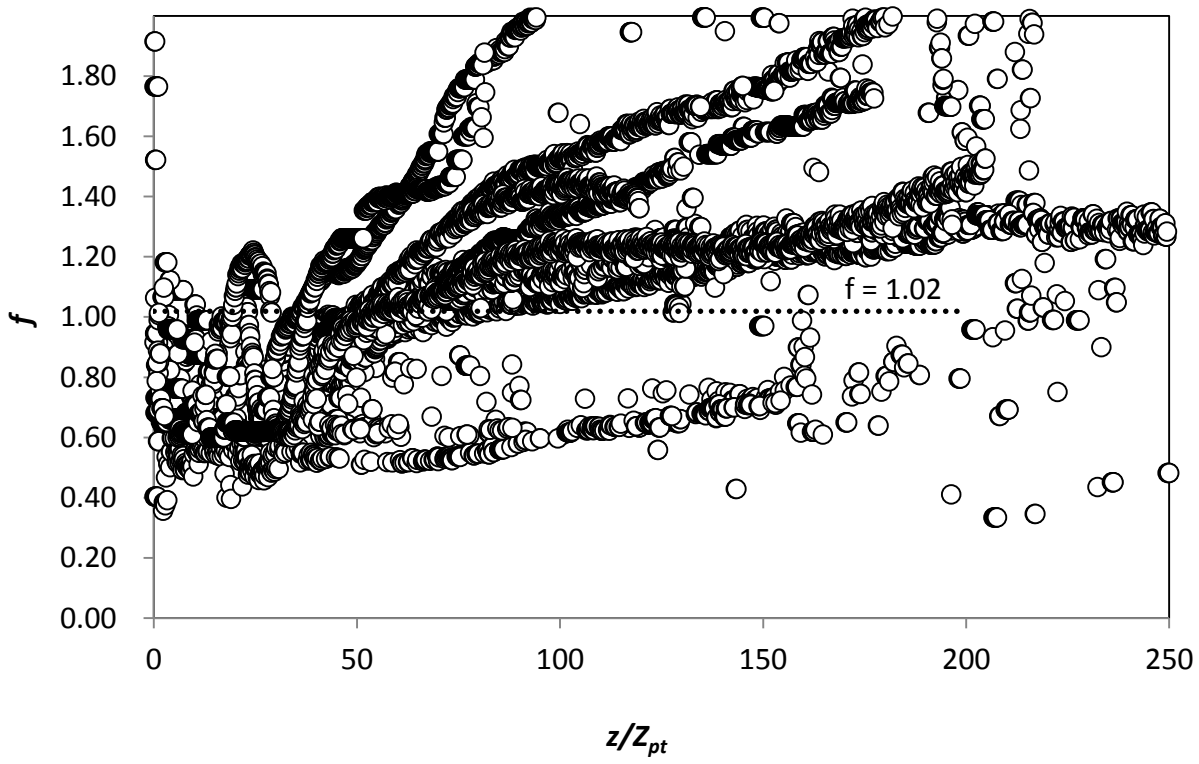

Figure 5-38: *f*-value for 45° experiments. The *f*-value from chapter 3 is included for reference.

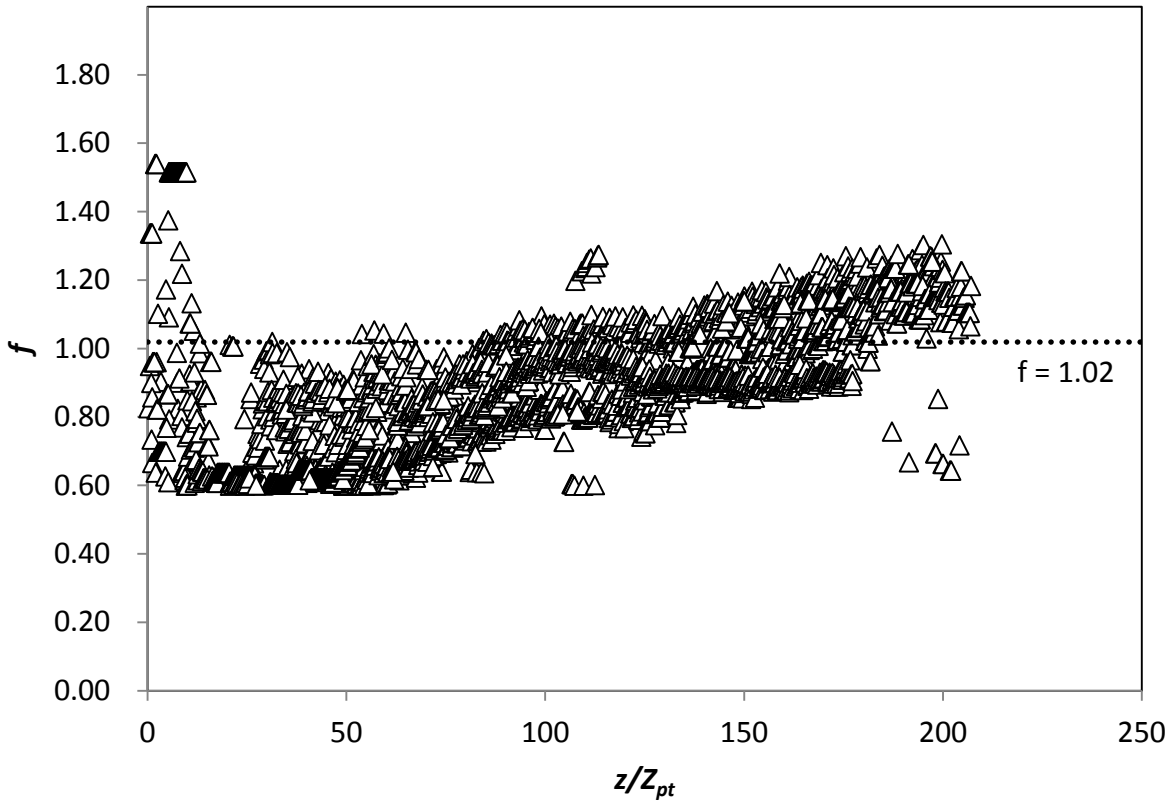

Figure 5-39: *f*-value for 22° experiments. The *f*-value from chapter 3 is included for reference.

Table 5-6: *f* value results

Discharge Angle	Lowest *f*-value	Highest *f*-value	Average *f*-value	Standard deviation in *f*-value
22	0.92	1.22	1.06	0.12
45	1.24	1.40	1.33	0.06
90	0.79	1.30	1.08	0.20

Figure 5-40, Figure 5-41, and Figure 5-42 contain the *h*-values from experimental sets 3, 6 and 7 (Table 5-2), where the discharge angles are 90°, 45° and 22° respectively. Although significant scatter is present, the *h*-values of 1.54 and 1.60 for the 90° and 45° cases are consistent with those found for 2D trajectory flows in chapter 3. Interestingly *h* values for the 45° case do not show the severe variation and lack of consistency evident in the *f* values and in contrast to the diverging *f*-values of the 45° discharge, the *h*-values tend towards the expected range.

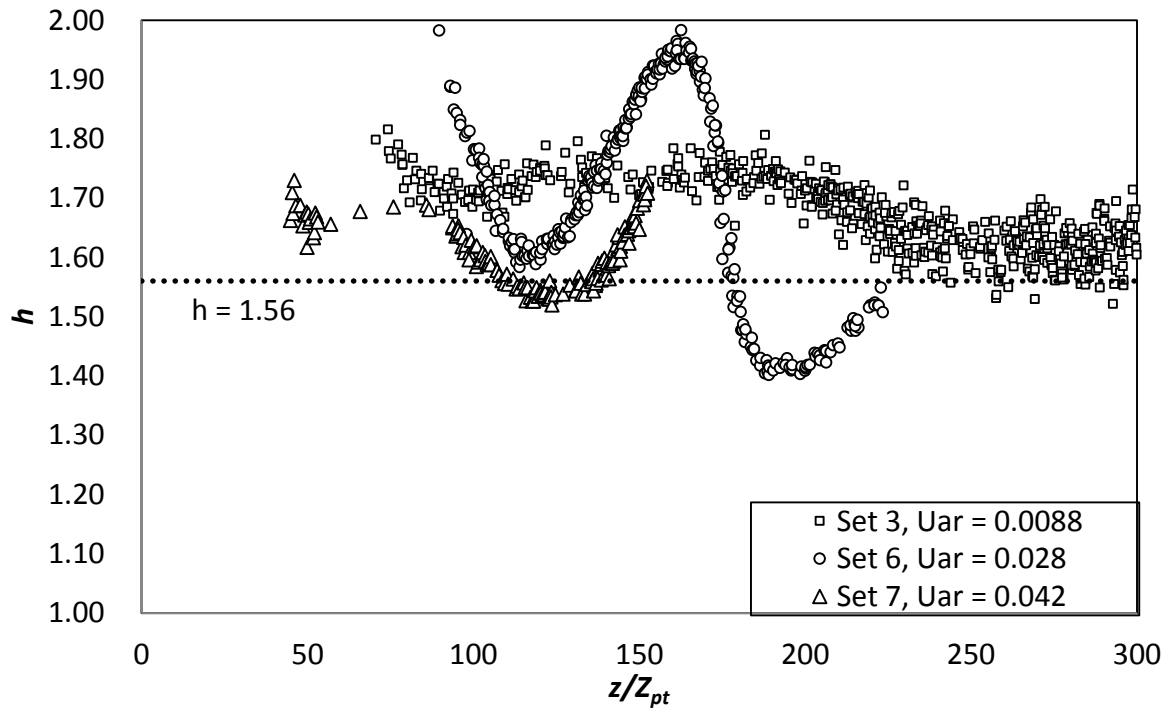

Figure 5-40: *h*-values from experiments 90° discharge with various U_{ar} numbers. The *h*-value from chapter 3 is shown for comparison.

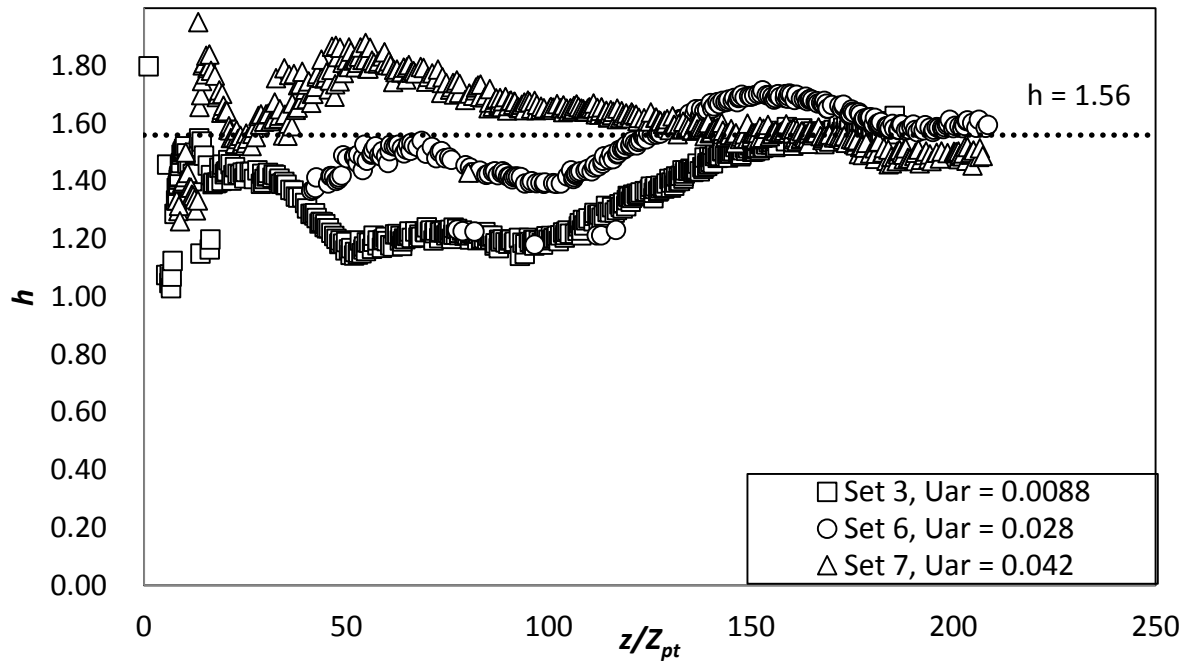

Figure 5-41: *h*-values from experiments 45° discharge with various U_{ar} numbers. The *h*-value from chapter 3 is shown for comparison.

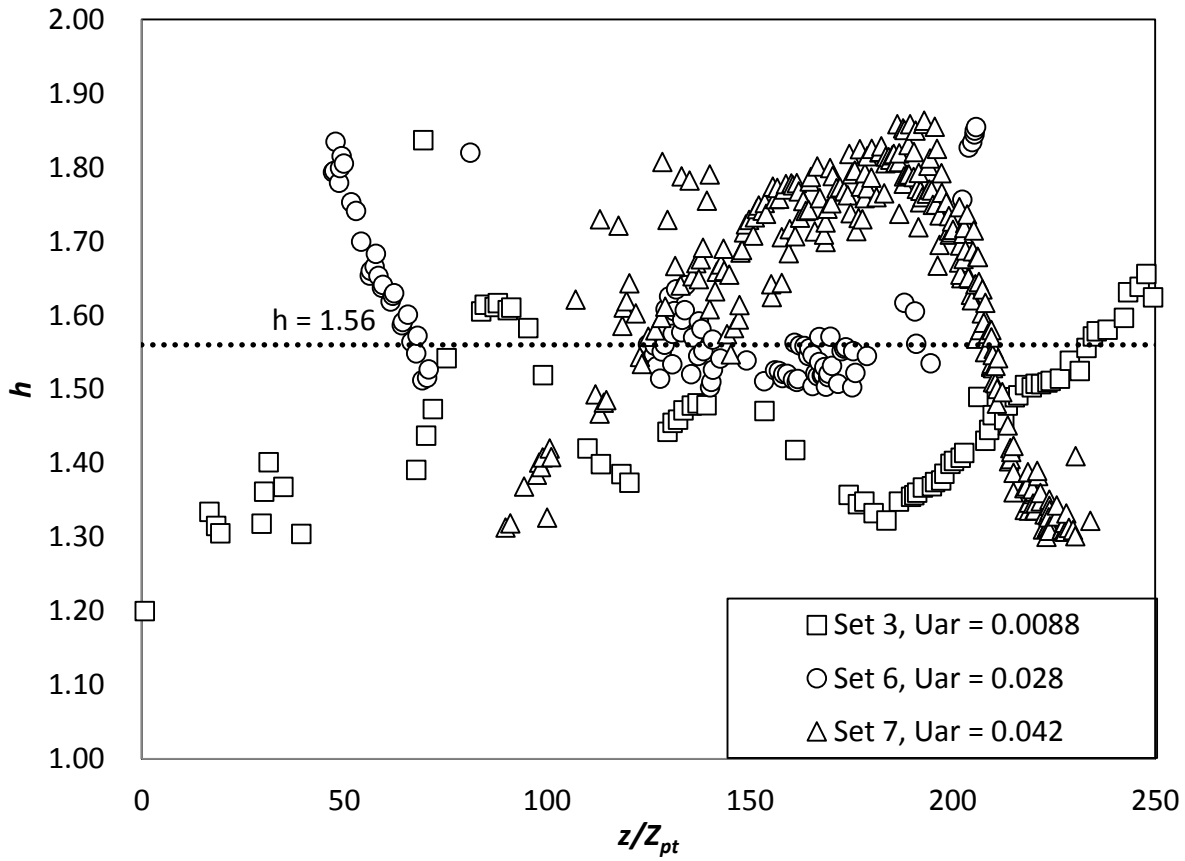

Figure 5-42: *h*-values from experiments 22° discharge with various U_{ar} numbers. The *h*-value from chapter 3 is shown for comparison.

5.6 Summary

In this chapter a comprehensive set of experiments with 3D trajectories with a range of initial conditions has been presented. The flows were released horizontally at an angle of 90°, 45°, or are 22° to the ambient current. The initial Reynolds number was approximately 7000, the initial Froude number approximately 92 and the relative gravity was 0.42. These conditions were kept constant. The ambient to initial velocity ratio varied from 0.0042 to 0.057. The experiments have been conducted in two phases, the first phase provided detailed information for two sets of initial conditions, and an indication of the effect of sampling time and number of realisations per experiment on the reliability of the data. In the second phase a broader exploration of the initial conditions was carried out with reduced sampling times. In order to compare the experimental results with expected results, the mathematical model used in chapter 4 has been extended to include flows with three-dimensional trajectories.

Results from the phase I experiments demonstrate that double peak distributions develop for discharges at 90° and 45° to the ambient motion. There is clear evidence of both line momentum puff and advected thermal behaviour. The development of the double peak distribution in the case of the 45° had not been observed in a previous investigation, but was clearly evident here. The consistent appearance of the double peaked distribution within the advected thermal regime is consistent with the results from chapter 3, alleviating previously published concerns about the ability to transfer the understanding gained from relatively simple discharges configurations to these more complex flows.

However, the transition from line momentum puff to advected thermal was more complex than previously thought, because of the differing orientations of the line vortex pair within these regimes. The double peak integrated concentration distribution (typical of the vortex pair) disappeared for an extended distance in the transition between these two regimes. According to the dilution plots this area does not show increased mixing, but these areas are too short to give a definitive description thereof. In this context is also interesting to note that the data from the phase I and phase II experiments collapsed most effectively under the plume to thermal length scale, despite the fact that a plume was not expected to form. This suggests that role of buoyancy in determining the transition from line momentum puff to advected thermal is more significant than previously thought. The initial variability of individual realisations within the more comprehensive phase I experiments reduced once the flow became strongly advected, with a relative standard deviation of approximately 10%. It is notable that this relative standard deviation increased to approximately 20% when determining the horizontal location of discharges released at 45° to the ambient. Hence there is some indication that the initial discharge angle has an influence on the variability of the final flow structure.

The second phase of these experiments broadened the range of previously considered initial conditions and also introduced and additional discharge angle of 22°. Results from chapter 4 suggest that in the latter case the intermediate regime between the jet and advected thermal regimes would change to a strongly-advected jet and hence a double peaked distribution would not develop until the flow evolves into an advected thermal. Data extracted for this discharge configuration was consistent with the expectations. A comprehensive data set has been obtained for each of the discharge configurations, where the flows follow three-dimensional paths. A more detailed analysis of the flow profiles shows that these are generally consistent with expectations

based on the results from chapters 3 and 4, particularly for the 22° and 90° discharges configurations. While the spreading of the profiles for the 45° case was consistent with results from these earlier chapters, the peak separation data showed significant variability and the reasons for this require further investigation.

A developed numerical integral model that takes into account the initial conditions and the final stage of the flow, the advected thermal, has proven to be able to predict the experimental data accurately. For the dilution and trajectory data, the transitional behaviour is also reasonably accurately predicted.

Chapter 6 - Conclusions and recommendations

A review of the literature on the behaviour of two dimensional and three dimensional discharges revealed that there was extensive experimental data available for some flow configurations however for others there was only limited data. The experimental study outlined in this thesis compliments earlier studies by providing additional data for the flow configurations where limited experimental data currently exists. Comprehensive sets of new data have been generated for advected thermals, oblique non-buoyant discharges and discharges with three dimensional trajectories.

In order to measure the dilutions and trajectories of the various flows, the Light Attenuation (LA) technique has been used and employed and in doing so, improvements to the system have been made. The LA technique measures the amount of light that has been absorbed by a sample and correlates this to the amount of contaminant. Food dyes with a known light absorption spectrum are used to distinguish the flow of interest. It has been shown that is possible to use two dyes simultaneously the dynamic range of the measuring system can be extended. Parallax and scaling issues, which become more complex when the flows moves towards or away from the cameras, necessitated that a scaling dependent on the distance from the camera was set up for these experiments. Because of measured temperature effects the difference between the discharge flow and ambient water has been kept below 0.2°C. A submerged tank containing the discharge fluid was constructed for this purpose.

An advected thermal and a momentum puff display a cross sectional flow structure that is similar and resembles a double vortex, but little information was available on the comparison between the flow structures. Models currently employed to predict flow parameters, such as Visjet and Corjet make use of the same spread constants for both these flows. A series of detailed experiments has been carried out to study the behaviour of line advected thermals evolving from discharges parallel and perpendicular to an ambient cross flow. The dual-camera LA system has been employed to record spatially-integrated tracer distributions of these flows. A double-Gaussian approximation provided the basis for characterizing the flow behaviour. The new data shows that the mean tracer distributions for buoyant and non-buoyant discharges are distinct, with the former having a greater peak separation than the latter. Thus the relationships between the peak and centreline (typically measured) concentrations differ. Differences are also evident

in the conversions needed to estimate these peak values from integral model predictions, where simplified mean profiles are assumed, such as top-hat or single Gaussian forms. Peak concentrations are of particular interest when determining compliance within a specified mixing zone and it is important therefore that these conversions are accurately defined. While these differences in the cross sectional mean profiles appear to be subtle, they are significant when mapping the assumed mean cross sectional profiles to the measured profiles to determine peak values. An analysis of the mapping coefficients for the Visjet and Corjet models indicates that the coefficient employed by Visjet underestimates the peak concentrations for line momentum puffs by approximately 8% and overestimates the peak concentrations of advected thermals by just 4%. It was also noted that mapping coefficients employed in the Corjet model are not consistent with conserving fluxes in the flow cross-section, but are instead determined so they provide reasonable predictions of peak values. Although the measured spreading rates for the two flow types are similar, the distinctive forms of the puff and thermal profiles require significantly different spreading rates for the equivalent top-hat models, if fluxes are to be maintained between the top-hat and measured cross sectional forms. The top-hat spreading rates obtained from this analysis are consistent with those obtained directly from comparisons between trajectory data and relevant analytical solutions. Thus the experimental results confirm the inherently similar mean structure of advected line thermals and advected line momentum puffs, but they also highlight subtle differences, which must be treated with some care when modelling these flows.

The literature indicated that the difference between a strongly-advected jet and a momentum puff is based on initial discharge angle, for discharge angles less than 20° the flow in the strongly-advected region resembles a strongly-advected jet and for discharge angles larger than 40° the flow resembles an advected line momentum puff. In this study the focus was on the initial discharge angles where the expected strongly-advected behaviour is not as clear, initial discharge angles between 20° and 40°. Two numerical integral models have been formulated to help clarify the results, the Advected Line Momentum Puff model (ALMP) and the Strongly-Advected Jet (SAJ) model. The experimental results show that data from discharge angles (39° to 52°) collapsed under scaling based on analytical solutions of line momentum puffs and were consistent with predictions based on the ALMP model. A double peak profile, typical of a momentum puff, was evident. Similarly, data from experiments with initial discharges angles of 28.9° and 32.4° collapsed under scaling based on the strongly-advected jet analytical solutions, were consistent with predictions from the SAJ model and showed a typical single peak

concentration profile. Data from the 35.9° discharge sometimes appeared to be single peak and at other times double peak. It did not demonstrate consistent behaviour under either form of scaling and was not generally consistent with either of the integral models. Ensemble averages of the flow profiles resulted in a broad single peak profile suggesting that the integrated concentration profiles (viewed along the *z* axis) do not form a stable profile, single-Gaussian nor double-Gaussian. Whether this broad profile is evidence of two closely spaced double vortices cannot accurately be determined with the present LA method and needs further investigation with other techniques.

Finally there is very limited experimental data available for discharges with three dimensional (3D) trajectories and additional data is needed to verify the predicative capabilities of existing models (eg. Corjet and Visjet) for these more complex discharge configurations and to provide the basis for evaluating the performance of new models. A comprehensive set of experimental investigations into the behaviour of discharges with 3D trajectories has been carried out. The flows were released horizontally at an angle of 90°, 45°, or at 22° to the ambient current and the ambient to initial velocity ratio varied from 0.0042 to 0.057, extending the range of initial conditions previously considered. Experiments were repeated to obtain representative information, and variability of individual realisations was seen to reduce once the flow became strongly advected, with a relative standard deviation of approximately 10% location; the values for integrated dilution also varied little from the ensemble average, once the advected thermal had formed. A relatively high standard deviation was noted for the horizontal location of the discharges released at 45° to the ambient, indicating that this variability has some sensitivity to discharge angle.

In terms of flow evolution, it is evident that for initial discharges angles of 90° and 45° to the ambient motion, there is both line momentum puff and advected thermal behaviour. The development of the double peak distribution in the case of the 45° discharge had not been observed in a previous investigation, but was clearly evident here. The consistent appearance of the double peaked distribution within the advected thermal regime alleviates previously published concerns about the ability to transfer the understanding gained from discharges that follow a two-dimensional path. However, the differing orientations of the line vortex pair within these flow regimes introduces additional complexity into the transition region. It was evident in experiments with an initial discharge angle of 22° that a double peak distribution did not develop until the flow evolved into an advected thermal and hence the intermediate regime between the

jet and advected thermal regimes had changed, presumably to a strongly-advected jet. A more detailed analysis of the flow profiles provided further evidence of the above observations and results that were generally consistent with those obtained from less complex discharges in earlier chapters. There were some inconsistencies in the data obtained for discharges at 45°, particularly with respect to peak separation and this requires further investigation.

Although the LA system has some distinct advantages in providing an overview of the flow behaviour in terms of the bulk parameters (spread, concentration and trajectory), the specific flow structure cannot be directly measured. Further research in this area should include additional measurements of specific flow profiles (concentration and velocity) within the transitions regions for 3D trajectory discharges and at the transitional angle of approximately 36 degrees, for non-buoyant oblique discharges, would provide further insight into these flows. There is evidence that existing numerical models can be improved by incorporating differences in advected line momentum puff and advected thermal behaviour. More detailed comparisons of the new data with existing numerical integral models would also be beneficial and could provide the basis for further development of these models to more effectively predict flow behaviour.

References

Adamczyk, A. A. and Rimai, L. (1988). "2-Dimensional tracking velocimetry (PTV): Technique and image processing algorithms." *Experiments in Fluids*, 6, 373-380.

Ayoub, G.M. (1971). "*Dispersion of buoyant jets in a flowing ambient fluid*." Imperial College of Science & Technology, University of London, London.

Abraham, G. (1963). "*Jet diffusion in stagnant ambient fluid*." Dissertation, Department of Civil Engineering and Geosciences, TU Delft, Netherlands.

Boyer, R.F. (1993). "*Modern Experimental Biochemistry*." 2nd ed. California: Benjamin/Cummings Publishing.

Bown, M. R, MacInnes, J.M., Allen, R.W.K. and Zimmerman, W.B.J. (2006). "Three-dimensional, three-component velocity measurements using stereoscopic micro-PIV and PTV". *Measurement Science and Technology*, 17, 2175-2185.

Cheung, S.K.B., Leung, D.Y.L., Wang, W., Lee, J.H.W., and Cheung, V. (2000). "VISJET - a computer ocean outfall modelling system." *Computer Graphics International*, proceedings, 75-80.

Cheung, V. (1991). "*Mixing a round buoyant jet in a current*." University of Hong Kong, Hong Kong.

Chu, P. C. K. (1996). "*Mixing of Turbulent Advected Line Puffs*." University of Hong Kong, Hong Kong.

Chu, V. H. (1975). "Three-dimensional forced plumes in a laminar crossflow." *Proceedings of the 16th International Association for Hydraulic Research (IAHR) Congress*, 5 (paper 2.1), 31-38.

Chu, V. H. and Goldberg, M. B. (1974). "Buoyant forced plumes in crossflow." American Society of Civil Engineers (ASCE), *Journal of the Hydraulics Division*, 122, 1, 27-34.

Chu, V. H., and Lee, J. H. W. (1996). "General integral formulation of turbulent buoyant jets in cross-flow." American Society of Civil Engineers (ASCE), *Journal of the Hydraulics Division*, 122,1, 27-34.

Chu, P. C. K., Lee, J. H., and Chu, V. H. (1999). "Spreading of turbulent round jet in coflow." *Journal of Hydraulic Engineering*, 125(2), 193-204.

Chu, V. H. (1977). "A line-impulse model for buoyant jets in a crossflow." *Heat transfer and Buoyant Convention*, 1, 263-279.

Cenedese, A., Paglialunga, A. (1989). "A new technique for the determination of the third velocity component with PIV." *Experiments in Fluids*, 8, 228-230.

Cui, A., and Street, R. L. (2001). "Large-eddy simulation of turbulent rotating convective flow development." *Journal of Fluid Mechanics*, 447, 53-84.

Cuthbertson, A.J.S., Malcangio, D., Davies, P.A. and Mossa, M. (2006). The influence of a localized region on turbulence on the structural development of a turbulent, round, buoyant jet. *Fluid Dynamics Research*, 38: 683-698.

Davidson, M. J., Knudsen, M., and Wood, I. R. (1991). "The behaviour of a single, horizontally discharged, buoyant flow in a non-turbulent coflowing ambient fluid." *Journal of Hydraulic Research*, 29, 4, 545-566.

Davidson, M. J., and Pun, K. L. (1998). "Hybrid model for prediction of initial dilutions from outfall discharges." *Journal of Hydraulic Engineering*, ASCE, 124, 12, 1188-1197.

Davidson, M. J., and Pun, K. L. (1999). "Weakly advected jets in cross-flow." *Journal of Hydraulic Engineering*, ASCE, 125, 1, 47-58.

Davidson, M. J. and Wang, H. J. (2002), "A strongly advected jet in a coflow", *Journal of Hydraulic Engineering*, ASCE, 128, 8, 742-752.

Doneker, R.L. and Jirka, G.H. (2007). "*CORMIX User Manual: A Hydrodynamic Mixing Zone Model and Decision Support System for Pollutant Discharges into Surface Waters"*, EPA-823-K-07-001.

EPA (2001). "*Visual Plumes*". United States Environmental Protection Agency, retrieved 21 April 2011 from http://www.epa.gov/ceampubl/swater/vplume/.

Fellers, T.J. and Davidson M.W. "*Concepts in digital imaging technology*." Retrieved 27-10-2012 from http://learn.hamamatsu.com/articles/ccdsnr.html.

Fellers, T.J., Vogt, K. M., and Davidson M.W. "*Microscopy: The source for microscopy education.*" Retrieved 27-10-2012 from http://www.microscopyu.com/tutorials/java/digitalimaging/signalto noise/.

Fouras, A., Jacono, D. L., Nguyen, C. V., and Hourigan, K. (2009). "Volumetric correlation PIV: A new technique for 3D velocity vector field measurement." *Experiments in Fluids*, 47(4-5), 569-577.

Gaskin, S. J. (1995). "*Single Buoyant Jets in a crossflow and the advected line thermal*." PhD Thesis, Department of Civil Engineering, University of Canterbury, Christchurch, New Zealand.

Gaskin, S. J., McKernan, M., and Xue, F. (2004). "The effect of background turbulence on jet entrainment: an experimental study of a plane jet in a shallow coflow." *Journal of Hydraulic Research*, 42 (5), 531-540.

Green, F.J. (1990). "*The Sigma-Aldrich handbook of Stains, dyes, and Indicators.*" Milwaukee, Wisconsin: Aldrich Chemical Co.

Guo, Y., Malcangio, D., Davies, P.A. and Fernando, H.J.S. (2005). A laboratory investigation into the influence of a localized region on turbulence on the evolution of a round turbulent jet. *Fluid Dynamics Research*, 36: 78-89.

Halloin, V. L. and Jottrand, R. (1994). "A new technique for the experimental study of 3D velocity fields." *Experiments in Fluids*, 17, 1-2, 115-118.

Harrison, R. M. (2001). "Pollution: causes, effects and control". Cambridge, *Royal Society of Chemistry*, 4th edition.

Hoyer, K., Holzner, M., Luthi, B., Guala, M., Liberzon, A., and Kinzelbach,W. (2005). "3D scanning particle tracking velocimetry." *Experiments in Fluids* 39, 923–934.

Hunt, J.C.R. (1994). Atmospheric jets and plumes, In: Davies, P.A. and Valente Neves M.I. (eds.), *Recent Research Advances in the Fluid Mechanics of Turbulent Jets and Plumes*, NATO ASI Series E, 255: 309-334.

JAI – CV-M7+/M7+CL – Digital Double Speed Color Megapixel Progressive scan camera. Retrieved Aug. 6, 2012, from http://www.adept.net.au/cameras/jai/pdf/cv-m7plus.pdf.

Janesick, J. R. (2007). "*Photon transfer DN⟶λ.*" SPIE, Bellingham, Washington. USA.

Jirka, G. H. (2004). "Integral Model for Turbulent Buoyant Jets in Unbounded Stratified Flows Part 1: Single Round Jet." *Journal of Environmental Fluid Mechanics*, 4, 1-56.

Khalighi, B. (1991). "Study of the intake tumble motion by flow visualisation and particle tracking velocimetry." *Experiments in Fluids*, 10, 230-236.

Keffer, J. F., and Baines, W. D. (1963). "The round turbulent jet in a cross wind." *Journal of Fluid Mechanics*, 15, 481-496.

Kikkert, G.A. (2006). "*Buoyant jets with two and three dimensional trajectories*." PhD Thesis, Department of Civil Engineering, Christchurch, New Zealand.

Kikkert, G.A., Davidson, M.J., and Nokes R.I. (2007). "Characterising strongly advected discharges in the initial dilution zone". *Environmental Fluid Mechanics*, 7, 195–215.

Kikkert, G. A., Davidson, M. J., and Nokes, R. I. (2009). "Buoyant Jets with Three Dimensional Trajectories". *Journal of Hydraulic Research*, IAHR 48, 3, 292-301.

Kitchin, C.R. (1995). "*Optical astronomical spectroscopy*". Institute of physics publications. London, Great Britain.

Knudsen, M. (1988). "*Buoyant horizontal jets in an ambient flow.*" PhD thesis, Department of Civil Engineering, University of Canterbury, Christchurch, New Zealand.

Koochesfahani, M. M., and Dimotakis, P. E. (1985). "Laser-induced fluorescence measurements of mixed fluid concentration in a liquid plane shear layer." *AIAA Journal*, 23, 1700–1707.

Koochesfahani, M. M., and Dimotakis, P. E. (1986). "Mixing and chemical reactions in a turbulent mixing layer." *Journal of Fluid Mechanics*, 170, 83–112.

Khorsandi, B., Gaskin, S.J. and Mydlarski, L. (2007). "Effect of background turbulence on the velocity field of a turbulent jet." *Proceedings of Fifth International Symposium on Environmental Hydraulics (ISEH-V) IAHR*, Tempe, Arizona, 1-6.

Khorsandi, B., Gaskin, S.J. & Mydlarski, L.M. (2008) The effect of background turbulence on the entrainment into an axisymmetric turbulent jet, *2nd International Symposium on Shallow Flows (IAHR)*, Dec 10-12, Hong Kong.

Khorsandi, B., Gaskin, S.J. & Mydlarski, L.M. (2011) The dynamics of a turbulent jet in a turbulent background, *7th International Symposium on Stratified Flows*, Rome, Italy, August 22-26, pp.1-8.

Lai, C. C. K. and Lee, J. H. W. (2012). "Mixing of inclined dense jets in stationary ambient." *Journal of hydro-environmental research*, 6 (1), 9-28.

Lai, A.C.H., Yu, D., and Lee, J.H.W. (2011). "Mixing of a rosette jet group in a crossflow" *American Society of Civil Engineers (ASCE), Journal of the Hydraulic Engineering*, 137, 787-803.

Langford, V.S., McKinley, A.J. and Quickenden, T.I. (2001). "Temperature dependence of the visible-near infrared absorption spectrum of liquid water." *Journal of Physical Chemistry A*, 105: 8916-8921.

Lam, K.M. and Chan, H.C. (1995). "Investigation of turbulent jets issuing into a counter-flowing stream using digital imaging." *Experiments in Fluids*, 18 (3), 210-212.

Lam, K.M. and Chan, H.C. (1997). "Round Jet in Ambient Counterflowing stream." *Journal of Hydraulic Engineering*, October 1997, 895-903.

Lavertu, T.M. (2006). "*Differential diffusion in a turbulent jet*." Dissertation, Department of Mechanical Engineering, McGill University, Canada.

Law, A. W. K., and Wang, H. (2000). "Measurement of mixing processes with combined digital particle image velocimetry and planar laser induced fluorescence." *Experimental Thermal and Fluid Science*, 22(3), 213-229.

Lee J. W. H., Cheung V., Wang W. P and Cheung S. K. B. (2000) Lagrangian modeling and visualization of rosette outfall plumes, Proc. Hydrodynamics 2000, Iowa. July 23-27

Lee, J. H. W., Chu, V. H. (2003). "*Turbulent Jets and Plumes: A Lagrangian Approach*." Kluwer Academic Publishers, Dordrecht, Netherlands.

Lee. J. H. W and Neville-Jones, P. (1987). "Initial dilution of a horizontal jet in crossflow." *Journal of Hydraulic Engineering*, ASCE, 113, 615-630.

List, E. J., and Dugan, R. (1994). Transition from Jet Plume Dilution to Ambient Turbulent Mixing. In: Davies, P.A. and Valente Neves M.I. (eds.), Recent Research Advances in the Fluid Mechanics of Turbulent Jets and Plumes NATO ASI Series Volume 255, 1-11.

Liu, Z. –C., Landreth, C. C., Adrian, R. J., and Hanratty, T. J. (1991). "High resolution measurement of turbulent structure in a channel with particle image velocimetry." *Experiments in Fluids*, 10, 301-312.

Maas, H.G., Gruen, A., and Papantoniou, D. (1993). "Particle tracking velocimetry in three dimensional flows – part 1. Photogrammic determination of particle coordinates." *Experiments in Fluids*, 15, 133-146.

Margason, R. J. (1968). "*The path of a jet directed at large angles to a subsonic free stream.*" NASA TN D-4919.

Morton, B.R., Turner, G., and Turner, J.S. (1956). "Turbulent gravitational convection from maintained and instantaneous sources." *Proceedings of the Royal Society of London. Series A, Mathematical and physical sciences*, 234, 1196, 1-23.

Nickels, T. B. and Perry, A. E. (1996). "An experimental and theoretical study of the turbulent coflowing jet." *Journal of Fluid Mechanics*, 309, 157-182.

Nokes, R.I. (2007). "*ImageStream*." Version 6.02, Department of Civil and Natural Resources Engineering, University of Canterbury, Christchurch, New Zealand.

Oliver, C. J., Davidson, M. J., and Nokes, R. I. (2008). "k-ε Predictions of the initial mixing of desalination discharges." *Environmental Fluid Mechanics*, 8 (5-6), 617-625.

Papakonstantis, I.G., Christodoulou, G.C., Papanicolaou, P.N. (2011a). "Inclined negatively buoyant jets 1: geometrical characteristics." *Journal of Hydraulic Research*, IAHR, 49 (1) 3-12.

Papakonstantis, I.G., Christodoulou, G.C., Papanicolaou, P.N. (2011b). "Inclined negatively buoyant jets 2: concentration measurements." *Journal of Hydraulic Research*, IAHR, 49,1, 13–22.

Papanicolaou, P. N. (1984). "*Mass and momentum transport in a turbulent buoyant vertical axisymmetric jet.*" California Institute of Technology, Pasadena, California.

Papanicolaou, P. N., and List, E. J. (1988). "Investigations of round vertical turbulent buoyant jets." *Journal of Fluid Mechanics*, 195, 341-391.

Papantoniou , D., and List E.J. (1989) "Large-scale structure in the far field of buoyant jets." *Journal of Fluid Mechanics* 209:151–190.

Pavia, D.L., Lampman, G.M., Kriz, G.S., and Vyvyan, R. (2009). "*Introduction to spectroscopy".* Cengage learning, USA.

Platten, J. L., and Keffer, J. F. (1971). "Deflected turbulent jet flows." *Journal of Applied Mechanics*, 38(4), 756-8.

Potter, G.W.H. (1995). "*Analysis of Biological Molecules: an introduction to principles, instrumentation, and techniques*." Oxford: Alden Press.

Preisendorfer, R.W. (1986) "*Secchi Disk Science: Visual Optics of Natural Waters*." American Society of Limnology and Oceanography.

Pun, L. K. (1998). "Hybrid models for jets and plumes in a flowing ambient fluid." Hong Kong University of Science and Technology, Hong Kong.

Scheepbouwer, E. Davidson, M.J., and Nokes R.I. (2007*).* "Line advected thermals and puffs – revisited". *Fifth International Symposium on Environmental Hydraulics (ISEH V),* proceedings, Tempe, AZ, USA.

Scheepbouwer, E. Davidson, M.J., and Nokes R.I. (2008). "Tracer distributions of line advected thermals". *Environmental fluid mechanics*, 8, 5-6, 561-568.

Scheepbouwer, E. Davidson, M.J., and Nokes R.I. (2010). "Transitional behaviour of buoyant jets moving along three dimensional paths. Athens, Greece: 6th International symposium on Environmental Hydraulics, 23-25 Jun 2010. *Environmental hydraulics*: 129-134.

Richards, J. M. (1963). "Experiments on the motions of isolated cylindrical thermals through unstratified surroundings." *International Journal of Air and Water Pollution*, 7, 17–34.

Robinson, K. (2007). "*Spectroscopy: The key to the stars, reading the lines in stellar spectra*". Springer-Verlag, London, Great Britain.

Smith, S. H. and Mungal, S. G. (1998). "Mixing, structure and scaling of the jet in crossflow." *Journal of Fluid Mechanics*, 357, 83-122.

Taiz, L. and Zeiger, E. (2010). "*Plant physiology*", 5th edition, Sinhauer Associates Inc.

Tian, X., and Roberts, P.J.W. (2003). "A 3D LIF system for turbulent jet flows." *Experiments in Fluids*, 35, 636-647.

Tian, X., Roberts, P.H.W., and Daviero, G.J. (2004). "Marine Wastewater Discharges from Multiport Diffusers. I: Unstratified Stationary Water." *Journal of Hydraulic Engineering*, 130, 12, 1147-1155.

Van Cruyningen, I., Lozano, A., and Hanson, R. K. (1990). "Quantitative imaging of concentration by planar laser-induced fluorescence." *Experiments in Fluids*, 10, 1, 41-49.

Wang, H. (2000). "*Investigations of buoyant jet discharges using digital particle image velocimetry (DPIV) and planar laser induced fluorescence (PLIF)*." Nanyang Technological University, Singapore.

Wang, H. and Law, A. W. K. (2002). "Second-order integral model for a round buoyant jet." *Journal of Fluid Mechanics*, 459, 397-428.

Wong, C. (1991). "*Advected line thermals and puffs*." MS thesis, University of Hong Kong, Hong Kong.

Wong, D.R., and Wright, S.J. (1988). "Submerged turbulent jets in stagnant linearly stratified fluids." *Journal of Hydraulic Research*, 26(1), 153-157.

Wood, I. R. (1993). "Asymptotic solutions and behavior of outfall plumes." American Society of Civil Engineers (ASCE), *Journal of the Hydraulics Division*(119(5)), 555-580.

Wright, S. J. (1977). "*Effects of ambient crossflow and density stratification on the charateristic behavior of round turbulent buoyant jets*." W. M. Keck Laboratory of Hydraulic and Water Resources, California Institute of Technology, Pasadena, Carlifornia.

Wright, S. J. (1994). The effect of ambient turbulence on jet mixing, In: Davies, P.A. and Valente Neves M.I. (eds.), *Recent Research Advances in the Fluid Mechanics of Turbulent Jets and Plumes*, NATO ASI Series E, 255: 13-27.

Wu, J.S., and Faeth, G.M. (1995). "Effect of ambient turbulence intensity on sphere wakes at intermediate Reynolds numbers". *AIAA Journal*, 33(1), 171-173.

Yuan, L. L., Street, R. L., and Ferziger, J. H. (1999). “Large-eddy simulations of a round jet in crossflow.” *Journal of Fluid Mechanics*, 379, 71-104.

Appendix A - Derivations

In a marine outfall generally three major phases are recognised. Figure 1 shows the initial dilution Region or 'near-field' dilution for which the time scales are in magnitude <1000s, and the length scales <100m.

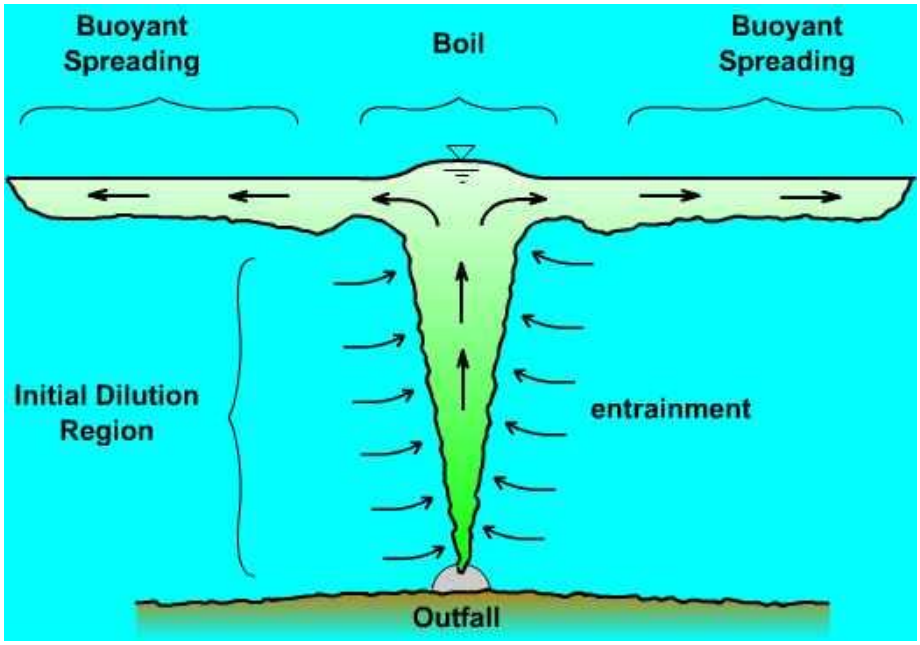

Figure 1: Three modelling phases in a marine outfall [From Lecture notes Dr. M. J. Davidson, 2009]

Parameters

The used parameters from this thesis are shown in figure 2. The source has a diameter, d, and expels fluid with a velocity, U_0, and density, ρ_0. The ambient density is ρ_a. The flow of the initial discharge, Q_0, is then $U_0\ \pi d^2/4$. The initial momentum flux per unit density, M_0 equals $U_0^2\ \pi d^2/4$ and the initial buoyancy flux per unit density, B_0, equals $(\rho_a-\rho_0)g/\rho_a\ U_0\ \pi d^2/4$ or $\Delta_0\ U_0\ \pi d^2/4$. As the flow mixes with the ambient it entrains ambient fluid, which can be represented as $U_a Q_\alpha$, or the entrained ambient momentum per unit density (M_a), where Q_α is the entrained flow.

In a weakly advected flow the ambient velocity, U_a, does not influence the mixing process but is of influence on the trajectory of the flow (advection term). In a strongly advected flows the ambient velocity, U_a does become significant to the mixing process.

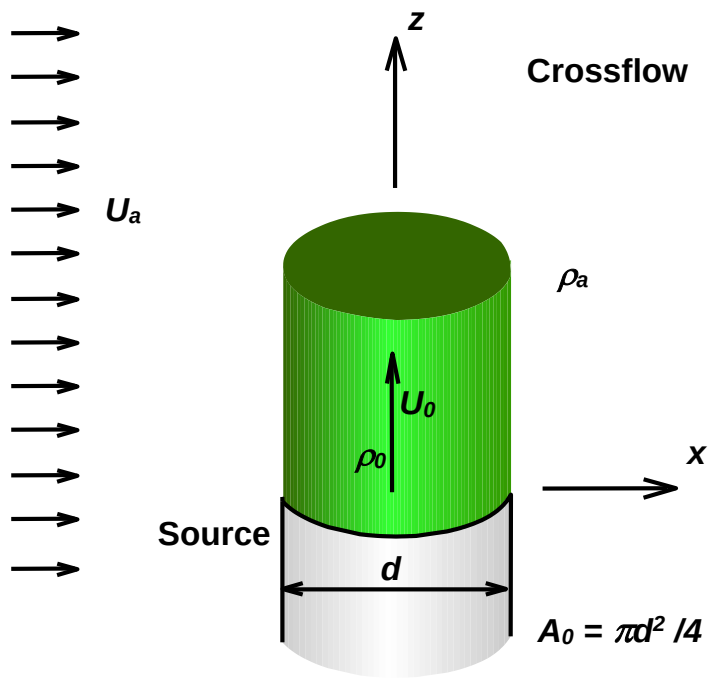

Figure 2: Discharge schematic showing relevant parameters.

Weakly advected jet or strong jet

Assumptions

- The ambient velocity is relatively small, so dilution, velocity and spread predictions are based on those of a jet in a still ambient fluid.
- In case of an ambient flow the predictions of the flow path needs to incorporate the impact of ambient motion.
- There is no density difference between discharged and ambient fluids.

The following formulae (table 1) describe the top-hat velocity, top-hat spread and top-hat dilution and trajectory and use the spread assumption $\frac{db}{dx} = k$ (Abraham 1965).

Table 1: Relevant formulae for a strong jet.

Velocity	$\frac{u_T}{U_0} = \frac{1}{2\left(\frac{k_T x_J}{d}\right)}$	(1)
Spread	$b_T = k_T x$	(2)
Dilution	$\frac{C_0}{c_T} = 2\left(\frac{k_T x_J}{d}\right)$	(3)

Trajectory	$\frac{x}{d} = \frac{k_T}{2}\frac{U_a}{U_0}\left(\frac{z}{d}\right)$	(4)

Weakly advected plume

Assumptions

- The ambient velocity is relatively small, so dilution, velocity and spread predictions are based on those of a plume in a still ambient fluid.
- The predictions of the flow path needs to incorporate the impact of ambient motion.
- There is a density difference between discharged and ambient fluids, but initial momentum approaches zero.

The following formulae (table 2) describe the top-hat velocity, top-hat spread and top-hat dilution and trajectory use the spread assumption $\frac{db}{dx} = k$.

Table 2: Relevant formulae for a weakly advected plume.

Velocity	$u_T = \left[\frac{3}{4\pi}\Delta_0 Q_0 \frac{1}{k_T^2}\right]^{1/3} \frac{1}{z_P^{1/3}}$	(5)
Spread	$b_T = k_T x$	(6)
Dilution	$\frac{\Delta_o}{\Delta_T} = \left[\frac{3\pi^2}{4} k_T^4 \frac{\Delta_0}{Q_0^2}\right]^{1/3} z_P^{5/3}$	(7)
Trajectory	$\frac{x}{d} = \frac{U_a}{U_0}\left(\frac{9 Fr_0^2 k_T^2}{4}\right)^{1/3}\left(\frac{z}{d}\right)^{4/3}$	(8)

Note, U_0 is 0, so the velocity has not been put in a dimensionless form (refer table 1). The tracer term T has been replaced with the density term Δ.

Weakly advected buoyant jets

Assumptions

- The ambient velocity is relatively small, so dilution, velocity and spread predictions are based on those of a plume (buoyancy generated parameters) and a jet (initial momentum) in a still ambient fluid.
- The predictions of the flow path needs to incorporate the impact of ambient motion.
- There is a density difference between discharged and ambient fluids, and the initial momentum is non-zero.

- Initially the flow will behave like a weakly advected jet and after a certain length scale the flow will behave like a plume. The length scale depends on the relative magnitudes of the initial and buoyancy generated momentums.

To derive the transition length scale, dimensional analysis is useful. The transitional length scale, l_{jp}, is a dimensionless distance dependant on the ratio of initial momentum and buoyancy generated momentum. Dimensions are given below in table 3.

Table 3: Dimensions of initial momentum and buoyancy generated momentum.

$M_o = \frac{\pi}{4} U_0^2 d^2$	$\frac{\mathrm{L}^4}{\mathrm{T}^2} = \frac{length^4}{time^2}$	(10)
$B_0 = \Delta_0 Q_0 = \Delta_o \frac{\pi}{4} U_0 d^2$	$\frac{\mathrm{L}^4}{\mathrm{T}^3}$	(11)

Using the ratio $l_{JP} \sim \frac{M_0^{3/4}}{B_0^{1/2}}$ gives:

$$l_{JP} = C_{JP} \frac{M_0^{3/4}}{\left[\Delta_0 Q_0\right]^{1/2}} \tag{12}$$

Where l_{JP} is the Jet to Plume transition length-scale and C_{JP} is a constant, determined from experimental data to be approximately 2.

Strongly advected line advected thermal

Assumptions

- The ambient velocity is large enough to influence the mixing behaviour.
- The formation of an advected thermal dramatically alters the nature of the discharge in terms of its trajectory, structure, rate of rise and dilution.
- The predictions of the flow path also needs to incorporate the impact of ambient motion.
- There is a density difference between discharged and ambient fluids, and the initial momentum is non-zero.
- Initially the flow will behave like a weakly advected jet and after a certain length scale the flow will behave like a line advected thermal.
- The flow can either transition from jet-plume-thermal or het-momentum puff-thermal, depending on the relevant length scales.

- The relevant length scale are the ratios between initial, buoyancy generated and entrained momentums (see table 5-3).

In a flow as described above, the buoyancy generated momentum can be given by:

$$M_B = \left[\frac{3}{4}\pi^{1/2}\Delta_0 Q_0\right]^{1/3} z^{4/3} \tag{13}$$

And the entrained ambient momentum by:

$$M_a = U_a\left(Q - Q_0\right) \approx U_a Q = U_a\left[\frac{3\pi^2}{4}k_T^4 \Delta_0 Q_0\right]^{1/3} z^{5/3} \tag{14}$$

Then the ratio of the entrained momentum and the buoyancy generated momentum becomes:

$$\frac{M_a}{M_B} \approx \left[\frac{3\pi^2}{4}k_T^4 \frac{U_a^3 d}{\Delta_0 Q_0}\right]^{1/3} z_*^{1/3} = \left[\frac{16}{3}k_T^2 U_a^3 F_{r0}^2\right]^{1/3} z_*^{1/3} \tag{15}$$

At the transition point from weakly to strongly-advected behaviour, Z_{pt}, we expect $M_a \sim M_B$. It follows that here:

$$1 \sim \left[\frac{16}{3}k_T^2 U_a^3 F_{r0}^2\right]^{1/3} Z_{PT*}^{1/3} \tag{16}$$

And

$$Z_{PT*} \sim \frac{3}{16}\frac{1}{k_T^2}\frac{1}{U_a^3 F_{r0}^2} \tag{17}$$

Following is an expansion to calculate the integral solution for the dilution and trajectory of line advected thermals (equations 3-1 and 3-2) (Figure 3),

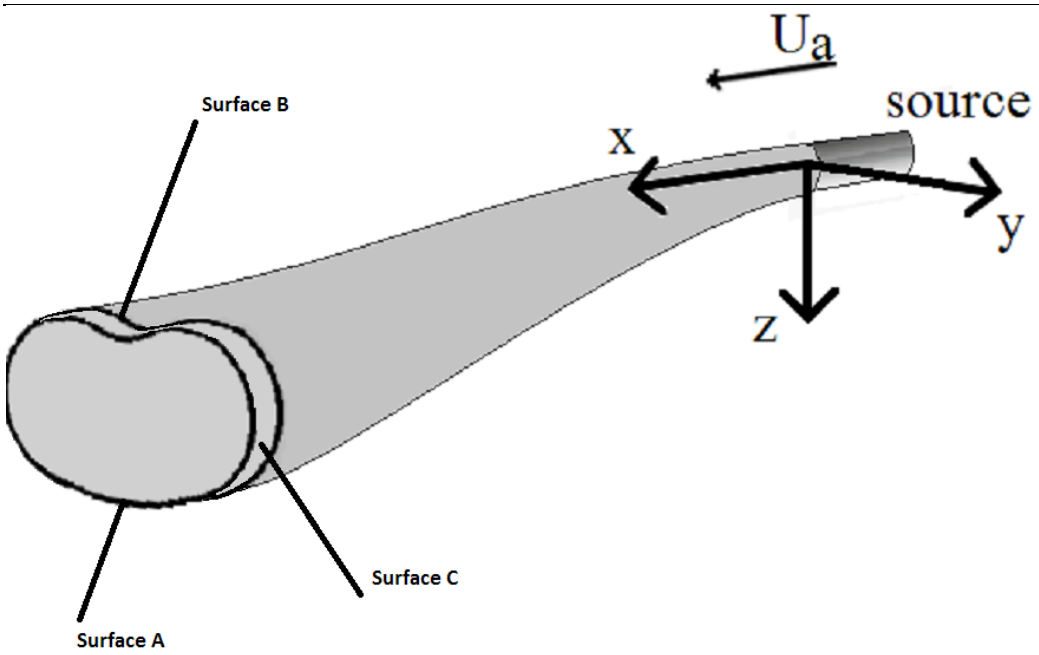

Figure 3: Drawing (cf. fig 3-1) now showing control volume, moving with the ambient, U_a, and is bordered by surfaces A, B and C.

There is no flux of mass or momentum across surfaces A & B, because the control volume is moving with the ambient current.

The equation for conservation of momentum in the vertical direction is given by,

$$\sum F_z = \frac{\partial}{\partial t}\left(\int_{CV} \rho u_z dV\right) + \int_{CS} \rho v_z(\bar{u}\cdot\bar{n})dA \tag{18}$$

The control volume is moving with the ambient velocity, and the vertical momentum within the control volume changes with time (first term on the RHS of the momentum equation). There is a flux of momentum into the control volume due to the entrained flow. However, the entrainment velocities are very small at the control volume boundary (surface C) and the inflow is symmetrical.

The force due to the density difference between the discharge and the ambient fluid dominates. So follows that buoyancy minus weight equals the change of vertical momentum within the control volume with time. The momentum equation can therefore be written as:

$$g\Delta\rho_T \pi b_T^2 \Delta x = \frac{d}{dt}\left(u_T \rho \pi b_T^2 \Delta x\right) \tag{19}$$

After dividing by Δx and ρ this can then be written as:

$$\Delta_T \pi b_T^2 = \frac{d}{dt}\left(u_T \pi b_T^2\right) \tag{20}$$

Rewriting with $U_a = \frac{dx}{dt}$:

$$\Delta_T \pi b_T^2 = \frac{d}{dx}\left(U_a u_T \pi b_T^2\right) \tag{21}$$

Within the moving control volume the buoyancy flux will also be conserved. This is because there is no mass flux into the control volume through surface A and B, and the mass flux through surface C contains no density deficit.

The equation for conservation of buoyancy (mass) flux:

$$0 = \frac{\partial}{\partial t}\left(\int_{CV} \Delta\rho dV\right) + \int_{CS} \Delta\rho(\bar{u}\cdot\bar{n})dA \tag{22}$$

Where $(\vec{u}\cdot\vec{n})dA \neq 0$, $\Delta\rho$=0 so equation (22) becomes:

$$\frac{d}{dt}\left\{g\frac{\Delta\rho_T}{\rho}\pi b_T^2 \Delta x\right\} = 0\frac{g}{\rho} \tag{23}$$

Using $U_a = \frac{dx}{dt}$, follows $$\frac{d}{dx}\left\{u_T \Delta_T \pi b_T^2\right\} = 0 \tag{24}$$

Finally integrating gives $$U_a \Delta_T \pi b_T^2 = const \tag{25}$$

The constant can be set at the initial value (at the source) of the flux deficit of $Q_0\Delta_0$, so the deficit equation becomes:

$$U_a \Delta_T \pi b_T^2 = Q_0 \Delta_0 \tag{26}$$

The trajectory can be found by looking at the geometric relationship:

$$\frac{dz}{dx} = \frac{M_B}{M_a} = \frac{u_T Q}{U_a Q} = \frac{u_T}{U_a} \tag{27}$$

The spread assumption is of the form:

$$\frac{db_T}{dz} = k_T$$

This equation is based on Richard's experiments (1963) and the value of "k_T" is 0.73. (Chapter 3). The solution now comes by restating equation 26 to,

$$\Delta_T b_T^2 = \frac{\Delta_0 Q_0}{\pi U_a} \tag{28}$$

And substituting equation 28 into the vertical momentum equation (21) gives,

$$\frac{d}{dx}\left[u_T U_a \pi b_T^2\right] = \frac{\Delta_0 Q_0}{U_a} \tag{29}$$

Integrating (29) gives:

$$u_T U_a \pi b_T^2 = \frac{\Delta_0 Q_0}{U_a} x + const \tag{30}$$

The integration constant, *const*, equals 0 because at $x = 0$ the vertical momentum flux equals 0. Dividing (30) by U_a^2 gives:

$$\pi \frac{u_T}{U_a} b_T^2 = \frac{\Delta_0 Q_0}{U_a^3} x \tag{31}$$

Implementing a virtual source assumption,

$$\frac{dz}{dx} = \frac{u_T}{U_a} \text{ and } b_T = kz \text{, so}$$

$$\pi \frac{dz}{dx} k^2 z_T^{\,2} = \frac{\Delta_0 Q_0}{U_a^{\,3}} x \tag{32}$$

$$\Rightarrow \quad z^2 dz = \frac{1}{\pi k^2} \frac{\Delta_0 Q_0}{U_a^{\,3}} x dx \tag{33}$$

After integration,

$$\frac{z^3}{3} = \frac{1}{\pi k^2} \frac{\Delta_0 Q_0}{U_a^{\,3}} \frac{x^2}{2} \tag{34}$$

Non-dimensionalising

$$\frac{z^3}{d^3} = \frac{3}{2} \frac{1}{\pi k^2} \frac{\Delta_0 Q_0}{d U_a^3} \frac{x^2}{d^2} \tag{35}$$

$$\Rightarrow \quad \left(\frac{z}{d}\right)^3 = \left(\frac{3}{8}\frac{1}{k^2}\right) \frac{1}{Fr_0^{\,2}} \left(\frac{U_0}{U_a}\right)^3 \left(\frac{x}{d}\right)^2 \tag{36}$$

Thus the flow trajectory is given by:

$$\frac{z}{d} = \left[\frac{3}{8}\frac{1}{m^2}\right]^{1/3} \frac{1}{F_{r0}^{2/3}} \left(\frac{U_0}{U_a}\right) \left(\frac{x}{d}\right)^{2/3} \tag{37}$$

In equation 3-2, the non-dimensionalising has been done by B_0/U_a^3 which follows directly from equation 37 conform,

$$\frac{z}{\Delta_0 U_0 A_0 / U_a^3}$$

$$= \left[\frac{3}{8}\frac{1}{k^2}\right]^{2/3} \frac{d}{\left(\Delta_0 U_0 A_0 / U_a^3\right)^{1/3}} \frac{U_0}{U_a} \left(\frac{U_0}{\sqrt{\Delta_0 d}}\right)^{-2/3} \left(\frac{1}{d^{2/3}}\right) \left(\frac{x}{\Delta_0 U_0 A_0 / U_a^3}\right)^{2/3}$$

$$\Rightarrow \quad \frac{z}{\Delta_0 U_0 A_0 / U_a^3} = \left[\frac{3}{8}\frac{1}{k^2}\right]^{2/3} \left(\frac{4}{\pi}\right)^{2/3} \left(\frac{x}{\Delta_0 U_0 A_0 / U_a^3}\right)^{2/3}$$

So

$$\frac{z}{B_0 / U_a^3} = \left[\frac{3}{2\pi}\frac{1}{k^2}\right]^{2/3} \left(\frac{x}{B_0 / U_a^3}\right)^{2/3}$$

Integrating the spread assumption gives:

$$\frac{b_T}{d} = m\frac{z}{d} \tag{38}$$

Combining the vertical momentum and buoyancy flux equations gives:

$$\pi \frac{u_T}{U_a} b_T^2 = \frac{\Delta_0 Q_0}{U_a^3} x \tag{39}$$

$$\Rightarrow \quad \frac{u_T}{U_0} = \frac{\Delta_0 Q_0}{U_a^2} \frac{1}{\pi} \frac{x}{b_T^2} \frac{1}{U_0} \tag{40}$$

$$\Rightarrow \quad \frac{u_T}{U_0} = \Delta_0 \frac{1}{4} \frac{U_0 d^2}{U_a^2} \frac{1}{U_0} \frac{x}{b_T^2} \tag{41}$$

$$\Rightarrow \quad \frac{u_T}{U_0} = \frac{\Delta_0 d}{U_0^2} \frac{1}{4} \left(\frac{U_0}{U_a}\right)^2 \frac{d^2}{b_T^2} \frac{x}{d} \tag{42}$$

$$\Rightarrow \quad \frac{u_T}{U_0} = \frac{1}{4} \frac{1}{F_{r0}^2} \left(\frac{U_0}{U_a}\right)^2 \frac{d^2}{z^2 m^2} \left[\frac{8m^2}{3}\right]^{1/2} F_{r0} \left(\frac{U_a}{U_0}\right)^{3/2} \left(\frac{z}{d}\right)^{3/2} \tag{43}$$

$$\Rightarrow \quad \frac{u_T}{U_0} = \left[\frac{1}{16}\frac{8}{3m^2}\right]^{1/2} \frac{1}{F_{r0}} \left(\frac{U_0}{U_a}\right)^{1/2} \left(\frac{d}{z}\right)^{1/2} \tag{44}$$

$$\Rightarrow \qquad \frac{u_T}{U_0} = \left[\frac{1}{6m^2}\right]^{1/2} \frac{1}{F_{r0}} \left(\frac{U_0}{U_a}\right)^{1/2} \left(\frac{d}{z}\right)^{1/2} \tag{45}$$

The buoyancy flux then gives the dilution:

$$U_a \Delta_T \pi b_T^2 = \frac{\pi}{4} U_0 d^2 \Delta_0 \tag{46}$$

$$\Rightarrow \qquad \frac{\Delta_o}{\Delta_T} = 4 \frac{U_a}{U_0} \frac{b_T^2}{d^2} \tag{47}$$

$$\Rightarrow \qquad \frac{\Delta_o}{\Delta_T} = 4 m_T^2 \frac{U_a}{U_0} \left(\frac{z}{d}\right)^2 \tag{48}$$

Again non-dimensionalising with B_0/U_a^3 gives equation 3-1.

Momentum Puff

Assumptions

- The ambient velocity is large enough to influence the mixing behaviour.
- The formation of a momentum puff dramatically alters the nature of the discharge in terms of its trajectory, structure, rate of rise and dilution.
- The predictions of the flow path also needs to incorporate the impact of ambient motion.
- There is no density difference between discharged and ambient fluids, and the initial momentum is non-zero.
- Initially the flow will behave like a weakly advected jet and after a certain length scale the flow will behave like a line advected thermal.
- The flow will transition from jet to momentum puff.
- The relevant length scale are the ratios between initial and entrained momentums (see table 5-3).

The ratio of the entrained momentum and the *initial momentum* in weakly-advected jet region is given by:

$$\frac{M_a}{M_0} \approx \frac{U_a Q}{M_0} = \frac{U_a \pi b_T^2 u_T}{M_0} = \frac{U_a}{M_0} \pi k_T^2 s^2 \left(\frac{M_0}{\pi}\right)^{1/2} \frac{1}{k_T s}$$

$$\frac{M_a}{M_0} \approx \frac{U_a d}{M_0^{1/2}} \pi^{1/2} k_T s_*$$

At the transition ($s=S_{JMP}$) to strongly-advected behaviour $M_a \sim M_0$ and letting at this location gives:

$$1 \sim \frac{U_a d}{M_0^{1/2}} \pi^{1/2} k_T S_{JMP*}$$

So: $$S_{JMP*} \sim \frac{1}{\pi^{1/2} k_T} \frac{M_0^{1/2}}{U_a d}$$

Momentum Conservation can be set around a moving control volume conform Figure 3:

$$\sum F_z = \frac{\partial}{\partial t}\left(\int_{CV} \rho v_z d\forall\right) + \int_{CS} \rho v_z (\vec{v} \bullet \vec{n}) dA$$

In this case the vertical momentum within the control volume remains constant as it moves downstream and the momentum conservation should be applied in the direction of discharge.

There is a flux of momentum into the control volume due to the entrained flow. However, the entrainment velocities are very small at the control volume boundary (surface C) and the inflow is symmetrical. We can therefore neglect the second term on the RHS of the equation.

The momentum equation can therefore be written as:

$$0 = \frac{d}{dt}\left(u_T \rho \pi b_T^2 \Delta x\right)$$

Dividing by Δx and ρ gives: $$0 = \frac{d}{dt}\left(u_T \pi b_T^2\right)$$

Note that $U_a = \frac{dx}{dt}$ so: $$0 = \frac{d}{dx}\left(U_a u_T \pi b_T^2\right)$$

Integrating we get: $$M_0 = U_a u_T \pi b_T^2$$

Spread assumption of the form: $$\frac{db_T}{dz} = m_T$$

Kikkert (2006) has shown the value of m_T for a line momentum puff is 0.74.

Combining the spread assumption with the momentum conservation equations gives:

$$u_T = \frac{M_0}{U_a}\frac{1}{\pi m_T^2}\frac{1}{z^2}$$

The flow trajectory is given by: $$\frac{dz}{dx} = \frac{M_0}{M_a} = \frac{u_T Q}{U_a Q} = \frac{u_T}{U_a} = \frac{M_0}{U_a^2}\frac{1}{\pi m_T^2}\frac{1}{z^2}$$

Integrating this we get: $$\frac{z^3}{3} = \frac{M_0}{U_a^2}\frac{1}{\pi m_T^2}x$$

or: $$\frac{x}{M_0^{1/2}/U_a} = \frac{\pi}{3}m_T^2\left(\frac{z}{M_0^{1/2}/U_a}\right)^3$$

Within the moving control volume the tracer flux will also be conserved. This is because there is no mass flux into the control volume through surface A and B, and the mass flux through surface C contains no tracer. Starting with a general equation for conservation of tracer flux:

$$0 = \frac{\partial}{\partial t}\left\{\int_{CV} c\, d\forall\right\} + \int_{CS} c(\vec{u}\bullet\vec{n})dA$$

Now where $(\vec{u}\bullet\vec{n})dA \neq 0$, c = 0 so this term disappears and thus:

$$\frac{d}{dt}\left\{c_T \pi b_T^2 \Delta x\right\} = 0$$

And this becomes: $$\frac{d}{dx}\left\{U_a c_T \pi b_T^2 \Delta x\right\} = 0$$

or $$U_a c_T \pi b_T^2 = const$$

At the source the flux of tracer is $Q_0 C_0$, and thus:

$$U_a c_T \pi b_T^2 = Q_0 C_0$$

The tracer flux equation then is given by:

$$U_a c_T \pi b_T^2 = \frac{\pi}{4}U_0 d^2 C_0$$

$$\Rightarrow \frac{C_0}{c_T} = 4\frac{U_a}{U_0}\frac{b_T^2}{d^2}$$

$$\Rightarrow \frac{C_0}{c_T} = 4m_T^2\frac{U_a}{U_0}\left(\frac{z}{d}\right)^2$$

Strongly advected jet

Assumptions

- The ambient velocity is large enough to influence the mixing behaviour.
- The predictions of the flow path also needs to incorporate the impact of ambient motion.
- There is no density difference between discharged and ambient fluids, and the initial momentum is non-zero.
- Initially the flow will behave like a weakly advected jet and after a certain length scale the flow will behave like a strongly advected jet.
- The flow will transition from weakly advected jet to strongly advected jet.
- The relevant length scale are the ratios between initial and entrained momentums (see table 5-3).

Arguments for the development of the strongly-advected jet are essentially the same as those for a line momentum puff, however, the principle difference is the direction of discharge relative to the ambient motion. Here the discharge is in the same direction as the ambient.

Using the conservation of momentum:

$$M_0 = -U_a Q_\alpha + (U_a + u_T) Q_T$$

And

$$Q_\alpha = Q_T - Q_0$$

So

$$M_0 - U_a Q_0 = (U_0 - U_a) Q_0 = u_T Q_T$$

gives:

$$(U_0 - U_a) Q_0 = U_{e0} Q_0 = u_T (U_a + u_T) \pi b_T^2$$

For situations where the ambient is not moving the spread was given by:

$$\frac{db_T}{dx_{(U_a=0)}} = k_T$$

In this situation:

$$dx_{(U_a=0)} = u_T \, dt$$

With an ambient current the distance travelled is given by:

$$dx = (u_T + U_a)dt$$

Hence:

$$\frac{dx_{(U_a=0)}}{dx} = \frac{u_T}{(u_T + U_a)}$$

And the spread assumption becomes:

$$\frac{db_T}{dx} = k_T \frac{u_T}{(u_T + U_a)}$$

Conserving Pollutant gives:

$$C_0 Q_0 = c_T (U_a + u_T)\pi b_T^2$$

As $u_T/U_a << 1$ the relationships simplify to:

$$U_{e0} Q_0 \approx u_T U_a \pi b_T^2$$

With

$$\frac{db_T}{dx} \approx k_T \frac{u_T}{U_a}$$

And

$$C_0 Q_0 \approx c_T U_a \pi b_T^2$$

Momentum equations gives:

$$\frac{U_{e0} Q_0}{U_a^2} \frac{1}{\pi b_T^2} \approx \frac{u_T}{U_a}$$

So the spread relationship becomes:

$$\frac{db_T}{dx} \approx k_T \frac{U_{e0} Q_0}{U_a^2} \frac{1}{\pi b_T^2}$$

Integrating the spread relationship we get (assuming relatively large x):

$$b_T \approx \left[\frac{3}{\pi} k_T \frac{U_{e0} Q_0}{U_a^2} x \right]^{1/3}$$

Substituting back into the momentum equation gives us the velocity:

$$\frac{u_T}{U_a} \approx \left[\frac{1}{3k_T} \left(\frac{U_{e0} Q_0}{\pi U_a^2} \right)^{1/2} \frac{1}{x} \right]^{2/3}$$

The velocity and spread relationships then enable us to determine the dilution:

$$\frac{C_0}{c_T} \approx \left[3\pi^{1/2} k_T \frac{U_{e0}}{(U_a Q_0)^{1/2}} x \right]^{2/3}$$

The equations can be written in a more convenient form by letting $U_{e0}\, Q_0 = Me_0$ and recognising that $M_{e0}{}^{1/2}/U_a$ has the dimension of length. We can then write:

Spread

$$\frac{b_T}{M_{e0}^{1/2}/U_a} \approx \left[\frac{3}{\pi} k_T \frac{x}{M_{e0}^{1/2}/U_a} \right]^{1/3}$$

Velocity

$$\frac{u_T}{U_a} \approx \left[\frac{1}{3k_T \pi^{1/2}} \frac{M_{e0}^{1/2}/U_a}{x} \right]^{2/3}$$

Dilution

$$\frac{C_0}{c_T} \approx \frac{U_{e0}}{U_a} \left[3\pi^{1/2} k_T \frac{x}{M_{e0}^{1/2}/U_a} \right]^{2/3}$$

In the weakly-advected region, where u_T/U_a is much greater than 1 the governing equations become:

$$U_{e0} Q_0 \approx u_T^2 \pi b_T^2$$

with $$\frac{db_T}{dx} \approx k_T$$

and $$C_0 Q_0 \approx c_T u_T \pi b_T^2$$

These give the same solutions as those for a weakly advected jet.

To integrate dilution in y-direction, the midline dilution (eqn. 4-3) is combined with the spread (eqn. 4-5) according to (Kikkert 2007)

$$\frac{C_0}{C} = \frac{C_{i0}}{C_{iy}} \frac{b_c \sqrt{\pi}}{d} = \frac{C_{i0}}{C_{iy}} \frac{b\lambda\sqrt{\pi}}{d}$$

Then equation 4-3 becomes

$$\frac{1}{cos\theta_0{}^{2/3}} \frac{U_{ar}}{1 - U_{ar}} \frac{C_{i0}}{C_{iy}} \frac{b\lambda\sqrt{\pi}}{d} = I_c \left(\frac{3k}{C_{jk} I_q} \right)^{2/3} \left(\frac{x}{l_{jwj}} \right)^{2/3}$$

Eqn. 4-5 is non-dimensionalised with l_{jwj}, so

$$cos^{2/3}\theta_0 \frac{b}{l_{jwj}} = \left(\frac{3k}{C_{Jk} I_q} \right)^{1/3} \left(\frac{x}{l_{jwj}} \right)^{1/3}$$

Or

$$\frac{b\lambda}{d} = \left(\frac{b}{l_{jwj}}\frac{l_{jwj}}{d}\lambda\right) = \left(\frac{3k}{C_{Jk}I_q}\right)^{1/3}\left(\frac{x}{l_{jwj}}\right)^{1/3}\frac{l_{jwj}}{d}\frac{1}{cos^{2/3}\theta_0}\lambda$$

Fill in:

$$\frac{1}{cos\theta_0{}^{2/3}}\frac{U_{ar}}{1-U_{ar}}\frac{C_{i0}}{C_{iy}}\left(\frac{3k}{C_{Jk}I_q}\right)^{1/3}\left(\frac{x}{l_{jwj}}\right)^{1/3}\frac{l_{jwj}}{d}\frac{\lambda\sqrt{\pi}}{cos^{2/3}\theta_0} = I_c\left(\frac{3k}{C_{jk}I_q}\right)^{2/3}\left(\frac{x}{l_{jwj}}\right)^{2/3}$$

Simplified:

$$\frac{1}{cos\theta_0{}^{4/3}}\frac{U_{ar}}{1-U_{ar}}\frac{C_{i0}}{C_{iy}}\frac{l_{jwj}}{d}\lambda\sqrt{\pi} = I_c\left(\frac{3k}{C_{jk}I_q}\right)^{1/3}\left(\frac{x}{l_{jwj}}\right)^{1/3}$$

$$\frac{l_{jwj}}{d} = \frac{M_{e0}^{1/2}\cos\theta_0\Big/U_a}{d} = \frac{\left((U_0-U_a)U_a\frac{\pi}{4}d^2\right)^{1/2}\cos\theta_0\Big/U_a}{d} = \frac{(U_0-U_a)^{1/2}\sqrt{\pi}\cos\theta_0}{2U_a^{1/2}}$$

so

$$\frac{l_{jwj}}{d} = \frac{\cos\theta_0\sqrt{\pi}}{2}\left(\frac{1-\frac{U_a}{U_0}}{\frac{U_a}{U_0}}\right)^{1/2} = \frac{\cos\theta_0\sqrt{\pi}}{2}\left(\frac{1-U_{ar}}{U_{ar}}\right)$$

Fill in above eqn:

$$\frac{1}{cos\theta_0{}^{4/3}}\frac{U_{ar}}{1-U_{ar}}\frac{C_{i0}}{C_{iy}}\frac{\cos\theta_0\,\lambda\sqrt{\pi}}{2}\left(\frac{1-U_{ar}}{U_{ar}}\right)^{1/2}\sqrt{\pi} = I_c\left(\frac{3k}{C_{jk}I_q}\right)^{1/3}\left(\frac{x}{l_{jwj}}\right)^{1/3}$$

Then

$$\frac{1}{cos\theta_0{}^{1/3}}\left(\frac{U_{ar}}{1-U_{ar}}\right)^{1/2}\frac{C_{i0}}{C_{iy}} = \left(\frac{3k}{C_{jk}I_q}\right)^{1/3}\left(\frac{x}{l_{jwj}}\right)^{1/3}$$

The trajectory of a strongly advected jet is given as eqn. (4-6). The derivation for uses the momentums in z and x direction, conform (larger x):

$$\frac{dz}{dx} = \frac{M_{e0}\sin\theta_0}{U_aQ} = \frac{U_{e0}Q_0\sin\theta_0}{U_ab^2\frac{\pi}{4}UQ}$$

Then fill in the spread, b, from the spread equation:

$$\frac{dz}{dx} = \frac{U_{e0} Q_0 \sin\theta_0}{U_a \frac{\pi}{4} UQ} \left(\frac{1}{\left(\frac{3k}{C_{Jk} I_q}\right)^{1/3} \left(\frac{x}{l_{jwj}}\right)^{1/3} \frac{l_{jwj}}{cos^{2/3}\theta_0}} \right)^2$$

Which then becomes:

$$dz = \frac{1}{U_a \frac{\pi}{4} UQ} \frac{U_{e0} Q_0 \sin\theta_0}{\left(\frac{3k}{C_{Jk} I_q}\right)^{2/3} \left(\frac{x}{l_{jwj}}\right)^{2/3} \frac{\left(l_{jwj}\right)^2}{cos^{4/3}\theta_0}} dx$$

Simplifying, integrating and non-dimensionalising with l_{jwj} gives:

$$\frac{1}{tan\theta_0 cos^{1/3}\theta_0} \frac{z}{l_{jwj}} = \frac{4}{3\pi^2 \left(\frac{3k}{C_{Jk} I_q}\right)^{2/3}} \left(\frac{x}{l_{jwj}}\right)^{1/3}$$

Appendix B – Concentration figures

In figure 1 the integrated instantaneous concentration plots of a 3D 22° discharge plot are shown. The three plots show the integrated development of the flow in time. In figure 2, the summated resultant plot of the entire flow is shown. This plot is the result of the addition of 2591 instantaneous integrated concentration images. It is worth noting that the instantaneous images from the LA system represent integrated concentration information and hence a significant averaging process is inherent in these images. The LA system does not provide instantaneous local information and thus the flow structures evident in these instantaneous images are more difficult to interpret.

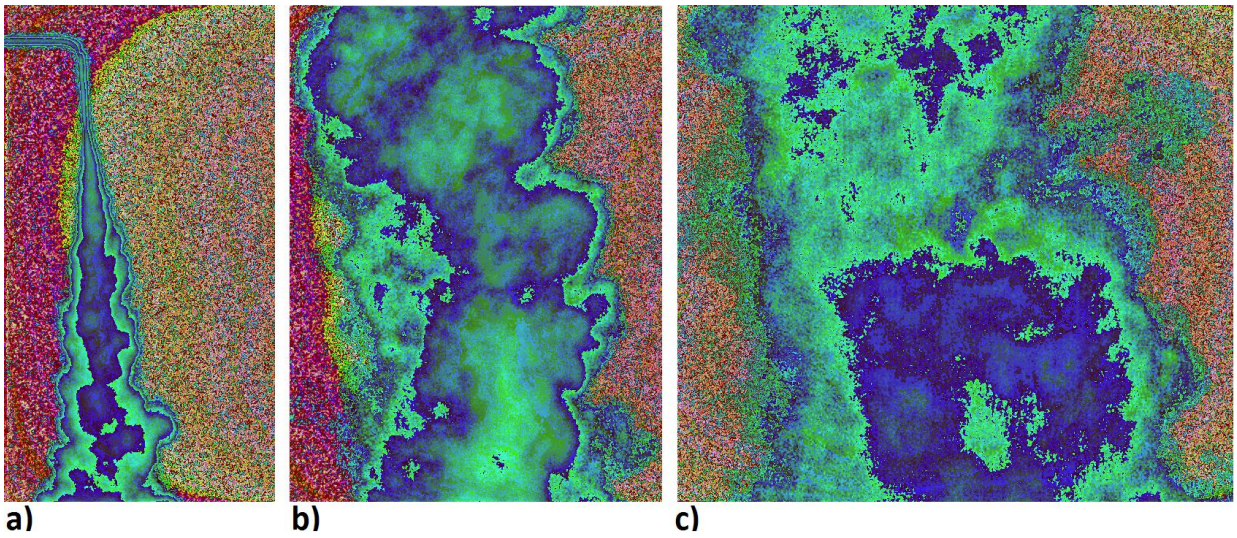

Figure 1: Integrated instantaneous concentration plots of a 3D 22° discharge, figure 1a) was taken at time 11 seconds after the start of the experiment, figure 1b) after 23.4 seconds after the start and figure 1c) after 43.2 seconds.

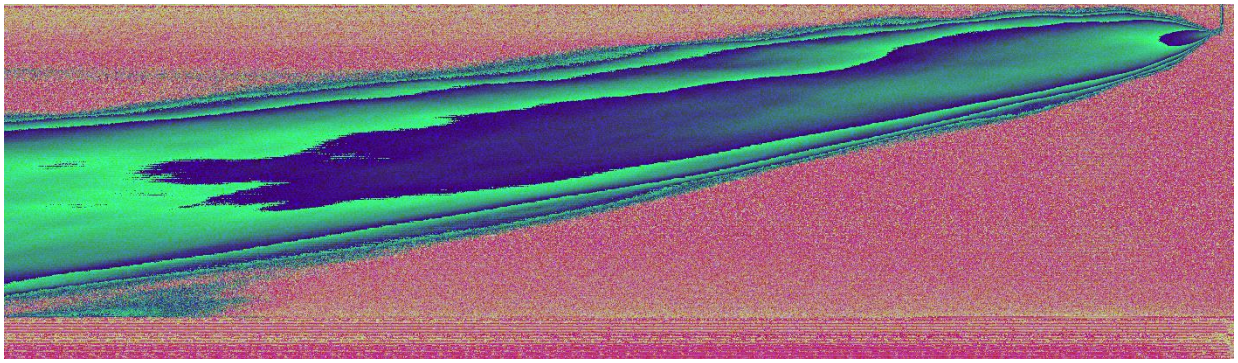

Figure 2: Entire integrated flow of a 22° discharge, the result of the addition of 2591 separate instantaneous images.